Réseaux de vortex contrôlés et lumière non-classique avec des polaritons de microcavité

Thomas Boulier

THÈSE DE DOCTORAT
DE L'UNIVERSITÉ PIERRE ET MARIE CURIE

Spécialité : Physique quantique

École doctorale : « Physique en Île-de-France »

Réalisée au Laboratoire Kastler Brossel

Controlled vortex lattices and non-classical light with microcavity polaritons

---

Présentée par :

Thomas BOULIER

Pour obtenir le titre de :

DOCTEUR DE L'UNIVERSITÉ PIERRE ET MARIE CURIE

Soutenue le 25 novembre 2014

Devant le jury composé de :

Mauro Antezza	Rapporteur
Pavlos Savvidis	Rapporteur
Raffaele Colombelli	Examinateur
Maxime Richard	Examinateur
Valia Voliotis	Examinateur
Alberto Bramati	Directeur de thèse

Abstract

Polaritons are bosonic quasiparticles coming from the strong coupling between photons and excitons in a solid-state semiconductor microcavity. Due to their short lifetime and their strong nonlinear interactions, polaritons are an ideal system to study fundamental problems of out-of-equilibrium quantum hydrodynamics as well as more applied problematic in quantum optics, such as the implementation of ultrafast opto-electronic switches or the generation of non-classical states of light.

In this thesis the two themes are treated. In the first part of my thesis I will depict several schemes by which we optically inject a controlled angular momentum in a polartion superfluid, in order to observe its nucleation into elementary vortices. The impact of the geometry, disorder, and polariton-polariton nonlinear interactions is studied. We show the conservation of angular momentum in the steady state regime despite the open, out-of-equilibrium nature of the system. In the linear regime, an interference pattern containing phase defects is visible. In the nonlinear (superfluid) regime, the interference disappear and the vortices nucleate as a consequence of the angular momentum conservation. Finally, constraining the geometry we were able to create in a controlled way a stable ring of elementary vortices of the same sign, opening the way to the study of vortex-vortex interactions in quantum fluids of light [1].

A second aspect of polaritons is the quantum properties of their emitted light. In the second part of the manuscript I describe a novel source of continuous-variable squeezed light in pillar-shaped semiconductor microcavities in the strong coupling regime. Indeed, the generation of squeezed and entangled light fields is a crucial ingredient for the implementation of quantum information protocols. In this context, semiconductor materials offer a strong potential for the implementation of on-chip devices operating at the quantum level. Here, degenerate polariton four-wave mixing is obtained by exciting the pillar at normal incidence. We observe a bistable behavior and we demonstrate the generation of squeezing near the turning point of the bistability curve. The confined pillar geometry allows for a larger amount of squeezing than planar microcavities due to the discrete energy levels protected from excess noise. By analyzing the noise of the emitted light we obtain a measured intensity squeezing of 20.3%, inferred to be 35.8% after corrections for losses in the detection setup.

Preface

Les polaritons sont des quasi-particules bosoniques venant du couplage fort entre des photons de cavité et des excitons confinés dans une hétérostructure semiconductrice. De par leur temps de vie très court et leur très fortes interactions, les polaritons sont un système idéal pour étudier des problèmes fondamentaux d'hydrodynamique quantique hors équilibre ainsi que des aspects plus appliqués d'optique quantique, comme l'implémentation de transistors opto-electroniques ultra-rapides ou la génération d'états non-classiques de la lumière.

Ces deux thèmes sont traités dans cette thèse. Dans la première partie j'y dépeins plusieurs méthodes par lesquelles on injecte optiquement un moment angulaire donné dans un superfluide de polaritons, afin d'observer sa nucléation en plusieurs vortex élémentaires. L'impact de la géometrie, du désordre et de l'interaction nonlinéaire de type "polariton-polariton" sont étudiés. Nous démontrons la conservation du moment angulaire dans le régime stationnaire malgré la nature hors équilibre et ouverte du système. Dans le régime linéaire, un reseau d'interférences contenant des singularités de phase (vortex optiques) est visible. Dans le régime nonlinéaire (superfluide), les interférences disparaissent et des vortex du même signe se forment en conséquence de la conservation du moment angulaire injecté. Enfin, en ajoutant une contrainte sur la géométrie du système nous avons créé de manière controlée un anneau stable de vortex élémentaire du même signe, ce qui pourrait ouvrir la voie à l'étude des interactions inter-vortex dans les fluides quantiques de lumière [1].

Un autre aspect des polaritons sont les propriétés quantiques de la lumière qu'ils émettent. Dans la seconde partie de cette thèse, je décris une source améliorée de lumière comprimée en régime de variables continues dans des micropiliers semiconducteurs en régime de couplage fort. En effet, la génération de lumière comprimée et intriquée est un ingrédient crucial pour l'implémentation de protocoles en information quantique. Dans ce contexte, les matériaux semiconducteurs ont un grand potentiel pour la réalisation d'éléments sur puce opérant au niveau quantique. Ici, un mélange à quatre ondes dégénérées est obtenu en excitant le micro-pilier à incidence normale. Nous observons un comportement bistable et démontrons la génération de lumière comprimée près du point tournant de la courbe de bistabilité. La nature confinée de la géométrie du piller permet d'atteindre un taux de compression bien supérieur que dans les microcavités planaires, grâce aux niveaux d'énergies discrets protégés des excès de bruits. En analysant le bruit dans la lumière émise par les micro-piliers, nous obtenons une réduction du bruit d'intensité mesurée à 20.3%, et estimée à 35.8% après correction des pertes de détection.

Acknowledgements

Taking a few steps back to contemplate the last three years, one can see that this PhD thesis is not the the fruit of an individual work, but a team effort. I wish here to thank all those who helped me.

First, let me thank Paul Indelicato and Antoine Heidmann, who directed the laboratory during my PhD. I also own a hearty thank you to Monique Granon, whose remarkable efficiency and amiability contributed to make of my time in the laboratory a pleasant experience.

Of course, this PhD would not have been possible without the kind guidance of my advisor, Alberto Bramati, to whom I am very thankful. Thanks to his scientific excellence, his patience and his relaxed demeanor, it was a real pleasure to work for him. Likewise, I am thankful to Elisabeth Giacobino and Quentin Glorieux for their availability and their always-excellent advice, scientific and otherwise.
I also own much to the group's previous generation of PhD students and postdocs, especially Romain Hivet, Emiliano Cancellieri and Godefroy Leménager, from whom I learned much and who contributed much to the good atmosphere that transpired in the group. In addition, I would like to thank my colleagues and friends, whether from our team of not, for their ever-present friendship and comradery. In particular thanks to Mathieu Manceau, Theo Rybarczyk and Christelle Tuambilangana for their patient support in stressful times, and for being themselves. I wish them good fortune in their futures, wherever their professional paths lead them.
Thanks also to Adrien, Amaury, Baptiste, Lucile, Stefano, Panayotis, Roman, Valerian, Sacha, ... and the many people I am probably forgetting here, but not in my heart.
Finally, I am thankful to many LKB members, both scientific and administrative, for the help they provided in my researches.

A PhD takes time and investment, and the work does not necessarily stop at your home doorsteps. Therefore I give a loving thank you to Quang Long, and to my whole family, for simply being there and for keeping on supporting me for so long, even in my many moody days.

To you all, from the bottom of my heart, thank you.

« Le savant n'étudie pas la nature parce que cela est utile,
il l'étudie parce qu'il y prend plaisir,
et il y prend plaisir parce qu'elle est belle. »

— Henri Poincaré, 1854–1912

Contents

Introduction **1**

1. Microcavity polaritons **3**
1.1. Excitons in a bulk semiconductors . . . 3
1.1.1. Band theory and conduction properties . . . 3
1.1.2. Optical excitation in direct gap semiconductors . . . 4
1.2. Excitons in a semiconductor quantum well . . . 7
1.2.1. Bidimensional exciton confinement . . . 7
1.2.2. Properties of bidimensional excitons . . . 9
1.3. Photons in an optical microcavity . . . 10
1.3.1. Optical microcavity . . . 11
1.3.2. Cavity photon properties . . . 13
1.4. Strong coupling between excitons and photons . . . 16
1.4.1. Hamiltonian description of the strong coupling regime . . . 18
1.4.2. Physical interpretation . . . 21
1.4.3. Dispersion relation and anticrossing . . . 23
1.4.4. Polaritons as bosonic spinors . . . 25
1.4.5. All-optical control . . . 26
1.5. 0D confinement in micropillars . . . 27
1.6. Nonlinear aspects of polariton many body systems . . . 29
1.6.1. Self energy and nonlinear Hamiltonian . . . 29
1.6.2. Limits of the bosonic model . . . 31

I. Vortex lattices in polariton superfluids **33**

2. Bose-Einstein condensation, superfluidity and elementary votices **37**
2.1. Bose-Einstein condensation and superfluidity . . . 37
2.1.1. Polariton Bose-Einstein condensation . . . 38
2.1.2. Gross-Pitaevskii equation . . . 39
2.1.3. Landau criterion for superfluidity . . . 43
2.1.4. Elementary excitation spectrum . . . 44

2.2. Quasi-resonant injection of polaritons . . . 46
2.2.1. Gross-Pitaevskii for polaritons: driven-dissipative equation . . . 46
2.2.2. Bistability . . . 47
2.2.3. Polariton superfluidity . . . 50
2.3. Elementary vortices . . . 52
2.4. State of the Art: interacting fluids of light . . . 56

3. Interaction-shaped vortex-antivortex lattices 61
3.1. Setup . . . 62
3.2. Trapped vortex-antivortex lattices: metallic mask setup . . . 72
3.2.1. General setup description . . . 73
3.3. Annihilation of vortex-antivortex pairs: multi-pumps setup . . . 84
3.3.1. Multi-beam pumping: experimental description . . . 84
3.3.2. Results . . . 86
3.3.3. Comparison with related research activities . . . 92
3.3.4. Theoretical work . . . 94

4. Angular momentum conservation in polariton superfluids 101
4.1. Motivations and Method . . . 101
4.1.1. Injection method and vortex confinement . . . 102
4.1.2. Limitations . . . 104
4.2. Results . . . 107
4.2.1. Direction of rotation . . . 107
4.2.2. Low density regime . . . 109
4.2.3. High density regime . . . 109
4.3. Conclusion . . . 114

5. Injection of angular momentum: single rotating superfluid 115
5.1. Theoretical predictions . . . 115
5.2. Experimental setup . . . 116
5.2.1. Laguerre-Gauss beam preparation . . . 116
5.2.2. Effect of the bistability . . . 120
5.3. Results . . . 120
5.3.1. Low density regime . . . 121
5.3.2. High density regime . . . 123
5.4. Interpretation . . . 123

6. Vortex chains in polariton superfluids 127
6.1. Deterministic same-sign vortex chains . . . 127

6.2. Experimental setup . . . 128
6.2.1. Pump preparation . . . 128
6.3. Results . . . 132
6.3.1. Low density regime . . . 132
6.3.2. Medium to high density regimes . . . 133
6.3.3. Phase freedom in the nonlinear regime . . . 134
6.4. Conclusion . . . 139
6.5. General Conclusion . . . 139

II. Squeezed states driven by polariton-polariton interactions in semiconductor micropillars 143

7. Polariton-based generation of squeezed states 145
7.1. Noise properties of a scalar field . . . 146
7.1.1. Notions of fluctuations and shot-noise . . . 146
7.1.2. Quantum fluctuations for a laser . . . 147
7.1.3. Effect of losses on squeezing . . . 147
7.2. Generation of squeezing in a polariton field . . . 149
7.2.1. The Heisenberg-Langevin equation . . . 149
7.2.2. Extra-cavity fluctuations . . . 151
7.3. Squeezing in polaritons: context . . . 157
7.3.1. Advantages of polaritons . . . 157
7.3.2. Previous experimental results on a planar microcavity . . . 158
7.3.3. Micropillar design . . . 159
7.4. Experimental setup: Sample, cooling and pumping . . . 160
7.4.1. Sample . . . 160
7.4.2. Laser source . . . 161
7.4.3. Cryogenic setup . . . 163
7.5. Experimental setup: detection . . . 163
7.5.1. Homodyne detection . . . 165
7.5.2. Balanced detection . . . 166
7.5.3. Practical description . . . 166
7.6. Results . . . 169
7.6.1. Bistable behavior . . . 169
7.6.2. Intensity noise as a function of the pump power . . . 174
7.6.3. Amplitude quadrature detection at fixed pump intensity . . . 178
7.6.4. Amplitude quadrature spectrum . . . 179
7.6.5. Homodyne detection . . . 179

7.7. Conclusion 181

A. Phase reconstruction method **183**

B. Publications **185**

C. List of publications and oral presentations **205**

Bibliography **209**

Introduction

With the explosion of information technologies that started in the 70s, quantum mechanics has slowly found its place in the technological landscape. Direct commercial applications such as quantum cryptographers are beginning to appear while indirect applications have been common for decades through condensed matter physics, and in particular semiconductors.

Semiconductors are a type of insulator material that can be made conductive when electrically or optically excited. While electrical excitation has been leading in the development of semiconductor physics for many years due to the advent of electronics, optical excitation yields faster responses and a greater control. With the great improvements over the control of photons in the past decades physicists have since turned towards the study of optically controlled semiconductor heterostructures. These structures offer a great opportunity to revisit in solid state materials the interaction between light and matter, previously explored in the context of atomic physics and which led to many developments.

In the last decade of the twentieth century, new techniques of heterostructures growth allowed to create nanometer-thin layers of material. This made possible to engineer planar quantum wells embedded into micrometer thick optical cavities. It was in such a microcavity that C. Weisbuch first observed in 1992 [2] the strong coupling between light and matter in a semiconductor system: bosonic quasiparticles called Exciton-Polaritons, arising from the strong coupling between an electron-hole pair (the quantum well first excited state) and a cavity photon.

Since then microcavity polaritons have been extensively studied and their basic properties (dispersion curve, lifetime and relaxation) are well known [3] [4] [5]. Their photonic part gives them a very low effective mass allowing to form and to study non-equilibrium Bose–Einstein condensates at high temperatures (between 5 K and room temperature [6]), while their excitonic part makes of polariton fluids a very nonlinear optical system able to show interesting behaviors such as four-wave mixing [7], squeezing [8] and promising otpo-electronic devices [9, 10, 11, 12] in the micrometer scale.

These outstanding properties make of polaritons an ideal system to study fundamental problems of quantum hydrodynamics (such as superfluidity [13, 14] and bidimensional

topological defects in scalar [15, 16, 17, 18, 19] and spinor [20] fields), as well as to treat more applied problematic in quantum optics such as the generation of non-classical states of light.

In this thesis, I will treat both aspects. Chapter 1 is a general description of semiconductor microvavities and an introduction to the quantum description of exciton-polaritons. The rest of the manuscript is divided into two parts. The first part (chapters 2-6) is a study of the injection of angular momentum in a resonantly pumped superfluid of polaritons, leading to the spontaneous nucleation of elementary vortices. Their spatial organization is studied for differents angular momentum injection schemes. Chapter 2 gives the theoretical tools needed to fathom Bose–Einstein condensation, superfluidity and elementary vortex physics. Chapter 3 is a crossover with the previous group thesis with which I was deeply involved and describes a new phenomenon by which several superfluids merge together and stop interfering. Building on this result, chapters 4, 5 and 6 each describe a different experimental realization of angular momentum injection. The second part (chapters 7-8) describes the engineering of intensity squeezed light using the highly nonlinear properties of polaritons. We show the great improvement brought by the spatial confinement of polaritons in a specifically designed pillar-shaped microcavity. Chapter 7 lays the quantum optical basis of squeezing in the continuous variable regime and the theoretical aspects of the polariton noise, while chapter 8 details the corresponding experiment, in a confined and resonantly pumped polariton condensate.

The appendix cover the method used to extract the polariton phase from optical interferences, as well as publications.

Chapter 1.

Microcavity polaritons

Polaritons are mixed states of light and matter, arising from the strong coupling between photons and excitons. To introduce the physics of polariton we must first describe excitons, cavity photons and how their confinement in a planar microcavity allows the strong coupling regime to be reached.

1.1. Excitons in a bulk semiconductors

The concept of excitons was first proposed by Yakov Frenkel in 1931 [21], when he described the excitation of atoms in a lattice of insulators. He proposed that this excited state would be able to travel in a particle-like fashion through the lattice without a net transfer of charge. It is an electrically neutral quasiparticle that exists in insulators, semiconductors and in some liquids. The exciton is regarded as an elementary excitation of condensed matter that can transport energy without transporting net electric charge [22].

1.1.1. Band theory and conduction properties

Quantum mechanics imposes quantized energy levels to electrons orbiting a single atom nucleus. Different levels correspond to different orbitals and give rise to the notion of electron shells found in chemistry. A chain of N atoms, each spaced by approximately their Bohr radius, cannot be described as a juxtaposition of N single atoms. Indeed, the coupling between neighboring atoms removes the degeneracy of each electronic level into N distinct energy levels. In this case an electron is not bound to a single atom but is delocalized over the entire chain of atoms. The high densities found in solid matter make the energy levels so numerous that they can be treated as a continuous band of energy, as is described in figure 1.1.

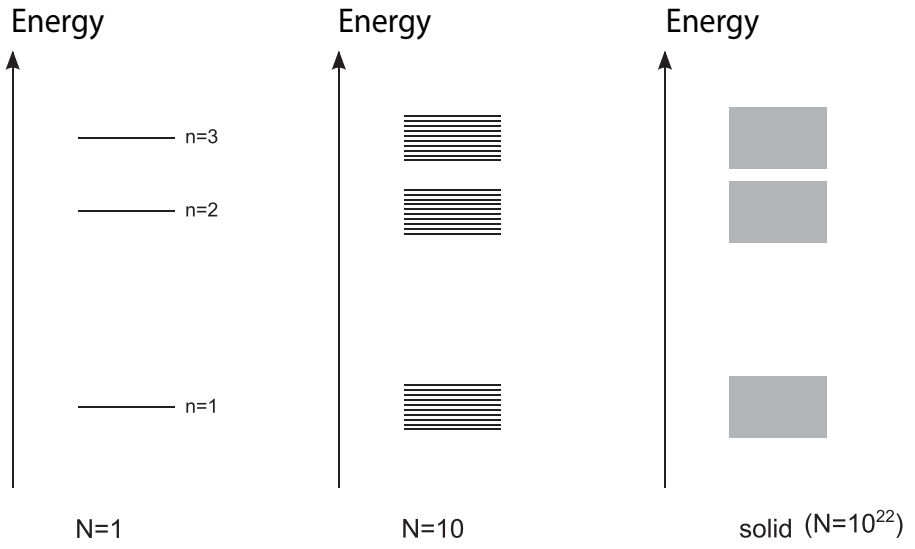

Figure 1.1.: Formation of conduction bands - Schematic representation of an electron energy in an atom, a chain of 10 atoms and a solid. In the latter the numerous energy levels form a continuum. From [23].

At zero temperature, electrons fill the lowest energy bands up to the Fermi energy level or chemical potential. The most energetic of the completely filled band is called the valence band (coming from the coupling of single atoms p-orbitals, with orbital angular momentum $l = 1$) and the next band is the conduction band (coming from the coupling of single atoms s-orbitals, with $l = 0$). They are separated by an energy gap band E_g. A material is called a metal if its Fermi energy is in its conduction band as the electrons can then freely propagate through the material. If the Fermi energy falls within the gap band, then the valence band is full while the conduction band is empty and the material properties depend on the gap size: for high E_g (several electronvolts (eV)) the electron density in the conduction band will be low (even at room temperature) and the material will be an insulator. If, however, E_g is low enough (around 1 eV) then electrons can be excited to the conduction band and the material is a semiconductor. While there are many ways of exciting an electron into the conduction band, in this discussion we will focus on optical excitation.

1.1.2. Optical excitation in direct gap semiconductors

Electron eigenstates in a material are labeled with the vector $\mathbf{k}$ representing the particle wavevector. A semiconductor is said to have a "direct gap" if in the energy-momentum

space the maximum of the valence band is at the same wavevector $\mathbf{k}$ as the minimum of the conduction band (see for example figure1.2). In such a direct gap semiconductor it is possible to excite an electron from the valence band into the conduction band by photon absorption if the photon energy satisfies $\hbar\omega > E_g$. This leaves an empty state in the valence band, called a *hole*. The excited free electron and its hole have opposite charges and momentum, and form an *electron-hole pair*. Nonetheless if the semiconductor is excited with a photon of energy $\hbar\omega < E_g$ we can observe discrete resonances corresponding to charge-induced bound states between the electron and its hole. Those bound electron-hole pairs are called *excitons*.

Excitons are analogues of Rydberg atoms as the Hamiltonian of both systems has the same expression with the same structure of energy levels and eigenmodes, giving exciton energy levels of type 1s, 2s, 2p and so on. The energy of the excitonic resonance can be written as:

$$E_{exc} = E_g - E_b + \frac{\hbar^2 K^2}{2m^*}, \tag{1.1}$$

where E_b is the electron-hole binding energy, $\hbar\mathbf{K}$ is the exciton momentum as defined in the electron-hole pair center of mass and m^* is the exciton effective mass given by the sum of the of the electron (e) and hole (h) effective masses $m^*_{e,h}$, each derived from their dispersion curve $E_{e,h}(k)$, following:

$$\frac{1}{m_i^*} = \frac{1}{\hbar^2}\frac{\partial^2 E_i}{\partial k^2}(k=0)\ ;\ i = e, h. \tag{1.2}$$

In most semiconductors the conduction band is unique as it arises from the coupling of single atoms s-orbitals (with orbital angular momentum $l_s = 0$) while the valence band (arising from single atoms p-orbitals coupling, with orbital angular momentum $l_p = 1$) can be multiple due to the spin-orbit coupling lifting the states degeneracy. In InGaAs semiconductors, an indium-doped version of which we used in this work, there is an energy split-off in the valence band between total angular momentum $J = \frac{1}{2}$ and $J = \frac{3}{2}$ with the $J = \frac{1}{2}$ band having a lower energy, as can be seen in figure 1.2. This $J = \frac{1}{2}$ band has two spin projections on the z quantization axis: $J_z = \pm\frac{1}{2}$, which are degenerate for all $\mathbf{k}$. The $J = \frac{3}{2}$ valence band, however, has two sub-bands corresponding to the two different values of $|J_z|$ ($J_z = \pm\frac{1}{2}$ and $J_z = \pm\frac{3}{2}$). These sub-bands are degenerate only for $\mathbf{k} = 0\,\mu\text{m}^{-1}$ and thus possess each a different curvature (i.e. two distinct effective masses), giving two different types of holes: "heavy hole" for the $J_z = \pm\frac{3}{2}$ band and "light holes" for $J_z = \pm\frac{1}{2}$. Since there are two kinds of holes, there are two types of excitons: "heavy excitons" and "light excitons" with, as their names suggest, different masses.

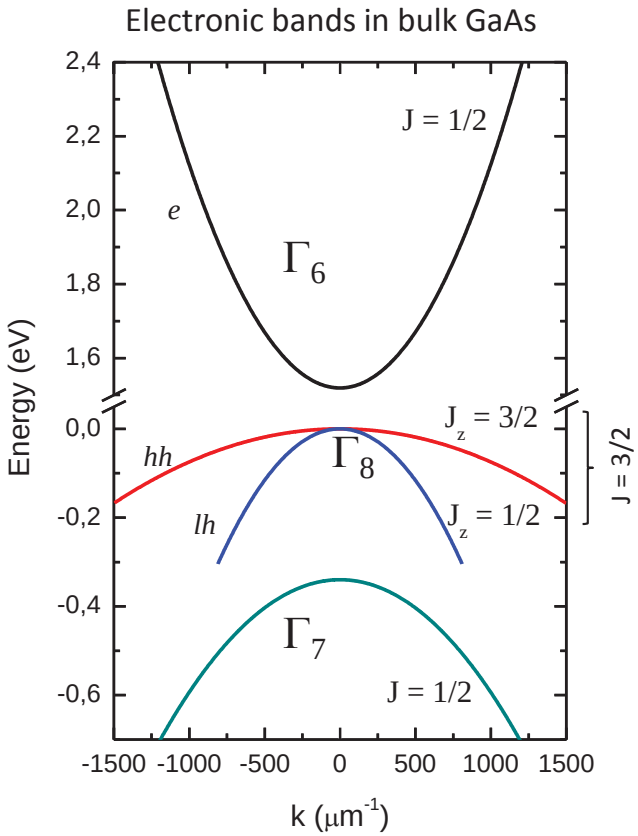

Figure 1.2.: GaAs Band structure – Conduction and valence band dispersion of bulk GaAs close to the fundamental gap, well approximated by parabolas. The black line is the electron conduction band while the red and blue lines are the dispersion curves of, respectively, the heavy and light holes for $J = \frac{3}{2}$. The green line is the $J = \frac{1}{2}$ valence band. Source: [24].

Excitons inherit their spin properties from their constituent electrons and holes. In particular for heavy excitons the combination of the electronic spin, with $J_z^{(e)} = \pm\frac{1}{2}$, and the heavy hole spin, with $J_z^{(hh)} = \pm\frac{3}{2}$, gives rise to two possible values for the excitonic spin, $J_{exc} = 1$ and $J_{exc} = 2$. Some selection rules need to be satisfied for an optical transition to take place. In the dipolar approximation, conservation of the total linear momentum and angular momentum is required. In particular since photons have total intrinsic angular momentum equal to one, it follows that only excitons with $J_{exc} = 1$ can be optically excited by one photon absorption. Excitons with $J_{exc} = 2$ cannot decay by photon emission and they are therefore called *dark excitons*. In a bulk semiconductor the excitonic spectrum is a 3D continuum of states $|K, J_z\rangle$ and the selection rules induce a one-to-one correspondence with the electromagnetic field modes $|k, \sigma\rangle$.

1.2. Excitons in a semiconductor quantum well

Excitons in bulk semiconductors have a limited coupling to light, making difficult the observation of polaritons. A key element towards strong coupling is the confinement of excitons, which we will describe now, as it allows stronger exciton-photon interactions.

1.2.1. Bidimensional exciton confinement

In the 70's, new methods of crystal growth, such as molecular beam or vapor phase epitaxy, allowed the realization of semiconductor hetero-structures small enough to confine excitons to 2, 1 or 0 dimensions. In this work we used quantum wells providing a bi- or zero-dimensional confinement. A quantum well is made of a semiconductor layer "sandwiched" by two layers of a different semiconductor possessing a higher band gap energy, usually a differently doped version of the same material. This creates a "notch" in the band structure, as illustrated in figure 1.3.

As a result, along the growth direction z, the translational invariance is broken, the excitonic eigenenergies are quantized and excitons are confined inside the well. On the other hand, translational invariance is preserved in the in-plane directions (x,y) for planar microcavities and the in-plane eigenenergies thus show a continuous parabolic dispersion (figure 1.4): The exciton wavevector $\mathbf{K}$ can be rewritten $\mathbf{K} = \left(\mathbf{k}_\parallel^{exc}, k_z^{exc}\right)$ where $\mathbf{k}_\parallel^{exc}$ lays on a bidimensional continuum while k_z^{exc} can only take discrete values.

In the in-plane direction, the band structure of a quantum well displays a remarkable difference with respect to bulk materials: the bands of heavy and light holes are no more degenerate at $\mathbf{k}_\parallel^{exc} = 0\ \mu\text{m}^{-1}$. This is due to the fact that in a quantum well the confining

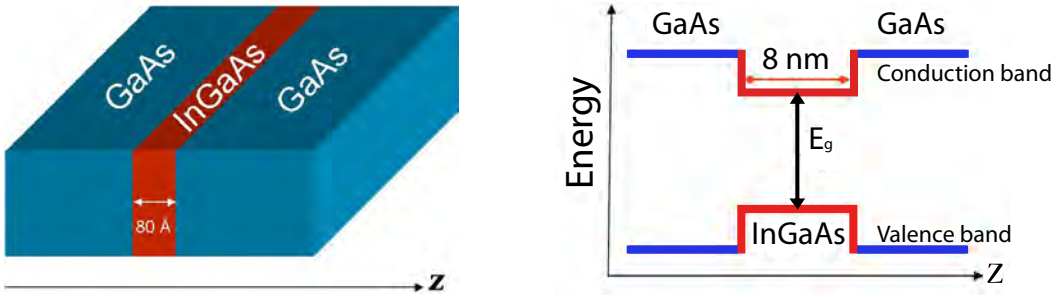

Figure 1.3.: Physical and energetic structures of a GaAs-InGaAs quantum well – (Left) 3D structure of a quantum well where the z-axis is the growth axis. (Right) Schematic energy vs z-position plot. The upper line is the conduction band and the lower line is the valence band in the GaAs (blue) and InGaAs (red) layers. This heterostructure creates a notch in energy where the excitons are trapped.

energy depends on the mass of the particle. Usually this splitting is quite large (about 15 meV in the InGaAs quantum well at low temperature we use), therefore we can account for only heavy holes in our experiments.

The heavy exciton Hamiltonian can be written as

$$\hat{H}_{exc}^{2D} = \hat{H}_{\mathbf{k}_\parallel^{exc}} + \hat{H}_b^{2D}, \tag{1.3}$$

with $\hat{H}_{\mathbf{k}_\parallel^{exc}}$ the kinetic Hamiltonian, which has a parabolic continuum of eigenenergies:

$$E(\mathbf{k}_\parallel^{exc}) = E_g + \frac{\left(\hbar k_\parallel^{exc}\right)^2}{2m_{exc}^*}, \tag{1.4}$$

and $\hat{H}_b^{2D}$ is the 2D equivalent to the bulk exciton Hamiltonian in the center of mass referential, which has discrete eigenvalues. In our InGaAs quantum well the binding energy in about 20 meV so that the ground state energy is well separated from the other energy levels and we can consider only E_{1s}^{2D}, the fundamental state of $\hat{H}_b^{2D}$ (called bidimensional 1s exciton by analogy with the bidimensional hydrogen atom model). The energy of the 2D exciton we work with can thus be written:

$$E_{exc}^{2D}\left(\mathbf{k}_\parallel^{exc}\right) = E_g + E_{1s}^{2D} + \frac{\left(\hbar k_\parallel^{exc}\right)^2}{2m_{exc}^*}, \tag{1.5}$$

and corresponds to excitons that, while confined in the z direction, are free to move in the in-plane directions.

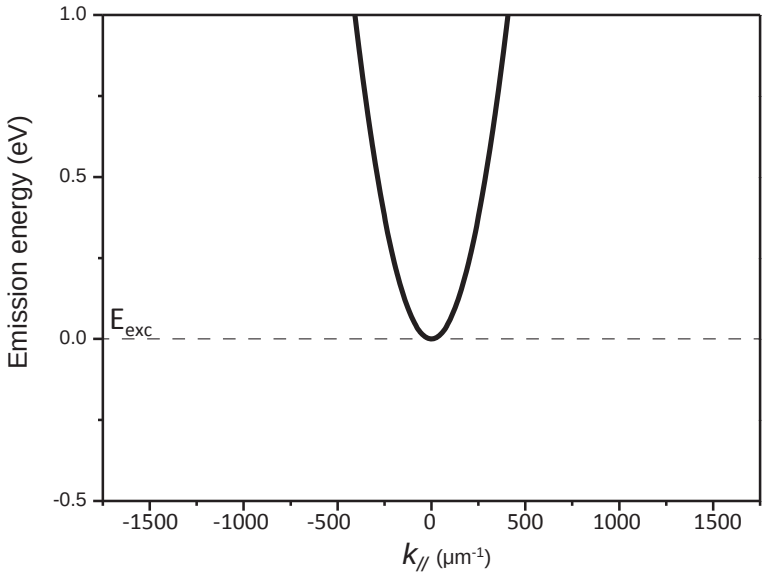

Figure 1.4.: Exciton dispersion relation – In-plane exciton dispersion curve in a semiconductor quantum well, renormalized to the bottom of the band. This corresponds to equation (1.5) and describes a free massive particle in the quantum well plane. The effective exciton mass is a fraction of the electron mass m_e, $m_{exc} \simeq 0.3 m_e$. From [24].

1.2.2. Properties of bidimensional excitons

In quantum wells, the selection rule regarding momentum conservation is modified with respect to bulk semiconductors: conservation of the in-plane momentum $\hbar k_{\parallel}^{exc}$ is required, instead of conservation of the total momentum. As a consequence, an exciton is coupled to a continuum of modes of the electromagnetic field since once the energy, spin and in-plane momentum are conserved, light with any z-axis component k_z^{γ} of its wavevector can excite the system. Nevertheless, the energy conservation during exciton-photon interaction requires the following condition to be satisfied:

$$E_{exc} + \frac{\left(\hbar k_{\parallel}^{exc}\right)^2}{2m} = \frac{\hbar c}{n}\sqrt{\left(k_{\parallel}^{\gamma}\right)^2 + \left(k_z^{\gamma}\right)^2}, \tag{1.6}$$

where $E_{exc} = E_g + E_{1s}^{2D}$, writing the photon wavevector $\mathbf{k}^{\gamma} = \left(\mathbf{k}_{\parallel}^{\gamma}, k_z^{\gamma}\right)$ and where the right-hand term corresponds to the energy of a photon having wavevector $\mathbf{k}_{\parallel}^{\gamma} = \mathbf{k}_{\parallel}^{exc}$ moving in the quantum well characterized by a refractive index n. This relation implies:

$$E_{exc} + \frac{\left(\hbar k_{\parallel}^{exc}\right)^2}{2m} \geq \frac{\hbar c}{n}|k_{\parallel}^{exc}|. \tag{1.7}$$

For small $|\mathbf{k}_{\parallel}^{exc}|$, i.e. close to the bottom of the band, this gives the condition

$$|k_{\parallel}^{exc}| \lesssim \frac{nE_{exc}}{\hbar c}, \tag{1.8}$$

which for the III-V type semiconductor used here corresponds to $|k_{\parallel}^{exc}| \lesssim 30\,\mu\text{m}^{-1}$. Excitonic modes that do not satisfy this condition are thus non-radiative. Our setup, however, always respects this condition since only small angles of incidence ($|k_{\parallel}^{exc}| < 3\,\mu\text{m}^{-1}$) are used.

As we have seen, for a quantum well in free space an exciton is coupled to a continuum of optical modes. The radiative emission of a photon through exciton recombination is an irreversible process (i.e. the probability of finding the exciton in the excited state decreases exponentially with time). This can be described by the Fermi golden rule and it takes place on typical timescales of tens of ps (in 10 nm GaAs based quantum wells the radiative lifetime is $\tau_{exc} \simeq 10\,\text{ps}$ [25]) and corresponds to a radiative broadening of the excitonic line. As we will discuss in the following sections, the radiative broadening of the excitonic line is strongly modified as we embed the quantum well in an optical microcavity. In this case the excitonic transition is not coupled to a continuum of modes but to only one longitudinal optical mode: the resonant cavity mode.
One advantage of quantum wells over bulk semiconductors is that the overlap of the electron and hole wavefunctions constituting the exciton is greatly enhanced due to the reduced exciton Bohr radius owned to the 2D confinement. This has important consequences for the exciton optical properties, in particular as it results in an increased oscillator strength (i.e. an increase in the coefficient describing exciton-photon interaction). This is a fundamental property necessary to reach the strong coupling regime [26].

Nonradiative relaxation mechanisms take place in the quantum well (both in free space and cavity-embedded), causing an additional broadening of the excitonic linewidth and limiting the excitonic lifetime. The main causes of broadening are natural disorder related to imperfections in the material, interaction with crystal lattice phonons and exciton-exciton interactions. The typical nonradiative exciton lifetimes are on the order of hundreds of picoseconds [27].

1.3. Photons in an optical microcavity

In the previous section we saw that confined excitons are coupled to a continuum of the electromagnetic field. In order to have a strong exciton-photon coupling, it is possible to confine photons along one direction in an optical cavity. This way an exciton will be coupled to only one mode of the electromagnetic field. If the coupling strength is high

enough compared to the photon and exciton lifetimes this results in what is called the "strong coupling regime", which we will describe in the next section.

1.3.1. Optical microcavity

The quantum well we work with is embedded in an optical cavity. This cavity is a semiconductor Fabry-Perot made of two Bragg mirrors, as presented schematically on figure 1.5.

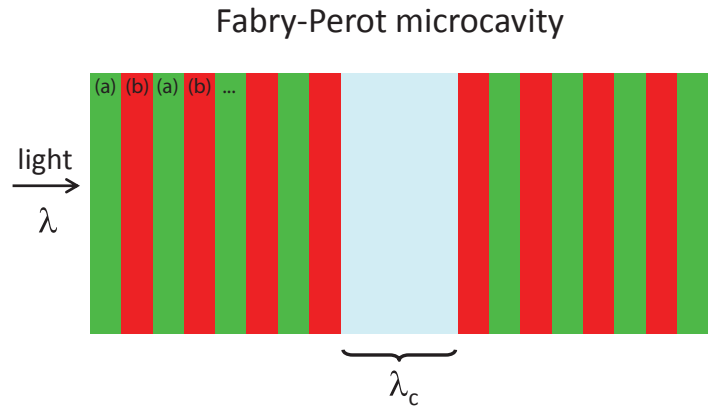

Figure 1.5.: Fabry-Perot cavity – Schematic view of the optical cavity used in the experiment. Two parallel Bragg mirrors separated by $\lambda_c = m\frac{\lambda_0}{2n_c}$ (where n_c is the refractive index of the cavity medium and m is an integer) form a Fabry-Perot cavity resonant at λ_0 at normal incidence. From [24].

Bragg mirrors

A Bragg mirror is a dielectric mirror made of a succession of layers alternating two distinct materials (named for description purpose a and b, with $n_a > n_b$) whose thicknesses and optical indexes are fine-tuned so that for light at a given angle of incidence and at the target wavelength λ_0 the transmission is almost zero. In this work we use $a = Ga_{0.9}Al_{0.1}As$ and $b = AlAs$, with respective optical indexes $n_a = 3.48$ and $n_b = 2.95$.

For a normally incident wave, each layer has a thickness $e_i = \frac{\lambda_0}{4n_i}$ with $i = (a, b)$ where λ_0 is the wavelength for which the transmission is minimal. This structure behaves like a high-reflectivity mirror for a range of frequencies called the *stop-band* centered on λ_0 and of bandwidth [28]:

$$\Delta\lambda = \frac{4\lambda_0}{\pi} \arcsin\left(\frac{n_a - n_b}{n_a + n_b}\right), \tag{1.9}$$

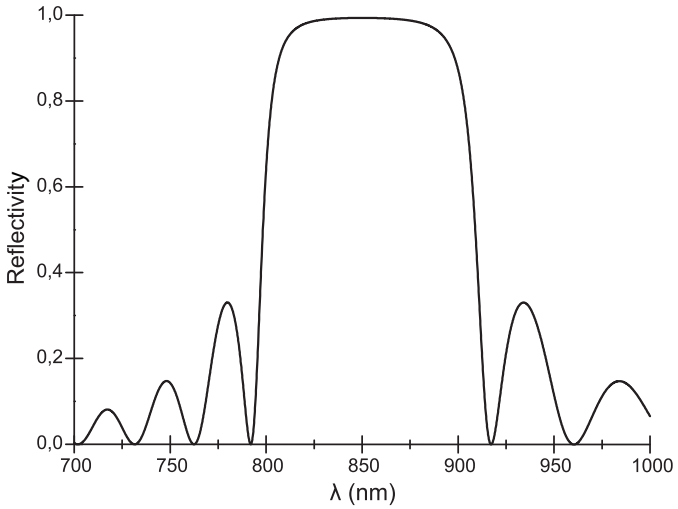

Figure 1.6.: Bragg mirror reflectivity – Plot of the reflectivity versus wavelength at normal incidence for a Bragg mirror made of 20 pairs of $Ga_{0.9}Al_{0.1}As/AlAs$ of optical indexes $n_{Ga_{0.9}Al_{0.1}As} = 3.48$ and $n_{AlAs} = 2.95$, with $\lambda_0 = 850$ nm. From [23].

as visible in the reflectivity against wavelength plot in figure 1.6.
The mirror reflectivity is [29]:

$$R = \left[\frac{n_{in}(n_a)^{2N} - n_{out}(n_b)^{2N}}{n_{in}(n_a)^{2N} + n_{out}(n_b)^{2N}}\right]^2, \tag{1.10}$$

where n_{in} and n_{out} are respectively the refractive indexes of the medium before and after the mirror (relative to the direction of light propagation) and N is the number of (a)–(b) layers pairs.

The number of layers pairs in each mirror is controlled during the growth process so that asymmetric cavities are possible, as we will see later.

Fabry-Perot microcavity

Two parallel Bragg mirrors separated by a distance $\lambda_c = m\frac{\lambda_0}{2n_c}$, where n_c is the refractive index of the cavity medium and m an integer, form a Fabry-Perot cavity that is resonant for the wavelength λ_0 at normal incidence. Figure 1.7 represents the reflectivity at normal incidence of a cavity made of two Bragg mirrors identical to the one presented in figure 1.6 separated by a distance $\frac{2\lambda_0}{n_c}$ (m=4). We observe a sharp dip in the reflectivity at $\lambda = \lambda_0$ corresponding to the Fabry-Perot resonance.

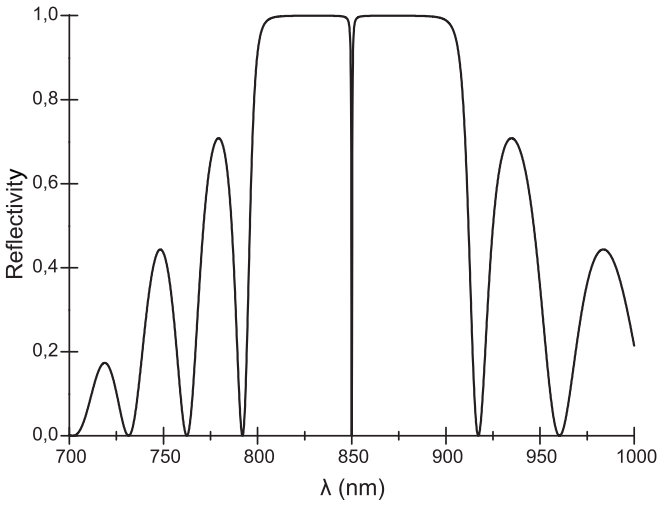

Figure 1.7.: Fabry-Perot cavity reflectivity – Plot of the reflectivity versus wavelength at normal incidence for a Fabry-Perot cavity made of the same Bragg mirror as figure 1.6 separated by $\lambda_c = 2\frac{\lambda_0}{n_c}$. The cavity is resonant for $\lambda = \lambda_0$. From [23]

.

The mirrors reflectivities (and thus their thicknesses) control the cavity finesse, following the approximate relation:

$$F = \pi \frac{\sqrt{R}}{1-R}, \tag{1.11}$$

which is accurate for two mirrors of similar reflectivity $R > 0.5$.

In this study we used two cavities (described in greater details later) of finesses 3000 (part I) and 700 (part II). With recent epitaxy techniques finesses of the order of several hundreds of thousands are possible in semiconductor microcavities.

The quantum description of the resonant intra-cavity electromagnetic field gives rise to the notion of "cavity photon", a photon whose properties are altered by the Fabry-Perot confinement.

1.3.2. Cavity photon properties

Photon lifetime

Increased finesses enhance the cavity photon lifetime. A simplistic picture is that the finesse is roughly the number of "bounces" a cavity photon will make on the two Bragg

mirrors before escaping the cavity. A more detailed analysis gives the relation [30]:

$$\tau_c = L_{eff}\frac{n_c}{\pi}\frac{F}{c} \tag{1.12}$$

where c is the speed of light in vacuum and $L_{eff} = \lambda_c\left(1 + 2\frac{n_a n_b}{(n_b - n_a)}\right)$ is the effective length of the cavity taking into account the fact that the electromagnetic field penetrates the Bragg mirrors following an exponential decay (evanescent field); the other terms where described previously. In our cavities this formula gives cavity photon lifetimes of 13 ps (part I) and 3 ps (part II).

Dispersion relation

If the cavity is not excited at normal incidence but at an angle θ with respect to the normal, the interference condition defining the resonant cavity mode changes slightly. More explicitly, the cavity imposes the quantization condition on the k_z^γ component of the photon wavevector $\mathbf{k}^\gamma = \left(\mathbf{k}_\parallel^\gamma, k_z^\gamma\right)$. Since our cavities were built to only have one resonance in the Bragg mirrors stop-band, this condition is:

$$k_z^\gamma = \frac{2\pi n_c}{\lambda_0}. \tag{1.13}$$

Since $\mathbf{k}_\parallel^\gamma$ remains unconstrained the energy can be written:

$$E_\gamma\left(k_\parallel^\gamma\right) = \frac{\hbar c}{n_c}\sqrt{\left(\frac{2\pi n_c}{\lambda_0}\right)^2 + \left(k_\parallel^\gamma\right)^2}, \tag{1.14}$$

which approximates to a parabolic dispersion for $\frac{2\pi n_c}{\lambda_0} \gg k_\parallel^\gamma$:

$$E_\gamma\left(k_\parallel^\gamma\right) \simeq \frac{hc}{\lambda_0}\left[1 + \frac{1}{2}\left(\frac{\lambda_0 k_\parallel^\gamma}{2\pi n_c}\right)^2\right]. \tag{1.15}$$

The energy of a cavity photon is plotted on figure 1.8 in the small $\mathbf{k}_\parallel^\gamma$ limit.

From here it is possible to define an effective mass for the cavity photon by applying the relation (1.2). This gives

$$m_\gamma^* = \frac{n_c^2 h}{\lambda_0 c}, \tag{1.16}$$

which for GaAs microcavities is about 10^{-5} times the electron mass and 10^{-4} times the effective exciton mass. This huge difference between the exciton and photon masses means

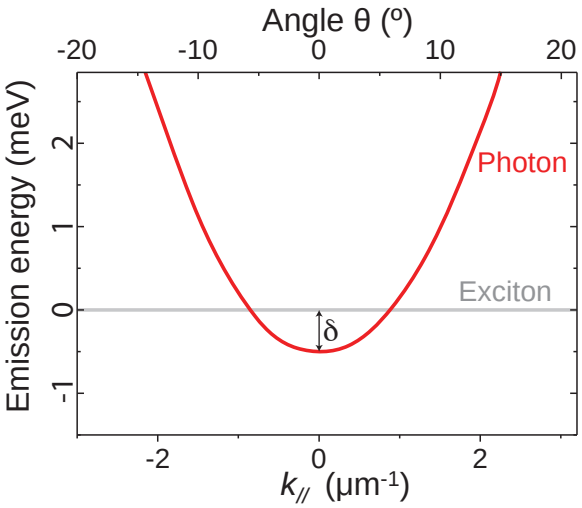

Figure 1.8.: Cavity photon dispersion – Plot of the cavity photon energy versus in-plane wavevector $\mathbf{k}_{\|}^{\gamma}$ for the cavity previously described. For comparison the exciton line is also drawn (using the same scale): its curvature is negligible compared to the photonic curvature. The energy reference is the exciton energy at $\mathbf{k}_{\|} = 0\ \mu\text{m}^{-1}$. Note that at $\mathbf{k}_{\|} = 0\ \mu\text{m}^{-1}$ the exciton and photon dispersion curves do not necessarily overlap and the energy difference (called δ, the exciton-photon detuning) can be chosen during the sample growth.

that the curvature of the exciton dispersion relation is negligible relative to the photon dispersion curvature and in future calculations we will consider the exciton dispersion to be flat for small $\mathbf{k}_{\|}$.

Leaky modes

When exciting the cavity at a non-normal angle the intracavity wavelength is reduced since $\mathbf{k}_{\|}$ increases while $\mathbf{k}_z$ remains constant. If the angle of incidence is too high the intracavity wavelength will fall outside of the Bragg mirrors stop-band and their reflectivity will drop (see figure 1.6), so the cavity photons will not be confined anymore due to the lowered cavity finesse. The electromagnetic field "leaks" efficiently from the cavity through these modes since, as visible in figure 1.9, they are larger than the main ($\theta = 0°$) mode. Note, however, that in our experiments only small angles ($\theta < 15°$) are used.
Figure 1.9 is a measure of the wavevector (equivalently, the angle of incidence) dependence of our cavity reflectivity for the resonant wavelength λ_0 [31]. For small angles the reflectivity is flat but for $\left|k_{\|}^{\gamma}\right| \gtrsim 2.5\ \mu\text{m}^{-1}$ (18°) oscillations take place. The dips in reflectivity are the secondary "leaky" modes with a much lower lifetime (wider linewidth) than the main mode. This limits the working region in which we can expect to attain the strong coupling regime to $\left|k_{\|}^{\gamma}\right| < 2.5\ \mu\text{m}^{-1}$, for higher $\left|k_{\|}^{\gamma}\right|$ vectors the system will be in the weak coupling

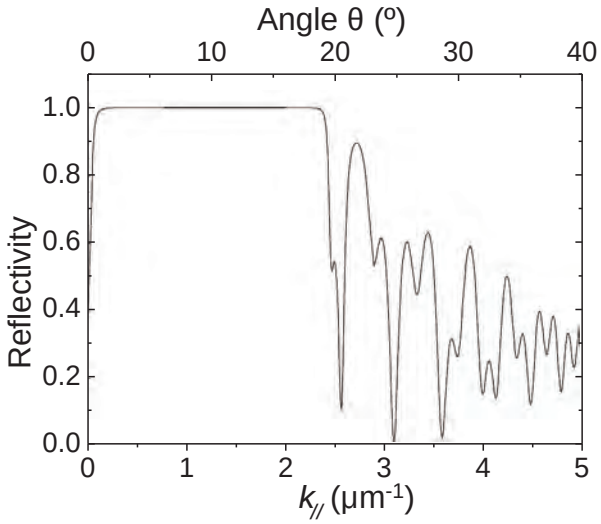

Figure 1.9.: Limits of non-normal pumping – Plot of the cavity reflectivity versus in-plane wavevector $\mathbf{k}_{\parallel}^{\gamma}$ for the cavity previously described, at the resonant wavelength λ_0. Beyond $k_{\parallel}^{\gamma} = 2.5\ \mu\text{m}^{-1}$ ($\theta = 18°$) the reflectivity drops and oscillate, with several $k_{\parallel}^{\gamma}$ for which the cavity transmission is high. From [31].

regime.
However for GaAs samples the total reflection angle between the Bragg medium and air is $16,6°$, so that those modes can only leak through the substrate, present on only one face of the sample.

1.4. Strong coupling between excitons and photons

The strong coupling regime is obtained by embedding one or more semiconductor quantum wells in a semiconductor Fabry-Perot microcavity, with the optical mode quasi-resonant with the excitonic transition. In particular, the quantum wells are placed in correspondence to the antinodes of the electromagnetic field in order to maximize the coupling, as shown schematically in figure 1.10. For simplicity we shall thereafter refer to this heterostructure containing one or several of quantum wells in a Fabry-Perot simply as "a microcavity".

A small (a few meV) energy shift between the exciton and photon energies at $\mathbf{k}_{\parallel}^{exc} = \mathbf{k}_{\parallel}^{\gamma} = 0\ \mu\text{m}^{-1}$ can be engineered to modify the strongly coupled system properties. It is called $\delta = E_{\gamma}(0) - E_{exc}(0)$, the exciton-photon detuning, and is represented in figure 1.8. This detuning is experimentally implemented by inducing a wedge in the optical cavity: the two Bragg mirrors are not strictly parallel and the cavity photon energy varies linearly with the position on the sample while the exciton energy remains constant. This way we have a fine control over δ through the spatial position of the laser on the sample.

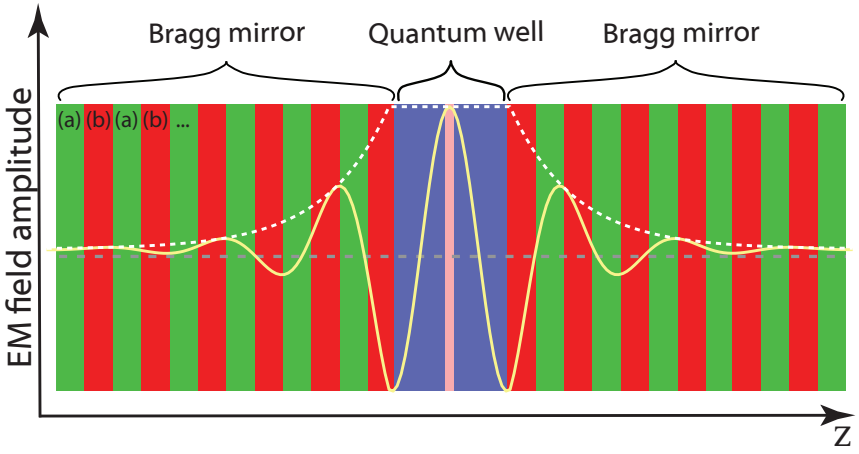

Figure 1.10.: Cavity-embedded quantum wells – Schematic representation of a semiconductor microcavity with one embedded quantum well. The green and red layers constitute the two Bragg mirrors making up the optical cavity while the blue and salmon layers represent the quantum well. The electromagnetic field amplitude (yellow line) as well as its envelope (white dashed line), showing the exponential decay in the Bragg mirrors, are represented. The quantum well is placed at an antinode of the electromagnetic field inside the cavity.

We saw in section 1.2 that an exciton in a quantum well in free-space with in-plane momentum $\mathbf{k}_{\parallel}^{exc}$ is coupled to a continuum of photonic modes due to the fact that $\mathbf{k}_{z}^{exc}$ can take any value and still satisfy momentum conservation. We also saw in section 1.3 that $\mathbf{k}_{z}^{\gamma}$ is quantized according to (1.13). So, as mentioned before, in a microcavity an exciton is coupled to a single photon mode. This allows us to excite a single exciton mode $\mathbf{k}_{\parallel}^{exc} = (k^{exc}, \varphi^{exc})$, in polar coordinates, where φ^{exc} is the azimuthal direction of propagation. The in-plane wavevector amplitude is simply selected with the extra-cavity photon angle of incidence θ on the microcavity according to:

$$k^{exc} = k^{\gamma,c} = \frac{En_c}{\hbar c} \sin\theta^c = \frac{E}{\hbar c} \sin\theta, \tag{1.17}$$

where E is the photon energy and θ^c is the photon angle of refraction inside the cavity, linked to θ by the Snell-Descartes law (from now on the extra-cavity medium is air). Here we suppose the exciton and cavity photon lifetimes to be infinite in order to define a precise energy E with zero linewidth. Correspondingly, the detection of a fluorescence photon with an angle of emission (θ, φ) is a direct signature of a radiative exciton recombination with in-plane momentum $k_{\parallel}^{exc} = (k^{exc}, \varphi^{exc})$ satisfying (1.17).

1.4.1. Hamiltonian description of the strong coupling regime

At first we describe the strong coupling between excitons and photons with the same approximation of infinitely precise energies as in the previous paragraph and with the added hypothesis that we only excite a few particles, in order to neglect exciton-exciton interactions that would add nonlinear terms to the Hamiltonian. These nonlinearities being one of the highlights of polariton systems, we will describe them in section 1.6. Under these approximations the system behaves like two coupled harmonic oscillators, one oscillator being the excitonic transition with wavevector $k_{\parallel}^{exc}$, the other a quasi-resonant optical mode with $k_{\parallel}^{\gamma} = k_{\parallel}^{exc}$. From now on, we will omit the index $\parallel$ to simplify the notations: $k \equiv k_{\parallel}$. We write the Hamiltonian using a quantum approach, even if a mean-field classical approach would give equivalent results [32]:

$$\hat{H} = \sum_k \hat{H}_k = \sum_k \left(E_{exc}(k)\hat{b}_k^\dagger \hat{b}_k + E_\gamma(k)\hat{a}_k^\dagger \hat{a}_k + \frac{\hbar\Omega_R}{2}\left(\hat{a}_k^\dagger \hat{b}_k + \hat{b}_k^\dagger \hat{a}_k\right)\right), \tag{1.18}$$

where $\hat{b}_k^\dagger$, $\hat{b}_k$ and $\hat{a}_k^\dagger$, $\hat{a}_k$ are respectively the creation and annihilation operators for an exciton and a photon with wavevector $\mathbf{k}$ lying in the plane transversal to the growth axis. They satisfy the bosonic commutation relations [33] since both photons and excitons are bosons (at least for moderate exciton densities, as we will discuss in subsection 1.6.2). $E_{exc}(k)$ and $E_\gamma(k)$ correspond to the energies of excitons and photons, given by the dispersion relations (1.5) and (1.14). The last term in (1.18) is the photon-exciton coupling and contains one term corresponding to the simultaneous creation of a photon and annihilation of an exciton (radiative decay of an exciton) and a term corresponding to the simultaneous creation of an exciton and annihilation of a photon (optical excitation). The coefficient $g = \hbar\frac{\Omega_R}{2}$ is the coupling energy. Ω_R is called the *Rabi splitting* or the *Rabi frequency* and corresponds to the frequency at which excitons and photons convert into one another. It is expressed as:

$$\Omega_R = 2\sqrt{\frac{2c\gamma_{exc}}{n_c L_{eff}}} \propto \sqrt{\frac{f_{osc}}{L_{eff}}}, \tag{1.19}$$

where γ_{exc} is the radiative decay rate of excitons at $k = 0\ \mu\text{m}^{-1}$ in absence of optical cavity and L_{eff} is the previously described effective cavity length in which the optical mode is confined. f_{osc} is the oscillator strength of the exciton, characterizing the strength of its dipolar coupling to the electromagnetic field. Therefore the coupling constant depends both on the exciton oscillator strength (higher in a quantum well than in bulk semiconductors due to the enhanced overlap of the electron and hole wavefunctions) and on the volume over which the electromagnetic field is confined. This volume is particularly small in semiconductor microcavities, which also contributes to achieve high values of

$\hbar\Omega_R$ (typically of the order of $\sim 5\,\text{meV}$ in our GaAs-based samples and up to two orders of magnitude larger for ZnO-based microcavities).

This linear Hamiltonian can be diagonalized as follows:

$$\hat{H} = \sum_k \left(E_{UP}(k)\hat{p}_k^{(UP)\dagger}\hat{p}_k^{(UP)} + E_{LP}(k)\hat{p}_k^{(LP)\dagger}\hat{p}_k^{(LP)} \right). \tag{1.20}$$

The two eignenstates annihilation (creation) operators $\hat{p}_k^{(UP)(\dagger)}$ and $\hat{p}_k^{(LP)(\dagger)}$ are found by applying to the photon and exciton operators $\hat{a}_k$ and $\hat{b}_k$ the unitary transformation:

$$\begin{pmatrix} \hat{p}_k^{(LP)} \\ \hat{p}_k^{(UP)} \end{pmatrix} = \begin{pmatrix} -C_k & X_k \\ X_k & C_k \end{pmatrix} \begin{pmatrix} \hat{a}_k \\ \hat{b}_k \end{pmatrix} \tag{1.21}$$

where C_k and X_k are the Hopfield coefficients [26], real positive numbers defined as:

$$C_k^2 = \frac{\sqrt{\delta_k^2 + \hbar^2\Omega_R^2} - \delta_k}{2\sqrt{\delta_k^2 + \hbar^2\Omega_R^2}}, \tag{1.22}$$

$$X_k^2 = \frac{\delta_k + \sqrt{\delta_k^2 + \hbar^2\Omega_R^2}}{2\sqrt{\delta_k^2 + \hbar^2\Omega_R^2}}, \tag{1.23}$$

with the **k**-dependent photon-exciton energy detuning $\delta_k = E_\gamma(k) - E_{exc}(k)$, a generalization of δ to any **k**.

The new eigenstates are called *exciton-polaritons*, a mixed state of light and matter. More precisely they are the *upper polaritons* and the *lower polaritons*, represented by the indexes (UP) and (LP). The squared Hopfield coefficients C_k^2 and X_k^2 respectively are the photonic and excitonic fractions and together represent the mixing ratio between the exciton and photon making up a polariton. Their sum is therefore $C_k^2 + X_k^2 = 1$ for any **k** and for $\delta_k = 0\,\text{meV}$ a polariton is an equal quantum superposition of an exciton and a photon, since $C_k^2 = X_k^2 = \frac{1}{2}$.
The eigenenergies $E_{UP}(k)$ and $E_{UP}(k)$ can be written explicitly:

$$E_{UP}(k) = \frac{1}{2}\left(E_{exc}(k) + E_\gamma(k) + \sqrt{\delta_k^2 + (\hbar\Omega_R)^2} \right), \tag{1.24}$$

$$E_{LP}(k) = \frac{1}{2}\left(E_{exc}(k) + E_\gamma(k) - \sqrt{\delta_k^2 + (\hbar\Omega_R)^2} \right). \tag{1.25}$$

If we now take into account the finite lifetime of both excitons and photons we have to introduce their respective relaxation (or decay) rates γ_{exc} and γ_{ph}, induced by the fact that photons can couple to the extra-cavity electromagnetic field and excitons can couple with phonons [33], other excitons [34] or disorder naturally present in crystalline structures [35]. They are phenomenologically added to the previous calculations as an imaginary part in $E_{exc}(k)$ and $E_\gamma(k)$. However this method is in reality an approximation which neglects the influence of exciton-photon coupling on relaxation. This approximation does not take into account the effects arising from the shape of the polariton dispersion relation, such as the asymmetry between the higher and lower branches, or the dependence on $\mathbf{k}$ of the relaxation rates [36]. Such an approximation is reasonable if we limit our study to polaritons near $k = 0\ \mu\text{m}^{-1}$. For more details on the introduction of complex energies the reader is invited to look into the chapter 2 of reference [33].
The complex exciton and photon energies are then written:

$$\begin{cases} E^*_{exc} = E_{exc} - i\hbar\gamma_{exc}, \\ E^*_{\gamma} = E_{\gamma} - i\hbar\gamma_{ph}. \end{cases} \tag{1.26}$$

And the complex polariton eigenenergies are:

$$E^*_{UP}(k) = \frac{E_{exc}(k) + E_\gamma(k)}{2} - i\hbar\frac{\gamma_{exc} + \gamma_{ph}}{2} + \frac{\sqrt{\left(\delta_k - i\hbar(\gamma_{ph} - \gamma_{exc})\right)^2 + (\hbar\Omega_R)^2}}{2} \tag{1.27}$$

$$E^*_{LP}(k) = \frac{E_{exc}(k) + E_\gamma(k)}{2} - i\hbar\frac{\gamma_{exc} + \gamma_{ph}}{2} - \frac{\sqrt{\left(\delta_k - i\hbar(\gamma_{ph} - \gamma_{exc})\right)^2 + (\hbar\Omega_R)^2}}{2} \tag{1.28}$$

which simplifies for $\delta_{\mathbf{k}} = 0\,\text{meV}$ to:

$$E^*_{UP}(k) = \frac{E_{exc}(k) + E_\gamma(k)}{2} - i\hbar\frac{\gamma_{exc} + \gamma_{ph}}{2} + \frac{\hbar}{2}\sqrt{\Omega_R^2 - (\gamma_{ph} - \gamma_{exc})^2} \tag{1.29}$$

$$E^*_{LP}(k) = \frac{E_{exc}(k) + E_\gamma(k)}{2} - i\hbar\frac{\gamma_{exc} + \gamma_{ph}}{2} - \frac{\hbar}{2}\sqrt{\Omega_R^2 - (\gamma_{ph} - \gamma_{exc})^2} \tag{1.30}$$

The last term in (1.27) and (1.28) being the coupling term it generates an energy separation between the two branches for any $\mathbf{k}$ - what we will come to know as the *anticrossing*, characteristic of the strong coupling - if:

$$\Omega_R > \left|\gamma_{ph} - \gamma_{exc}\right| \quad \Omega_R > \gamma_{ph},\ \gamma_{exc}. \tag{1.31}$$

This relation rigorously defines the strong coupling regime.
The upper and lower polariton linewidth are then described as a pondered average of γ_{ph} and γ_{exc}:

$$\begin{pmatrix} \gamma_k^{(UP)} \\ \gamma_k^{(LP)} \end{pmatrix} = \begin{pmatrix} C_k^2 & X_k^2 \\ X_k^2 & C_k^2 \end{pmatrix} \begin{pmatrix} \gamma_{exc} \\ \gamma_{ph} \end{pmatrix} \tag{1.32}$$

It follows that the polaritons are characterized by short lifetimes, usually on the order of some tens of ps.
The short polariton lifetime defines polaritons as an intrinsically out-of-equilibrium system, characterized by a continuous decay of the population corresponding to photons escaping out of the cavity. This property represents a great advantage as it allows a direct way of detection: since photons emitted from the cavity are in a one-to-one correspondence with polaritons inside the cavity, the properties of polaritons can be fully reconstructed by analyzing the cavity emission. Moreover this property makes of polaritons a suitable system to study out-of-equilibrium quantum gases.

The first observation of strong light-matter coupling in a semiconductor microcavity was made by Claude Weisbuch *et al* in 1992 [2]. In order to reach this regime it is necessary to create structures that maximize the exciton-photon coupling. This is why the quantum wells are placed at the amplitude maxima of the electromagnetic field in the cavity. Increasing the number of quantum wells N_{QW} also facilitate the strong coupling since it increases Ω_R, as $\Omega \propto \sqrt{N_{QW}}$ [37]. Furthermore, tuning the coupling with the environment (engineering γ_{ph} to be similar to γ_{exc}) by choosing the cavity finesse is crucial as seen in (1.31). Ideally, both γ_{ph} and γ_{exc} should be low so as to decouple polaritons from the environment and have longer polariton lifetimes.

1.4.2. Physical interpretation

The non-diagonalized Hamiltonian (1.18) provides a simple physical picture for polaritons, which is useful to keep in mind. The interaction term in (1.18) is formally equivalent to the coupling between the energy levels in a two-levels system via an external electromagnetic field. The usual physical associated picture is the virtual absorbtion (emission) of a photon and the corresponding excitation (deexcitation) of the system. This is precisely what happens for a polariton, the two level system being the exciton. There is however a difference in the interpretation: technically the ground state of an exciton is the *absence* of exciton, since the recombination of the electron with its heavy

hole is the state of lowest energy where the exciton system will spontaneously go to after a long enough time. The first excited state of the exciton system is thus the 1s exciton previously described (the exciton resonance). So a polariton can actually be seen as a cavity photon that will randomly disappear to create a 1s heavy exciton, which then recombines to release a photon (identical to the original photon if no interaction with excitons, phonons or disorder changed the system energy or momentum in between). This released photon propagates before converting into another exciton which will die and release another photon, and so on. This corresponds to the description of polaritons as a coherent sum of the electromagnetic (photonic) and polarization (excitonic) fields. A diagrammatic visualization is provided in figure 1.11.

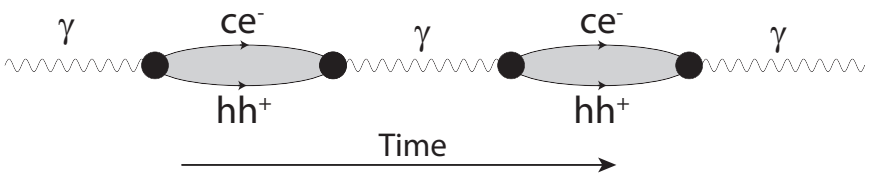

Figure 1.11.: Diagrammatic view of a noninteracting polariton – Visualization of a virtual process by which a microcavity photon (γ) excites a conduction electron (ce^-) - heavy hole (hh^+) bound pair (exciton 1s) that radiatively recombines to emit a photon, which creates an exciton, and so on. The black dots are three-body interaction points (called vertexes). A wealth of other, more complex diagrams are possible to represent interactions such as between polaritons, between a polariton and a phonon or between a polariton and a photon.

This view implies a simple interpretation for the Rabi frequency and the Hopfield coefficients. The Rabi frequency would be the average conversion rate between exciton and photon states while the Hopfield coefficients can be seen as the time ratio the system is in its "photon" or "exciton" state: the exciton (photon) properties dominate if the polariton system spends on average "more time" in the exciton (photon) state. Also note that around $\mathbf{k} = 0\,\mu\text{m}^{-1}$ the exciton mass being 10^4 times that of the cavity photon, the exciton in this picture should be considered as quasi-immobile. Of course one must remember that this description is nothing but a simplistic approximation to help visualize polaritons. Only the mathematical analysis should be considered to carry out physical predictions.

Since excitons provide an effective interaction term between cavity photons, polariton gases qualify as a type of interacting quantum fluid of light [1]. Equivalently, the nonlinearity can be seen as originating from the medium (here the semiconductor quantum well) and polariton can be reinterpreted in a purely nonlinear optics framework.

1.4.3. Dispersion relation and anticrossing

The two eigenenergies $E_{UP}(\mathbf{k})$ and $E_{LP}(\mathbf{k})$ are functions of the wavevector. We can hence directly compute and plot the polariton dispersion curve from (1.24) and (1.25). The result is presented in figure 1.12 for different values of the detuning δ when the strong coupling condition ((1.31)) is satisfied. The two polariton branches are non-degenerate for all $\mathbf{k}$ and for any δ; this energy levels separation is characteristic of the strong coupling regime.
In this study we will focus on the lower polariton branch, the shape of which can be approximated around $\mathbf{k} = 0\ \mu\text{m}^{-1}$ by a parabola. From this approximation and eq.1.2 we can derive the effective mass of polaritons. It is apparent from the dispersion curves in figure 1.12 that this mass is of the same order of magnitude as the cavity photon mass and depends on δ as well as Ω_R. As a rule of thumb it is useful to remember that at $\delta = 0\,\text{meV}$ we have $m_{pol} \simeq 10^{-5} m_e$, m_e being the electron mass.

As stated earlier the strong coupling lifts the degeneracy at $\mathbf{k} = 0\ \mu\text{m}^{-1}$ between the exciton and cavity photon energies. However, as $|\delta|$ is increased the effect of the strong coupling becomes less and less important, up to a point where the system eigenmodes are the bare cavity or excitonic modes (i.e. the polaritonic modes coincide with the photonic or excitonic modes). This is explicitly shown in the anticrossing figure (figure 1.13) where the energies of the upper and lower polariton branches at $\mathbf{k} = 0\ \mu\text{m}^{-1}$ are plotted as a function of the photon-exciton detuning. For comparison the exciton and photons energies are also plotted on the same figure and the anticrossing behavior, characteristic of the strong coupling regime, is clear around $\delta = 0\,\text{meV}$.

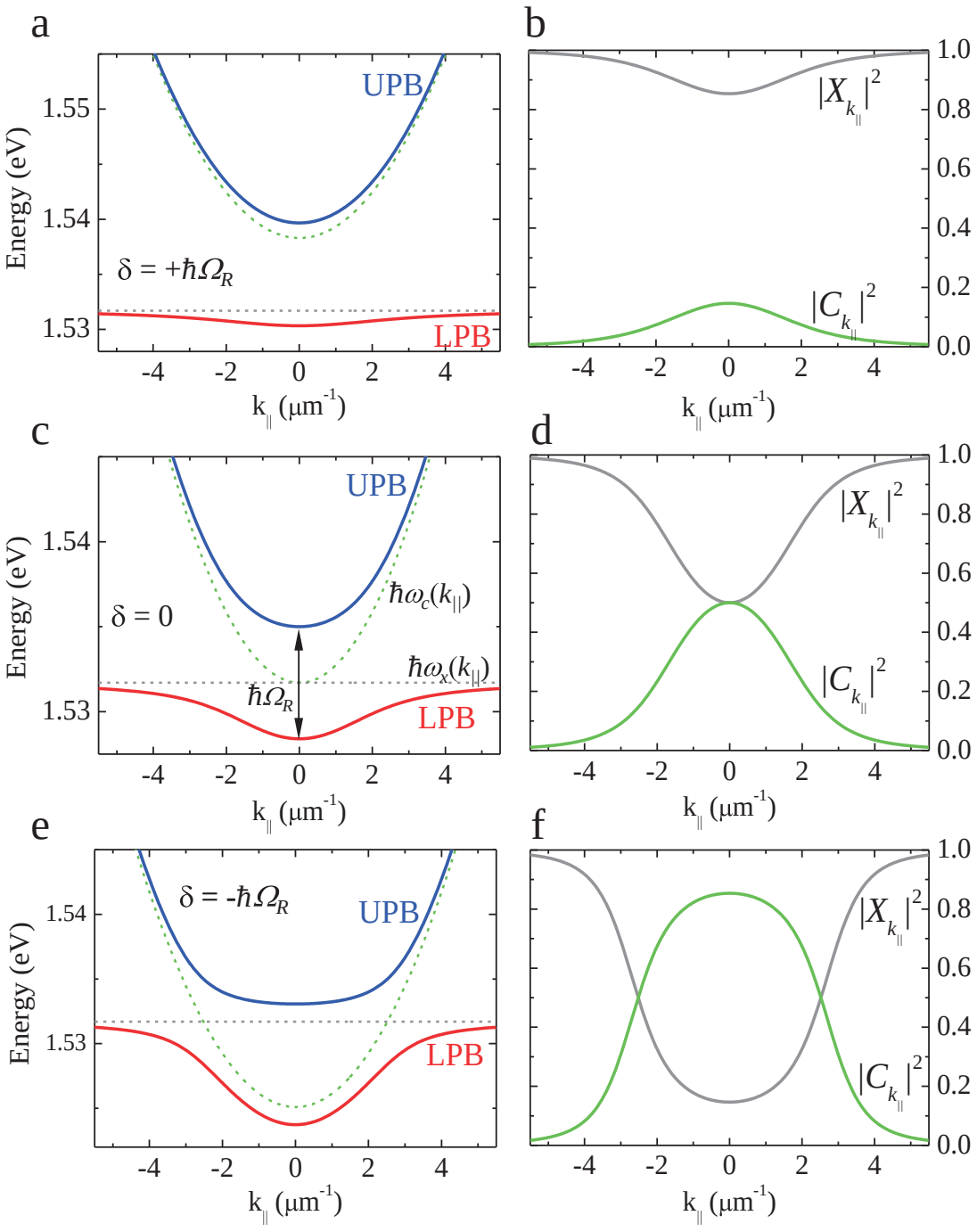

Figure 1.12.: Dispersion relation and Hopfield coefficients – Left panels: calculated bare exciton and cavity mode dispersions (dashed lines) as well as polariton dispersions (solid lines) for different photon-exciton detunings δ in a microcavity with a Rabi splitting $\hbar\Omega_R = 6.6\,\text{meV}$. Right panels: corresponding Hopfield coefficients for the lower polariton branch obtained from Eqs.1.22, 1.23. The detunings are: (a)-(b) $\delta = \hbar\Omega_R$, (c)-(d) $\delta = 0\,\text{meV}$, (e)-(f) $\delta = -\hbar\Omega_R$. From [24].

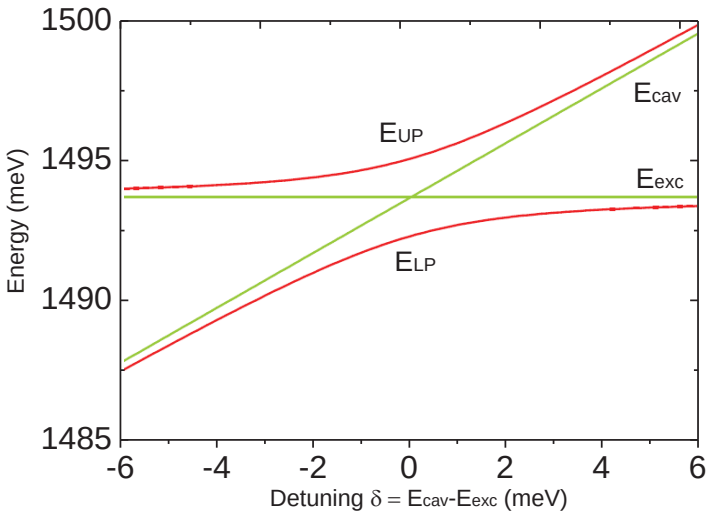

Figure 1.13.: Energy levels anticrossing – Energies of the upper and lower polariton branches at $\mathbf{k} = 0\,\mu\text{m}^{-1}$, as a function of the photon-exciton detuning δ. The exciton energy remains constant while the photon energy is changed, in order to change δ. The anticrossing behavior is well visible around $\delta = 0$ meV. From [24].

1.4.4. Polaritons as bosonic spinors

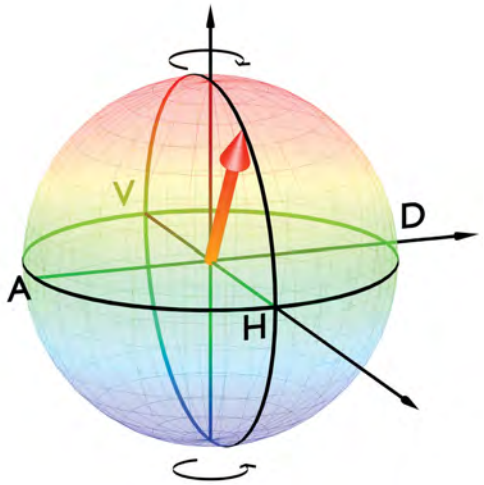

Figure 1.14.: Bloch sphere – Representation on a Bloch sphere of the polariton pseudospin, in a one-to-one correspondence with the polarization of the emitted photons. The poles represent circularly polarized states while the equator describes linearly polarized states: H = horizontal, V = vertical, D = diagonal (+45°) and A = antidiagonal (−45°). Inspired from [23].

Up to now we considered a scalar theory for polaritons. Actually polaritons are also characterized by a spin degree of freedom inherited, just like their bosonic properties, from their constituent particles: exciton and photon. In particular, as mentioned in section 1.2, quantum well excitons are composite bosons (getting their spin properties

from their constituents electron and heavy hole) characterized by two possible values for their total internal angular momentum $J = 1$ and $J = 2$. Due to the selections rules for electromagnetic interaction only $J = 1$ excitons can couple to single photons while $J = 2$ excitons constitute the dark-excitons. Therefore polaritons only have two possible projections for their angular momentum on the quantization axis z (the microcavity growth axis) $J_z = \pm 1$ and behave effectively as $\frac{1}{2}$-spin particles, whose pseudospin state can be represented on a Bloch sphere (see figure 1.14) and calculated with the usual quantum mechanical tools for spin-$\frac{1}{2}$ particles.
Thanks to the one-to-one relation between intra-cavity polaritons and extra-cavity photons each polariton spin state corresponds to a well defined polarization in the emitted light. Therefore by studying the polarization properties of the emitted light we can fully reconstruct the pseudospin properties of polaritons at their time of radiative death.

1.4.5. All-optical control

Let us briefly note that this one-to-one relation between emitted photons and polaritons provides an all-optical control of microcavity polaritons, meaning that polariton injection and detailed observations are done from outside the microcavity by solely optical means. Indeed, the injection can be done with a resonant laser beam whose energy, angle of incidence and polarization can be tuned to create a specific polariton population of spin J and energy-momentum $(E, \hbar\mathbf{k})$ lying on the dispersion curve (which can be engineered with a specific Ω_R and δ during the cavity growth). Analyzing the properties of the cavity emission is sufficient to fully characterize the polariton system at the time of the polariton radiative decay since we have the following correspondences:

Emission	**Polariton**	**Result of detection**
intensity	density (proportional)	density map
phase	phase	phase map
angle	wavevector $\mathbf{k}$	momentum map
energy	energy	energy map / energy-momentum plot
polarization	pseudospin state	pseudospin map
linewidth	lifetime	lifetime estimation
statistics	fluctuations	noise behavior

Table 1.1.: Emitted photon – intracavity polariton properties correspondance

The experimental setups required to achieve this are described in parts I and II.

1.5. 0D confinement in micropillars

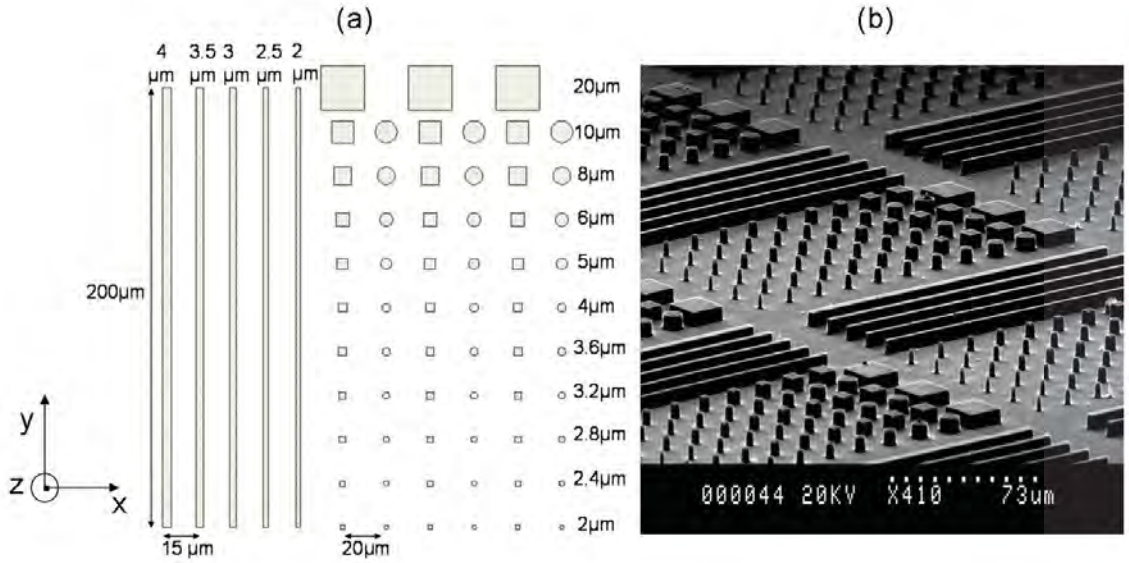

Figure 1.15.: Micropillar arrays – Image of the sample obtained with scanning electron microscopy, showing both microwires and micropillars. The round and square shapes as well as the different sizes ($2 - 20\mu$m) of the pillars are visible. From [24].

Planar microcavities can be etched into lower dimensional structure: 1D microwires or 0D micropillars, with a typical lateral size of few µm. Part I of this thesis was done on a 2D planar microcavity while in part II we focus on the study of noise in micropillars. Readers interested in the physics of polaritons in microwires or other aspects of 0D confined polaritons are invited to look into [38] and [24].

Micropillars provide a strong 3D confinement of the optical mode thanks to the difference in the refractive index between the semiconductor and air. This confinement breaks the translational invariance present in planar microcavities, resulting in a quantization of all three component of the optical field. For a rectangular cross-section of size (L_x, L_y), the optical mode energy can be written:

$$E_\gamma^{p_x,p_y} = \frac{\hbar c}{n_c}\sqrt{\left(\frac{p_x\pi}{L_x}\right)^2 + \left(\frac{p_y\pi}{L_y}\right)^2 + \left(\frac{2\pi n_c}{\lambda_0}\right)^2}, \tag{1.33}$$

where p_x and p_y are integers describing the mode. On the contrary, excitons do not "feel" the effect of confinement, their Bohr radius (about 5 nm) being several orders of magnitude below the pillar typical size. In the strong coupling regime the quantum well 1s exciton is not coupled to a continuum but to discrete optical modes. Inserting the quantized energies (1.33) in the hamiltonian (1.18) results in a quantization of the polariton energy and momentum similar to that of the cavity photon. The polaritons energy and the

wavevector being quantized, their dispersion curve presents discrete structures, depicted in figure 1.16 for round-shaped micropillars of size 10 µm, 5 µm and 2.8 µm.

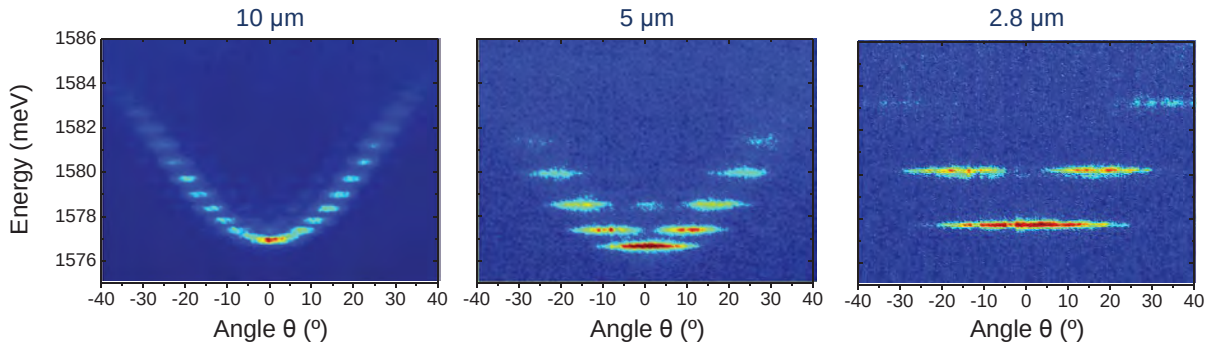

Figure 1.16.: Micropillar dispersion curve – Energy spectrum of cylindrical micropillars, for three different pillar diameters: 10 µm, 5 µm and 2.8 µm. From [24].

The wavevector quantization results in specific spatial modes when observing the momentum space. In a square pillar the first energy level $E_{0,0}$ corresponds to one symmetric mode with $p_x = p_y = 0$, the second energy level corresponds to the four degenerate modes $(p_x = +1, p_y = 0)$; $(p_x = -1, p_y = 0)$; $(p_x = 0, p_y = +1)$; $(p_x = 0, p_y = -1)$, the third level corresponds to the four degenerate modes $(p_x = +1, p_y = -1)$; $(p_x = +1, p_y = +1)$; $(p_x = -1, p_y = +1)$; $(p_x = -1, p_y = -1)$, and so on for the next modes. These spatial modes are clearly visible in the experimental data (upper panel) and numerical simulations (lower panel) in figure 1.17.

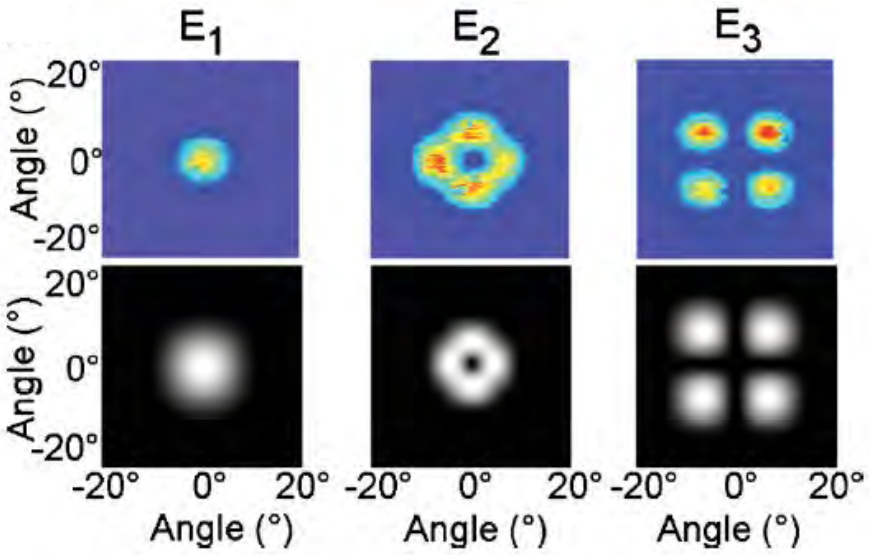

Figure 1.17.: Spatial modes – Momentum space (angle–resolved) images of a square micropillar emission, for the first three energy levels. From [38].

Polariton condensation has been experimentally demonstrated in micropillars [37] and the effects of the interactions with the excitonic reservoir have been shown to strongly affect the spatial distribution of condensates in micropillars with sufficiently large lateral size [39]. For high enough polariton densities, polariton-polariton interaction can change the spatial mode shape.

1.6. Nonlinear aspects of polariton many body systems

As mentioned in section 1.4, we only considered up to now very low densities of polariton in order to neglect polariton-polariton interactions in the Hamiltonian description. However these interactions are at the core of the nonlinearities found in high density polariton fluids which make polariton physics so rich. The results presented in this work all rely on strong polariton nonlinearities, and we will now describe them.

Since we only use lower branch polaritons in this work, for commodity we will from now on restrain our Hamiltonian description to the lower branch only. So unless otherwise mentioned we now write $E(\mathbf{k}) \equiv E^{LP}(\mathbf{k})$ and $\hat{p}_k \equiv \hat{p}_k^{LP}$. The linear Hamiltonian described in equation (1.20) is reduced to:

$$\hat{H}_k^{lin} = \hat{H}_k^{LP} = E(\mathbf{k})\hat{p}_k^\dagger \hat{p}_k \tag{1.34}$$

1.6.1. Self energy and nonlinear Hamiltonian

Excitons being made of charged particles, an interaction of Coulombian origin between excitons exists. This generates exciton-exciton scattering in the semiconductor quantum well. While negligible for low densities, it is possible in GaAs microcavities to reach a density regime where these interactions have to be taken into account. The exciton-exciton interaction is not a simple electrostatic force but is better described in term of charge carrier (electron or heavy hole) exchange [40]. So polaritons inherit a nontrivial interaction from their excitonic part.

To first order approximation these interactions can be described by introducing in the Hamiltonian (1.34) a contact two-body interaction potential term of the form [40, 41, 42]:

$$\hat{H}_{int} = \frac{1}{2}\sum_{\mathbf{k},\mathbf{k'},\mathbf{q}} V^{pol-pol}_{\mathbf{k},\mathbf{k'},\mathbf{q}} \hat{p}^\dagger_{\mathbf{k}-\mathbf{q}} \hat{p}^\dagger_{\mathbf{k'}+\mathbf{q}} \hat{p}_{\mathbf{k}} \hat{p}_{\mathbf{k'}} \tag{1.35}$$

where $V^{pol-pol}_{\mathbf{k},\mathbf{k'},\mathbf{q}}$ is the effective polariton-polariton interaction potential, which has no simple expression. The considered Hamiltonian is now:

$$\hat{H} = \hat{H}_{lin} + \hat{H}_{int} = \sum_{\mathbf{k}} \left[E_k \hat{p}^\dagger_k \hat{p}_k + \frac{1}{2} \sum_{\mathbf{k'},\mathbf{q}} V^{pol-pol}_{\mathbf{k},\mathbf{k'},\mathbf{q}} \hat{p}^\dagger_{\mathbf{k}-\mathbf{q}} \hat{p}^\dagger_{\mathbf{k'}+\mathbf{q}} \hat{p}_{\mathbf{k}} \hat{p}_{\mathbf{k'}} \right] \tag{1.36}$$

The interaction term (1.35) corresponds to the exchange of a momentum $\hbar\mathbf{q}$ between two colliding polaritons of wavevector **k** and **k'**. This type of scattering is commonly called *polariton four-wave mixing*. This third-order nonlinearity is responsible for the spontaneous generation of new populations of polaritons when the conservation of energy and momentum is satisfied, such as in the polariton optical parametric oscillator (simply called OPO, by analogy with the (second-order nonlinear) OPO found in nonlinear optics) described in [7].

It is useful to consider the effect of this Hamiltonian on a particular polariton mode. Let us assume only two modes $\mathbf{k}_i = \{\mathbf{k}_1, \mathbf{k}_2\}$. The exchanged wavevector in this case has to be $\mathbf{q} = |\mathbf{k}_1 - \mathbf{k}_2|$ and the sum in the interaction term has only two contributions $\hat{p}^\dagger_{\mathbf{k_2}} \hat{p}^\dagger_{\mathbf{k_1}} \hat{p}_{\mathbf{k_1}} \hat{p}_{\mathbf{k_2}}$ and $\hat{p}^\dagger_{\mathbf{k_1}} \hat{p}^\dagger_{\mathbf{k_2}} \hat{p}_{\mathbf{k_2}} \hat{p}_{\mathbf{k_1}}$. However $\hat{p}_{\mathbf{k_1}}$ and $\hat{p}_{\mathbf{k_2}}$ being eigenmodes of the system they commute, which mean the two terms in the sum are equal. When examining the dynamic of the eigenmode $\hat{p}_{\mathbf{k_1}}$ we have:

$$i\hbar \frac{d}{dt} \hat{p}_{k_1} = \left[\hat{p}_{k_1}, \hat{H} \right] = \left[\hat{p}_{k_1}, \hat{H}_{lin} \right] + \left[\hat{p}_{k_1}, \hat{H}_{int} \right] \tag{1.37}$$

A detailed calculation tells us that the commutator $\left[\hat{p}_{k_1}, \hat{H}_{int} \right]$ is proportional to $\hat{p}^\dagger_{\mathbf{k_2}} \hat{p}_{\mathbf{k_2}} \hat{p}_{\mathbf{k_1}}$. If we note the operator describing the number of polaritons in the $\mathbf{k}_2$ mode $\hat{N}_{k_2} \equiv \hat{p}^\dagger_{\mathbf{k_2}} \hat{p}_{\mathbf{k_2}}$, the interaction term in the dynamic equation (1.37) is:

$$\left[\hat{p}_{k_1}, \hat{H}_{int} \right] = \hbar g_{LP} \hat{N}_{k_2} \hat{p}_{k_1} \tag{1.38}$$

where g_{LP} is the interaction strength, a function of $V^{pol-pol}$. If we consider the $\mathbf{k}_2$ mode to be a macroscopically populated pump mode we see that in a mean field treatment (justified in most applications in polariton systems) and if we normalize our equations by the quantization area A, the energy of mode $\hat{p}_{\mathbf{k_1}}$ is increased by a value proportional to the density of polaritons in the mode $\mathbf{k_2}$. This density $\rho_{k_2} = \frac{\langle \hat{N}_{k_2} \rangle}{A}$ behaves like an external potential for the polaritons in mode $\mathbf{k_1}$, since (1.37) gives:

$$\frac{d}{dt} \hat{p}_{k_1} = -i \left(\frac{E(\mathbf{k}_1)}{\hbar} + g_{LP} \rho_{k_2} \right) \hat{p}_{k_1} \tag{1.39}$$

and induces an *energy renormalisation*. This effect increases the polariton energy by:

$$\Delta E_{k_1} = \hbar g_{LP} \rho_{k_2} \tag{1.40}$$

This renormalisation of the energy works the same way for a continuum of modes, though in this case all the contributions from all the modes have to be taken into account. The energy shift also happens on the pump itself and this self energy renormalisation is related to the *Kerr effect* as known in nonlinear parametric optics (this will be treated in greater details in part II).

When analyzing the pumped mode dynamics, it is necessary to take this energy shift into account. In quasi-resonant pumping schemes [1] it is usual to set a small (of the order of 0.1 meV) energy detuning between the pump laser and the *bare* (non-renormalized) polariton lower branch. This detuning is named Δ, with:

$$\Delta = E_l - E(\mathbf{k}_l) \tag{1.41}$$

for a laser pumping at the energy E_l and at the in-plane wavevector $\mathbf{k}_l$. Therefore when mentioning Δ it is necessary to remember that the actual energy detuning Δ_{eff} between the pump laser and the polariton population will be:

$$\Delta_{eff} = E_l - \big(E(\mathbf{k}_l) + \hbar g_{LP} \rho\big) \tag{1.42}$$

ρ being the polariton density in the pumped mode(s). Between polaritons of the same spin g_{LP} is quite strong and it is possible for the energy to be renormalized to the laser energy, so that despite having values of Δ up to 1 meV we can observe $\Delta_{eff} = 0$ meV for high enough pump intensities. This nonlinear effect is responsible for the bistable behavior observed in polaritons [43] which will be described in the next section.

1.6.2. Limits of the bosonic model

Note that increasing the polariton density even further results in an even stronger repulsion between their excitonic part. Although being formally (composite) bosons, interacting excitons can reach a regime where their repulsion is so strong that they cannot be in the same state anymore: a fermion-like behavior emerges from their repulsion. In this regime excitons are described as *hard-core* bosons; meaning that despite exhibiting Pauli-like repulsion the N-excitons wavefunction is still symmetric with regard to the

1. This pumping method will be presented in greater details in section 2.2

exchange of two excitons.

The critical density above which excitons cannot be considered as "simple" bosons is called *saturation density*, ρ_{sat}. Using the Usui transformation [44] applied to quantum wells [41] one can obtain the bosonic Hamiltonian describing exciton interactions up to the second order, which allows one to compute the saturation density. In our GaAs samples this treatment gives [45] $\rho_{sat} \simeq 4.10^4\ \mu\text{m}^{-2}$, which is more than two orders of magnitude above the $\rho \simeq 100\ \mu\text{m}^{-2}$ we use in the present work. Additionally, when pumping a microcavity with a very high pump intensity, a transition can be made from the strong coupling to the weak coupling regime. This happens before reaching ρ_{sat} in our sample. Since we remain in the strong coupling regime for all the experiments described here, we can safely assume the bosonic nature of the polaritons we use.

Part I.

Vortex lattices in polariton superfluids

There are many aspects to polariton physics, one of which is the study of interacting quantum fluids. The dimensionality of the system can be controlled by the shape one can etch the microcavity: 0D for pillars, 1D for wires, 2D for planar structure. The richest physics for the study of polariton quantum fluids dynamics remains in the realm of 2D systems since the diversity of topological defects increases with the dimensionality. As such, in planar cavities it is possible to observe macroscopic quantum effects (condensation [46], superfluidity [13]) as well as a wealth of topological defects (bright and dark solitons [16, 17], half-solitons [23], elementary vortex dynamics [30], half vortices [47, 48], ...) exhibiting rich behaviors. For example, dark solitons were shown in our group to behave like magnetic monopoles (see the publication on Annex B).

In this Part we study the physics of elementary vortices, first for a static trapped fluid (chapter 3), then for a rotating polariton fluid (chapters 4 - 6), in the linear and in the superfluid regimes. Two schemes are presented to inject a polariton fluid possessing a global angular momentum and observe the nucleation of angular momentum into elementary vortices, each documented in a separate chapter.

Chapter 2.

Bose-Einstein condensation, superfluidity and elementary votices

Before the different experimental schemes and their results are presented, an overview of polariton superfluidity and polariton vortex must be given. In this Part we consider an interacting condensate in two dimensions with no spin degree of freedom. While polaritons have a $\frac{1}{2}$-spin analog (± 1 pseudospin, see chapter 1.4.4) we can consider just one spin population when the resonant pump laser is circularly polarized. Indeed, under such pumping scheme only one type of polariton is created and it is reasonable to neglect the opposite spin population (insignificant spin relaxation phenomena and opposite-spin polariton interactions) [23]. This enables us to consider the polariton field as a scalar field.
In the first section we present a general description of Bose-Einstein condensation and superfluidity while in the next we focus on the implications of quasi-resonant pumping on polaritons fluids. Finally the last section presents the properties of elementary vortices.

2.1. Bose-Einstein condensation and superfluidity

Bose-Einstein condensation (BEC) and superfluidity are two examples of macroscopic quantum behavior. While the equilibrium atomic BECs are very powerful tools to explore the quantum world, polaritons gases have the peculiarity of being a strongly out-of-equilibrium system which can lead to new physics. To model these macroscopic quantum fluids and their excitations, a well-established approach is the Gross-Pitaevskii model [49, 50, 51]. In the case of polariton quantum fluids a modified version of this approach is used, and will be described in section 2.1.2.

2.1.1. Polariton Bose-Einstein condensation

In quantum physics particles can be categorized into two distinct classes that characterize their wavefunction symmetry: fermions and bosons. While fermions have an antisymmetric wavefunction under the exchange of two particles, bosons have a symmetric wavefunction under this operation. These two classes are governed by two distinct statistics called Fermi-Dirac for fermions, and Bose-Einstein for bosons. In particular, the Bose–Einstein statistic allows a macroscopic number of bosons to accumulate in the same quantum state. In 1925, following the work of Satyendra Nath Bose [52], Albert Einstein theoretically showed the existence of a phase transition in a non-interacting boson gas [53]: for sufficiently low temperatures, the bosonic ground state is macroscopically populated. Indeed for N non–interacting bosons at a given temperature T confined in a volume V in d dimensions, the Bose–Einstein statistic is:

$$f_B\left(\mathbf{k}, T, \mu\right) = \frac{1}{\exp\left(\frac{E(\mathbf{k})-\mu}{k_B T}\right) - 1}, \tag{2.1}$$

where $\mathbf{k}$ is the d-dimensions wavevector, $E(k)$ is the single-boson energy, k_B is the Boltzmann constant and μ is the chemical potential. The value of μ is determined by the normalization condition for the total number of particles N:

$$N(T, \mu) = \sum_{\mathbf{k}} f_B(\mathbf{k}, T, \mu). \tag{2.2}$$

We can separate the ground state contribution to the particle number:

$$N(T, \mu) = \frac{1}{\exp\left(\frac{E_0-\mu}{k_B T}\right) - 1} + \sum_{\mathbf{k}\neq 0} f_B(\mathbf{k}, T, \mu), \tag{2.3}$$

E_0 being the ground state energy. In the thermodynamic limit we consider an infinite volume and the sum is replaced by an integral:

$$n(T, \mu) = \lim_{V\to\infty} \frac{N(T, \mu)}{V} = n_0 + \frac{1}{(2\pi)^d} \int_0^\infty f_B(\mathbf{k}, T, \mu)\, d^d\mathbf{k}, \tag{2.4}$$

where n_0 is the ground state contribution: $n_0(T, \mu) = \lim_{V\to\infty} \frac{1}{V} \frac{1}{\exp\left(\frac{E_0-\mu}{k_B T}\right)-1}$.

The maximum particle density in the excited states n_c is achieved for $\mu = E_0$:

$$n_c = \lim_{\mu\to E_0} \frac{1}{(2\pi)^d} \int_0^\infty f_B(\mathbf{k}, T, \mu)\, d^d\mathbf{k}. \tag{2.5}$$

For particles with a parabolic dispersion (free particle) $E(k) - E_0 = \frac{(\hbar \mathbf{k})^2}{2m}$ the integral (2.5) can be computed analytically. It diverges for $d \leq 2$ and converges for $d > 2$. In the latter, n_c is thus a critical density above which no particle can be added to the excited states. This explains why all particle added above this threshold condensate into the ground state and $n_0(T) = n(T) - n_c(T)$ becomes macroscopic. This distinctly quantum behavior is called the *Bose-Einstein condensation*.

The first experimental BEC dates from 1995 [54] in a 3D diluted atomic gaz of Rubidium-87. This pioneer experiment inaugurated a whole new domain of physics allowing the study of an impressive number of quantum phenomena. We saw in section 1.6.2 that in the usual density conditions, polaritons obey the Bose–Einstein statistic. However semiconductor microcavities are systems of dimensionality $d \leq 2$ and we just established that a finite solution to equation (2.5) is only possible for $d > 2$. So, condensation is *a priori* impossible in confined systems. In reality this divergence simply indicates that for $d \leq 2$ systems the BEC is impossible in the thermodynamic limit. In a finite-size system a quasi-condensation is possible. Indeed in this case the system is quantized and the sum in (2.3) excludes the ground state region which is responsible for the divergence of (2.5). Dimensionality is hence not an issue in semiconductor microcavities due to their small size. However in order to observe polariton condensation, the very short polariton lifetime presents a technological challenge. It imposes to realize structures that stimulate the polariton relaxation in order to allow their thermalization. This challenge was met and the polariton BEC phenomenon was observed for the first time in 2006 by Jacek Kasprzak *et al.* [46] with a non-resonant excitation, as illustrated by figure 2.1. In this experiment the laser pump injects hot electron-hole pairs, whose excess energy can be dissipated via phonon emission and then Coulomb scattering processes to form a polariton population at the bottom of the lower polariton branch (see the left panel). For sufficiently high pump powers, the density of the polaritons exceeds the critical density for Bose-Einstein condensation and a coherent condensate appears (middle and left panels). While the system is still a driven-dissipative one, a quasi-thermal equilibrium state is achieved if the loss rate is sufficiently low compared to the thermalization time of the polariton gas.

2.1.2. Gross-Pitaevskii equation

The Gross-Pitaevskii equation describes BEC of dilute, non-uniform, interacting particle gases. It follows from the Bogoliubov theory for uniform Bose gases. It is in essence a *nonlinear Schrödinger equation*, developed independently in 1961 by Pitaevskii [50] and Gross [49]. This evolution equation is the main theoretical tool to explore dilute non-uniform Bose gases in their quantum regime (low temperature).

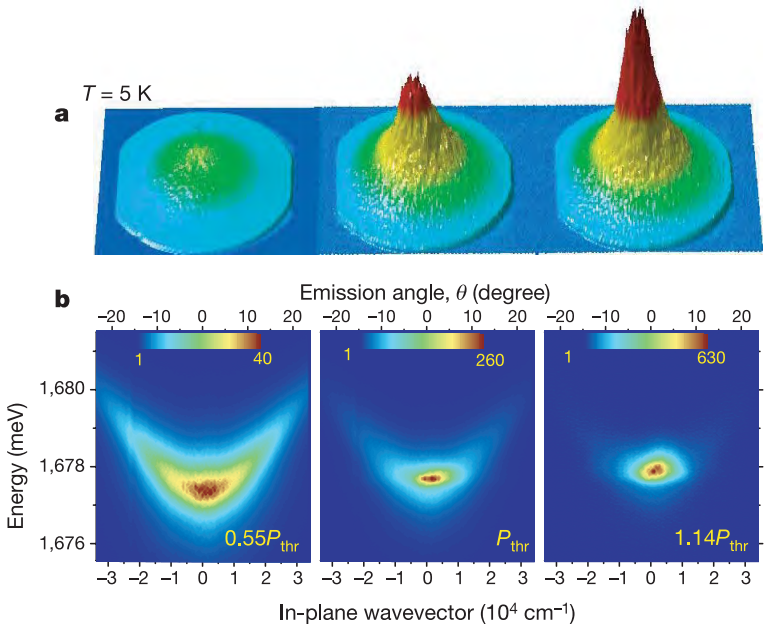

Figure 2.1.: Polariton condensation – Experimental figure of polariton condensation, in real space (3D representation, (a)) and energy-impulsion space (b). Above a pump intensity threshold polaritons macroscopically populate the lowest energy level. From [46].

Here we detail this approach for generic Bose gas by following the logic of reference [51], then expand it to the case of resonantly injected macroscopic populations of polaritons in section 2.2.1, by adding a pump and losses terms that take into account the non-equilibrium nature of polaritons. Let's start with a field approach $\hat{\psi}(r)$ to the Bose gas, where $\hat{\psi} = \sum_i \phi_i \hat{a}_i$. $\hat{a}_i^\dagger$ ($\hat{a}_i$) is the creation (anihilation) operator for a particle in the state ϕ_i and obeys the commutation relations $\left[\hat{a}_i, \hat{a}_j^\dagger\right] = \delta_{i,j}$ and $\left[\hat{a}_i, \hat{a}_j\right] = 0$.

The ground state population ($i = 0$) is macroscopic since we want to describe an interacting condensate. This is why, here like for (2.3) it is relevant to separate the ground state from the rest of the sum:

$$\hat{\psi} = \phi_0 \hat{a}_0 + \sum_{i \neq 0} \phi_i \hat{a}_i. \tag{2.6}$$

We now realize the Bogoliubov approximation by replacing $\hat{a}_0$ and $\hat{a}_0^\dagger$ by N_0. This is equivalent to neglect the non-commutation of $\hat{a}_0$ and $\hat{a}_0^\dagger$, which in turn is equivalent to take a semiclassical approach on the macroscopic field in the ground state. Equation (2.6) can then be rewritten:

$$\hat{\psi} = \psi_0 + \delta\hat{\psi}, \tag{2.7}$$

with $\psi_0 = \sqrt{N_0}\phi_0$ and $\delta\hat{\psi} = \sum_{i\neq 0} \phi_i \hat{a}_i$. At zero temperature, $\delta\hat{\psi} = 0$ and the field operator is equal to ψ_0 the classical field, and all particles are condensed. For small but finite temperature, $N_0 \gg 1$ [1] and $\delta\hat{\psi}$ is a perturbation to the condensate.

Now considering a nonuniform condensate, equation (2.7) becomes:

$$\hat{\psi}(\boldsymbol{r}) = \psi_0(\boldsymbol{r}) + \delta\hat{\psi}(\boldsymbol{r}), \tag{2.8}$$

$\psi_0(\boldsymbol{r})$ is called the *condensate wavefunction* and plays the role of an order parameter. It is a complex field normalized to the particle number $\int |\psi_0|^2 (\boldsymbol{r}) d\boldsymbol{r} = N_0$, which implies that the squared amplitude coincides with the density of the gas: $\left|\psi_0(\mathbf{r})\right|^2 = n_0(\mathbf{r})$. Therefore the amplitude is $\left|\psi_0(\mathbf{r})\right| = \sqrt{n_0(\mathbf{r})}$ and the phase is $\theta(\mathbf{r})$:

$$\psi_0(\mathbf{r}) = \sqrt{n_0(\mathbf{r})} e^{i\theta(\mathbf{r})}. \tag{2.9}$$

The Bogoliubov ansatz (2.9) can be interpreted as a mean field approach. The condensate wave function takes a particular phase [2], such that $\langle\hat{\psi}\rangle$ is non-zero and equal to the complex number ψ_0. Physically this means that for $N_0 \gg 1$ adding or subtracting a particle will not change the condensate. Taking the mean value over the N-particles stationary states with a time dependence $e^{-iEt/\hbar}$, the time evolution of the order parameter is given by:

$$\psi_0(t) = \langle\hat{\psi}\rangle(t) = \psi_0 e^{-i(E(N)-E(N-1))t/\hbar} \simeq \psi_0 e^{-i\mu t/\hbar}. \tag{2.10}$$

Where $\mu = \frac{\partial E}{\partial N} \simeq E(N) - E(N-1)$ is the chemical potential.

The Hamiltonian for an interacting boson gas is:

$$\hat{H} = \int d\mathbf{r} \hat{\psi}^\dagger(\mathbf{r}) \left[\frac{\nabla^2\hbar^2}{2m} + V_{ext}(\mathbf{r}) + \int d\mathbf{r}' \frac{1}{2} \hat{\psi}^\dagger(\mathbf{r}') V(\mathbf{r}-\mathbf{r}') \hat{\psi}(\mathbf{r}') \right] \hat{\psi}(\mathbf{r}). \tag{2.11}$$

The field operator in the Heisenberg representation then follows the equation:

$$i\hbar \frac{\partial\hat{\psi}(\mathbf{r},t)}{\partial t} = \left[\hat{\psi}(\mathbf{r},t), \hat{H}\right] = \left(-\frac{\nabla^2\hbar^2}{2m} + V_{ext}(\mathbf{r},t) + \int d\mathbf{r}' \hat{\psi}^\dagger(\mathbf{r}',t) V(\mathbf{r}-\mathbf{r}') \hat{\psi}(\mathbf{r}',t) \right) \hat{\psi}(\mathbf{r},t). \tag{2.12}$$

1. This condition is required for the Bogoliubov approximation to be valid.
2. This spontaneously breaks the $U(1)$ symmetry of the non-condensed system.

The Gross-Pitaevskii equation is obtained by replacing $\hat{\psi}(\mathbf{r},t)$ by $\psi_0(\mathbf{r},t)$ and by taking a contact-point interaction between particles $V(\mathbf{r}-\mathbf{r}') = g\delta(\mathbf{r}-\mathbf{r}')$:

$$i\hbar\frac{\partial\psi_0(\mathbf{r},t)}{\partial t} = \left(-\frac{\nabla^2\hbar^2}{2m} + V_{ext}(\mathbf{r},t) + g\left|\psi_0(\mathbf{r},t)\right|^2\right)\psi_0(\mathbf{r},t) \tag{2.13}$$

and thus, in the stationary case (equation (2.10)):

$$\left(-\frac{\nabla^2\hbar^2}{2m} + V_{ext}(\mathbf{r}) - \mu + g\left|\psi_0(\mathbf{r})\right|^2\right)\psi_0(\mathbf{r}) = 0. \tag{2.14}$$

Note that for an homogeneous gas ($V_{ext}(\mathbf{r}) = 0$) we find a constant chemical potential $\mu = gn_0$ depending on the interaction strength and the density.

In this approach the number of particles is preserved, so that we can find an equation of conservation for $\psi_0(\mathbf{r})$. By multiplying the Gross-Pitaevskii equation (2.13) with $\psi_0^*(\mathbf{r})$ and subtracting the complex conjugate we obtain

$$i\hbar\left(\psi_0^*(\mathbf{r},t)\frac{\partial\psi_0}{\partial t}(\mathbf{r},t) - \psi_0(\mathbf{r},t)\frac{\partial\psi_0^*}{\partial t}(\mathbf{r},t)\right) = -\frac{\hbar}{2m}\left(\psi_0^*(\mathbf{r},t)\nabla^2\psi_0(\mathbf{r},t) - \psi_0(\mathbf{r},t)\nabla^2\psi_0^*(\mathbf{r},t)\right), \tag{2.15}$$

which is a conservation equation of the form $\frac{\partial n}{\partial t} = -\boldsymbol{\nabla}\cdot\mathbf{j}$, where the current density is:

$$\mathbf{j}(\mathbf{r},t) = \frac{\hbar}{2m}\left(\psi_0^*(\mathbf{r},t)\nabla\psi_0(\mathbf{r},t) - \psi_0(\mathbf{r},t)\nabla\psi_0^*(\mathbf{r},t)\right) \tag{2.16}$$

Defining the velocity field of polaritons as $\mathbf{v}(\mathbf{r},t) = \frac{\mathbf{j}(\mathbf{r},t)}{n_0(\mathbf{r},t)}$ and taking the explicit value (2.9) of ψ_0 we find:

$$\mathbf{v}(\mathbf{r},t) = \frac{\hbar}{m}\nabla\theta(\mathbf{r},t). \tag{2.17}$$

From there it is easy to see that the velocity field is irrotational, meaning that $\boldsymbol{\nabla}\times\mathbf{v} = \mathbf{0}$. This fact, characteristic of BECs is responsible for the appearance of exotic topological defects such as quantized vortices, as we shall see in section 2.3. A great advantage of polariton systems is that the density and phase describing the order parameter are conserved during the interaction of excitons with the electromagnetic field. This is why measuring the intensity and phase of the microcavity emission gives directly the amplitude and the phase of the condensate. This phase reveals a long range coherence between polaritons [46, 55].

2.1.3. Landau criterion for superfluidity

Superfluidity was discovered by P. Kapitza, J.F. Allen and D. Misseneren in 1937 in Helium 4 [56, 57]. They observed that under a given temperature called λ *point*, $T_\lambda = 2.17\,\mathrm{K}$, the fluid viscosity becomes extraordinarily weak. In 1938, Fritz London notices that T_λ for helium 4 is close to the BEC temperature for a perfect gas of the same density as helium (3.2 K). He then suggested a link between the two phenomena [58]. The explanation of superfluidity came in 1941 by Landau, who showed that if the fluid elementary excitation spectrum satisfies a specific criterion, quantum mechanics does not allow the moving fluid to have any dissipation [59].

In the Landau formulation of superfluidity, the laws of energy and momentum transformation under the Galilean group are central. Let E and $\mathbf{P}$ be the energy and the momentum of a fluid in the Galilean referential R. The fluid energy and momentum in the referential R_0 moving at a velocity $\mathbf{V}$ relative to R are given by:

$$E' = E - \mathbf{P}.\mathbf{V} + \frac{1}{2}M\mathbf{V}^2, \tag{2.18}$$

$$\mathbf{P}' = \mathbf{P} - M\mathbf{V}, \tag{2.19}$$

where M is the total mass of the fluid. We now look for a condition on the creation of elementary excitation that are responsible for dissipation, and thus for the fluid viscosity.

We consider a fluid at very low temperature flowing in a tube at constant speed $\mathbf{v}$ and describe it in the frame of reference moving with the fluid. In such a frame the fluid is immobile. For an excitation with momentum $\mathbf{p}$ the total energy is $E_0 + \epsilon(p)$ where E_0 and $\epsilon(p)$ are respectively the non-excited fluid energy and the excitation energy. In the referential at rest (the tube referential), the energy E' and the momentum $\mathbf{P}'$ of the fluid are:

$$E' = E_0 + \epsilon(\mathbf{p}) + \mathbf{p}.\mathbf{v} + \frac{1}{2}M\mathbf{v}^2, \tag{2.20}$$

$$\mathbf{P}' = \mathbf{p} + M.\mathbf{v}, \tag{2.21}$$

since in the fluid referential the tube moves at speed $-\mathbf{v}$. In the above equations we can see that the energy contribution of the excitation is $\epsilon(\mathbf{p}) + \mathbf{p}.\mathbf{v}$. If the fluid loses energy by getting excited (if $\epsilon(\mathbf{p}) + \mathbf{p}.\mathbf{v} < 0$) then the non-excited state of the fluid is unstable and excitations spontaneously appear: the fluid viscosity increases. This is possible for

$|\mathbf{v}| > \frac{\epsilon(\mathbf{p})}{p}$. If, however, the fluid velocity $v = |\mathbf{v}|$ is inferior to a critical velocity:

$$v_c = \min_{\mathbf{p}} \frac{\epsilon(\mathbf{p})}{p}, \tag{2.22}$$

then no excitation can spontaneously form and the fluid is bound to stay in its ground state. In this case the viscosity is null and the fluid is in a superfluid state. This criterion, written simply:

$$v < v_c, \tag{2.23}$$

is called the *Landau criterion* and ensures a viscosity-free flow.

2.1.4. Elementary excitation spectrum

We now compute the spectrum for elementary excitations of an interacting BEC. For this we suppose that there is no external potential and that the BEC obeys the Gross-Pitaevskii equation (2.13). Let us consider a small perturbation propagating in the condensate with a momentum $\boldsymbol{p} = \hbar\boldsymbol{k}$. The BEC is initially described by the static wavefunction ψ_0 and the density n_0. The perturbed order parameter undergoes the Bogoliubov transformation:

$$\psi(\mathbf{r}, t) = \left[\phi_0(\mathbf{r}) + Ae^{i(\mathbf{k}.\mathbf{r}-\omega t)} + B^* e^{-i(\mathbf{k}.\mathbf{r}-\omega t)}\right] e^{-i\frac{\mu t}{\hbar}}, \tag{2.24}$$

where the energy origin is fixed at the static condensate energy (for $\mathbf{k} = \mathbf{0}$) and where A and B^* are the perturbations amplitudes. It is possible to inject this function in (2.13) and isolate the terms that evolve as $e^{\pm i\omega t}$ with time to obtain the set of coupled equations:

$$\hbar\omega A = \left(\frac{\hbar^2 k^2}{2m} - \mu + 2gn_0\right) A + gn_0 B, \tag{2.25}$$

$$-\hbar\omega B = \left(\frac{\hbar^2 k^2}{2m} - \mu + 2gn_0\right) B + gn_0 A. \tag{2.26}$$

If we consider the gas uniform then $\mu = gn_0$, this two-equation system is then easily solvable and we get the energies:

$$\hbar\omega_\pm = \pm\sqrt{\left(\frac{\hbar^2 k^2}{2m}\right)^2 + \frac{\hbar^2 k^2}{m} gn_0}. \tag{2.27}$$

For small $\boldsymbol{k}$ this dispersion relation become linear [60] and we can define a speed of sound for the condensate:

$$c_s = \sqrt{\frac{gn_0}{m}}. \tag{2.28}$$

In this small momentum limit the critical velocity for the Landau criterion (2.23) in a BEC is c_s, the speed of sound. It means that a moving BEC is superfluid if it remains in the subsonic regime. To obtain the energy and momentum of such a flowing BEC, a simple Galilean transformation is enough. In agreement with the Landau criterion, we observe on figure 2.2 that the condensate is superfluid for $v = \frac{\hbar k_0}{m} < \sqrt{\frac{gn_0}{m}} = c_s$, since the condensate of energy E_0 and momentum k_0 does not have any available state with the same energy in which to elastically scatter. If $v > c_s$ such states are available and the fluid is in the *Cerenkov regime*, where a peculiar kind of conic excitation appear.

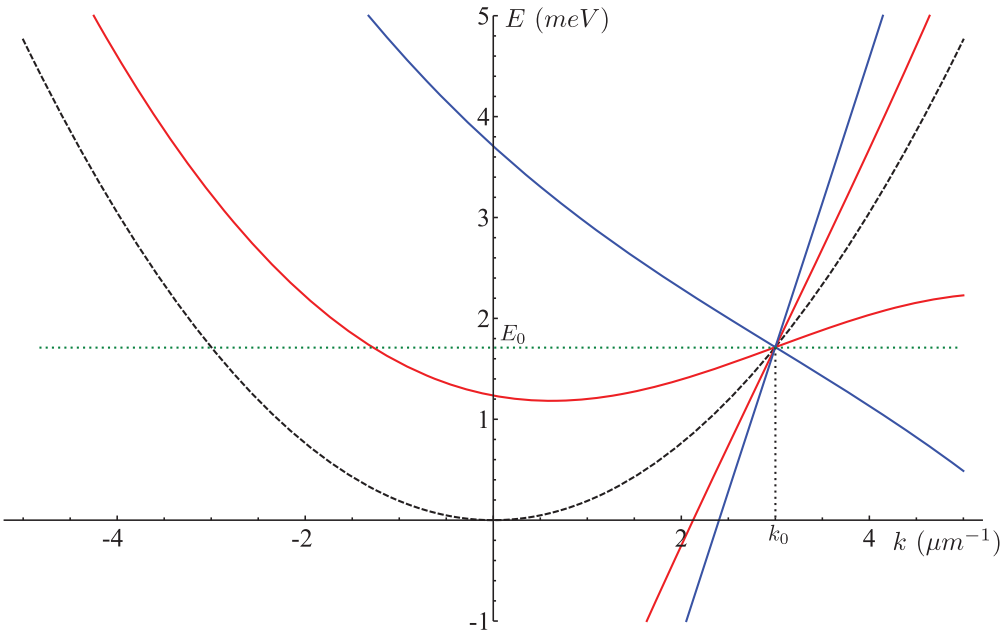

Figure 2.2.: Dispersion relation of excitation in a BEC – Dispersion relation for elementary excitation of a condensate having a fixed $k_0 = 3\ \mu\text{m}^{-1}$ and an energy E_0. The dashed line represents the (parabolic) dispersion without interactions. The blue (red) line shows the dispersion for a superfluid $v < c_s$ (supersonic fluid $v > c_s$). In the superfluid case no elastic diffusion is possible, while an elastic diffusion is possible for the supersonic (also called Cerenkov) regime. The green horizontal line is a guide for the eye at E_0 as its intersection with the dispersion curves shows the accessible diffusion states.

2.2. Quasi-resonant injection of polaritons

There are two ways of injecting polaritons in a microcavity. One is the so-called "out-of-resonance" pumping and consists of injecting high energy photons ($E_\gamma \gg E_X$) with a laser. Depending on the efficiency of the relaxation phenomena polaritons can thermalize and form a quasi-BEC [46]. With this injection method a large exciton population is created in addition to the polariton population. The second technique to create a fluid of polaritons is the "resonant injection" (or "quasi-resonant"). It consists of injecting laser photons directly at an energy and in-plane wavevector that are resonant with the (lower) polariton branch. This way the energy and the wavevector of the resulting polariton population are completely controlled. Using a continuous laser we can create a large polariton populations whose properties (pseudospin, momentum, energy, density, ...) are inherited from the pump. This controlled injection allows the study of propagation-related phenomenon [13, 14, 61, 17], and quantum fluid dynamics experiments are achievable under this pumping scheme. Note that this is unlike the out-of-resonance setup, where the pump properties (in-plane wavevector, energy, polarisation, ...) are lost during the relaxation process.

In the resonant scheme one can induce a small energy difference between the laser and the polariton energy. This is called the quasi-resonant pumping scheme, and the energy difference is the variable $\Delta = E_{las} - E_{LP}$ introduced in section 1.6.1. With a quasi-resonant pumping the nonlinearities play an important role and induce a bistable behavior accompanied by many interesting phenomena, such as modifications of the field fluctuations (see chapter 7.3.3) and bistability, that results in density jumps that enable to achieve higher densities than through sheer (resonant) pump power. This bistability will be detailed in subsection 2.2.2 of the present chapter.

2.2.1. Gross-Pitaevskii for polaritons: driven-dissipative equation

For resonantly injected polaritons, we cannot consider the system as being at the thermodynamic equilibrium. It is necessary to add time-dependent terms such as the laser pump $F_L(\mathbf{r},t)$ which generates polariton with controlled wavevector $\mathbf{k}_L(\mathbf{r},t)$ and energy E_L: $F_L(\mathbf{r},t) = A_{LC}(\mathbf{r},t)e^{i(\mathbf{k}_L(\mathbf{r},t)r-\omega_L t)}$ [3]. A_{LC} is the amplitude of the pump fraction that enters the cavity and couples to excitons, and is linked to A_L the extracavity laser amplitude by: $A_{LC} = C_0\sqrt{2\gamma_1}A_L$. $\gamma_1 = \frac{T_1}{\tau}$ is the intracavity field decay rate through the front mirror, where τ is the two-ways propagation time of photons in the cavity (see [33] for detailed calculations) and T_1 is the front mirror transmission. $C_0 \equiv C_{\boldsymbol{k}=0}$ is the

3. As we will see in chapter 5 the pump can take any form, hence the space-time dependence of $\mathbf{k}_L$ and A_{LC}

Hopfield coefficient defined in 1.22.
Likewise we need to add the relaxation term for the (lower) polaritons $\gamma_{\mathbf{k}}^{LP} \equiv \gamma$ defined in (1.32). The *driven-dissipative* Gross-Pitaevskii equation, in absence of time-dependent external potential and with a resonant pump ($\Delta = 0\,\text{meV}$) is [62, 63]:

$$i\hbar\frac{\partial\psi_0(\mathbf{r},t)}{\partial t} = \left(-\frac{\nabla^2\hbar^2}{2m} + g\left|\psi_0(\mathbf{r},t)\right|^2 - i\frac{\hbar\gamma}{2}\right)\psi_0(\mathbf{r},t) + F_L(\mathbf{r},t). \tag{2.29}$$

It is this equation that we use to simulate the system and predict the polariton flow. This model was able to make accurate numerical predictions for the quantum fluid experiments presented in this Part (Part I).

This out-of-equilibrium system can lead to stationary density states for a stationary pump. The steady-state equation is:

$$F_L(\mathbf{r}) = \left(i\frac{\hbar\gamma}{2} + \frac{\nabla^2\hbar^2}{2m} - g\,n_0(\mathbf{r})\right)\psi_0(\mathbf{r}). \tag{2.30}$$

The density and the phase (and thus the polariton velocity) can hence be made constant in time despite the dissipative nature of the system.

2.2.2. Bistability

Polaritons can be seen as photons propagating in an effective Kerr media, due to the exciton-exciton interaction. Indeed the interaction term is of the third order and (2.29) is analog to an electromagnetic wave in resonance with a cavity containing a Kerr medium. From this point of view phenomenon such as bistability and squeezing are not surprising, since well-known to occur in Kerr media [64, 65, 66]. Bistability was experimentally observed in microcavity polaritons in the early 2000s [43, 67, 68]. Adding the spin parameter one can also observe multistability [69, 70, 71, 72], that is to say a bistability for each polariton spin population.

When the pump-polariton detuning $\Delta = \hbar\omega_L - E_{LP}$ is negative, the absorption diminishes with the pump intensity because the interaction-induced energy renormalization drives the mode away from resonance (optical limiter regime). However when the detuning is positive, an increase in pump intensity will increase the polariton density and renormalize the polariton energy closer to the laser energy, which increases the wavefunctions overlap and in turn increases the polariton density. Hence the existence of an intensity threshold above which an infinitesimal increase in polariton density will self-amplify. Beyond this threshold the polariton energy is directly renormalized to the laser pump energy. In this bistability *higher branch*, the lower polariton branch and the laser are resonant.

We describe the bistable behavior starting from the steady-state driven-dissipative Gross-Pitaevskii equation (2.30). As mentioned earlier the bistability stems from the quasi-resonant pumping; we thus need to take into account the pump-polariton detuning Δ. Also, we want to focus on the effect of this pumping scheme on the density and, in Part II, on the fields fluctuations. To do this and put aside any propagation effect, we impose $k = 0\,\mu\text{m}^{-1}$. This so-called *degenerate four-wave mixing* is realized when pumping the sample at normal incidence. The physical process at play here can be seen as the two-by-two interaction ("four wave mixing") between identical, at rest (hence "degenerate") polaritons. Under these conditions the steady-state equation is [33]:

$$F_L(\mathbf{r}) = \big(i\hbar\gamma + \Delta - g\,n_0(\mathbf{r})\big)\,\psi_0(\mathbf{r}), \tag{2.31}$$

and when multiplying by the complex conjugate we get:

$$I_{LC}(\mathbf{r}) = \big((\hbar\gamma)^2 + (\Delta - g\,n_0(\mathbf{r}))^2\big)\,n_0(\mathbf{r}), \tag{2.32}$$

where $I_{LC}(\mathbf{r}) = C_0^2 2\gamma_1 A_L^2(\mathbf{r})$ is the intracavity laser pump intensity and where $\psi_0(\mathbf{r})\psi_0^*(\mathbf{r}) = n_0(\mathbf{r})$. This equation is very similar to the one giving the intensity of an electromagnetic field in a cavity containing an ideal passive Kerr medium, whose reduced formulation is [73]:

$$I_i' = I_t'(1 + (x + I_t')^2). \tag{2.33}$$

I_i' and I_t' are dimensionless quantities [4] proportional to the incident intensity and to the transmitted intensity, respectively, while x is a dimensionless parameter that characterizes the detuning to the cavity resonance.

If Δ is sufficiently high, this third order polynomial in n_0 can give rise to two possible values of the polariton density for a fixed pump intensity: the system is bistable. $n_0(I_{LC})$ is plotted in figure 2.3 for parameter values that show a clear bistable region. To find the two turning points we need to solve:

$$\frac{\partial I_{LC}}{\partial n_0} = 3g^2 n_0^2 - 4\Delta g n_0 + (\hbar\gamma)^2 + \Delta^2 = 0. \tag{2.34}$$

The discriminant is $(2g)^2(\Delta^2 - 3(\hbar\gamma)^2)$. The previous equation has two distinct real roots only if $\Delta > \sqrt{3}\hbar\gamma$: when this condition is realized the bistable behavior appears. The onset of bistability is thus given by:

$$\Delta = \Delta_c = \sqrt{3}\hbar\gamma, \tag{2.35}$$

4. Their exact expressions depend on the cavity parameter.

meaning:

$$\omega_L = \omega_p + \sqrt{3}\gamma. \tag{2.36}$$

In that case the density values at the two bistability turning points are:

$$n_0^{\pm} = \frac{2\Delta \pm \sqrt{\Delta^2 - 3(\hbar\gamma)^2}}{3g}, \tag{2.37}$$

and the extracavity laser intensity at which they happen are:

$$I^{\pm} = \frac{I_{LC}^{\pm}}{2C_0^2\gamma_1} = \frac{(2\Delta \pm \sqrt{\Delta^2 - 3(\hbar\gamma)^2})\left((\hbar\gamma)^2 + \frac{\Delta}{3}(\Delta \mp \sqrt{\Delta^2 - 3(\hbar\gamma)^2})\right)}{9gC_0^2\gamma_1}. \tag{2.38}$$

We see from (2.32) and (2.37) that the threshold density increases approximately linearly with Δ. For a fixed pump intensity I, the density in presence of bistability is always higher in the upper branch than the density in the non-bistable regime ($\Delta = 0$). This mechanism is used in the experiments presented in this thesis to control the density and reach higher nonlinearities than would be possible in a purely resonant setup.

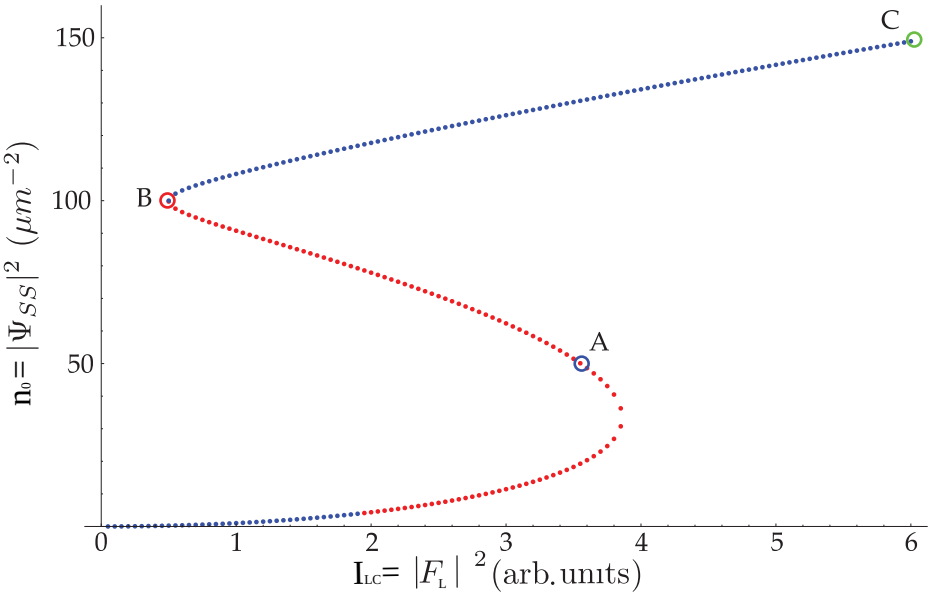

Figure 2.3.: Bistability– Numerical resolution of equation (2.32) for the parameters: $\hbar\gamma = 0.1$ meV, $\mathbf{k}_p = 0$, $\Delta = 1$ meV. The blue zone represents the stable zone while the red zone indicates the region of non-physical solutions [62]. The density jumps from one blue zone to the other at turning points (blue-red frontier). The A, B and C points are respectively referring to the blue, red and green curves of figure 2.4.

2.2.3. Polariton superfluidity

We saw that with the quasi-resonant injection it is possible to populate macroscopically a state with $k \neq 0\ \mu\text{m}^{-1}$. We then recover a physical situation very similar to the moving BEC which we found to be superfluid for $v < c_s$. A generalized Landau criterion can be applied to polaritons, if we take into account their driven-dissipative nature. Taking the same perturbation as in (2.24):

$$\psi(\boldsymbol{r},t) = \left(\psi_0(\boldsymbol{r}) + Ae^{i(\boldsymbol{kr}-\omega t)} + B^* e^{-i(\boldsymbol{kr}-\omega t)}\right) e^{i(\boldsymbol{k}_L \boldsymbol{r}-\omega_L t)}, \tag{2.39}$$

where ω_L and $\boldsymbol{k}_L$ are respectively the laser angular frequency and in-plane wavevector, replacing this expression into the modified Gross-Pitaevskii equation (2.29), retaining only linear terms in A and B and noticing the zeroth order terms cancel out we get:

$$-gn_0 B = A\left(\frac{\hbar^2\left(\boldsymbol{k}_L+\boldsymbol{k}\right)^2}{2m} - \frac{i\hbar\gamma}{2} + 2gn_0 - \hbar\left(\omega_L+\omega\right)\right), \tag{2.40}$$

$$-gn_0 A = B\left(\frac{\hbar^2\left(\boldsymbol{k}_L-\boldsymbol{k}\right)^2}{2m} + \frac{i\hbar\gamma}{2} + 2gn_0 - \hbar\left(\omega_L-\omega\right)\right), \tag{2.41}$$

which implies the following dispersion relation:

$$\hbar\omega_\pm = \frac{\hbar^2\boldsymbol{k}_L\boldsymbol{k}}{m} - \frac{i\hbar\gamma}{2} \pm \sqrt{\left(\frac{\hbar^2(\boldsymbol{k}_L^2+\boldsymbol{k}^2)}{2m} - \hbar\omega_L + 2gn_0\right)^2 + (gn_0)^2}. \tag{2.42}$$

The real part of this spectrum (the solution $\hbar\omega_+$ is represented with thick lines while $\hbar\omega_-$ is represented with dashed lines) is plotted in figure 2.4 for three different polariton mean densities, each corresponding to a point in figure 2.3, for $\boldsymbol{k}_L = 0\ \mu\text{m}^{-1}$ [62].

We observe different spectra depending on the ratio between the interaction energy gn_0 and the energy detuning Δ. Indeed for $\frac{gn_0}{\Delta} > 1$ we observe an energy gap (C), for $0 < \frac{gn_0}{\Delta} \lesssim 1$ the spectrum possesses a flat region (A) and we recover the linear Bogoliubov spectrum observed in interacting condensates if $\frac{gn_0}{\Delta} = 1$ (B) [13, 61]. The imaginary part of (2.42) gives useful information on the stability of the different real-part spectra [62]: we observe that spectra with a flat zone ($0 < \frac{gn_0}{\Delta} \lesssim 1$) have a negative imaginary part, making them unstable. This corresponds to densities laying on the unstable section of the bistability curve. Note however that if $\frac{gn_0}{\Delta} \ll 1$ (lower bistability stable zone) or if $\frac{gn_0}{\Delta} > 1$ (upper bistability branch) the solution is stable. The three spectra (A,B,C) correspond to the three A, B and C working points on the bistability curve in 2.3. $\frac{gn_0}{\Delta} = 1$ constitutes a critical case where the imaginary part is zero [62].

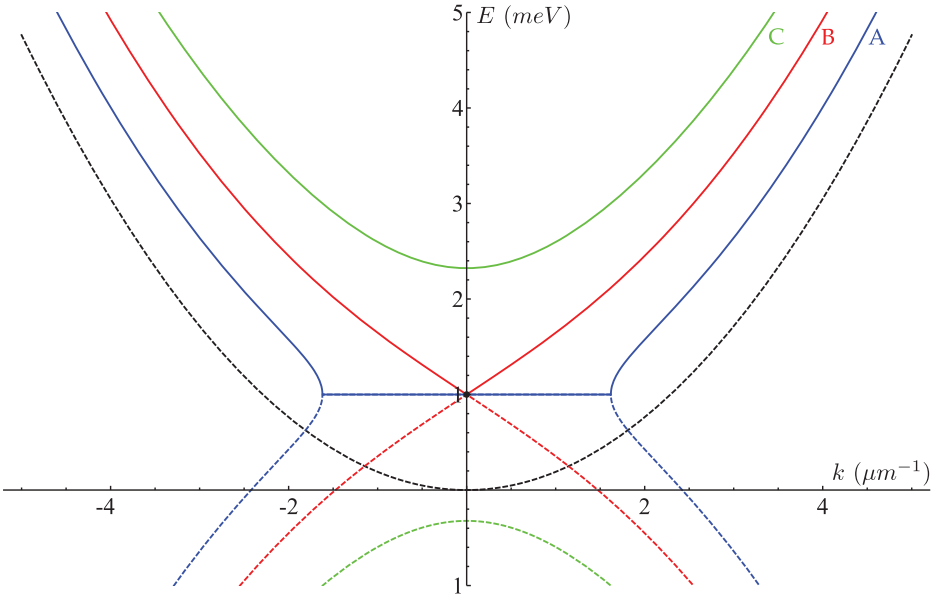

Figure 2.4.: Excitation spectrum – Dispersion relation for elementary excitations in a static polariton population pumped quasi-resonantly ($\boldsymbol{k}_p = 0\ \mu\text{m}^{-1}$). Here $\Delta = 1$ meV is fixed and each spectrum is plotted for a different density n_0 lying in the bistability curve 2.3 (a precise n_0 is reached by changing the pump intensity): $n_0 < \frac{2}{3}\frac{\Delta}{g}$ (A, in blue), $n_0 = \frac{\Delta}{g}$ (B, in red) and $n_0 > 2\frac{\Delta}{g}$ (C, in green). A, B and C refer to the three points of figure 2.3. The black curve represents the parabolic dispersion of non-interacting polaritons and its minimum is taken as the energy reference. Curve A presents an exotic shape that is shown to be unstable [62], and indeed corresponds to the unstable zone of the bistability. The solution $\hbar\omega_+$ is represented with thick lines while $\hbar\omega_-$ is represented with dashed lines. From [23].

In this case (2.42) can be simplified:

$$\omega = k\sqrt{\frac{gn_0}{m}}, \tag{2.43}$$

and we can define a speed of sound c_s:

$$c_s = \sqrt{\frac{gn_0}{m}}, \tag{2.44}$$

which is identical to the speed of sound for a BEC at equilibrium. Following the same reasoning as in section 2.1.3 we find that when $\frac{gn_0}{\Delta} = 1$ the polariton fluid moving at $v = \frac{\hbar k_L}{m}$ remains superfluid up to the critical speed $v_c = c_s$. Above c_s the fluid becomes supersonic and enters the Cerenkov regime, where states are available for polariton elastic scattering. Figure 2.5 illustrates different regimes for a moving polariton population satisfying $\frac{gn_0}{\Delta} = 1$. The excitation spectrum depends on the pump wavevector and energy. For low $\boldsymbol{k}$ the Landau criterion is respected and the pumped state has no other state available and thus cannot scatter, this is the superfluid regime. However if the fluid

velocity is increased so that the Landau criterion is not respected, scattering is possible and lead to the formation of a Cerenkov cone in the density.

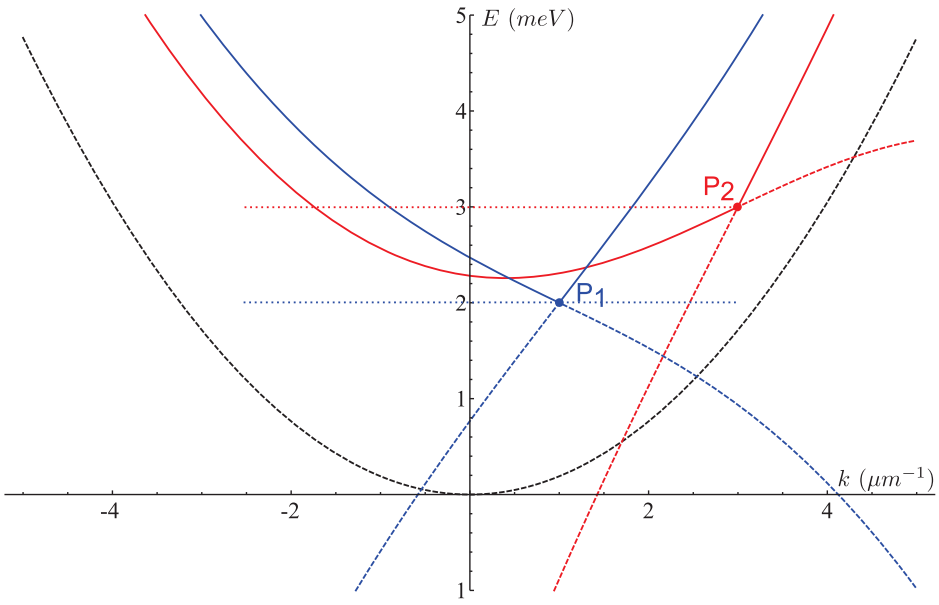

Figure 2.5.: Superfluid and Cerenkov regimes – Elementary excitation spectra for a resonantly pumped polariton condensate. The solution $\hbar\omega_+$ is represented with thick lines while $\hbar\omega_-$ is represented with blue and red dashed lines. The density and the pump-polariton detuning are set to satisfy $\frac{gn_0}{\Delta} = 1$. The blue curve is for $k_L = 1\,\mu\text{m}^{-1}$ and $\Delta = 2\,\text{meV}$ so that the Landau criterion is satisfied. We can see the fluid has only one state available and cannot elastically scatter: it is superfluid. This is not the case for the red curve, for which $k_L = 3\,\mu\text{m}^{-1}$ and $\Delta = 3\,\text{meV}$. The fluid can scatter and it is in the Cerenkov regime. The horizontal dashed line in blue (red) represents the pump energy for the blue (red) curve. The dashed black line represents the bare lower polariton branch.

Polariton superfluidity and Cerekov regime under quasi-resonant pumping where observed at LKB in 2009 [13] (see section 2.4). The model used here only considers a parabolic dispersion for polaritons, which is valid for small wavevectors. A refined model taking into account the full polariton dispersion is available in [62]. This model contains additional unstable zones due to the parametric amplification phenomena taken into account [74, 75, 76].

2.3. Elementary vortices

This section follows the work of Lev Pitaevskii and Sandro Stringari [51] for defining a vortex. Let us start with the relation (2.17) establishing the condensate speed as proportional to its phase gradient. We saw this means a condensate is irrotational, which

translates mathematically as $\boldsymbol{\nabla} \times \mathbf{v} = 0$. Consider a classical fluid rotating at the angular momentum $\boldsymbol{\Omega}$. Its velocity field $\mathbf{v}(\mathbf{r}) = \mathbf{r} \times \boldsymbol{\Omega}$ has for curl:

$$\boldsymbol{\nabla} \times \mathbf{v} = 2\boldsymbol{\Omega}, \tag{2.45}$$

in total contradiction with the irrotationality of a BEC. This means the BEC will not behave classically while rotating, and will show more exotic rotational excitations when stirred.

Let us now consider a 2D BEC having a disc shape of radius R. We want the system to be invariant by rotation around its central axis. Under these conditions the wavefunction takes the form:

$$\psi_0(r, \varphi) = \sqrt{n_0(r)} e^{i\theta(\varphi)} \tag{2.46}$$

where r and φ are the polar coordinates, n_0 is the density and θ is the phase. The gradient in polar coordinates being

$$\boldsymbol{\nabla} = \frac{\partial}{\partial r}\mathbf{u}_r + \frac{1}{r}\frac{\partial}{\partial \varphi}\mathbf{u}_\varphi \tag{2.47}$$

we deduce:

$$\mathbf{v}(r) = \frac{\hbar}{mr}\frac{\partial \theta}{\partial \varphi}\mathbf{u}_\varphi. \tag{2.48}$$

The hypothesis of a rotational invariance imposes that the speed is independent from φ. $\frac{\partial \theta}{\partial \varphi}$ is thus a constant. We call this constant ℓ and we will show that it is in fact an integer. Therefore the structure of a rotating condensate is radically different from a classical fluid: the velocity field decreases as $\frac{1}{r}$ in the rotating BEC while it increases as r for the classical fluid. This r-dependent velocity field amplitude is plotted in figure 2.6 (left) for $\ell = 1$.

Since $\frac{\partial \theta}{\partial \varphi}$ is a constant, the phase θ is proportional to φ. In addition, θ is defined modulo 2π so that on a closed loop around the disc center:

$$\oint \boldsymbol{\nabla}\theta \, \mathrm{d}\mathbf{l} = 2\pi n, \tag{2.49}$$

where n is an integer. This establishes that $n = \ell$. It also establishes that:

$$\oint \mathbf{v} \, \mathrm{d}\mathbf{l} = \frac{\hbar}{m}\ell, \tag{2.50}$$

meaning that the velocity field circulation around the center is quantized and independent from r. From (2.48) we see that if $\ell \neq 0$ the BEC speed diverges to infinity at $r = 0$. This

situation being physically impossible we expect the singularity to be "hidden" by a drop of density at the center: $n_0(r=0)=0$. This phase-and-density singularity defines the topological defect called a vortex.

We can derive the density profile $n_0(r)$ by using (2.46) into (2.13). The resulting equation is not solvable analytically, however an approximate derivation of the wavefunction is possible for $\ell = 1$ [77, 78]:

$$\left|\psi_0^{\ell=1}\right| = \sqrt{n_\infty}\frac{\left(\frac{r}{\xi}\right)}{\sqrt{\left(\frac{r}{\xi}\right)^2+1}}, \tag{2.51}$$

where n_∞ is the BEC density far from the vortex core and $\xi = \frac{\hbar}{\sqrt{2mgn_\infty}}$ is the condensate *healing length*, the characteristic distance from the singularity needed to recover the density $\frac{n_\infty}{2}$. The corresponding density profile is plotted on figure 2.6 and the experimental density and phase maps for an elementary ($\ell = 1$) vortex of polariton is presented in figure 2.7.

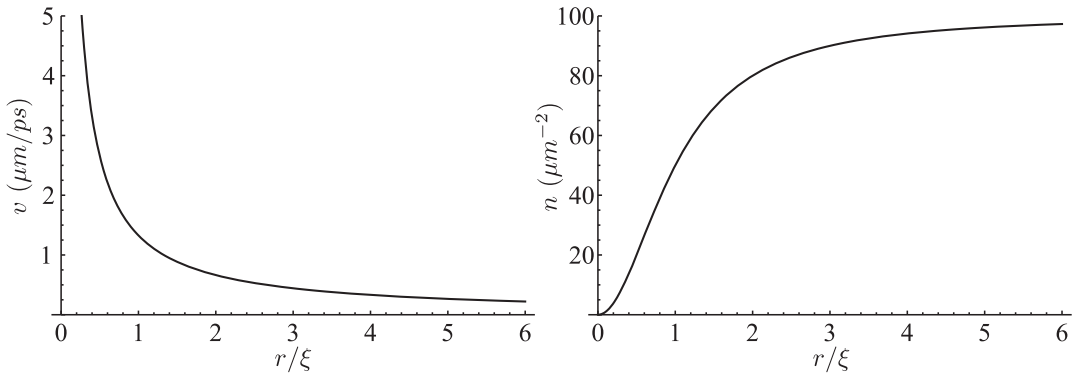

Figure 2.6.: Velocity and density profiles – The left panel represents the tangential speed as a function of the distance to the singularity, normalized to the healing length. On the right is plotted an approximate solution for the density versus the distance (normalized to the healing length). Both panels are for $\ell = 1$. Parameters are set to the usual values for polaritonic systems: $m = 2\,10^{-4}\,m_e$, $g = 0.01\,\mathrm{meV\mu m^2}$, $n_\infty = 100\,\mu\mathrm{m}^{-2}$ (cf. chapter 1). In our polariton system the typical healing length is on the order of 1 μm.

From all these vortex characteristics we refine the conditions a topological defect must meet to be labeled as an elementary polariton vortex, in the quantum hydrodynamic sense:

— A phase singularity around which the phase winds by 2π must be present.

— The density must be zero at the phase singularity.

— The density must be non-zero away from the singularity, so that the healing length is measurable.

The first two requirements are simply what we just established for BEC vortices. The third condition ensures that a polariton vortex indeed contains rotating polaritons: if one or more phase singularities are observed in a large area where the density is quasi-zero and if no healing length can be measured, then they should be considered as optical vortex (quantum optics) rather than polariton vortex (quantum hydrodynamics).

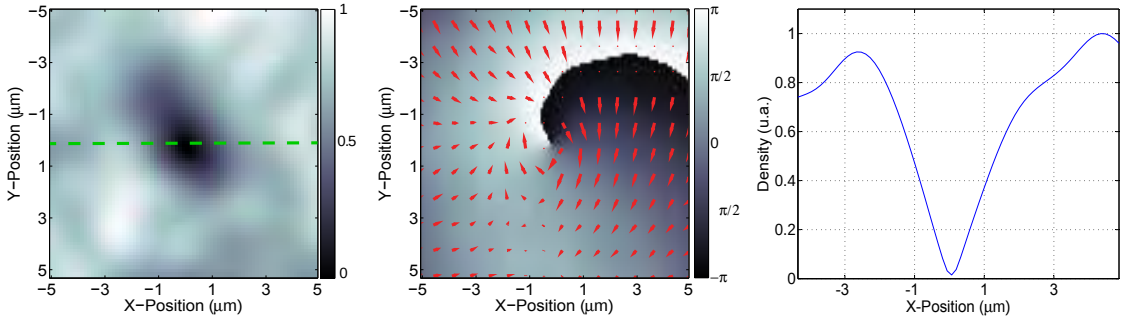

Figure 2.7.: Experimental elementary vortex– Zoom on the experimental density map (left), phase map (middle) and density profile (right) of a single elementary vortex ($\ell = 1$). The singularity is well visible at the center and the phase continuously winds from 0 to 2π around it. The red arrows show the polariton velocity field calculated from the phase gradient: they flow circularly around the singularity. The green dashed line on the density map indicates the direction of the cut used to produce the density profile.

We can also look into the energetic characteristics of vortices. The total polariton energy can be divided between contributions of the polariton kinetic energy and the polariton-polariton interaction energy. The interaction energy depends on the density $n_\ell(r)$ for each vortex of order ℓ, which is not accessible analytically [77, 78]. We can see however that in repulsively interacting quantum fluids such as polaritons, the energetically favorable solution is a homogeneous density. Adding vortices in the systems can only increase the interaction energy by creating inhomogeneities, for any ℓ. In the case of strongly interacting polaritons (high density regime reached using the bistability), as we will see in the next chapter, this can deeply modify the fluid behavior. In most dilute BECs, however, the energy is dominated by the kinetic energy. The study of kinetic energy E_k^ℓ brings interesting insights for vortex dynamics. We have, for the finite disc of radius R:

$$E_{kin}^\ell = \int\int \frac{1}{2} m v^2(\mathbf{r}) n_\ell(\mathbf{r})\, \mathrm{d}^2\mathbf{r}, \tag{2.52}$$

and thus:

$$E_{kin}^\ell = \frac{\pi\hbar^2\ell^2}{m} \int_0^R \frac{n_\ell(r)}{r}\, \mathrm{d}r. \tag{2.53}$$

First, we see that this energy is quadratic in ℓ. Therefore it is energetically more favorable to have N vortices of charge $\ell = 1$ than one vortex of charge $\ell = N$. This is why we observe angular momentum nucleation in atomic BECs [79] and why we expect to witness the same with polaritons. For $\ell = 1$ an analytical solution was calculated by Pitaevskii [50]:

$$E_{kin}^{\ell=1} = \frac{\pi\hbar^2 n_\infty}{m} \ln\left(1.46\frac{R}{\xi}\right). \tag{2.54}$$

We see that for $\ell = 1$ vortices, the energy dependence in n_∞ indicates that vortices should move towards lower density areas to minimize their energy. From there we can calculate the energy of a pair of vortices $\{\ell_1,\ \ell_2\}$. If the two vortices are separated by a distance d so that $R \gg d \gg \xi$:

$$E_{pair} \simeq \frac{2n_\infty}{m} \int\int \left(\mathbf{v}_1(\mathbf{r}) + \mathbf{v}_2(\mathbf{r})\right)^2 \mathrm{d}^2\mathbf{r}, \tag{2.55}$$

which can be written:

$$E_{pair} = E_{kin}^{\ell_1} + E_{kin}^{\ell_2} + E_{VInt}^{\ell_1\ell_2}, \tag{2.56}$$

where $E_{kin}^{\ell_1}$ and $E_{kin}^{\ell_2}$ are the kinetic energies for each vortex. $E_{VInt}^{\ell_1\ell_2}$, the cross term, is a vortex-vortex interaction energy term:

$$E_{VInt}^{\ell_1\ell_2} \simeq \frac{2\pi\hbar^2\ell_1\ell_2 n_\infty}{m} \ln\left(\frac{R}{d}\right). \tag{2.57}$$

The product $\ell_1\ell_2$ shows that two vortices of the same sign tend to repel each other, while vortices of opposite signs attract each other. It is this same-sign repulsion that is responsible for the self organization of vortices into an *Abrikosov lattice* in stirred atomic BECs [80, 81].

2.4. State of the Art: interacting fluids of light

As we saw polaritons can be understood in a purely nonlinear optics framework. Indeed, as an effective Kerr cavity medium system the polariton field can be seen as a photon field interacting with itself through the medium nonlinearity. In this sense it is part of a wider family of systems where an effective photon-photon interaction can be engineered, resulting in hydrodynamical-like behaviors. Such systems are labeled *quantum fluids of light*. Indeed, such a many-photon system can exhibit collective behaviors as a quantum

fluid with a number of novel features stemming from its intrinsically non-equilibrium nature [82].

In the last decades, the study of quantum fluids has attracted a strong interest in different many-particles systems, ranging from liquid Helium [83, 84], electrons in solid-state materials [85, 86, 87], trapped gases of ultracold atoms [88, 89, 90]), quark-gluon plasma [91, 92] and nuclei [93]. As for interacting photons, they have been predicted to happen even in vacuum via the virtual creation of electron-positron pairs [94]. However the cross section for such a process is incredibly small, so that it cannot play any significant role in a realistic optical system. However, the nonlinear polarization of nonlinear optical media is able to mediate significant interactions between photons [64, 95]. Among the different configurations studied for nonlinear optical applications, systems in the strong light-matter coupling regime, such as polariton, were found to be particularly promising to obtain the strong nonlinear interactions necessary to observe a fluid-like collective behavior.

Historically, the concept of photon fluid dates back to the work of Brambilla *et al.* (1991) [96] and Staliunas (1993) [97]. For the first time, the time-evolution of the coherent electromagnetic field in a laser cavity was reformulated in terms of hydrodynamic equations. This many-photon fluid description has strong analogies with the Gross-Pitaevskii equation for the superfluid order parameter that we described in section 2.1.2. Indeed, the local intensity corresponds to the photon density and the spatial phase gradient to the local current. The collective behavior then originates from the effective photon-photon interactions stemming from the nonlinear refractive index of the medium, like we saw in this chapter for polaritons.
After the first experimental observations in bulk nonlinear crystals [98], most of the literature addressed the physics of optical vortices in the context of the transverse dynamics of laser or photorefractive oscillators. The drift of vortices under the hydrodynamical effect of the Magnus force due to buoyancy was experimentally studied by Vaupel and Weiss in 1995. The hydrodynamical shedding of vortices in a moving photon fluid hitting a large defect was first predicted in the optical context [97] and a pioneering attempt of experimental investigation of this crucial superfluid hydrodynamics effect was reported soon after by Vaupel *et al.*, in 1996 [99].

The research on exciton-based interacting photons approached the physics of quantum fluids following a rather different path. At first, much focus has been devoted to the quest for BEC in gases of excitons [100, 101, 102, 103]. However so far none of these research axes has led to extensive studies of the quantum fluid properties of the exciton condensate. The situation is very different for exciton-polaritons in semiconductor microcavities. Following the pioneering proposal by Imamoglu *et al.* in 1996 [82], researchers have successfully

explored the physics of Bose-Einstein condensation in gases of exciton-polaritons. Thanks to the much smaller mass of polaritons, this system can display Bose degeneracy at much higher temperatures and/or lower densities. The first configuration where spontaneous coherence was observed in a polariton system was based on the coherent pumping of the cavity at a finite angle, close to the inflection point of the lower polariton branch. As experimentally demonstrated by both Baumberg *et al.* [104] and Stevenson *et al.* [105] in 2000, above a threshold value of the pump intensity a parametric oscillation [106, 107, 108] occurs in the planar microcavity and the parametric luminescence on the signal and idler modes acquires a long-range coherence both in time and space, as experimentally proven by Baas *et al.* in 2006 [109]. Interestingly, the onset of parametric oscillations in planar cavities can be interpreted as a non-equilibrium Bose-Einstein condensation, as theoretically discussed in [110]. Indeed, the coherence of the signal and idler is not inherited from the pump, but instead appears via the spontaneous breaking of the phase symmetry. After some preliminary claims ([74, 111, 112, 113]), a conclusive demonstration of Bose-Einstein condensation in a thermalized polariton gas under incoherent pumping was reported by Kasprzak *et al.* in 2006 [46]. The Bose-Einstein condensation of a gas of exciton-polaritons was shown both in momentum-energy space from the macroscopic accumulation of particles into the lowest-energy states, and in real space from the appearance of a long-range coherence. The principle of these experiments is illustrated in Figure 2.1: the laser pump injects hot electron-hole pairs, whose excess energy can be dissipated via phonon emission and then Coulomb scattering processes. For sufficiently high pump powers, the density of the incoherently injected polaritons exceeds the critical density for Bose-Einstein condensation and a coherent condensate appears. Even if the system is still a driven-dissipative one, a quasi-thermal equilibrium state is achieved if the loss rate is sufficiently low compared to the thermalization time of the polariton gas. It is important to note that these observations are unlike the strongly non-equilibrium regimes of laser operation observed in a vertical cavity surface emitting laser (VCSEL) devices, such as reported by Scheuer and Orenstein in 1999 [114], since there the thermalization into the lowest energy state is very ineffective and the condensate possesses a complex structure, with arrays of vortices.

Simultaneously to these studies on Bose-Einstein condensation and spontaneous coherence effects, a lot of effort has also been devoted to the theory of the hydrodynamic properties of quantum fluids of light. The adaptation of the concept of the Bogoliubov dispersion of elementary excitations for a photon condensate was first investigated for a planar cavity in the pioneering works of Chiao and Boyce [115], and Tanzini and Sorella [116] in 1999. None of these works however addressed the crucial role of dissipation in the physics of photon fluids. The first steps in this direction appeared in 2001 in the work

of Bolda *et al.* [117], where the nucleation of vortices in a moving photon fluid past an impenetrable defect was investigated theoretically.

The possibility of specifically using exciton-polariton gases for studies of quantum hydrodynamics was first proposed in [63], where a coherent pump configuration was adopted as in [117]. In contrast to the case of non-resonant excitation, the resonant pump configuration allows to perform a theoretical description in terms of a generalized Gross-Pitaevskii equation without having to deal with a phenomenological description of complex relaxation processes. In spite of its relative simplicity, a coherently injected condensate can show peculiar superfluid properties. Indeed, the density perturbation resulting from the fluid hitting a detect can be interpreted in terms of the Landau criterion of superfluidity using the generalized Bogoliubov dispersion of excitations. At low flow speeds, superfluidity manifests itself as the suppression of scattering. It is visible in real-space as the vanishing of the density modulations around the defect and, correspondingly, in the disappearance of the Rayleigh scattering ring in k-space, as reported on the upper panels in Figure 2.8, where the transition from a dissipative flow (panels I and IV) to a superfluid one (panels III and VI) is apparent in both the real- and the momentum-space. Experimental verification of these predictions was reported at LKB in 2009 [13, 14]. Remarkably, the same work showed that photon-photon interactions are responsible for the appearance of a "sound mode" in the polariton fluid: a Cerenkov-Mach cone was reported at "supersonic" flow speeds. The experimental data is reported on the lower panels in Figure 2.8.
Previous (Lagoudakis *et al.*, 2008 [15]) and following experimental works (Nardin *et al.*, 2011 [18]; Sanvitto *et al.*, 2011 [118]) have shown the hydrodynamic nucleation of vortex-antivortex pairs and of dark solitons (Amo *et al.*, 2011 [16]; Grosso *et al.*, 2011 [19]) in polariton superfluid. But so far, works on arrays of vortices of the same sign lack from the current experimental landscape. Therefore, questions about the conservation of angular momentum in such open systems remain unexplored.

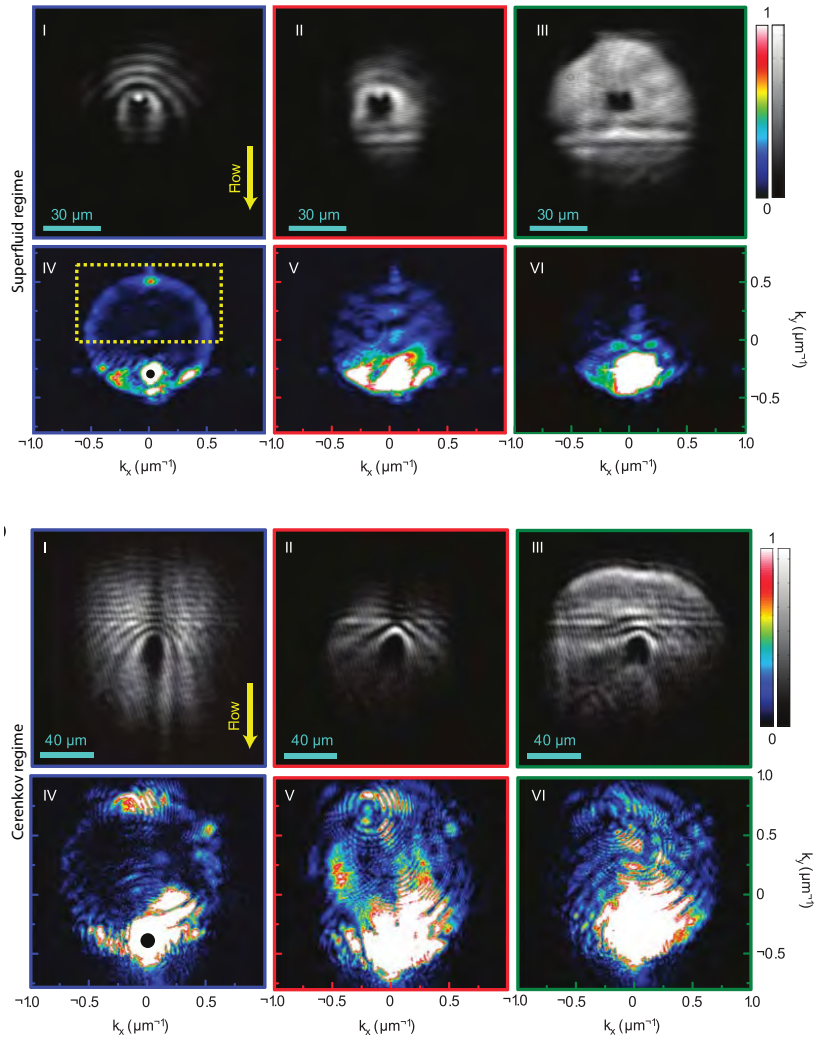

Figure 2.8.: Polariton superfluidity – From Amo *et al.*, 2009 [13]. Polaritons are coherently injected into the microcavity with a resonant laser: in contrast to the non-resonant and incoherent pumping scheme of Figure 2.1, this pumping scheme allows to precisely control the density and the in-plane flow speed of the polariton fluid by changing the parameters (intensity, frequency, incidence angle) of the driving laser. Upper panels: experimental images of the real- (panels I-III) and momentum- (panels IV-VI) space polariton density. The different columns correspond to increasing polariton densities from left to right: for the highest density value, polariton superfluidity is apparent as a suppression of the real-space density modulation (panel III) and the corresponding disappearance of the Rayleigh scattering ring (panel VI). Lower group of panels: experimental images of the real- (panels I-III) and momentum- (panels IV-VI) space polariton density at a higher wavevector, so that the flow is supersonic. The different columns correspond to increasing polariton densities from left to right: the dark linear "shockwave" characteristic of the Cerenkov regime gradually widens and for high densities it disappear, as the sound velocity increases above the fluid velocity.

Chapter 3.

Interaction-shaped vortex-antivortex lattices

Vortices and vortex-antivortex pairs are found throughout quantum fluid systems, including quantum fluids of light [119, 120]. They were theoretically proposed [121] and experimentally reported [122, 18, 118, 15, 123] in polariton fluids. Interest stems from their link with polariton superfluidity [1] since it can lead to a better understanding of polariton superfluid dynamics, polariton vortex behavior, as well as possible applications in quantum information technologies [124, 125, 126].

This chapter presents results on the generation and trapping of stable vortex-antivortex lattices, meaning a 2D array with an *equal* number of vortices and antivortices observable with time-averaged experiments. Two schemes are described: the first one uses a square or triangle trap potential (or energy well) inside which polaritons are free to evolve. A stable vortex-antivortex lattice is observed as the result of interferences and its characteristics are studied. Interestingly, polariton-polariton interactions are observed to reduce the number of vortex-antivortex pairs and change the lattice geometry. This first scheme, useful to understand the experiments presented in the next chapters and to which I participated, is mainly the work of Romain Hivet, whose thesis [23] covers in much details this experiment. This is why section 3.2, describing this trapping scheme, is only briefly presented here under the form of the publication it resulted in.
To overcome some experimental limitations inherent to the first trapping scheme, a second experiment was realized. It makes use of several pumping beams to create several coherent polariton populations that propagate toward one another, without carrying any global angular momentum. By carefully setting the pumps positions and angles of incidence, results similar to that of the previous trapping scheme were retrieved. It was also possible to increase the polariton density further that the previous scheme. In the very high density regime we observe the complete vanishing of the interference and of the vortex-antivortex

1. However the presence of elementary vortices is in no way a proof of superfluidity.

pairs, resulting in the merging of the different polariton superfluids into one. This setup, described in details in section 3.3, is the basis for multi-pump angular momentum injection presented in section 4.

For simplicity "vortex-antivortex" shall be shortened "V-AV" from now on.

3.1. Setup

The two vortex trapping schemes have many parts in common, the only notable difference being the pump shape. Before explaining the schemes individually, a general description of the equipment and methods used is given here.

Planar microcavity sample

The planar microcavity used in the present work was built at the EPFL [2], Switzerland, by Romuald Houdré [127, 128]. This kind of sample is realized by molecular beam epitaxy, a method that reaches a precision of the order of a few Ångstroms. Our sample is made of three $In_{0.04}Ga_{0.96}As$ quantum wells placed at the antinodes of the cavity electromagnetic field.

The cavity is GaAs-based with a typical length of $\frac{2\lambda}{n_c}$ for $\lambda = 835\,\text{nm}$ (the excitonic resonance) and where $n_c = 3.54$ is the cavity GaAs substrate optical index. The Bragg mirrors that form the cavity are made of 21 (front mirror) and 24 (back mirror) GaAs-AlAs pairs. This gives a finesse of about 3000, corresponding to a theoretical photon lifetime of 13 ps. The measured polariton linewidth is less than 85 μeV (limited by the spectrometer resolution), and the polariton lifetime is estimated to about 15 ps from time resolved measurements. The back mirror lays on a GaAs substrate that was polished to allow working in transmission mode. A lateral cut of the microcavity is presented in figure 3.1. During the epitaxial growth a very small angle on the order of 10^{-4} degrees was induced between the Bragg mirrors so as to continuously change the cavity thickness with the position. This angle permits a very fine control over the photon-exciton detuning δ defined in chapter 1. The change in cavity thickness modifies linearly the cavity photon energy with the position while the exciton energy remains constant. Detunings from $+8\,\text{meV}$ to $-4\,\text{meV}$ are achieved, with an energy gradient of about $710\,\mu\text{eV mm}^{-1}$.

Figure 3.2 is the experimental anticrossing figure for our microcavity sample. The wedge is well visible as a linear increase of the cavity photon energy with the position

2. École Polytechnique Fédérale de Lausanne

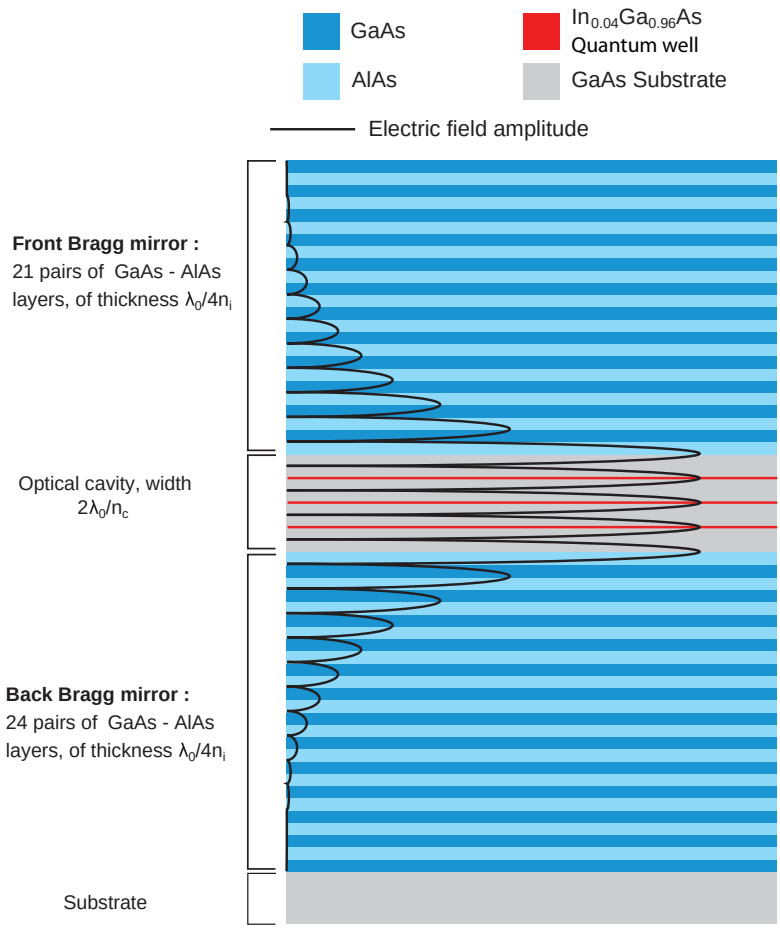

Figure 3.1.: Microcavity structure – Scheme of a lateral cut for our microcavity. Three $In_{0.04}Ga_{0.96}As$ quantum wells are placed at the antinodes of the electromagnetic field, in a high finesse optical cavity. The cavity is made of two GaAs/AlAs Bragg mirrors. From [23].

while the exciton energy remains approximately constant. The Rabi energy for our sample is measured to be $\hbar\Omega_R = 5.07\,\text{meV}$ from this figure.

Figure 3.3 is an experimental picture of our planar sample on a zone covering 3.2 mm by 0.9 mm. It was realized by exciting the sample at normal incidence with two different wavelengths. Because of the angle between the two Bragg mirrors, the cavity zone resonant with a given wavelength forms a line orthogonal to the thickness gradient. It is the energy isoline, as visible on figure 3.3 under the form of two lines: one for each excitation wavelength. The angle between the two Bragg mirrors is small enough for the lines thickness (about 100 µm) to offer a comfortable margin when working with excitation spot (plus propagation length) smaller than 60 µm: the wedge can be neglected for such sizes or for propagation directions perpendicular to the thickness gradient.

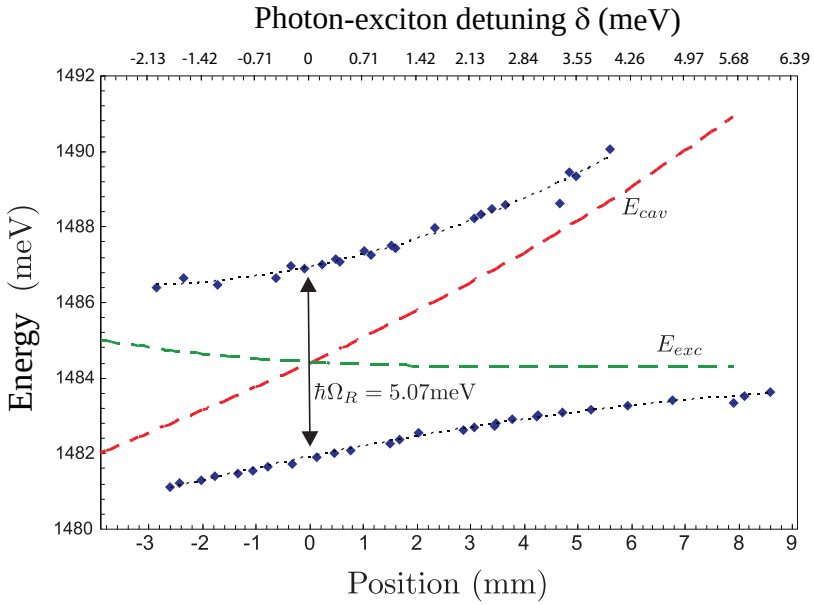

Figure 3.2.: Experimental anticrossing – Anticrossing figure obtained experimentally for the sample presented in this section. By pumping with an out-of-resonance laser, the energies at $\boldsymbol{k} = 0\ \mu\text{m}^{-1}$ of the lower and the higher polariton branches are measured. The data points are obtained by changing the position, which changes the photon-exciton detuning. This provides an experimental value for the Rabi energy: $\hbar\Omega_R = 5.07$ meV. From [23]

.

One observes on this figure (3.3) many defects inducing locally a variation of the potential [3] for polaritons. Several types of defects can be observed:

— Narrow horizontal and vertical lines corresponding to the crystal axes, created by mechanical constrains accumulated at the interface between the different microcavity layers during growth. This kind of defect creates weak amplitude, high density potentials. They are the main contributors to the elastic scattering polaritons undergo, revealing the Rayleigh ring in k-space [129].

— Point-like defects due to thickness defects formed during the sample growth. They mostly affect the cavity width and therefore are photonic defects. This kind of defect forms high amplitude potentials. Depending on whether the thickness is increased or decreased, they can form wells or barriers. These are useful to study the dynamics of polariton fluids against a defect and were used to demonstrate polariton superfluidity [13], polariton vortex dynamics [130, 121, 131] and solitons [20, 16].

— Thick curly black lines, attributed to dust and scratches deposited during sample manipulation.

3. Or, equivalently, a variation of the polariton resonance energy.

For the experiments described in this chapter we avoided as much as possible all those defects by selecting a "clean" zone on the sample.

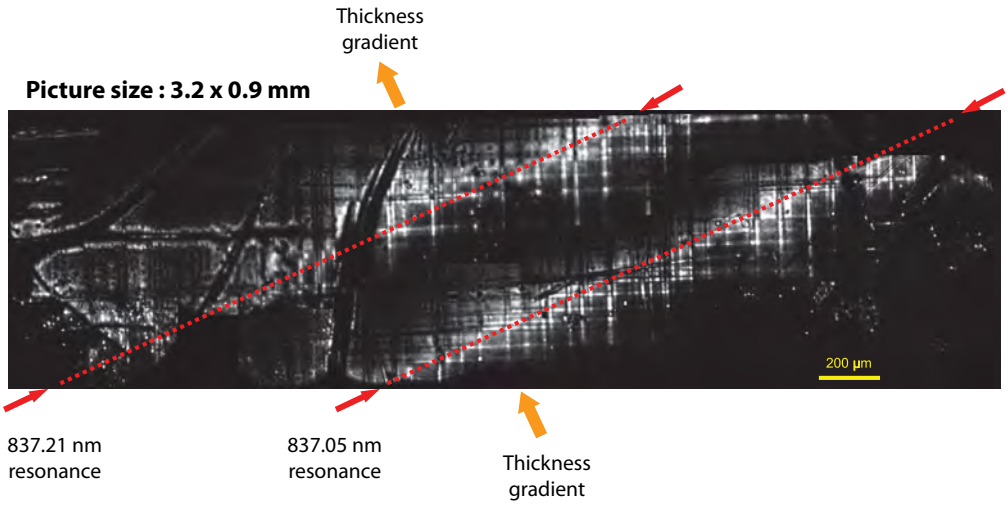

Figure 3.3.: Cavity transmission– Composite image over a large area showing two resonance lines for two laser excitation wavelength, in transmission mode. The lines are due to the wedge in the optical cavity changing linearly the photon energy along one direction. Different kinds of defects are visible.

Laser source

The laser source used in this experiment is a "homemade" titanium sapphire (Ti:Sa) pumped by a commercial doubled Nd:Yag green laser (the *Verdi V10* from Coherent). The "Verdi" pump laser has a fixed wavelength of 532 nm and its output power can be set up to 10 W. The Ti:Sa laser was designed at the Kastler Brossel Laboratory as a single-mode, continuously tunable, near-infrared, CW [4] source by François Biraben. The wavelength tuning ranges from 820 nm to 850 nm. At 835 nm its power can reach up to 1 W in the TEM_{00} mode. The spectral linewidth is less than 1 MHz, with a linear output polarization.

The single-mode characteristic is ensured by placing three frequency-selective filters. The working frequency is first roughly set by a *Lyot filter* made of four birefringent blades. Its free spectral range is about 17 THz (36 nm at 830 nm) for a spectral width of about 200 GHz (4 nm at 830 nm): this filter can select a working region for the frequency but

4. Continuous wave

not a single mode. A second filter made of a simple fused silicate plate, called a *solid etalon* or *thin etalon*, works as a low finesse Fabry-Perot (free spectral range 200 GHz) thanks to the multiple reflections at its interface. Finally a two-prisms etalon (also called a *thick etalon*) acting as a finer Fabry-Perot cavity with a free spectral range of 20 GHz and a spectral width of 500 MHz selects a single mode. A schematic view of this laser is presented in figure 3.4.
A Faraday rotator acts like an optical diode with the many components placed at the Brewster angle and ensures the light propagates only in one direction inside the laser cavity. More details about this laser can be found in Gaëtan Messin's thesis [76].

Outside of the laser cavity a feedback loop stabilizes the laser frequency against thermal fluctuations by locking it on a stable, high-finesse optical cavity. The feedback action is done on a piezoelectric transducer in the thick etalon that modifies the prism distance. The output beam is coupled to a single mode, polarization-preserving fiber. This is handy to decouple the laser source from the rest of the experiment and to ensure a Gaussian profile for the output beam.

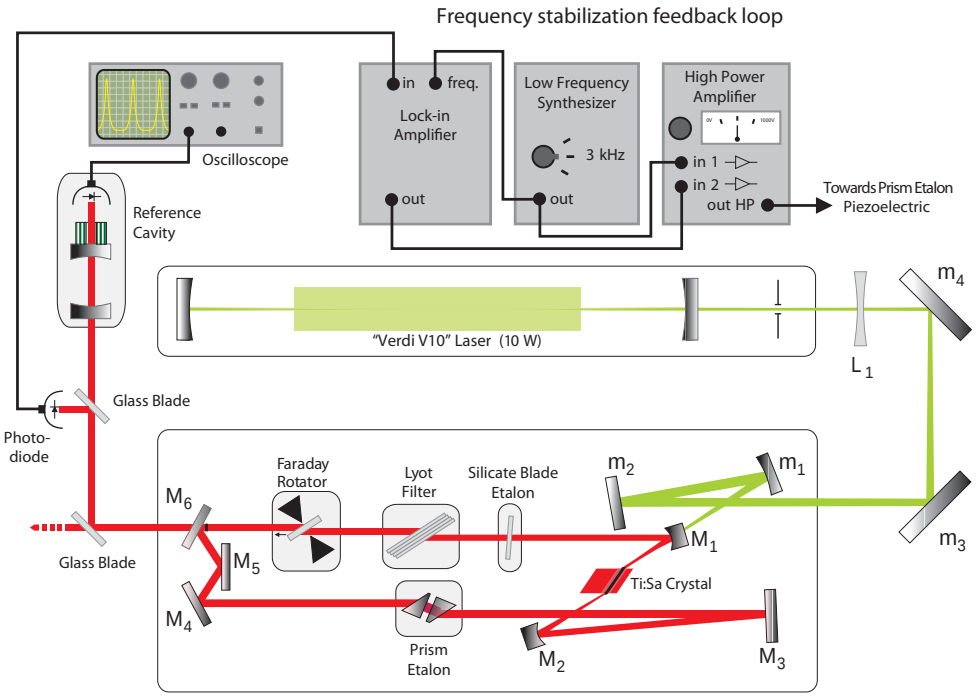

Figure 3.4.: Laser source – Biraben-design Ti:Sa CW laser, showing optical elements in the cavity as well as the external frequency lock. From [132].

Cryogenic setup

To cool down the sample we use a *Microstat* continuous helium flow cryostat from *Oxford Instruments*. This cryostat possesses two large angular aperture (72°) windows

(one on the front and one on the back). This allows to work both in reflection and in transmission configurations.

The sample is glued on the sample holder with a thin silver lac layer. It is placed in the cryostat vacuum chamber, pumped to 10^{-5} Torr ($1.3\ 10^{-3}$ Pa) with a vacuum pump system. The pump system, from the brand *Alcatel*, is made of a primary vacuum pump, a turbo-pump ATP80 and an electronic controller ACT 200. With such a vacuum it is possible to cool the sample down to 4 K with liquid helium, which is well enough to see the strong coupling in our InGaAs microcavity.

The cryostat is mounted on a high-precision two-axis *Newport* translation stage, allowing a fine positioning of the sample in the vertical and horizontal directions. The typical precision on the position is 5 µm which, through the microcavity thickness gradient, corresponds to a precision better than 5 µeV on the photon-exciton detuning δ.

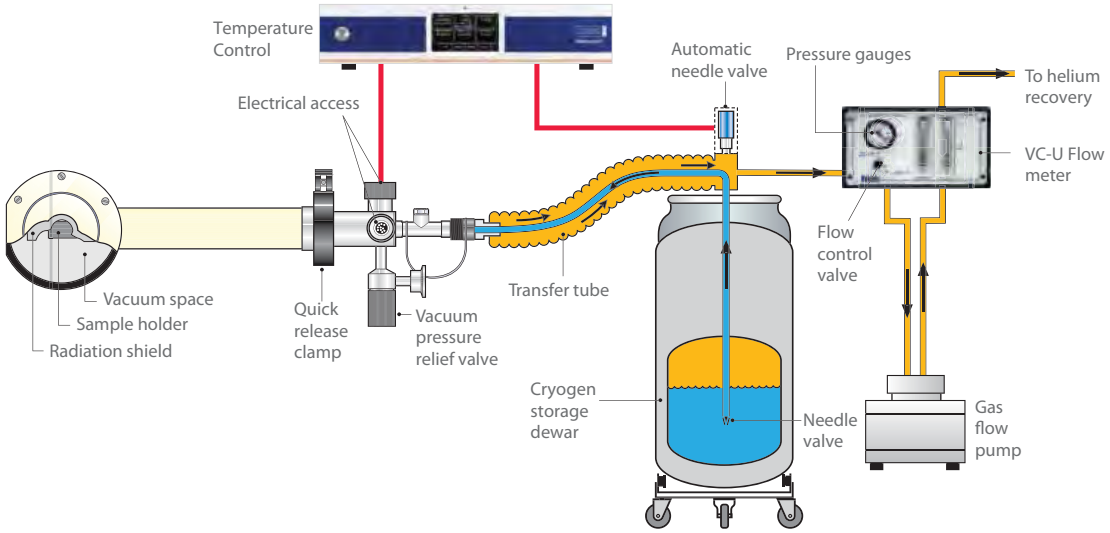

Figure 3.5.: Cryogenic system - Schematic representation of the setup used to cool the sample. Liquid helium-4 is stocked in a cryogenic storage dewar and pumped into an *Oxford Instruments* mini-cryostat. The temperature can be set with a feedback loop acting on the flow rate.

The liquid helium-4 is stored in a 60 L cryogenic storage dewar linked to the cryostat with a vacuum transfer tube (see figure 3.5). Helium circulation is ensured by a vacuum pump linked to a passive flow controller. The flow can be manually controlled with a precision of 0.05 L/h. The temperature is measured inside the cryostat by an embedded thermometer [5]. From this measurement an optional temperature control feedback loop can be implemented (visible on figure 3.5). The feedback action is done on the transfer

5. Note that while inside the cryostat, the thermometer cannot be placed exactly where the sample is glued. This means that the measured temperature, while still a valid estimate, may not precisely correspond to the sample temperature.

tube needle valve to precisely regulate the helium flow. However this temperature lock was not found useful for this study as we worked at the minimum possible temperature.

Detection

The detection is made simultaneously in real space, momentum space and energy. An objective of focal $f_{obj} = 16\,\text{mm}$ and angular aperture 84° (numerical aperture of 0.995) collects the sample emission. A quarter-wave plate (QWP) followed by a polarizing beam splitter (PBS) is set to only transmit circularly-polarized light, therefore filtering out any spin-flip effect. CCD cameras are used for direct imaging of the real space and the momentum space while the energy (wavelength) is measured with a spectrometer, as visible on figure 3.11. Indeed, after the polarization filtering the collected light is split into two arms. On one arm, two lenses form on the spectrometer entrance an angle-resolved image (optical Fourier transform) of the sample, giving access to the momentum space. On the other arm a single lens makes on the real-space CCD camera a direct image of the sample, with a x100 magnification factor.

The CCD cameras are from the brand *Princeton Instruments*. The real space imaging is done with a model *PIXIS1024BR eXcellon* camera. It contains a square 1024-by-1024 13 µm-pixels back-illuminated CCD chip, providing 95% of quantum efficiency at 830 nm. The typical integration time is 3 ms. The spectrometer and k-space detection share the same CCD camera, an older version of the real space CCD. The model is a *PIXIS1024F* containing a square 1024-by-1024 13 µm-pixels front-illuminated CCD chip, providing 40% of quantum efficiency at 830 nm. Both cameras possess a maximum CCD reading rate of 100 kHz. The cameras as well as the spectrometer are controlled with the *Winspec* (Windows XP PCs).

The light spectral properties are analyzed with an *Acton Series SP2750* spectrometer from *Princeton Instruments*. An adjustable and removable slit on the spectrometer entrance allows a minimal aperture inferior to the pixel size of the CCD camera, which is placed at the spectrometer exit. Two gratings (1800 and 1200 lines per millimeter) are available as well as a plane mirror to couple the slit entrance plane with the CCD exit plane. This system provides a maximum spectral resolution of 0.005 nm (8.5 µeV at 830 nm). Thanks to the lenses making an optical Fourier transform before the spectrometer entrance, the slit axis provides the angle-resolved information necessary to directly record the polariton dispersion curve ((k, E)-space).
To image the reciprocal space (k-space), one simply needs to remove the slit and set the spectrometer grating on "mirror" with a 0° angle (0 nm setting in Winspec).

The polariton phase is measured on the real-space arm with an off-axis interferometry setup. A beam splitter splits the real space image into two parts, one of which is expanded to generate a flat phase reference beam used to make an off-axis interference pattern. With this method, the vortex position on the CCD is independent from the phase of the reference beam [133], and is unambiguously visible as a fork-like dislocation in the interference pattern. The actual phase map is then numerically reconstructed with a standard off-axis phase detection method described in Appendix A. To this end a *Matlab* code was written to treat the data exported from *Winspec* after ASCII conversion.

Polariton density control

We saw in subsection 2.2.2 that above some critical value[6] $\Delta_C = \sqrt{3}\hbar\gamma$ of Δ, the pump-polariton detuning, a bistable behavior appears [43]. For $\Delta = 0\,\text{meV}$ the polariton density is proportional to the pump amplitude; which means that without bistability the polariton density increases as the square root of the pump intensity. This increase is generally too slow to reach the high density regime where the interaction energy dominates the system within the available pump intensity. However when the bistability is present its jump increases with Δ, meaning that the higher is Δ the higher is the density we can reach. This method allows, for a given pump intensity, to achieve very high densities so long as the pump intensity is enough for the system to remain on the bistability upper branch. This method is actually needed to reach the regime where nonlinearities dominate. We therefore use the bistability to control the density as follows: in the upper bistability branch, at constant pump power, we modify Δ by tuning the laser wavelength. This in turn tunes the polariton density in the pumped region and allows to reach higher densities than by simply increasing the pump intensity. A schematic explanation is given in figure 3.6, where we consider three different cases: low density ($\Delta_1 \approx 0\,\text{meV}$, point (i)), higher density ($\Delta_2 = 0.4\,\text{meV}$, point (ii)) and very high density, near the bistability threshold ($\Delta_3 = 0.7\,\text{meV}$, point (iii)). This method is used on all the experiments in Part I.
To study the linear regime, where the effect of polariton-polariton interaction is negligible, we simply set $\Delta = 0\,\text{meV}$ or slightly negative. This way we use the optical limiter effect of the interactions. If this still yields a too high density for the phenomenon under study then the power can be decreased. If Δ is in the bistable regime, decreasing the pump power so as to reach the lower bistability branch usually results in extremely low densities.

6. γ is the polaiton decay rate.

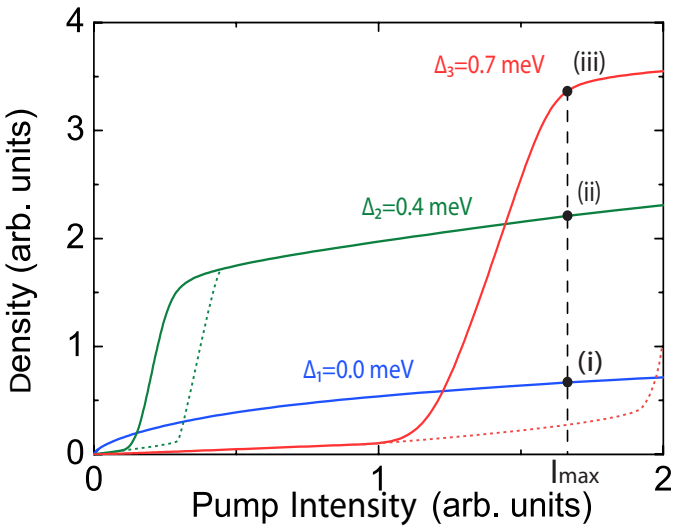

Figure 3.6.: Density control - Scheme of different bistability regimes used to reach high polariton densities. The relevant bistability in thick line while the dashed line represents the unused branch, see discussion 3.1. A stronger bistability (higher Δ) provides higher densities on the upper branch for a constant, high pump intensities. I_{max} indicates the pump peak intensity.

Pump spatial control

A consequence of using the bistable regime to control the polariton density is that it also spatially selects a pumping zone. Indeed, for $\Delta > \Delta_C$, the polariton energy is renormalized through self-interaction to the pump energy in the upper bistability branch. Therefore the pumping is resonant and yields high polariton densities. As we saw in chapter 2 this is not the case in the lower bistability branch, where the pumping is off-resonant and very inefficient. Since the pump laser is spatially extended and its intensity is not uniform, the low pump intensity regions lay on the lower bistability branch and are off-resonant. In these regions, non-resonant pumping yields a negligible polariton population and can be considered as a pump-free region. On the other hand, the pump regions where the local intensity is above the threshold will produce a massive amount of polaritons. Therefore the low intensity parts of the pump can be neglected, and the shape of the resonant zone can be controlled by changing the intensity threshold $I_{th}(\Delta)$, itself depending on the parameter Δ. In addition, since the upper bistability branch is in the optical limiter regime, the resonant part of the pump will have only little spatial structure. Indeed, regions where the intensity strongly increase above the threshold will actually yield a slightly higher polariton density. This allows to create a quasi top-hat polariton density, a useful feature if one wants to neglect the resonant region spatial structure. This phenomenon is illustrated in figure 3.7, for a Gaussian pump laser. The result for the driven polariton population is a density profile similar to a top-hat.

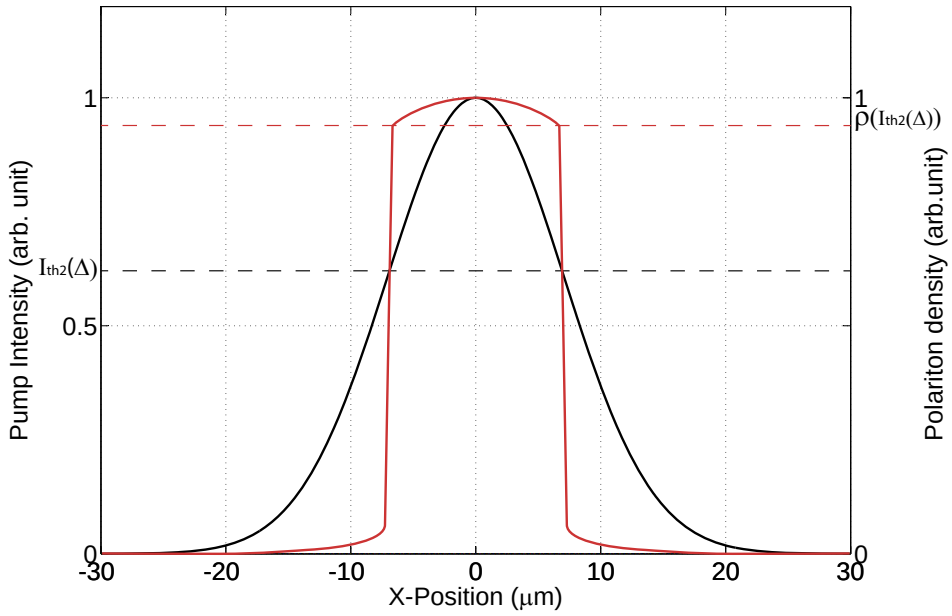

Figure 3.7.: Spatial bistability - Schematic view of a Gaussian pump (black) intensity profile, and the triggered polariton (red) population density (both normalized to peak value). The function $\rho(I)$ being highly nonlinear in the bistable regime, only the regions where the pump intensity is above the upper threshold (reached when decreasing the pump intensity on the bistability curve) is resonant. The result is a polariton density profile that does not correspond to the pump, but that is rather like a "top-hat" function.

Note that out of the two bistable thresholds, the one relevant to the pumped spot size is the second (upper) one. Indeed, the region where the pump intensity is between the first and the second threshold is on the bistability lower branch at the moment the pump is turned on. This region is thus initially sub-threshold, and a small amount of polariton would be enough to make it jump to the upper branch. However, it is spatially bordered by the resonant region (where the intensity is above the first threshold and the polariton density is high). Since polaritons propagate easily, the high density region can inject enough polaritons to the neighbor sub-threshold region to make it jump to the upper branch [10]. Through this effect, the part of the lower bistability branch between the two threshold is made unstable, and the corresponding region becomes resonant (it jumps to the upper branch). Therefore through this local "switch-on" effect, all regions above the second threshold are resonant after the pump is turned on, rather than simply the areas above the first threshold as would suggest the system history. Figure 3.8 illustrates this mechanism.

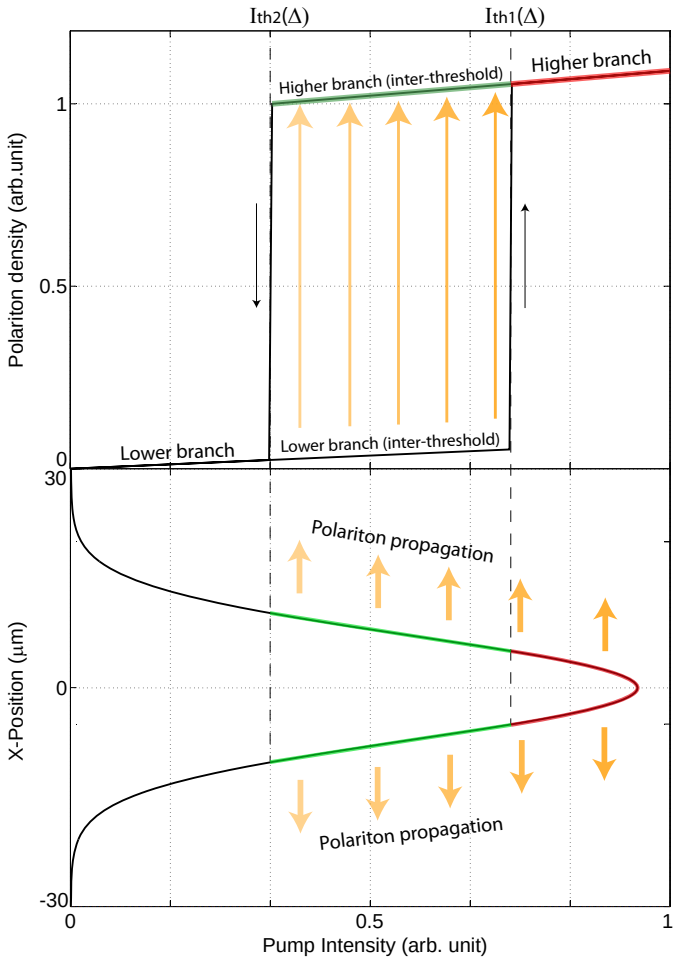

Figure 3.8.: Instability of the inter-threshold region - Schematic view of the polariton bistability (up) and the corresponding regions of a Gaussian pump (down). When the pump is turned on the intensity increases and therefore only the regions of the pump above the first threshold (above I_{th1}, in red) should light up. However the neighbor regions are between the two thresholds and on the lower branch. A small amount of polariton is enough to make this region jump (represented by the yellow arrows on the bistability) to the upper branch (in green). This is realized by the proximity of the resonant region and the high mobility of polaritons, which make the inter-threshold region unstable.

3.2. Trapped vortex-antivortex lattices: metallic mask setup

Vortex dynamics were extensively studied in several experiments, which showed the hydrodynamical nucleation of V-AV pairs [122, 18, 118, 15, 123], single vortex stability in pulsed pumped regime [134, 135, 130, 131] and V-AV trapping by natural disorder [15]. Few studies focused on the steady state solution for polariton vortices held in controlled traps [121, 136].

3.2.1. General setup description

In the continuity of the previously mentioned trapped polariton vortex studies [121, 136], our goal is here study the geometric self-organization of vortices in a steady state regime. Indeed, steady state regime is observable with a time-averaged setup such as the one we use in this study. To observe the formation of a stable V-AV lattice we use a square trap potential controlled with an especially engineered pump made of a Gaussian beam whose intensity is spatially modulated with an opaque mask. This well-shaped trap potential is created by making use of polariton-polariton interactions: by cutting the center of the Gaussian pump laser with the mask, the polariton density (and thus the polariton-polariton potential energy) is maintained high around the masked region and very low in it. The shape of the trap is chosen by the spatial geometry of the masked zone, created with a metallic mask whose shape we can engineer at will.

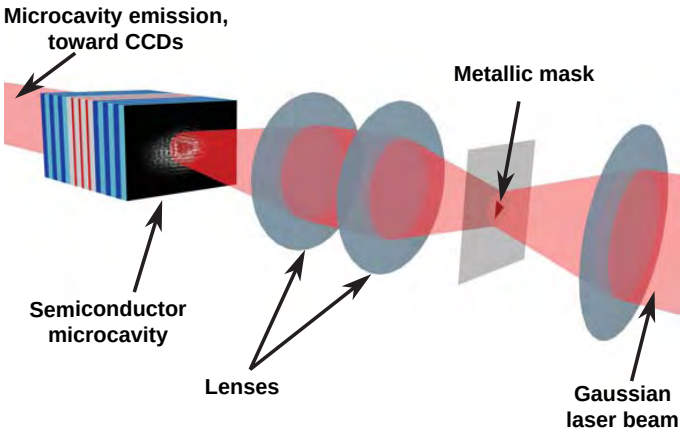

Figure 3.9.: Pump shaping - Scheme of the pumping setup for the polariton trap. A Gaussian beam is focused on a small metallic mask so as to cut a given shape into the beam center. In this example the mask is a triangle but it can have any shape. The mask image is then focused on the sample at normal incidence, generating both the polariton population and the trap.

In this study we chose a square and a triangular mask of size 45 µm. The laser, possessing waist diameter larger than 45 µm, is focused on the mask. The mask image is then projected on the microcavity at normal incidence, as shown in figure 3.9. Therefore the laser intensity is locally set to zero in the mask image, placed at the beam center. The difference of potential energy (or equivalently, polariton density) between the non-masked and masked regions accelerates polaritons towards the non-pumped center. Indeed, polaritons "fall" into the trap, their interaction energy being converted in kinetic energy, from the four (square) or three (triangle) sides. This is illustrated in figure 3.10. The absence of pump in the trap ensures the free evolution of the polariton phase; on the contrary in the pumped region the polariton phase is locked to the pump phase. Polaritons coming inside the trap from the trap sides meet and interact, giving rise to V-AV pairs

arranged in a lattice. The lattice geometry depends on the mask shape (see [23] as well as the publication in the next section). The trap depth determines the polariton speed when entering the non-pumped region as well as the total polariton density in the trap. The system being completely symmetric, it is bound to keep a total angular momentum equal to zero and, therefore, the number of generated vortices is always equal to the number of antivortices. In this sense vortices and antivortices are always generated in pairs, although they do not necessarily form bound states.

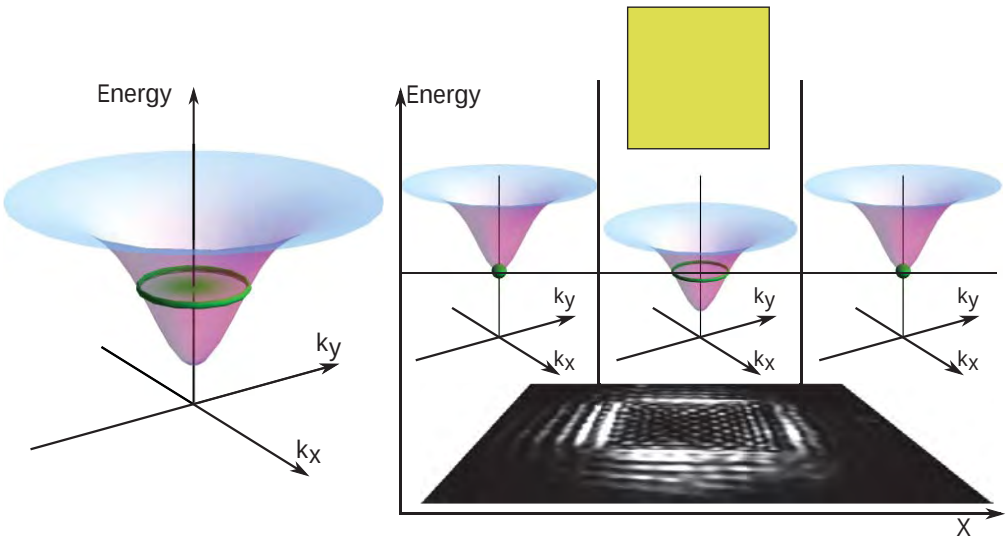

Figure 3.10.: Trap potential - (Left) Lower polariton branch. At low polariton density, the pump energy (green spot) is blueshifted with respect to the bare lower polariton branch (LP) at $\boldsymbol{k} = 0$ µm and crosses the LP at a $\boldsymbol{k}$ corresponding to the Rayleigh ring. Therefore, polaritons diffracted by the mask borders can be injected into the cavity at a wavevector $\boldsymbol{k_R}$ corresponding to the Rayleigh ring (green ring). (Right) At high laser intensities, the lower polariton branch outside of the masked region is renormalized due to polariton-polariton interactions and therefore polaritons are injected at $\boldsymbol{k} = 0$ µm (green dot). Inside the masked region (central region), the polariton density being lower, the polariton branch is not renormalized. Therefore, when polaritons enter by diffusion they acquire a momentum (green ring) in order to conserve the energy.

For low polariton densities in the trap we observe an interference-like lattice containing the V-AV pairs [23]. The polariton phase being free to evolve and the interactions being negligible in this regime, this is indeed what is expected. The lattice is well described by interference between four (three) polariton populations coming from the four (three) square (triangle) sides to the center [23].
However this is not the case at high densities: we observe a modification of the lattice geometry and a drastic decrease of the number of V-AV pairs when the polariton density in the trap is increased.

By extrapolating this result we deduce that for a high enough density inside the trap, all V-AV pairs must disappear and the interference pattern could then vanish. A major drawback to the use of masks is that the cut is done in the maximum intensity region of the Gaussian beam, leading to high losses of pump power and thus to limited densities in the trap. This is why a second scheme using four separate pumps was implemented (presented in section 3.3), since it allows to achieve a similar system without the power loss.

PHYSICAL REVIEW B **89**, 134501 (2014)

Interaction-shaped vortex-antivortex lattices in polariton fluids

R. Hivet,[1] E. Cancellieri,[1,*] T. Boulier,[1] D. Ballarini,[2] D. Sanvitto,[2] F. M. Marchetti,[3] M. H. Szymanska,[4] C. Ciuti,[5] E. Giacobino,[1] and A. Bramati[1]

[1]*Laboratoire Kastler Brossel, Université Pierre et Marie Curie, Ecole Normale Supérieure et CNRS, UPMC case 74, 4 place Jussieu, 75005 Paris, France*

[2]*CNB@UniLe, Istituto Italiano di Tecnologia, via Barsanti, 73100 Arnesano (Lecce), Italy*

[3]*Departamento de Física Teórica de la Materia Condensada & Condensed Matter Physics Center (IFIMAC), Universidad Autónoma de Madrid, Madrid 28049, Spain*

[4]*Department of Physics & Astronomy, University College London, Gower Street, London WC1E 6BT*

[5]*Laboratoire Matériaux et Phénoménes Quantiques, UMR 7162, Université Paris Diderot-Paris 7 et CNRS, 75013 Paris, France*

(Received 14 December 2013; revised manuscript received 14 March 2014; published 3 April 2014)

Topological defects such as quantized vortices are one of the most striking manifestations of the superfluid nature of Bose-Einstein condensates and typical examples of quantum mechanical phenomena on a macroscopic scale. Here we demonstrate the formation of a lattice of vortex-antivortex pairs and study its properties in the nonlinear regime at high polariton-density where polariton-polariton interactions dominate the behavior of the system. In this work first we demonstrate that the array of vortex-antivortex pairs can be generated in a controllable way in terms of size of the array and in terms of size and shape of its fundamental unit cell. Then we demonstrate that polariton-polariton repulsion can strongly deform the lattice unit cell and determine the pattern distribution of the vortex-antivortex pairs, reaching a completely new behavior with respect to geometrically generated vortex lattices whose shape is determined only by the geometry of the system.

DOI: 10.1103/PhysRevB.89.134501 PACS number(s): 71.36.+c, 03.75.Lm, 42.65.Hw, 67.90.+z

I. INTRODUCTION

Quantized vortices are topological excitations characterized by the vanishing of the field density at a given point, the vortex core, and the quantized winding of the field phase from 0 to $2\pi m$ around it (with m an integer number). Together with solitons, they have been extensively studied [1–3] and observed in nonlinear optical systems [4], superconductors [5], superfluid ^{4}He [6], vertical-cavity surface-emitting lasers [7], and, more recently, in cold atoms [8–10], where, as predicted by Abrikosov [11], vortices tend to arrange in triangular lattices due to their mutual interactions. Finally, in recent years, the study of vortices and vortex lattices has attracted much attention also in the field of coherent light-matter systems.

Semiconductor microcavities can be designed to strongly couple cavity photons to quantum well excitons. The eigenstates of this system are called exciton-polaritons and are characterized by specific properties such as low effective mass, inherited from their photonic component, and strong nonlinear interactions due to their excitonic part. Moreover, polaritonic systems are easily controllable by optical techniques and, due to their finite lifetimes are ideal systems for studying out-of-equilibrium phenomena [12,13]. In analogy with the atomic case [14,15] the superfluid behavior of polaritonic Bose-Einstein condensates [16] has been of great theoretical interest [17–20] and has been experimentally confirmed by the suppression of scattering in the case of a polariton fluid flowing past a defect [21,22] and by the persistence of circular quantized currents [23]. In particular, cavity-polariton systems have been predicted and shown to undergo formation of stable vortices [24] and half vortices [25,26], as well as formation of single vortex-antivortex (V-AV) pairs [27–29]. More recently, Amo *et al.* [30] and Hivet *et al.* [31] demonstrated the nucleation of hydrodynamic solitons and half solitons in resonantly pumped polaritons flowing against an extended obstacle. The formation of lattices of vortex and of V-AV pairs has been theoretically predicted and experimentally studied for cavity-polaritons [32–34], and their appearance has been observed in the case of patterns induced by metallic deposition on the surface of the cavity [35] and in the case in which the interplay between the excitation shape and the underlying disordered potential is able to pin the position of the vortices, allowing their detection in time-integrated experiments [36].

In the present work, we use a continuous-wave laser to resonantly inject polaritons outside of a masked region [37] and to observe vortex lattices trapped by an optically controllable potential that, at the same time, stimulates the lattice formation. Here the resonant pumping configuration allows for a fine tuning of the polariton density but does not generate an excitonic reservoir. For this reason, we can address theoretically and observe experimentally the effects of the polariton-polariton nonlinear interactions on the shape of the lattice of vortices. This is in contrast with the observations performed with an out-of-resonance setup [38,39]. In these latter cases, either the shape of the lattice was completely determined by the geometry of the pumping scheme [38] or a transition to trapped states was observed by bringing the pump spots closer to each other [39]. In these experiments the excitonic reservoir plays a fundamental role by determining the characteristic length and the shape of the formed vortex array and by generating the potential where the polariton condensate is trapped, leading to the disappearance of the vortex lattice.

The paper is organized in three main sections. In the first section we describe the setup used to perform the experiments. In the second we highlight our main results distinguishing between two main regimes: the linear regime at low polariton densities and the nonlinear regime at high polariton densities.

*emiliano.cancellieri@gmail.com

In this section we address ways to control the shape and the size of the generated array and show that a new regime can be reached in which polariton-polariton interactions determine the shape of the array. Finally, in the last section, we draw our conclusions.

II. EXPERIMENTAL SETUP

In our experiment we use a high-finesse GaAs microcavity ($F = 3000$) with a polariton lifetime $\tau = 15$ ps and a Rabi splitting of 5.1 meV [40–42] (see Appendix A). The microcavity is excited with a continuous-wave single-mode Ti:Sa laser quasiresonant with the lower polariton branch at 837 nm. The pump laser is circularly polarized in order to avoid any effect due to spin-dependent interactions [43]. The output beam can be made to interfere with a reference beam of constant phase from the same laser before being collected on a CCD camera, thus allowing for the reconstruction of the phase of the fluid with simple numerical treatment (see Appendix B). The experimental observations have been performed at 10 K in transmission configuration and for different positions of the laser spot on the cavity that correspond to different exciton-photon detunings $\delta_{\text{exc-photon}} = \omega_X(k = 0) - \omega_C(k = 0)$, where $\omega_{X(C)}(k = 0)$ are the excitonic and photonic energies at normal incidence ($k = 0$, where k is the projection of the light wave vector on the plane of the microcavity). In order to observe vortices, it is critical to let the polariton phase evolve freely after they have been injected by the laser. In previous studies polaritons were observed in a region of the microcavity where they have moved away from the laser spot, which was efficiently limited by a mask. This technique, ensuring a free evolution of the phase, allowed for the observation of solitons [30], half solitons [31], and vortices [37].

We focus the laser beam on a metallic gold-coated mask smaller than the beam waist that locally sets the laser intensity to zero. Using masks with different shapes and sizes (such as triangles and squares), it is possible to obtain laser beams with zero intensity regions of different shapes. This partially obscured waist is then imaged on the microcavity, thereby creating a polariton fluid outside a dark region whose size and shape can be set at will [Fig. 1(a)]. In this experiment the beam waist has a diameter of 110 μm with a square dark region in the center with a side of 45 μm and an energy set above the bare polariton energy at $k = 0$ for the considered point on the microcavity. Therefore, the laser energy crosses the bare lower polariton dispersion curve at a nonzero value of $|k| = |k_R|$ [Fig. 1(b)]. This crossing has the shape of a ring, corresponding to the Rayleigh ring. Since the beam is set at normal incidence, this value of k is not present in the laser beam. However, due to the presence of the mask, photons are diffracted with various values of $|k|$ perpendicular to the edges and can enter the cavity when they have the right $|k| = |k_R|$ value. Polaritons then enter into the dark region flowing with four directions perpendicular to the mask edges. When the laser intensity is increased, in the bright region of the spot, the lower polariton branch (LPB) is blueshifted into resonance with the laser energy at $k = 0$ due to the high polariton density [left and right regions of Fig. 1(c)]. In the dark region of the spot [central region of Fig. 1(c)] the LPB is not renormalized because the polariton density is low. Therefore, polaritons created at the edge of the bright region can travel into the dark region, getting a momentum $|k| = |k_R|$ that conserves their energy [44]. As in the nonresonant excitation case, polaritons flow into the dark region with four directions perpendicular to the mask edges.

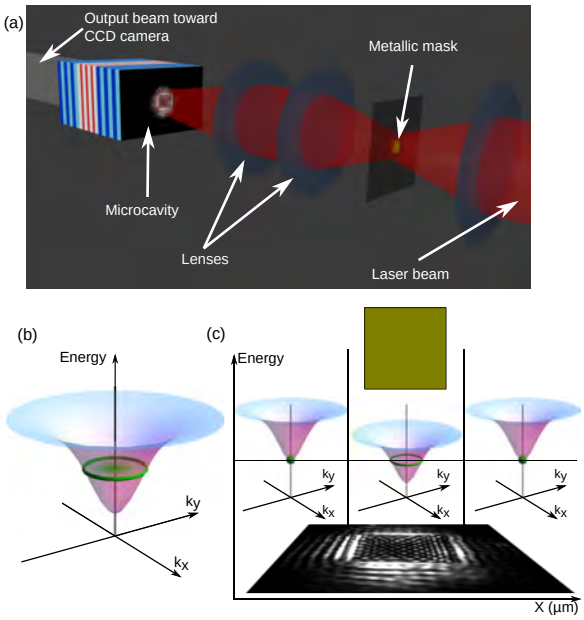

FIG. 1. (Color online) (a) Illustration of the excitation scheme. The waist of the beam is first imaged on a 0.5-mm square metallic mask, which is then imaged at $k = 0$ on the microcavity surface. The image of the mask generates a 45-μm-side square region at the center of bright Gaussian spot of 110 μm of full width at half maximum. (b) At low polariton density, the laser pump energy (green spot) is blueshifted with respect to the bare lower polariton branch (LP) at $k = 0$ and crosses the LP at a k corresponding to the Rayleigh ring. Therefore, polaritons diffracted by the mask borders can be injected into the cavity at a k corresponding to k_R of the Rayleigh ring (green ring). (c) At high laser intensities, the lower polariton branch outside of the masked region (left and right) is renormalized due to polariton-polariton interactions and therefore polaritons are injected at $k = 0$ (green dot). Inside the masked region (central region), the polariton density being lower, the polariton branch is not renormalized and, therefore, when polaritons enter by diffusion they acquire a momentum (green ring) in order to conserve the energy.

The system being completely symmetric, it is bound to keep a total angular momentum equal to zero and, therefore, the number of generated vortices is bound to be always equal to the number of antivortices. In this sense vortices and antivortices are always generated in pairs, although they do not necessarily form bound states. Here vortices and antivortices are characterized by a 2π or -2π rotation of the phase of the wave function around the core of the topological defect where the polariton density goes to zero [see inset of Fig. 2(b)].

III. RESULTS

In order to better highlight the mechanism lying beneath the formation of the V-AV lattice and the role of polariton-polariton interactions, we study the system as a function of the

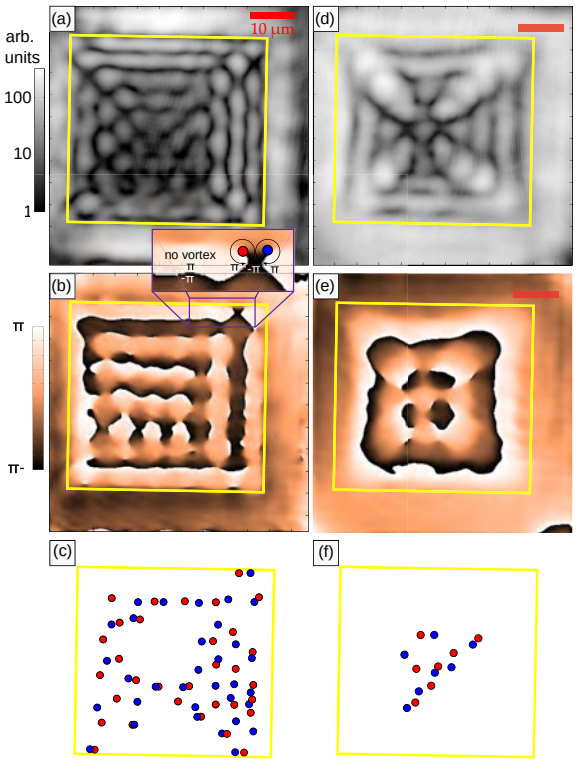

FIG. 2. (Color online) Experimental real-space emission intensity, phase, and vortex distribution in the linear and nonlinear regimes. The microcavity has a detuning $\delta_{\text{exc-photon}} = 0.32$ meV and the pump laser has a blueshift from the LPB at $k = 0$ of $\delta_{\text{pump-LPB}} = 0.6$ meV. (a)–(c) Linear regime, pump power 1 mW. In this regime the injected wave number is determined by the radius of the Rayleigh ring ($k_R = 1.1\ \mu\text{m}^{-1}$). (a), (b), and (c) correspond, respectively, to the experimental real-space emission, its corresponding phase, and the set of vortices (red dots) and antivortices (blue dots) formed inside the trapped region (in yellow). The positions of the vortices are obtained from a detailed analysis of the phase map (b). The inset shows a vortex (in red) with phase varying counterclockwise from $-\pi$ to π around the core and an antivortex (in blue). The wave number characterizing the size of the array is about $k_L = 0.9\ \mu\text{m}^{-1}$. The difference between k_R and k_L is attributed to uncertainty in the measurement. (d)–(f) Nonlinear regime with pump power equal to 35 mW. A strong modification of the vortex pattern is observed along with the disappearance of V-AV pairs from the borders. The grayscale used for real-space emission is logarithmic while the color scale for phase diagrams is linear from $-\pi$ to π.

polariton density. We identify two different regimes: a linear regime at low polariton density and a nonlinear regime at high polariton density. The linear regime is characterized by the polariton density lying on the lower branch of the bistability curve [45] everywhere in space, and its behavior is completely linear. The nonlinear regime corresponds to a polariton density that is on the upper branch of the bistability curve outside the masked region and that gradually decreases until it reaches the lower branch at the center of the trap. In this regime polariton-polariton interactions dominate the behavior of the system.

A. Linear regime

Figure 2(a) shows the experimental real-space distribution of the light transmitted by the cavity when a square mask partially blocks the pumping beam with pump power of 1 mW. The transmitted beam is made to interfere with a reference beam and the phase of the interferogram [Fig. 2(b)] is analyzed in detail in order to identify the position of the vortices [Fig. 2(c)]. Since in this case the laser intensity and the polariton density are low, polariton-polariton interactions play a negligible role and the system is analogous to the case of overlapping laser beams interfering in a medium with linear dispersion. In this first case, where a square mask is used, polaritons mainly flow from the four sides of the mask towards the center and the polaritonic system corresponds to the case of four plane waves coming from four orthogonal directions. These flows generate an interference pattern with a clearly identifiable wave vector k_L that, from now on, we define as the vortex-lattice characteristic wave vector. However, while for the case of four plane waves only a square interference pattern without any vorticity would appear, here V-AV pairs can form thanks to the nonuniform density distribution. The finite lifetime of cavity-polaritons, together with the fact that the local polariton density and the local polariton velocity are determined by the sum of the polariton flows coming from the different sides of the mask, induces a nonhomogeneous polariton distribution that, in turns, changes the direction of the polariton flows and allows the formation of vortices and antivortices.

Note that while a regular squared interference pattern generated by four plane waves is clearly visible in the experiment [Figs. 2(a) and 2(b)] in the entire masked region, Fig. 2(c) shows that there are areas (center and bottom) where vortices and antivortices do not appear. This is mainly due to the unavoidable presence of disorder and defects in the microcavity sample that might inhibit the formation of V-AV pairs; on the other hand, if the core of a vortex is very close to the core of an antivortex the experimental resolution in the phase measurements might be insufficient to resolve them. The comparison of these results with the Gross-Pitaevskii based simulations in Fig. 3 (for more details on the theoretical model, see Appendix A) shows that a regular interference pattern, with a characteristic wave vector $k_L = 0.9\ \mu\text{m}^{-1}$ similar to the one observed in Fig. 2, is clearly observed also in the numerical simulations, both in the emission intensity map [Fig. 3(a)] and in the phase map [Fig. 3(b)]. Despite these similarities one can see that the actual vortex distribution in Fig. 3(c) slightly differs from the one of Fig. 2(c); this is due to the aforementioned imperfections of the real experimental system that cannot be entirely reproduced by the simulations.

1. Control of the size of the unit cell

As the $|k_L|$ of the polaritons flowing into the trap is determined by the detuning between the energy of the pump and the bare LP at normal incidence, a change of the laser frequency allows for a fine tuning of $|k_L|$ and therefore for the control of the lattice unit-cell size: An increase (decrease)

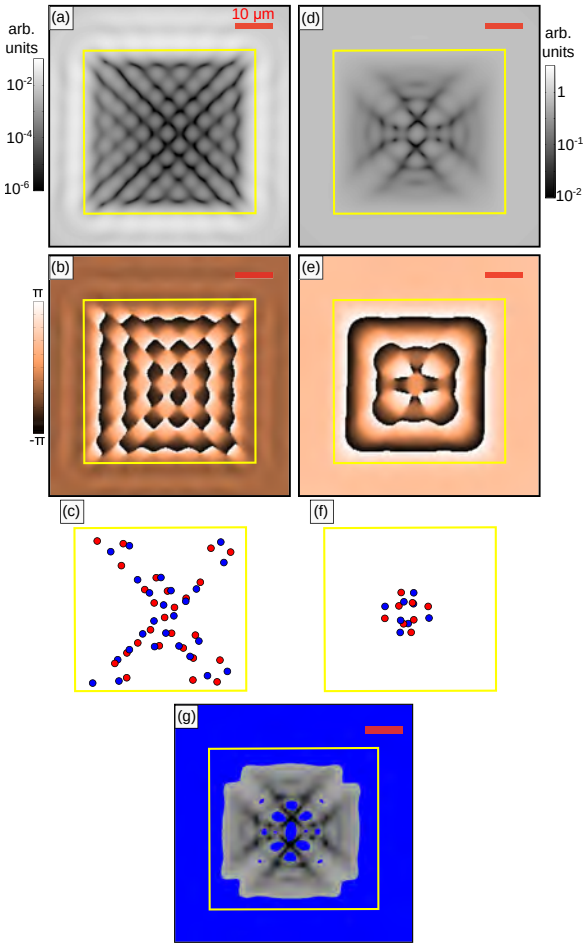

FIG. 3. (Color online) Numerical real-space images in the same conditions as in Fig. 2. Two sides of the square mask are set to be not perfectly parallel in order to simulate unavoidable asymmetries of the experimental setup. (a)–(c) Linear regime. (d)–(g) High-density regime. (g) Mach-number chart showing in blue the regions where the Mach number is smaller than 1 (i.e., the fluid is in a subsonic condition), while the real-space emission (d) is reproduced in gray in regions where the Mach number is larger than 1.

of the pump frequency corresponds to an increase (decrease) of the momentum of the injected polaritons and therefore to smaller (larger) size of the unit cell. Figures 4(a) and 4(b) represent the transmitted light in the same region of the microcavity in the case where only the frequency of the laser has been changed. The increase [from (a) to (b)] of the laser frequency results in the increase of the momentum of the injected polaritons and, therefore, in the decrease of the size of the unit cell. To study the relation between the unit-cell size and the laser-LP detuning, we extract, for several detunings, the characteristic wave vector of the lattice k_L and compare it with the k vector of the corresponding Rayleigh ring k_R given by the relation $E_{\mathrm{LPB}}(k_R) = E_{\mathrm{laser}}$. The results, shown in Fig. 4(c), demonstrate a linear dependence between the two k vectors.

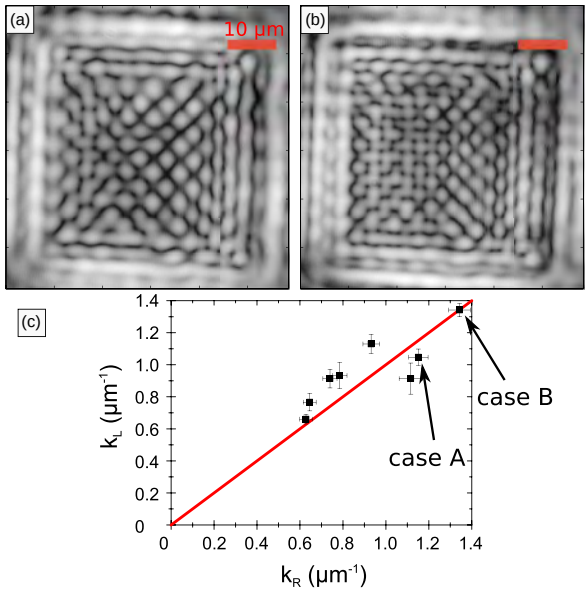

FIG. 4. (Color online) (a),(b) Real-space emission in the case of a 45-μm square mask in the linear regime with $\delta_{\text{exc-photon}} = 0.32$ meV and using different laser wavelengths. The wavelengths used are $\lambda_A = 836.40$ nm and $\lambda_B = 836.36$ nm, respectively, inducing a lattice width unit cell of 6 and 4.7 μm. The lattice sizes correspond to momenta $k_L^A = 1.0\ \mu\text{m}^{-1}$ and $k_L^B = 1.34\ \mu\text{m}^{-1}$, while the corresponding momenta from the Rayleigh rings are $k_R^A = 1.15\ \mu\text{m}^{-1}$ and $k_R^B = 1.34\ \mu\text{m}^{-1}$. In (c) we compare, for several different cases, the measured k_L with the corresponding measured k_R. Clearly, apart from the differences due to uncertainty in the experimental evaluation, the two values are equal.

2. *Control of the shape of the unit cell*

While the $|k|$ of the injected polaritons is governed by the detuning between the laser and the bare LP branch, the direction of the polaritons is determined by the shape of the mask used to block part of the laser spot. Therefore, the shape of the unit cell can be controlled by changing the shape of the masks. In the case of a triangular mask (Fig. 5), when the laser intensity and the polariton density are low and polariton-polariton interactions play a negligible role, the polaritonic fluid forms an array of V-AV pairs arranged in a hexagonal unit cell as expected for the superposition of three laser beams [46]. Figure 5 compares the experimental and theoretical output for a 35-μm side almost equilateral triangle and its corresponding phase. In the experimental output we can recognize up to 8–9 unit cells in very good agreement with the Gross-Pitaevskii-based simulations. In this regime the generation of the lattice is driven by the interferences between polaritons coming from each side of the triangle and flowing toward the center of the trap. The result is therefore analogous to the case of three overlapping laser beams interfering in a linear medium. Finally, let us mention that changing the size of the mask for fixed polariton wave vector $|k|$ and fixed mask shape results in a change of the overall lattice size only, while size and shape of the unit cells remain unchanged.

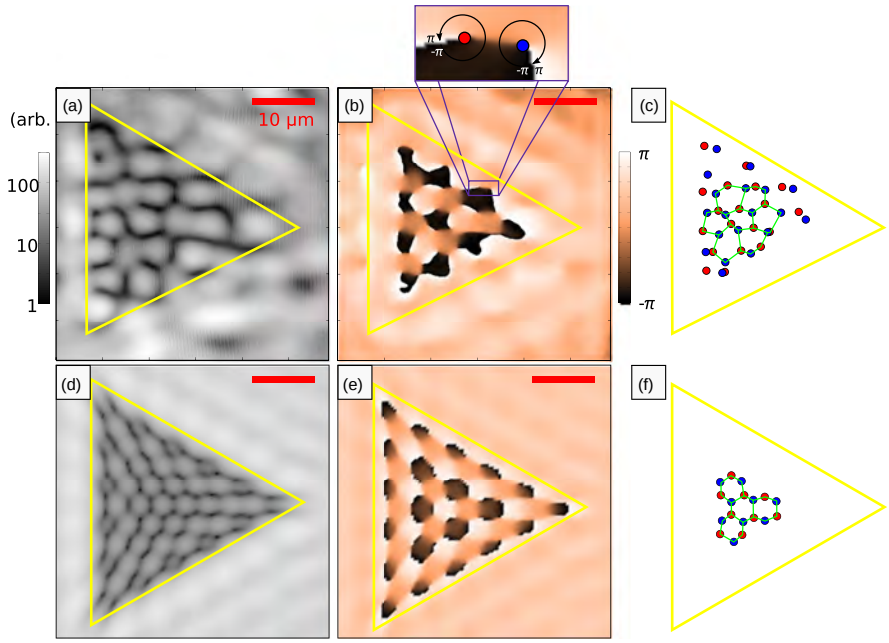

FIG. 5. (Color online) (a),(b) Experimental real-space emission output for a 45-μm side triangular mask and its corresponding phase. The yellow triangle represents the mask boundaries. In panel (b) the inset shows the phase rotating clockwise from $-\pi$ to π around the core of an antivortex (in blue), together with the clockwise rotating phase of a vortex (in red). (c) Representation of the hexagonal lattice of vortices (in red) and antivortices (in blue) corresponding to a wave vector $k_L = 0.75\ \mu\text{m}^{-1}$. (d)–(f) Theoretical simulations performed under the same conditions of excitations. The data have been taken at $\delta_{\text{exc-photon}} = 1.68$ meV, and the pump laser has a blueshift from the LPB at $k = 0$ of $\delta_{\text{pump-LPB}} = 0.16$ meV, corresponding to an injected momentum of $k_R = 0.65\ \mu\text{m}^{-1}$.

B. Nonlinear regime

Figures 2(d)–2(f) show the experimental polariton distribution in the case of high laser power (pump power has been increased from 1 to 35 mW) for the same mask, same position in the cavity, and same laser frequency as in Figs. 2(a)–2(c). Comparing the polariton distribution at low density [Figs. 2(a)–2(c)] with the one at higher density [Figs. 2(d)–2(f)] we see a drastic change in the distribution of the topological defects. At high densities, the repulsion between polaritons not only leads to an enlargement and to a deformation of the lattice unit cell, which is mostly due to a blueshift of the polariton energy, but also leads to a drastic change in the vortex distribution. In particular, as discussed below, the disappearance of the vortices from the outer part of the trap is linked to quantum fluid properties of the polariton condensate. This behavior is remarkably consistent with the theoretical simulations shown in Figs. 3(d)–3(f) for the same set of parameters as in the experimental case.

To better understand the vortex distribution, we study the correlations between the disappearance of the array of V-AV pairs and the subsonic character of the fluid. Since the distribution of the polariton fluid is not homogeneous, one has to define a local speed of sound $c_s(\mathbf{r}) = \sqrt{\hbar g_{LP}|\Psi_{LP}(\mathbf{r})|^2/m_{LP}}$, where $|\Psi_{LP}(\mathbf{r})|^2$, g_{LP}, and m_{LP} are the local polariton density, the coupling constant, and the polariton mass, respectively. In the local density approximation [47], $c_s(\mathbf{r})$ corresponds to the speed of sound defined in the case of high densities (i.e., when the polariton density lies on the upper branch of the bistability curve and the Bogoliubov dispersion of the collective excitations is linear [48]) and therefore hereinafter we simply call it *generalized speed of sound*. To study the existence of these correlations we evaluate the Mach number $[M(\mathbf{r})]$ defined as the ratio between the speed of the fluid $v_f(\mathbf{r}) = \hbar|\mathbf{k}(\mathbf{r})|/m_{LP}$ (locally evaluated as the derivative of the phase at the point $(\mathbf{r})$, and the generalized speed of sound $[c_s(\mathbf{r})]$):

$$M(\mathbf{r}) = \frac{v_f(\mathbf{r})}{c_s(\mathbf{r})} = \frac{\hbar|\mathbf{k}(\mathbf{r})|/m_{LP}}{\sqrt{\hbar g_{LP}|\Psi_{LP}(\mathbf{r})|^2/m_{LP}}}. \qquad (1)$$

Figure 3(g) shows the Mach-number chart corresponding to the case of Figs. 3(d)–3(f): In the region inside the trap but close to the borders, where V-AV pairs have disappeared, the system is in a subsonic regime due to its high density. Since a subsonic fluid cannot sustain strong phase modulations [49], V-AV pairs merge in the regions where the fluid becomes locally subsonic. Note that the disappearance of the V-AV pairs cannot be ascribed to a simple renormalization of the LPB since this mechanism would lead to an increase of the lattice characteristic length. This is not the case in our system since the periodicity related to this characteristic length is still visible in Figs. 2(d) and 3(d). In our case, V-AV pairs disappear because the increase of the polariton density forces vortices to overlap with antivortices and therefore to annihilate. On the other hand, as polaritons move towards the center of the trap, due to their finite lifetime, their density decreases and so does the sound velocity of the fluid so that the fluid

becomes mainly supersonic [$M(\mathbf{r}) > 1$]. In this inner region, V-AV pairs can survive and the array is only slightly deformed. Therefore, the finite lifetime of cavity-polaritons and their out-of-equilibrium character allow the observation of different behaviors, at the same time, in different regions of the system. The coexistence of the two behaviors is a specific feature typical of cavity-polariton systems distinguishing them from other equilibrium systems like nonlinear optics and atomic condensates.

IV. CONCLUSIONS

We have investigated the vortex lattice formation in exciton-polariton systems as a function of the polariton density. In the linear regime we have demonstrated the generation of a lattice of vortices in microcavity-polariton systems whose size, shape, and unit-cell size can be easily controlled and are solely determined by the geometry of the system. When the polariton density is increased, strong polariton-polariton nonlinear interactions dominate and substantially modify the previously observed array. Our results show not only that the repulsion between polaritons can modify the effect of plane-wave interference and determine the array pattern, but also that the interactions can destroy the topological excitations of opposite winding number by merging one excitation with the other. Our simulations show the correlation between the disappearance of V-AV pairs and the local onset of the superfluid regime. While our system has a zero total angular momentum and therefore cannot support any single free vortex, Abrikosov-like lattices could be observed by breaking this symmetry therefore opening the way to the observation of mutual vortex-vortex interactions.

ACKNOWLEDGMENTS

We would like to thank C. Tejedor for the use of the computational facilities of the Universidad Autonoma de Madrid, L. Martiradonna for the confocal mask, R. Houdré for the sample, and Iacopo Carusotto for useful discussions. This work has been partially funded by the Quandyde project of the ANR France, by the POLATOM ESF Research Network Program, and by the CLERMONT4 Network Progam. F.M.M. acknowledges financial support from the programs Ramon y Cajal and Intelbiomat (ESF) and M.H.S. from the EPSRC (Grant No. EP/I028900/1). A.B. is member of Institut Universitaire de France (IUF).

APPENDIX A: SAMPLE DESCRIPTION

In our experiment we use a high-finesse ($F = 3000$) 2λ GaAs microcavity containing three $In_0.05Ga_{0.95}As$ quantum wells. The top and bottom Bragg mirrors are formed by 20 and 24 pairs, respectively, of alternating layers of GaAs and AlAs with an optical thickness of $\lambda/4$, $\lambda = 835$ nm being the wavelength of the confined cavity mode. The Rabi splitting is about 5.1 meV, and the photon lifetime $\tau_C = 11$ ps. Since the exciton linewidth is of the order of or slightly lower than the photon linewidth (as considered in the theoretical model), we obtain a polariton lifetime τ_{LP} of the order of 10–15 ps. This value is consistent with other time-resolved experiments [42]. The Bragg mirrors of the cavity form a wedge of a few degrees to allow a fine tuning of the exciton-photon detuning. The microcavity is excited with a continuous-wave single-mode Ti:Sa laser quasiresonant with the LPB lying in the infrared domain around 837 nm.

APPENDIX B: PHASE EXTRACTION PROCEDURE

We detail here the phase extraction procedure. The signal coming from the microcavity $E_s = E_{s0}e^{i\Phi_s}$ (with amplitude E_{s0} and phase Φ_s) is sent into one arm of a Mach-Zehnder interferometer, while a reference beam $E_r = E_{r0}e^{i\phi_r}$ (with amplitude E_{r0} and phase Φ_r) is sent into the other arm of the interferometer. The intensity of the reference beam [Figs. 6(a) and 6(b)] is adjusted for each set of data in order to maximize the contrast of the interference pattern ($E_{r0} \approx E_{s0}$), and the interference pattern is collected on a CCD camera [Figs. 6(c) and 6(d)]. The detected intensity is therefore proportional to $\langle (E_s + E_r)^2 \rangle = E_s^2 + E_r^2 + 2E_{s0}E_{r0}\cos(\Phi_s - \Phi_r + \Delta\Phi)$, where we assumed a perfect coherence between the two components and where $\Delta\Phi$ is the phase shift induced by the geometry of the interferometer (angle between arms and lenses). In order to

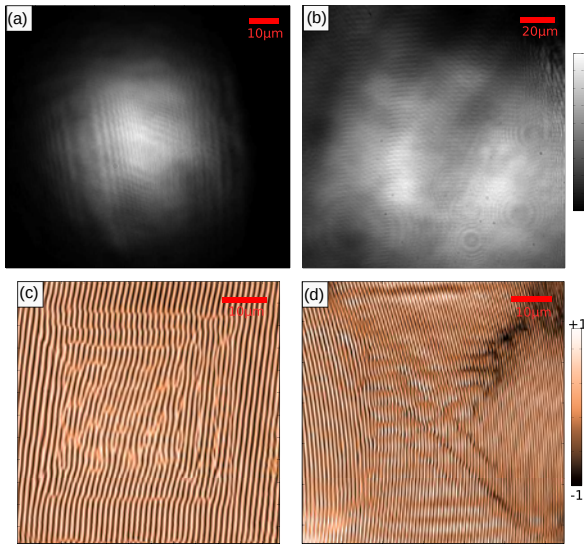

FIG. 6. (Color online) (a),(b) Real-space images of typical reference beams in linear grayscale. The reference beam can be either a part of the excitation beam (a) or a small part of the signal greatly enlarged to generate a plane wave (b). The small fringes observable in (a) are parasitic interferences due to reflection on optical elements of the setup. Due to their very low contrast these fringes do not alter the phase extraction procedure. Panels (a) and (b) have been used, respectively, to extract the phases in the linear and nonlinear regimes of Fig. 2 of the main text. Panel (c) [(d)] is the real-space interference pattern $\langle (E_s + E_r)^2 \rangle$, in linear grayscale, resulting from interferences between panel (a) [(b)] and the signal plotted in Fig. 2(a) [(2(d)] of the main text. Since the presence of a vortex is manifested by a fork in the interferogram, one can compare the positions of the forks on (c) with the vortex distribution represented in Fig. 2(b) of the main text.

extract the phase diagram we perform a numerical Fourier transform of the interferogram and isolate the off-axis component corresponding to the term $2E_{s0}E_{r0}\cos(\Phi_s - \Phi_r + \Delta\Phi)$. Then, we perform the inverse Fourier transform from which the phase $\Phi_s - \Phi_r$ (and the amplitude $2E_{s0}E_{r0}$) can be extracted by removing the geometrical term $\Delta\Phi$ that can be measured separately.

APPENDIX C: THEORETICAL MODEL

A standard way to model the dynamics of resonantly driven polaritons in a planar microcavity is to use a Gross-Pitaevskii (GP) equation for coupled cavity and exciton fields (Ψ_C and Ψ_X) generalized to include the effects of the resonant pumping and decay ($\hbar = 1$),

$$\partial_t \begin{pmatrix} \Psi_X \\ \Psi_C \end{pmatrix} = \begin{pmatrix} 0 \\ F \end{pmatrix} + \left[H_0 + \begin{pmatrix} g_X|\Psi_X|^2 & 0 \\ 0 & V_C \end{pmatrix} \right] \begin{pmatrix} \Psi_X \\ \Psi_C \end{pmatrix}, \tag{C1}$$

where the single-particle polariton Hamiltonian H_0 is given by

$$H_0 = \begin{pmatrix} \omega_X - i\kappa_X & \Omega_R/2 \\ \Omega_R/2 & \omega_C(-i\nabla) - i\kappa_C \end{pmatrix}, \tag{C2}$$

and

$$\omega_C(-i\nabla) = \omega_C(0) - \frac{\nabla^2}{2m_c} \tag{C3}$$

is the cavity dispersion, with the photon mass $m_C = 4 \times 10^{-5} m_0$ and m_0 the bare electron mass. For the simulations we have assumed a flat exciton dispersion relation $\omega_X(k) = \omega_X(0)$. The parameters Ω_R, κ_X, and κ_C are the Rabi frequency and the excitonic and photonic decay rates, respectively, and have been fixed to values close to experimental ones: $\Omega_R = 5.1$ meV, $\kappa_X = 0.04$ meV, and $\kappa_C = 0.06$ meV. In this model polaritons are injected into the cavity by a coherent and monochromatic laser field, with pump intensity f_p and a Gaussian spatial profile with width σ of 50 μm: $F(r) = f_p e^{-r^2/2\sigma^2}$. Here, in contrast to others cases [50], we simulate the polariton system with a simplified two-field model, discarding the role of the excitonic reservoir since our setup is based on the use of a continuous-wave laser with a linewidth orders of magnitudes smaller than the Rabi splitting and therefore the injection of a reservoir of excitons is strongly suppressed. Part of the laser beam profile is set to zero in order to reproduce the effect of the gold mask. To simulate the effect of not-perfectly reflecting edges of the mask, the pump intensity is set to decay exponentially from the border of the mask toward the center. The exciton-exciton interaction strength g_X is set to 1 by rescaling both the cavity and excitonic fields and the pump intensities. Our theoretical results come from the numerical solution of the GP equation over a two-dimensional grid (of 512×512 points) in a box with sides of 150×150 μm^2 using a fifth-order adaptive-step Runge-Kutta algorithm. All the analyzed quantities are taken when the system has reached a steady-state condition after a transient period of 200 ps.

[1] L. Onsager, Il Nuovo Cimento **6**, 279 (1949).
[2] R. Feynman, in *Progress in Low Temperature Physics* (North-Holland, Amsterdam, 1955), Vol. 1, pp. 17–53.
[3] J. F. Nye and M. V. Berry, Proc. R. Soc. London, Ser. A **336**, 165 (1974).
[4] A. S. Desyatnikov, Y. S. Kivshar, and L. Torner, in *Progress in Optics*, edited by E. Wolf (Elsevier, Amsterdam, 2005), Vol. 47, pp. 291–391.
[5] U. Essmann and H. Träuble, Phys. Lett. A **24**, 526 (1967).
[6] E. J. Yarmchuk, M. J. V. Gordon, and R. E. Packard, Phys. Rev. Lett. **43**, 214 (1979).
[7] J. Scheuer and M. Orenstein, Science **285**, 230 (1999).
[8] K. W. Madison, F. Chevy, W. Wohlleben, and J. Dalibard, Phys. Rev. Lett. **84**, 806 (2000).
[9] J. Denschlag, J. E. Simsarian, D. L. Feder, C. W. Clark, L. A. Collins, J. Cubizolles, L. Deng, E. W. Hagley, K. Helmerson, W. P. Reinhardt, S. L. Rolston, B. I. Schneider, and W. D. Phillips, Science **287**, 97 (2000).
[10] L. Khaykovich, F. Schreck, G. Ferrari, T. Bourdel, J. Cubizolles, L. D. Carr, Y. Castin, and C. Salomon, Science **296**, 1290 (2002).
[11] A. Abrikosov, Sov. Phys. JETP-USSR **5**, 1174 (1957).
[12] H. Deng, H. Haug, and Y. Yamamoto, Rev. Mod. Phys. **82**, 1489 (2010).
[13] I. Carusotto and C. Ciuti, Rev. Mod. Phys. **85**, 299 (2013).
[14] F. Dalfovo, S. Giorgini, L. P. Pitaevskii, and S. Stringari, Rev. Mod. Phys. **71**, 463 (1999).
[15] S. Burger, F. S. Cataliotti, C. Fort, F. Minardi, M. Inguscio, M. L. Chiofalo, and M. P. Tosi, Phys. Rev. Lett. **86**, 4447 (2001).
[16] J. Kasprzak, M. Richard, S. Kundermann, A. Baas, P. Jeambrun, J. M. J. Keeling, F. M. Marchetti, M. H. Szymanska, R. André, J. L. Staehli, V. Savona, P. B. Littlewood, B. Deveaud, and L. S. Dang, Nature (London) **443**, 409 (2006).
[17] I. Carusotto and C. Ciuti, Phys. Rev. Lett. **93**, 166401 (2004).
[18] M. Wouters and I. Carusotto, Phys. Rev. Lett. **105**, 020602 (2010).
[19] E. Cancellieri, F. M. Marchetti, M. H. Szymanska, and C. Tejedor, Phys. Rev. B **82**, 224512 (2010).
[20] E. Cancellieri, F. M. Marchetti, M. H. Szymanska, D. Sanvitto, and C. Tejedor, Phys. Rev. Lett. **108**, 065301 (2012).
[21] A. Amo, D. Sanvitto, F. P. Laussy, D. Ballarini, E. d. Valle, M. D. Martin, A. Lemaitre, J. Bloch, D. N. Krizhanovskii, M. S. Skolnick, C. Tejedor, and L. Vina, Nature (London) **457**, 291 (2009).
[22] A. Amo, J. Lefrère, S. Pigeon, C. Adrados, C. Ciuti, I. Carusotto, R. Houdre, E. Giacobino, and A. Bramati, Nat. Phys. **5**, 805 (2009).
[23] D. Sanvitto, F. M. Marchetti, M. H. Szymanska, G. Tosi, M. Baudisch, F. P. Laussy, D. N. Krizhanovskii, M. S. Skolnick, L. Marrucci, A. Lemaitre, J. Bloch, C. Tejedor, and L. Vina, Nat. Phys. **6**, 527 (2010).
[24] K. G. Lagoudakis, M. Wouters, M. Richard, A. Baas, I. Carusotto, R. André, L. S. Dang, and B. Deveaud-Plédran, Nat. Phys. **4**, 706 (2008).

[25] K. G. Lagoudakis, T. Ostatnický, A. V. Kavokin, Y. G. Rubo, R. André, and B. Deveaud-Plédran, Science **326**, 974 (2009).
[26] H. Flayac, I. A. Shelykh, D. D. Solnyshkov, and G. Malpuech, Phys. Rev. B **81**, 045318 (2010).
[27] G. Roumpos, M. D. Fraser, A. Löffler, S. Höfling, A. Forchel, and Y. Yamamoto, Nat. Phys. **7**, 129 (2011).
[28] G. Nardin, G. Grosso, Y. Léger, B. Pięrtka, F. Morier-Genoud, and B. Deveaud-Plédran, Nat. Phys. **7**, 635 (2011).
[29] G. Tosi, F. M. Marchetti, D. Sanvitto, C. Anton, M. H. Szymanska, A. Berceanu, C. Tejedor, L. Marrucci, A. Lemaitre, J. Bloch, and L. Vina, Phys. Rev. Lett. **107**, 036401 (2011).
[30] A. Amo, S. Pigeon, D. Sanvitto, V. G. Sala, R. Hivet, I. Carusotto, F. Pisanello, G. Leménager, R. Houdre, E. Giacobino, C. Ciuti, and A. Bramati, Science **332**, 1167 (2011).
[31] R. Hivet, H. Flayac, D. D. Solnyshkov, D. Tanese, T. Boulier, D. Andreoli, E. Giacobino, J. Bloch, A. Bramati, G. Malpuech, and A. Amo, Nat. Phys. **8**, 724 (2012).
[32] A. V. Gorbach, R. Hartley, and D. V. Skryabin, Phys. Rev. Lett. **104**, 213903 (2010).
[33] J. Keeling and N. G. Berloff, Phys. Rev. Lett. **100**, 250401 (2008).
[34] T. C. H. Liew, Y. G. Rubo, and A. V. Kavokin, Phys. Rev. Lett. **101**, 187401 (2008).
[35] K. Kusudo, N. Y. Kim, A. Löffler, S. Höfling, A. Forchel, and Y. Yamamoto, Phys. Rev. B **87**, 214503 (2013).
[36] F. Manni, T. C. H. Liew, K. G. Lagoudakis, C. Ouellet-Plamondon, R. André, V. Savona, and B. Deveaud, Phys. Rev. B **88**, 201303 (2013).
[37] S. Pigeon, I. Carusotto, and C. Ciuti, Phys. Rev. B **83**, 144513 (2011).
[38] G. Tosi, G. Christmann, N. G. Berloff, P. Tsotsis, T. Gao, Z. Hatzopoulos, P. G. Savvidis, and J. J. Baumberg, Nat. Commun. **3**, 1243 (2012).
[39] P. Cristofolini, A. Dreismann, G. Christmann, G. Franchetti, N. G. Berloff, P. Tsotsis, Z. Hatzopoulos, P. G. Savvidis, and J. J. Baumberg, Phys. Rev. Lett. **110**, 186403 (2013).
[40] R. Houdre, C. Weisbuch, R. P. Stanley, U. Oesterle, and M. Ilegems, Phys. Rev. B **61**, R13333 (2000).
[41] C. Adrados, T. C. H. Liew, A. Amo, M. D. Martin, D. Sanvitto, C. Anton, E. Giacobino, A. Kavokin, A. Bramati, and L. Vina, Phys. Rev. Lett. **107**, 146402 (2011).
[42] D. Sanvitto, S. Pigeon, A. Amo, D. Ballarini, M. D. Giorgi, I. Carusotto, R. Hivet, F. Pisanello, V. G. Sala, P. S. S. Guimaraes, R. Houdre, E. Giacobino, C. Ciuti, A. Bramati, and G. Gigli, Nat. Photon. **5**, 610 (2011).
[43] M. Vladimirova, S. Cronenberger, D. Scalbert, K. V. Kavokin, A. Miard, A. Lemaitre, J. Bloch, D. Solnyshkov, G. Malpuech, and A. V. Kavokin, Phys. Rev. B **82**, 075301 (2010).
[44] E. Wertz, L. Ferrier, D. D. Solnyshkov, P. Senellart, D. Bajoni, A. Miard, A. Lemaitre, G. Malpuech, and J. Bloch, Appl. Phys. Lett. **95**, 051108 (2009).
[45] A. Baas, J. P. Karr, H. Eleuch, and E. Giacobino, Phys. Rev. A **69**, 023809 (2004).
[46] J. Masajada and B. Dubik, Opt. Commun. **198**, 21 (2001).
[47] M. Wouters, I. Carusotto, and C. Ciuti, Phys. Rev. B **77**, 115340 (2008).
[48] C. Ciuti and I. Carusotto, Phys. Status Solidi B **242**, 2224 (2005).
[49] L. D. Landau and E. M. Lifshitz, in *Statistical Physics*, Course of Theoretical Physics, 2nd ed. (Pergamon Press, Oxford, 1986), Part 1, Chap. 6.
[50] M. D. Fraser, G. Roumpos, and Y. Yamamoto, New J. Phys. **11**, 113048 (2009).

3.3. Annihilation of vortex-antivortex pairs: multi-pumps setup

As previously explained a scheme with four pumping lasers was implemented to overcome the power losses present in the masked pump scheme. In this section we describe the specific experimental setup, the results and the theoretical predictions.

3.3.1. Multi-beam pumping: experimental description

Laser shaping

The fiber output from the previously described laser source is first spatially filtered by being focused on a 50 µm pinhole with a waist diameter of about 40 µm so that the Gaussian tail is cut (albeit for a small amount for diffraction). Lenses then modifies its size so that the collimated waist diameter is about 1.5 mm. The beam power can be reduced if needed by a half-wave plate (HWP) followed by a polarized beam splitter (PBS). Three beam splitter (BS) then divide the laser into four beams of equal intensities, as shown in figure 3.11. The four arms are then collected and sent along similar trajectories by mirrors. Note that to be all sent along a similar path all laser arms must be spatially gathered on a small zone, but on separate mirrors. This required to use the borders or corners of square, rectangle and half circular mirrors as schematically represented with half-mirrors on figure 3.11. The mirrors are all of dielectric type, to preserve both the laser power and the linear polarization. Each of these laser arms is focalized on the sample with a condenser lens of focal length $f_{cond} = 25\,\text{mm}$ and they each form an independent pump. Just before the condenser lens, the pumps are circularly polarized by a quarter-wave plate (QWP) in order to obtain only one polariton population and avoid any effect due to spin-dependent interactions [137]. For each pump, the real space positions and the angle of incidence can be controlled independently.

Pumps properties

The four pumps are spatially arranged on the sample to form a square, with their angles of incidence chosen so that polaritons from each pump propagate towards the square center. The four in-plane wavevectors are chosen with the same norm, meaning that all four pumps hit the sample with the same angle on incidence θ. For fixed θ it is possible to tilt the in-plane direction of propagation by an angle φ relative to the direction of the center, as summarized in figure 3.12, which allows to inject a non-zero angular momentum.

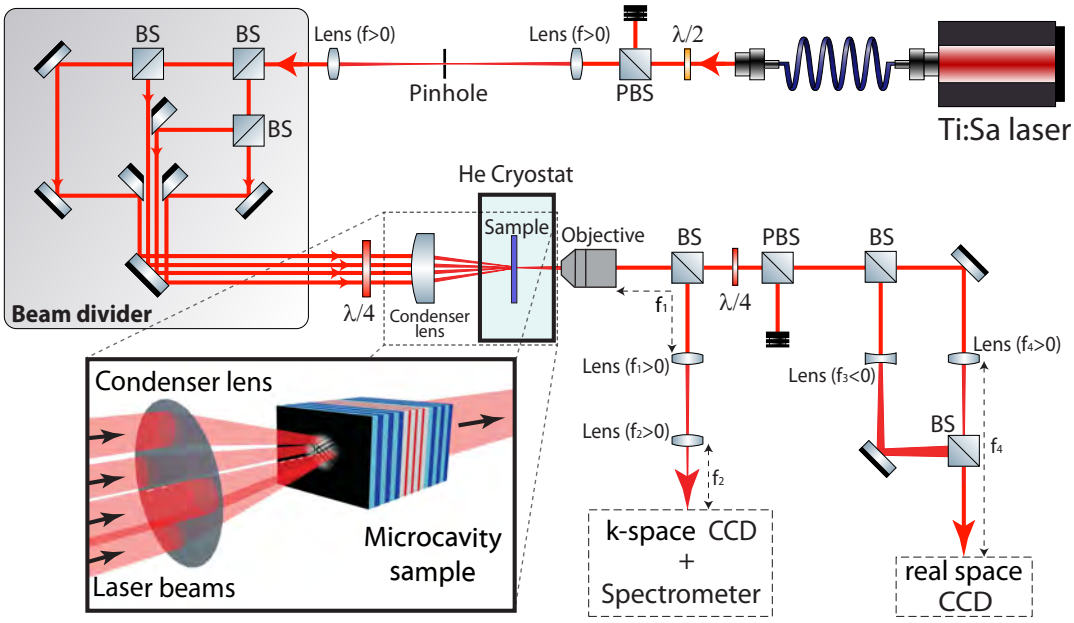

Figure 3.11.: Experimental setup - Scheme of the optical setup. The laser beam is focused on a pinhole of 50 µm of diameter before being divided into four equal beams sent along similar trajectories. The four laser are focused on the sample so that they form four polariton fluids propagating towards each other (see the inset). Polarization-resolved detection is done simultaneously in real space, momentum space and energy.

The limited polariton lifetime implies that their propagation distance is limited, so the four pumps must be relatively close to one another. This is especially important for $\varphi \neq 0$, since in this case the different polaritons populations do not propagate toward each other. Therefore the pumps separation is chosen small enough so that the four polariton populations can still meet and form a detectable density at the square center for $|\varphi| > 0$. It is critical to let the polariton phase evolve freely after they have been injected by the laser. In previous studies [138, 16, 20] polaritons were observed in a region of the microcavity where they have moved away from the laser spot, which was efficiently limited by a mask. Since before the division into four arms the laser beam is focalized on a pinhole, and since we work in the bistable regime (see discussion 3.1), the absence of Gaussian tails ensures that none of the pumps overlap and that in the central region polaritons are free to evolve. For $\theta = \varphi = 0$, polaritons do not propagate far enough from the pumps to form a substantial population at the center. For $\theta \neq 0$ and $\varphi = 0$, the four polariton populations collide at the system center without carrying any angular momentum; it is this case that we will describe in the present chapter (especially in subsection 3.3.2). If both θ and φ are non-zero, an angular momentum is injected and this case will be the subject of chapter 4.

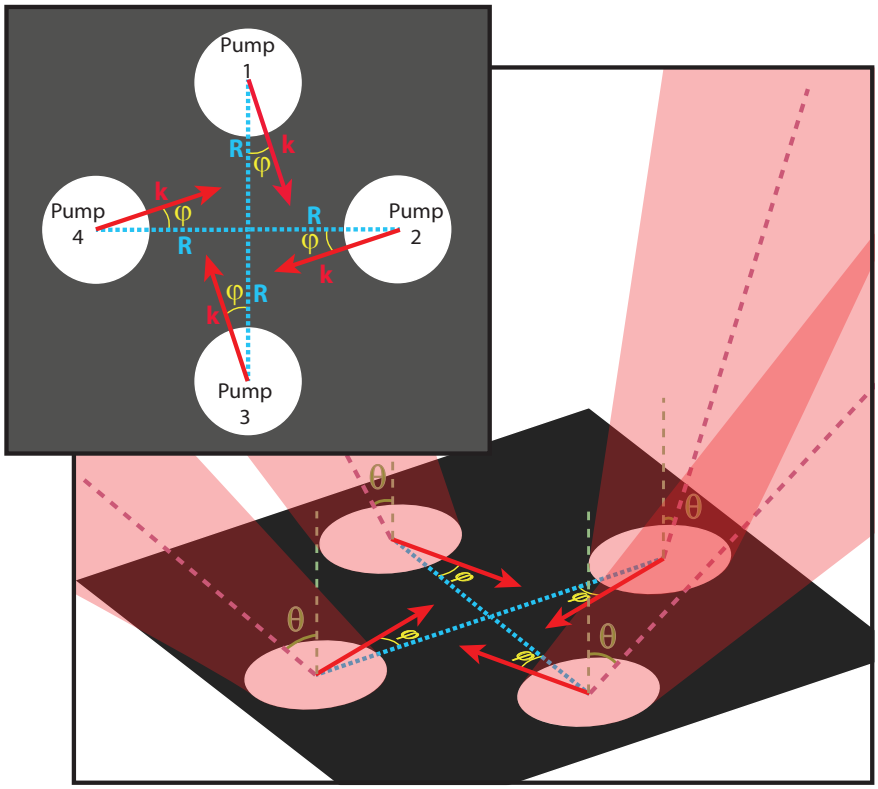

Figure 3.12.: Pumping scheme - Schematic representation of the four pumps arriving on the sample. θ is the incidence angle, on which depends the norm of the polariton wavevector. The in-plane polariton propagation direction is set through the azimuth angle φ. The blue dashed lines show the direction to the center ($\varphi = 0$) while the red arrows show the polariton direction of propagation for $\varphi \neq 0$.

3.3.2. Results

The main driving force behind the merging of V-AV pairs is the polariton-polariton interactions, controlled in our experiments with the polariton density. Thus we present here our results in different density regimes.

Let us remind the reader that in this section only the $\varphi = 0°$ (zero angular momentum) case is presented: the non-adjacent pumps create contra-propagating polaritons, so that the four populations propagate toward the square center. All measurements were done on a sample zone where the photon-exciton detuning is $\delta \simeq 0\,\text{meV}$, and with as little defects as possible.

Low density regime

When the density is low enough for the interaction energy to be neglected (compared to the kinetic energy) the pumps coherence, inherited by the polariton, simply makes the fours noninteracting fluids interfere [23]. This regime is also called the *linear regime* by

analogy with the purely photonic, linear optics case. Figure 3.13 shows the experimental and numerical results in this regime for the fluid density and phase in real space. The photon-exciton detuning is $\delta \simeq 0$ meV and the pump power is 10 mW for each pump. The hexagonal cells of this interference pattern is typical of a four-beam interference pattern [23]. We see that the interference nodes often (but not necessarily) contain a vortex or an antivortex and a vortex or antivortex is always placed at an interference node, so that the interference pattern determines the V-AV lattice. Those are in fact the same results as obtained with the mask setup (see section 3.2), showing the equivalence of the two systems for this regime. A more detailed description of this regime and comparison with the mask setup is available in [23].
Since the pumps relative phases are not controlled, they are random and fixed [7] by the path of the laser arms on the optical table. This is visible in figure 3.13 as phase discrepancies between the pumps, where a series of phase defects are present.

In k-space (figure 3.14) the collected signal corresponds to only the pumps wavevector. This was expected as in absence of nonlinearities each pump population propagates without its wavevector being modified, except through elastic scattering on the cavity natural disorder which gives rise to the Rayleigh ring regularly observed in many polariton experiments [24, 23, 139]. The Rayleigh ring is too dim to be visible in figure 3.14, due to the low scattering rate produced by the chosen low-disorder zone.

High density regime

For very high densities (a pump power of about 100 mW for each pumps) the destruction of the V-AV pairs is efficient, and is accompanied by the vanishing of the interference pattern. Indeed, the four coherent polariton fluids are, everywhere in real space, in the superfluid regime [16]. We observe that their phases are modified so as to form a single coherent superfluid. Polariton-polariton interactions, dominant in this regime, are responsible for this phase modification across all fluids. Figure 3.15 shows these results, obtained both experimentally and numerically.

This behavior is all the more striking as it is independent from the pumps relative phases. Indeed, the resulting superfluid shows a regular, smooth phase with no discrepancy. Therefore no phase domain can be detected, showing that the relative phases between the pumped polariton populations are reduced to zero. This is unlike the linear case. Additionally, while due to air density fluctuations the relative phases for each pump

7. If one neglects density fluctuations in the air, which only have a small impact on the pups phases for our setup.

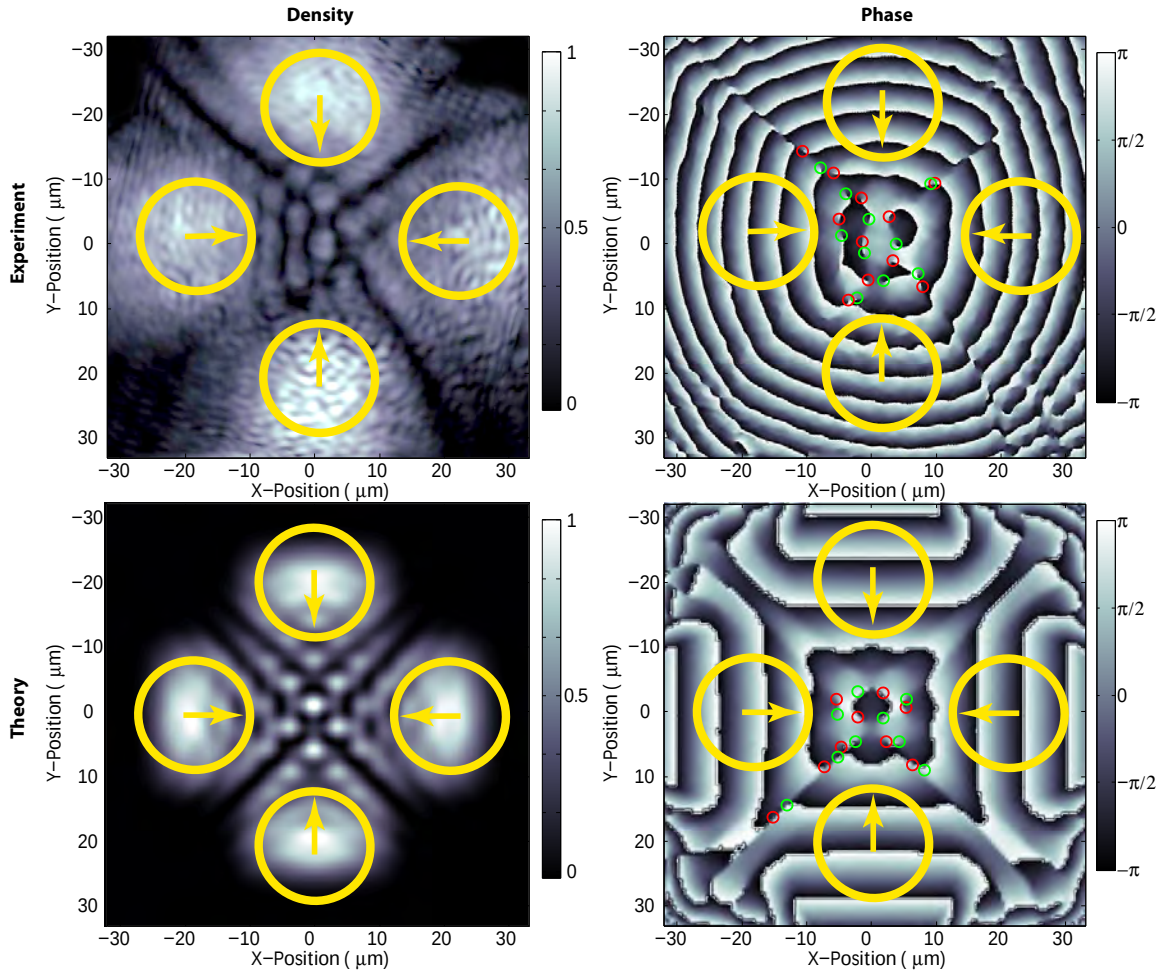

Figure 3.13.: Linear regime real space emission - Experimental (up) and theoretical (down) real space density (left) and phase (right) in the low interactions regime. The intensity scale is linear and normalized to the peak intensity. An interference pattern is visible between the contra-propagating pumps containing vortex-antivortex pairs, shown in the phase map as green (vortex) and red (antivortex) circles. The yellow circles delimit the pumps while the yellow arrows show their polariton population direction of propagation.

randomly fluctuate, the resulting superfluid shows no such fluctuation [8]. To test this in a controlled way a mirror implicated with only one of the four pumps was mounted on a piezoelectric transducer, so that the pump phase can be varied by more than 2π in a controlled way. The change in phase did not modify the superfluid, which confirms that once created in this high density regime polaritons gain a well-defined collective phase.

We can confirm the subsonic nature of the fluid by looking at the Mach number spatial map. The Mach number is the ratio between the local fluid velocity (derived from the phase gradient) and the local speed of sound (estimated from the density): any area with a Mach number smaller than one is subsonic. The measured Mach number is presented in

8. Such fluctuation are, however, visible in the low density regime. This constitutes an additional indication of the interferential origin of the V-AV pattern observed at low density.

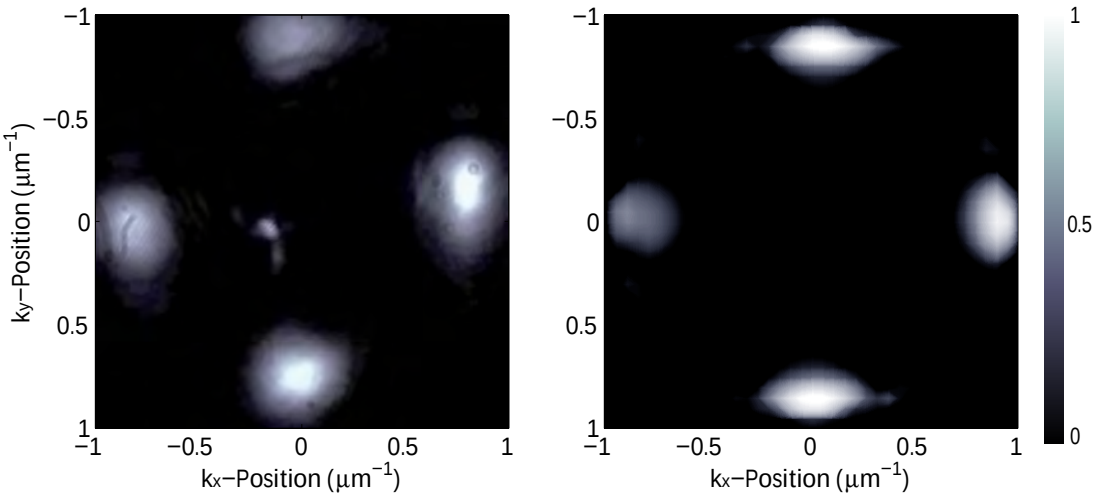

Figure 3.14.: Linear regime k-space emission - Experimental (left) and numerical (right) k-space emission in the low interactions regime. The intensity scale is linear and normalized to the peak intensity. Only the four pumps are visible. The spot near the center of the experimental figure is a parasite reflection.

figure 3.16. We can see that all regions with a significant density (that is to say everywhere inside and between the pumps) are indeed subsonic (in blue), as expected from the theory presented in the section 3.3.

In k-space (figure 3.17) the collected signal shows a more complex pattern. In accordance with the fluid velocity field (figure 3.16), a signal is present for low wavevectors (low velocities). This is unlike the low density regime. The real space localization of this low-velocity emission corresponds to the center of the square formed by the four pumps. Indeed, it appears in figure 3.16 that polaritons coming from each pump lose velocity as they approach the system center. This behavior, only visible at high densities, is consistent with the merging of the four superfluids into one. Indeed, with only one polariton population only one phase gradient is possible (whatever the direction a particular particle came from) and thus only a single polariton speed can be defined for each point in real space. For two contra-propagating fluids this phase harmonization implies the continuous transition from positive to negative speed values (since the direction changes), which in turns implies a zero-velocity population at the center.
The interference-like regular nature of the k-space pattern has not yet been theoretically explained, despite being also visible in the numerical simulations. It is, however, compatible with the time-resolved resonant polariton scattering experiment from B. Deveaud's group [18] where a very similar "deceleration" of the superfluid is observed during propagation. The explanation advanced in [18] involves the modification of the shape of the dispersion curve when the density decays and the fluid evolves from the superfluid to the Cerenkov regime before ending up in the linear regime for low densities. A similar explanation is possible in our case since multiple interacting polariton superfluids would definitely have

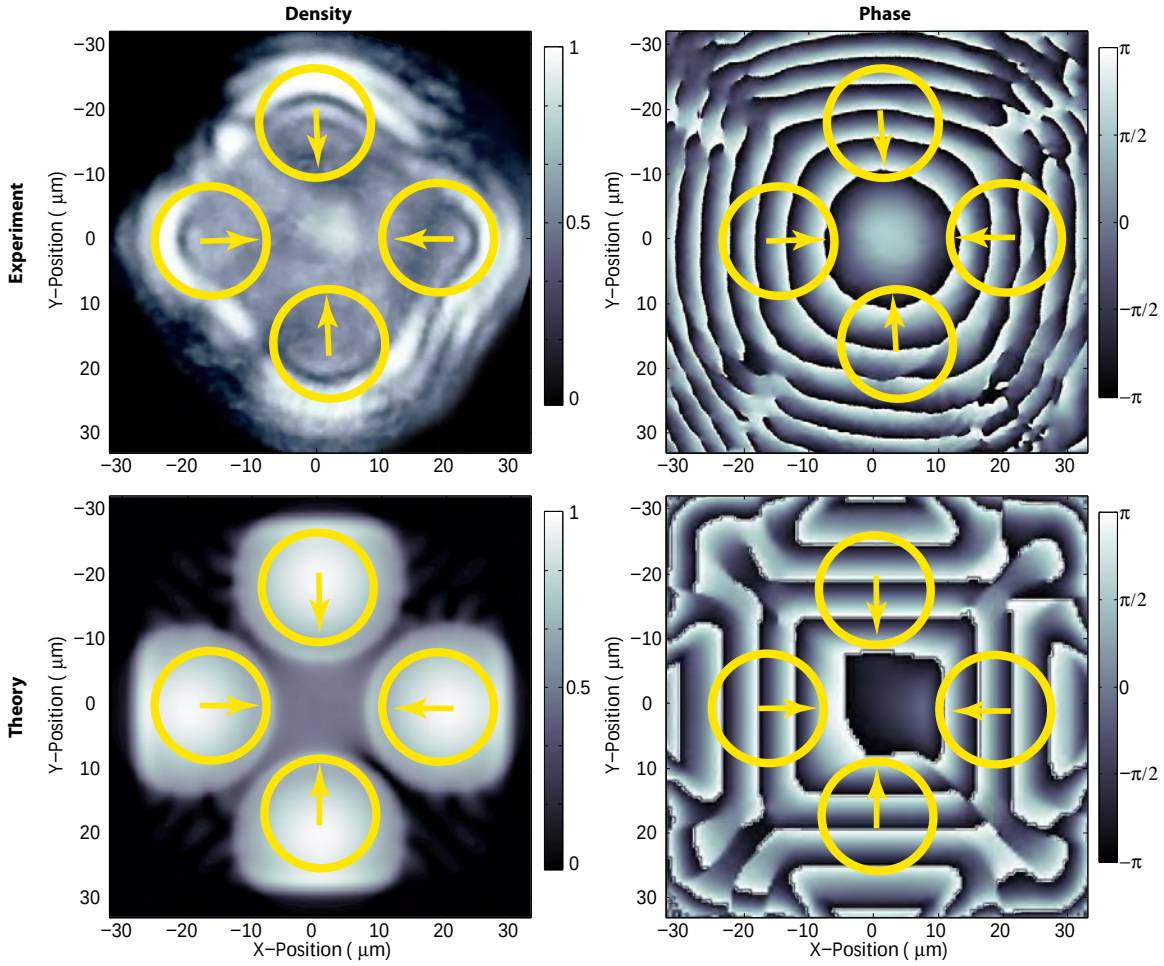

Figure 3.15.: Nonlinear regime real space emission - Experimental (up) and numerical (down) real space density (left) and phase (right) in the high density regime. The intensity scale is linear and normalized to the peak intensity. Here no interference pattern is visible as the four superfluids merge into one. This explains why no vortex can be observed.

a non-trivial dispersion relation (not yet theoretically derived).

As experimentally measured (figure 3.18 (a,b)) and numerically predicted (figure 3.18 (c,d)), the total (kinetic plus interaction) energy of the superfluid remains constant during propagation. This is expected for a resonant pumping setup. However, the density (and thus the potential energy) is approximately constant in real space, so that in a "classical" approach one would expect polaritons to retain its velocity while propagating to the center. It is therefore possible that for a multi-pump setup a new type of dispersion relation, that cannot be accessed with the theoretical tools developed in chapter 2, arises. It would possess zero-energy excitations able to disperse momentum while conserving the energy, a feature compatible with the flat "dispersion curve" measured between two pumps momenta (figure 3.18 (b), (d)). This would explain how polaritons can lose velocity while retaining their energy. No theoretical description is available at this time to test

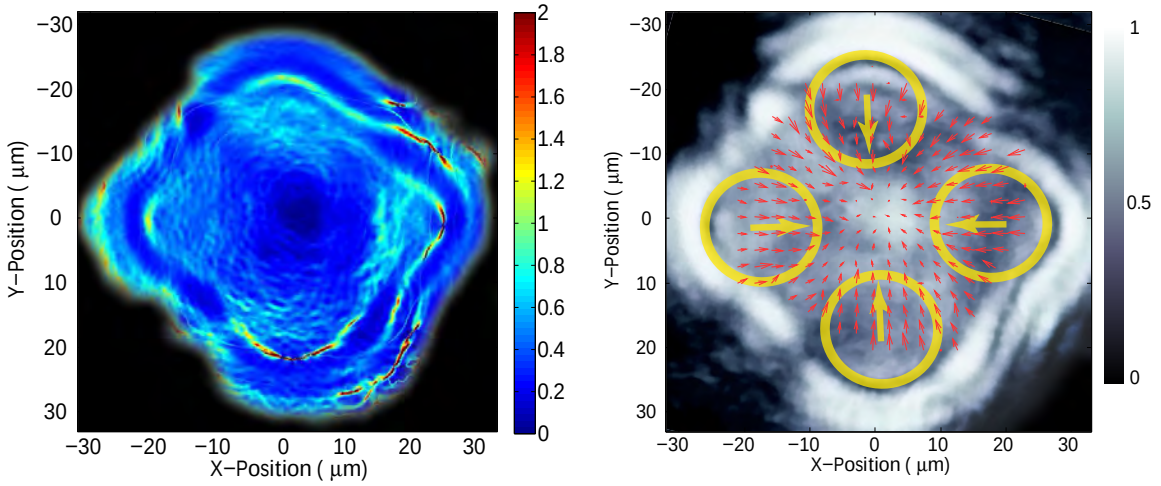

Figure 3.16.: Polariton velocity field - Experimental Mach number (left) and density map with overlaid velocity field (right) for polariton in the high density regime. The black zones in the Mach number map signify areas outside of the superfluid, where the polariton density is too low for the Mach number to have a clear meaning. The arrows length scale in the velocity field is arbitrary. In agreement with figure 3.17 a population with zero velocity is present, and located at the center of the real space image. The Mach number is below 0.5 between the pumps.

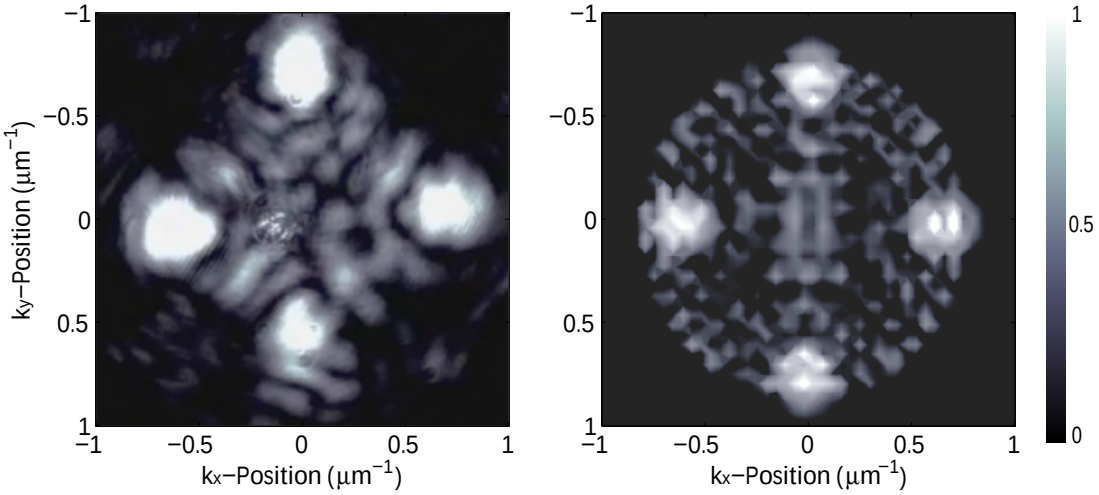

Figure 3.17.: Nonlinear regime k-space emission - Experimental (left) and numerical (right) k-space emission in the high density regime. The intensity scale is linear and normalized to the peak intensity. Here the interactions trigger the apparition of a population for low wavevectors. The interference-like structure of this signal has yet to be explained.

these hypothesis, however.

In any case, since the resonant pumping avoids any significant exciton population, this means no confining potential is present anymore at high density. Indeed, the polariton self interaction energy is the only one able to produce a potential, yet figure 3.18 clearly shows the absence of energy structure both in real space and k-space. Therefore one can

rule out any trapping effect to explain the merging of the four superfluids, as opposed to recent experiments with polariton condensates [9] [140].

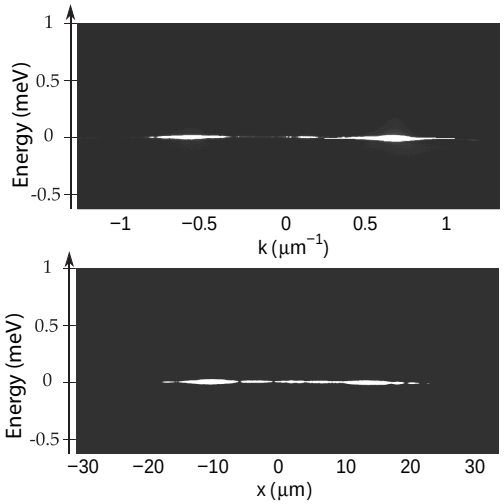

Figure 3.18.: Polariton energy - Experimental polariton energy in real space (down) and k-space (up) in the high density regime. Energies are normalized to the pump energy and the intensity scale is linear and normalized to the peak intensity. The energy does not depend on the fluid position nor on its velocity.

3.3.3. Comparison with related research activities

Very recently, a few other groups headed their research in the direction of multi-pumping in polaritons [140, 141]. In particular, a very similar non-resonant setup was implemented by G. Tosi *et al.* [136] and P. Cristofolini *et al* [140] in Pr. Baumberg's group, at the University of Cambridge. In this scheme, several polariton condensates are created at different places on the sample by several pumping spots. The equidistant spots are placed so as to outline a closed area. They form a triangle, a square, a hexagon, ... depending on their number. Their sample possess 12 quantum wells and the condensates are spontaneously formed from the far out-of-resonance pumping. In [136] the exciton population can be neglected and the reported result is the interference-locked V-AV lattice that we also observe in the linear regime. Quite remarkably, when the exciton reservoir is important [140] they observe, depending on the pumps distance, a regime in which a single condensate forms at the system center only. This result is presented in figure 3.19. If the pumps are further apart each creates a local condensate that, due to polaritons expelled from the pump by the local exciton reservoir, creates interferences between the pump spots.

9. This will be discussed at the end of the chapter.

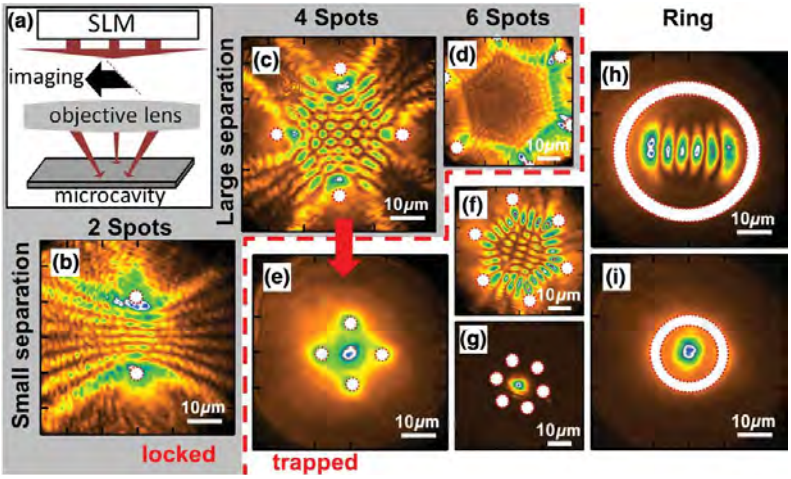

Figure 3.19.: Transition from locked to trapped condensates. – (a) Setup with SLM imaging multiple pump spots onto the microcavity sample. (b)-(i) Spatial images showing condensates formed from pump spots (red dashed line) at decreasing lateral separation (top to bottom), focused onto the semiconductor microcavity. Phase-locking ((b)-(d), regime III, grey background) switches to trapped ((e)-(i), regime II) condensates. Extracted from [140].

While these very interesting results seem similar to ours, the interpretation of the vanishing interference is that, for a small enough multi-pump traps, only the lowest energy spatial mode can be excited, and therefore their observation is the result of confinement. Indeed, the setup being non-resonant, a large exciton population acts like an external trapping potential independently from the polariton density.

Our results are singularly different. Indeed, let us note that, since we pump resonantly the exciton population is negligible. Therefore any trapping is due to polariton-polariton interactions only. As testified by figures 3.15 and 3.18 in the high density regime the polariton density (and thus the energy) is nearly constant. Therefore in the high density regime when the superfluids merge, no trapping is present. Additionally, if we make the hypothesis that the polaritons behave ballistically (locally parabolic dispersion curve), in the presence of a central trapping they would accelerate. On the opposite we observe a deceleration of polaritons approaching the center. This further indicates the absence of a trapping, and the likely non-parabolic nature of the strongly interacting polariton dispersion curve. Moreover, in the work by P. Cristofolini the non-resonant pumping implies that polaritons condensate at $\boldsymbol{k} = 0$. They are then isotropically expelled by polariton-exciton repulsion while in our setup we specifically inject polaritons with a given velocity towards the center. Therefore in our setup the polariton flow is of crucial importance for the V-AV annihilation while it is secondary (behind the exciton population trapping) in [140]. Finally, in our case the merging effect appears above a density threshold,

without modification of the geometry.
We conclude that while looking very similar, the two experiments and the two effects are in fact different. One is the spontaneous formation of a single condensate from multi-pumping due to geometrical trapping, while the other is the merging of several resonantly pumped superfluids due to polariton nonlinearities, without trapping.

3.3.4. Theoretical work

To further refine our comprehension of the reduction of V-A pairs and the interference disappearance, a numerical model was developed by Emiliano Cancellieri, at the time a postdoc in our group. The simulations show that V-AV pairs [10] disappear by the merging of a vortex with an antivortex rather than by escaping the system. It appear that increasing the polariton density on the edges of the system modifies the polariton flow surrounding the V-AV pairs. This in turn pushes them toward one another, until they merge and disappear. Thus by increasing the density, vortices and antivortices are pushed together in a small regions that, when small enough, gives the V-AV pairs the opportunity to annihilate. The draft presented below describes this phenomenon in detail.

10. Let us be reminded that here "pairs" is to be taken as the presence of a vortex and a nearby antivortex, they do not necessarily form a bound state.

Merging of vortices and antivortices in polariton superfluids

E. Cancellieri,[1,2] R. Hivet,[1] T. Boulier,[1] D. Ballarini,[3,4] D. Sanvitto,[3,4]
M. H. Szymanska,[5] C. Ciuti,[6] E. Giacobino,[1] and A. Bramati[1]

[1]*Laboratoire Kastler Brossel, Université Pierre et Marie Curie, Ecole Normale Supérieure et CNRS, UPMC case 74, 4 place Jussieu, 75005 Paris, France*
[2]*Department of Physics and Astronomy, University of Sheffield, Sheffield, S3 7RH, United Kingdom*
[3]*NNL, Istituto Nanoscienze - CNR, Via Arnesano, 73100 Lecce, Italy*
[4]*CNB@UniLe, Istituto Italiano di Tecnologia, via Barsanti, 73100 Arnesano (Lecce), Italy*
[5]*Department of Physics and Astronomy, University College London, Gower Street, London, WC1E 6BT, UK*
[6]*Laboratoire Matériaux et Phénoménes Quantiques, UMR 7162, Université Paris Diderot-Paris 7 et CNRS, 75013 Paris, France*

Quantised vortices are remarkable manifestations on a macroscopic scale of the coherent nature of quantum fluids, and the study of their properties is of fundamental importance for the understanding of this peculiar state of matter. Cavity-polaritons, due to their double light-matter nature, offer a unique controllable environment to investigate these properties. In this work we theoretically investigate the possibility to deterministically achieve the annihilation of a vortex with an antivortex through the increase of the polariton density in the region surrounding the vortices. Moreover we demonstrate that by means of this mechanism an array of vortex-antivortex pairs can be completely washed out.

PACS numbers: 03.75.Lm, 42.65.Hw, 71.36.+c

I. INTRODUCTION

Topological excitations such as quantised vortices, characterised by a phase winding from 0 to $2\pi m$ (with m an integer number) around a vortex core, have been extensively studied in several systems such as non-linear optical systems[1], superconductors[2], superfluid ^{4}He[3], vertical-cavity surface-emitting lasers[4], and more recently in cold atoms[5–7]. Finally, in recent years, the study of vortices and vortex lattices has attracted much attention also in the field of coherent cavity-polariton fluids. First because, being intrinsically out-of-equilibrium, they constitute a novel system to study Bose-Einstein condensation phenomena, and secondly because, due to their light-matter nature, polaritonic systems are fully controllable by optical techniques and therefore allow very detailed studies of quantum turbulence.

In particular, in the context of cavity-polariton systems, it has been shown that stable vortices and half-vortices[8–10], as well as single vortex-antivortex (V-AV) pairs[11–14] can be generated. The formation of lattices of vortices and of vortex-antivortex pairs has also been theoretically and experimentally studied in several different configurations: in the optical parametrical oscillator configuration[15], in non-resonantly generated condensates[16–18], and in the case of patterns induced by metallic deposition on the surface of the cavity[19]. However, the mechanisms lying beneath vortex-antivortex annihilation and vortex-vortex interaction are still not fully understood. This is related to the high degree of control needed to study such interactions.

For example, in the first experimental observations of vortex-antivortex lattices[17–19] the formation and the properties of the array were only partially controllable due to either the presence of a strong exciton reservoir, that influences the position of the formed vortex array and its disappearance, or due to the fact that the formed array depends on the structure of the metallic depositions over the cavity surface. To achieve a higher degree of control resonant pumping schemes have been proposed[20]. By using masks in the pumping beam, the formation of vortex-antivortex arrays with controllable shape and vortex distribution was achieved[21] and the evolution of the arrays was studied in correlation with the local onset of the superfluid regime. However, in this study the case of high polariton densities was not experimentally achievable since the masks used to generate the vortex array were blocking most of the laser power, and therefore was not theoretically investigated.

In this work we theoretically study the annihilation of a vortex with an antivortex when injecting polaritons resonantly, in a broad range of polariton densities. In our model we assume an excitation with four coherent laser beams resonant with the lower polariton branch similarly to[17] and[18] where, however, polaritons were injected non-resonantly. The four pump spots are supposed to have the same energy and k-vector modulus and to generate polaritons propagating toward the centre of a common area. The advantage of our model is that in the resonant configuration it is well known that there is no exciton reservoir and that, since the entire pump intensity is used to inject the coherent fluid, high polariton densities can be achieved. Moreover, since the pumps set the momentum and the density of the injected fluid we can directly correlate the vortex-antivortex annihilation and the washing out of an array of vortices with the increase of the regions where the fluid is subsonic and with the change in the polariton flow that comes with it.

The manuscript is structured as follows: In Sec. II we introduce the theoretical model used to simulate the sys-

tem, describe more in details the setup we have in mind and introduce the *generalized local speed of sound* that will be needed for the analysis of the results. In Sec. III we demonstrate the annihilation of V-AV pairs and correlate this annihilation with the change in the polariton flow caused by the widening of the regions where the fluid is subsonic. Finally in In Sec. IV we draw some conclusions and give prospects for future developments of the work.

II. MODEL

A standard way to model the dynamics of resonantly-driven polaritons in a planar microcavity is to use a Gross-Pitaevskii (GP) equation[22] for coupled cavity and exciton fields (Ψ_C and Ψ_X) generalized to include the effects of the resonant pumping and decay ($\hbar = 1$):

$$\partial_t \begin{pmatrix} \Psi_X \\ \Psi_C \end{pmatrix} = \begin{pmatrix} 0 \\ F \end{pmatrix} + \left[H_0 + \begin{pmatrix} g_X |\Psi_X|^2 & 0 \\ 0 & V_C \end{pmatrix} \right] \begin{pmatrix} \Psi_X \\ \Psi_C \end{pmatrix},$$

where the single particle polariton Hamiltonian H_0 is given by

$$H_0 = \begin{pmatrix} \omega_X - i\kappa_X/2 & \Omega_R/2 \\ \Omega_R/2 & \omega_C\left(-i\nabla\right) - i\kappa_C/2 \end{pmatrix},$$

and

$$\omega_C\left(-i\nabla\right) = \omega_C(0) - \frac{\nabla^2}{2m_c}$$

is the cavity dispersion, with the photon mass $m_C = 5 \times 10^{-5} m_0$ and m_0 the bare electron mass. For our simulations we assumed a flat exciton dispersion relation $\omega_X(\mathbf{k}) = \omega_X(0)$, set the exciton-photon detuning to zero $\delta_{ex-ph} = \omega_X(0) - \omega_C(0) = 0$ and set this energy value as the reference of the zero energy. The parameters Ω_R, κ_X and κ_C are the Rabi frequency and the excitonic and photonic decay rates respectively and have been given values close to the usual experimental ones: $\Omega_R = 5.1$ meV, $\kappa_X = 0.05$ meV, and $\kappa_C = 0.08$ meV[21]. In this model polaritons are injected into the cavity by four coherent and monochromatic laser fields with pump intensity f_p and Gaussian spatial profiles with σ_p of 20 μm: $F(\mathbf{x}) = \sum_{i=1}^{4} f_p e^{i\mathbf{k_{p_i}}\mathbf{x}} e^{-(\mathbf{x}-\mathbf{x_i})^2/2\sigma_p^2}$. Where $\mathbf{k_{p_i}}$ are the four wave vectors of the four pumps that we fix to have the same modulus $|\mathbf{k_{p_i}}| = |\mathbf{k}|$. In order to ensure that the phase of the polariton fluid is not imposed by the laser pumps in the central region of the system we set to zero the pump intensity outside of a $\sigma_{pin} = 9\mu$m radius circle. The exciton-exciton interaction strength g_X is set to one by rescaling both the cavity and excitonic fields and the pump intensities. The numerical solution of the GP equation is obtained over a two-dimensional grid (of 512×512 points) in a box with sides of 150×150 μm^2 using a fifth-order adaptive-step Runge-Kutta algorithm. All the analysed quantities are taken when the system has reached a steady state condition after a transient period of 200 ps.

To understand the role of the subsonic character of the fluid in the annihilation of a vortex-antivortex pair we define the local fluid velocity $v_f(\mathbf{x}) = \hbar|\mathbf{k}(\mathbf{x})|/m_{LP}$, where m_{LP} is the lower polariton mass and $\mathbf{k}(\mathbf{x})$ is the locally evaluated derivative of the phase at the point $\mathbf{x}$. Moreover we define the quantity $c_s(\mathbf{x}) = \sqrt{\hbar g_{LP}|\Psi_{LP}(\mathbf{x})|^2/m_{LP}}$, where $|\Psi_{LP}(\mathbf{x})|^2$ and g_{LP} are the local polariton density and the coupling constant. Since in the local density approximation $c_s(\mathbf{x})$ corresponds to the speed of sound defined in the case of high densities[23,24], we can take it as definition of a *generalized local speed of sound* valid also for low polariton densities and we define a generalized Mach number:

$$M(\mathbf{x}) = \frac{v_f(\mathbf{x})}{c_s(\mathbf{x})} = \frac{\hbar|k(\mathbf{x})|/m_{LP}}{\sqrt{\hbar g_{LP}|\Psi_{LP}(\mathbf{x})|^2/m_{LP}}}. \quad (1)$$

This will allow to establish a direct correlation between the subsonic or supersonic character of the fluid and the annihilation of a V-AV pair. Since the subsonic character of the fluid is induced by polariton-polariton interaction, this corresponds to studying the role of polariton-polariton interactions in the annihilation of the pairs and of the vortex-array. Although other techniques, like the study of the vortex-antivortex correlation function[25] or Reynolds-averaged Navier-Stokes equations[26], can be used to address this problem, we chose to focus on the study of the Mach number since it since it allows a simple and clear physical understanding of the V-AV merging process.

III. RESULTS

The mechanism lying beneath the annihilation of V-AV pairs and the role of polariton-polariton interactions in this annihilation can be better highlighted by studying the system behaviour as a function of the pump intensity and therefore of the polariton density. We start by studying the system in the two limiting cases of very low and very high pump intensities.

In the low intensity case the polariton density lies on the lower branch of the bistability curve everywhere in space and the system behaviour is purely linear. In this regime (fig. 1A-C), the formation of an array of vortices and antivortices is observed as in[17,18,21]. Here, like in[21], the shape and size of the unit cell only depend on the geometry of the pumping configuration and on the angle of incidence of the laser beams. Since we use four pumps with $|\mathbf{k}| = 0.7\mu\text{m}^{-1}$ the formed array has square unit cells with unit cell size of approximately 9μm (fig. 1A-C). This interference pattern generates an array of vortices (with a clockwise phase winding from $-\pi$ to π) and antivortices (with an anti-clockwise phase winding from $-\pi$ to π) that

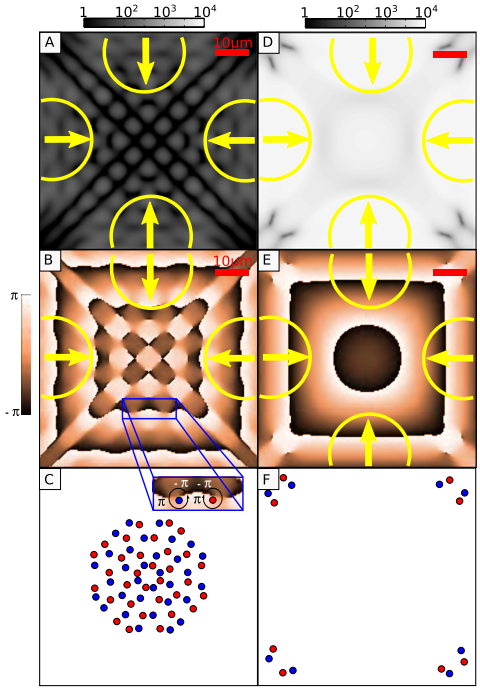

FIG. 1. Numerical Real space emission intensity, phase, and vortex distribution in the low and high density regimes. The four polariton ensembles are generated by pumps at $k_{pump} = 0.7\ \mu\text{m}^{-1}$ in different directions (yellow arrows) with $\omega_{pump} = -2.25$ meV. A: Real space image in the low density regime with pump intensity $f_p = 0.07 f_{th}$, a square interference pattern with a unit cell of about 9μm is formed. D: real space image in the high density regime $f_p = 3.33 f_{th}$. B and E: Phases corresponding to A and D showing an array of vortices and antivortices (B) and no phase modulations (E). C and F: Vortices (red) and anti-vortices (blue) distribution in real space corresponding to phase diagrams B to E.

is therefore due to purely linear mechanism (fig. 1C and inset for the definition of vortices and antivortices).

In the opposite limit the pump intensity is strong and polariton-polariton interactions play a dominant role. This regime is characterised by a polariton density everywhere lying on the upper branch of the bistability curve. As it can be seen in fig. 1D-F, in this regime the array of vortices and antivortices has completely disappeared due to the renormalisation of the lower-polariton branch.

From this, we can deduce that in the transition region between the low and the high density regimes vortices and antivortices either are expelled from the fluid or annihilate each-other. In order to investigate this transition we vary the pump intensity around the threshold value (f_{th}) at which V-AV pairs disappear. Note that in this non-homogeneous system four threshold intensities can be observed: two for increasing and two for decreasing pump intensities. When the intensity of the four pumps increases the regions directly pumped by the lasers jump from the lower to the upper branch of the bistability curve (first threshold). At this point, since polaritons have a finite lifetime, the central region between the four laser spots is still in the lower part of the bistability curve. As the pumps intensity is further increased also the central region eventually jumps from the lower to the upper branch (second threshold). This threshold corresponds to the intensity f_{th} at which V-AV pairs disappear. Similarly one can observe two threshold for decreasing pump intensity.

Figures 2 A-C(D-F) represent the polariton distribution (phase) for increasing pump intensity from just below to just above f_{th}. In fig. 2A ($f_p = 0.66 f_{th}$) some remaining of the interference pattern of fig. 1A is still visible together with four dark segments surrounding the centre of the image that correspond to four V-AV pairs. In this plot of the intensity distribution each V-AV pair looks like a straight dark segment rather than like two separated vortices because the core of the vortex is extremely close to the core of the antivortex. The fact that these four dark segments correspond to V-AV pairs is confirmed by the phase distribution of fig. 2D where the two phase rotations of the vortex and of the antivortex are visible in correspondence of each dark segment of fig. 2A. For the sake of clarity the phase distribution of the V-AV pair delimited by the red square in fig. 2D is also reported enlarged in fig. 2G. When the pump intensity is increased (fig. 2B ($f_p = 0.8 f_{th}$) and fig. 2C ($f_p = 1.0 f_{th}$)) the vortex and the antivortex cores get closer (i.e. the dark segments become shorter) until the four V-AV pairs disappear. For even higher pump intensities the density distribution becomes homogeneous as in fig. 1D. Again this moving closer and merging of the V-AV is confirmed by the corresponding phase distributions (fig. 2D-F), and by the corresponding zoom of the regions delimited by the red squares (fig. 2G-I).

This detailed analysis of the density and phase distributions and of the "on site" annihilation of V-AV pairs shows that the disappearance of the vortex array is not due to the expulsion of the vortices from the fluid. Therefore, the mechanism lying beneath the V-AV annihilation cannot be ascribed to a simple renormalisation of the lower polariton branch. First, the effect of the renormalisation is to decrease the wave vector of the injected polaritons and correspondingly to increase the size of the interference pattern of the array therefore leading to the expulsion of vortices from the fluid rather than the observed merging. Second, it can be seen in fig. 2C that when V-AV annihilation takes place, part of the interference pattern is still visible. Third, vortices and antivortices can exist in a fluid at rest, so the renormalization of the lower polariton branch can not justify *per se* the disappearence of the array.

Moreover, since all the plots show the system steady state for a given pump intensity, the fact that vortices

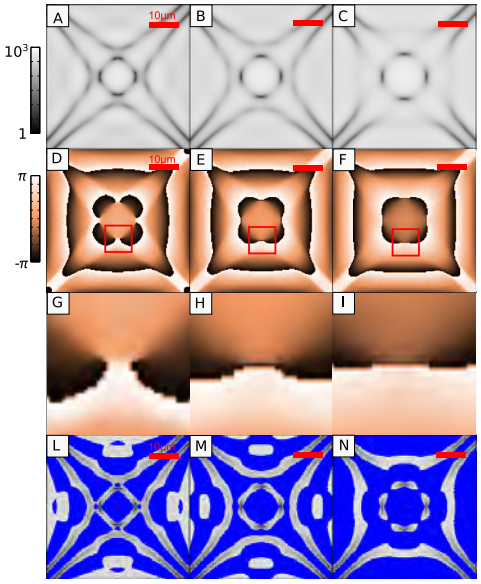

FIG. 2. A-C: Numerical Real-space emission intensity for three different pump intensities. D-F: real space phase-diagrams corresponding to the pumping condition of A-C. G-I: Enlargement of the red squared area in D-F. L-N: Mach charts corresponding to panels A-C, where the fluid is supersonic the Mach chart show the real-space emission intensity at that point, when the fluid is subsonic the Mach chart is blue. A V-AV pair is clearly visible in G, V and AV have almost merged in H, and no vortex pair is present any more in I. The pump parameters are the same as in fig. 1 and the pump intensities (from left to right) are $f_p = 0.66 f_{th}$, $0.8 f_{th}$, $1.0 f_{th}$.

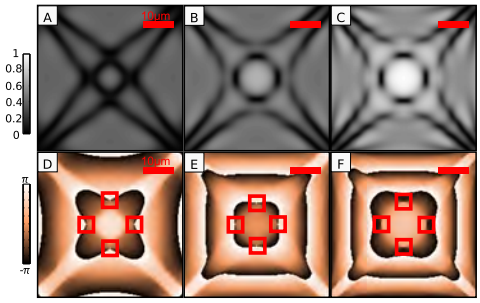

FIG. 3. A-C: Numerical real-space emission intensity (in linear greyscale) . D-F: Real space phase diagram (color scale) corresponding to A-C. The red squares indicate the regions where vortex and anti-vortex pairs have been annihilated. The plots correspond to pumps with increasing in plane momenta from left to right: $k_{pump} = 0.5, 0.7$ and $0.9\ \mu\mathrm{m}^{-1}$. In each case the pump intensity is chosen in order to drive the system at the threshold at which V-AV annihilation occurs ($f_p(B) = 4.33 f_p(A), f_p(C) = 8.66 f_p(A)$).

coexist with antivortices means that their position is the result of a tradeoff between vortex-vortex and vortex-antivortex interactions, direction of the polariton flow, and relative phase of the four pumps. In other words, this means that vortices and antivortices are not completely free to move in the system and therefore V-AV annihilation cannot be simply ascribed to V-AV attraction. In fact, if vortices and antivortices are completely free to move, due to their mutual attraction they must always annihilate, and the only possible steady state must be completely free of vortex dislocations independently from the intensity of the laser pumps. Finally, it is worth noting that due to the choice of the continuous-wave resonant pumping setup no exciton-reservoir is present in the system and all polaritons have the same energy therefore no trapping mechanism can be advocated to explain this annihilation as in[18].

To have a physical insight of the mechanism lying beneath V-AV annihilation it is useful to study the Mach-number charts in fig. 2L-N where blue regions correspond to a subsonic character of the fluid and grey regions correspond to a supersonic character. Clearly as the pump intensity is increased (from left to right) the polariton density increases and the regions where the fluid is subsonic becomes wider and wider. This spreading of the subsonic regions rearranges the polariton flow therefore changing the steady state position of vortices and antivortices until, when the pump threshold f_{th} is reached, vortices and antivortices annihilate. This mechanism can also be understood observing that vortices cannot enter subsonic regions since they are intrinsically related to regions where the fluid is supersonic, because at the centre of their core the fluid density vanishes while the fluid velocity does not and because a subsonic fluid tends to avoid strong phase modulations[27]. Since in our system the subsonic regions surround the V-AV distribution, when the pump intensity changes the polariton flows rearrange letting vortices overlap and annihilate with antivortices. This is different from the case of atomic Bose condensates where a single vortex cannot be destroyed by the superfluid character of a quantum fluid since the total angular momentum of the system must be conserved. Here, polariton-polariton interactions can affect the fluid distribution and make a vortex overlap with an antivortex, so that V-AV pairs can be completely suppressed in the fluid.

An additional proof of the correlation between the subsonic character of the fluid and the disappearance of V-AV pairs is given by the fact that higher sound velocities (i.e. higher polariton densities) are needed to destroy the array when polaritons have higher velocities. Figures 3 A-C show the real space distribution of the photonic field for three different increasing velocities of the injected polaritons ($k_{pump} = 0.5, 0.7$ and $0.9\ \mu\mathrm{m}^{-1}$) and a pump intensity corresponding to the threshold ($f_p = f_{th}$)

where V-AV pairs disappear. We find that the polariton density, and therefore the sound velocity, at which V-AV pairs annihilate is higher when the velocity of the injected polaritons is higher (see fig. 3 D-F where no phase cut corresponding to a V-AV pair can be observed in the four regions delimited by the red squares). This confirms that polariton-polariton interactions, causing the widening of the subsonic regions and the consequent rearrangement of the polariton flows, induce the disappearance of V-AV pairs.

IV. CONCLUSIONS

We have investigated the washing out of vortex-antivortex lattices in exciton polariton systems as a function of the polariton density. Our detailed analysis shows that V-AV annihilation and the washing out of the vortex lattice is due to polariton-polariton interactions that, through the renormalization of the lower polariton branch, induce the widening of the regions where the fluid is subsonic as the pump intensity is increased. This widening induce a modification in the polariton flows therefore changing the steady state position of vortices and antivortices until a threshold pump intensity is reached at which V-AV merging takes place. The complete washing out of the V-AV array can take place because in our system has the number of vortices is equal to the number of antivortices, i.e. the system has zero angular momentum. Our analysis applied to a system with net angular momentum could open the way to the study of vortex-vortex interactions.

ACKNOWLEDGMENTS

We would like to thank C. Tejedor for the use of the computational facilities of the Universidad Autonoma de Madrid and I. Carusotto and F. M. Marchetti for useful discussions. This work has been partially funded by the Quandyde project of the ANR France, by the POLATOM ESF Research Network Program and by the CLERMONT4 Network Progam. MHS from the EPSRC (grants EP/I028900/2 and EP/K003623/2). A. B. is member of Institut Universitaire de France (IUF).

[1] A. S. Desyatnikov, Y. S. Kivshar, and L. Torner, "Optical vortices and vortex solitons," in *Progress in Optics* (E. Wolf, ed.), vol. 47, pp. 291–391, Elsevier, Amsterdam, 2005.

[2] U. Essmann and H. Träuble, "The direct observation of individual flux lines in type II superconductors," *Physics Letters A*, vol. 24, pp. 526–527, May 1967.

[3] E. J. Yarmchuk, M. J. V. Gordon, and R. E. Packard, "Observation of stationary vortex arrays in rotating superfluid helium," *Physical Review Letters*, vol. 43, pp. 214–217, July 1979.

[4] J. Scheuer and M. Orenstein, "Optical vortices crystals: Spontaneous generation in nonlinear semiconductor microcavities," *Science*, vol. 285, pp. 230–233, Sept. 1999.

[5] K. W. Madison, F. Chevy, W. Wohlleben, and J. Dalibard, "Vortex formation in a stirred bose-einstein condensate," *Physical Review Letters*, vol. 84, pp. 806–809, Jan. 2000.

[6] J. Denschlag, J. E. Simsarian, D. L. Feder, C. W. Clark, L. A. Collins, J. Cubizolles, L. Deng, E. W. Hagley, K. Helmerson, W. P. Reinhardt, S. L. Rolston, B. I. Schneider, and W. D. Phillips, "Generating solitons by phase engineering of a bose-einstein condensate," *Science*, vol. 287, pp. 97–101, July 2000.

[7] L. Khaykovich, F. Schreck, G. Ferrari, T. Bourdel, J. Cubizolles, L. D. Carr, Y. Castin, and C. Salomon, "Formation of a matter-wave bright soliton," *Science*, vol. 296, pp. 1290–1293, May 2002.

[8] K. G. Lagoudakis, M. Wouters, M. Richard, A. Baas, I. Carusotto, R. André, L. S. Dang, and B. Deveaud-Plédran, "Quantized vortices in an exciton-polariton condensate," *Nature Physics*, vol. 4, pp. 706–710, Sept. 2008.

[9] K. G. Lagoudakis, T. Ostatnický, A. V. Kavokin, Y. G. Rubo, R. André, and B. Deveaud-Plédran, "Observation of half-quantum vortices in an exciton-polariton condensate," *Science*, vol. 326, pp. 974–976, Nov. 2009. PMID: 19965506.

[10] H. Flayac, I. A. Shelykh, D. D. Solnyshkov, and G. Malpuech, "Topological stability of the half-vortices in spinor exciton-polariton condensates," *Physical Review B*, vol. 81, p. 045318, Jan. 2010.

[11] G. Roumpos, M. D. Fraser, A. Löffler, S. Höfling, A. Forchel, and Y. Yamamoto, "Single vortex-antivortex pair in an exciton-polariton condensate," *Nature Physics*, vol. 7, pp. 129–133, Feb. 2011.

[12] G. Nardin, G. Grosso, Y. Léger, B. Pięt̨ka, F. Morier-Genoud, and B. Deveaud-Plédran, "Hydrodynamic nucleation of quantized vortex pairs in a polariton quantum fluid," *Nature Physics*, vol. 7, pp. 635–641, Aug. 2011.

[13] G. Tosi, F. M. Marchetti, D. Sanvitto, C. Antón, M. H. Szymanska, A. Berceanu, C. Tejedor, L. Marrucci, A. Lemaître, J. Bloch, and L. Viña, "Onset and dynamics of vortex-antivortex pairs in polariton optical parametric oscillator superfluids," *Physical Review Letters*, vol. 107, p. 036401, July 2011.

[14] D. Sanvitto, S. Pigeon, A. Amo, D. Ballarini, M. D. Giorgi, I. Carusotto, R. Hivet, F. Pisanello, V. G. Sala, P. S. S. Guimaraes, R. Houdré, E. Giacobino, C. Ciuti, A. Bramati, and G. Gigli, "All-optical control of the quantum flow of a polariton condensate," *Nature Photonics*, vol. 5, no. 10, pp. 610–614, 2011.

[15] A. V. Gorbach, R. Hartley, and D. V. Skryabin, "Vortex lattices in coherently pumped polariton microcavities," *Physical Review Letters*, vol. 104, p. 213903, May 2010.

[16] J. Keeling and N. G. Berloff, "Spontaneous rotating vortex lattices in a pumped decaying condensate," *Physical Review Letters*, vol. 100, p. 250401, June 2008.

[17] G. Tosi, G. Christmann, N. G. Berloff, P. Tsotsis, T. Gao, Z. Hatzopoulos, P. G. Savvidis, and J. J. Baumberg, "Ge-

ometrically locked vortex lattices in semiconductor quantum fluids," *Nature Communications*, vol. 3, p. 1243, Dec. 2012.

[18] P. Cristofolini, A. Dreismann, G. Christmann, G. Franchetti, N. G. Berloff, P. Tsotsis, Z. Hatzopoulos, P. G. Savvidis, and J. J. Baumberg, "Optical superfluid phase transitions and trapping of polariton condensates," *Physical Review Letters*, vol. 110, p. 186403, May 2013.

[19] K. Kusudo, N. Y. Kim, A. Loeffler, S. Hoefling, A. Forchel, and Y. Yamamoto, "Stochastic formation of polariton condensates in two degenerate orbital states," *arXiv:1211.3833*, Nov. 2012.

[20] T. C. H. Liew, Y. G. Rubo, and A. V. Kavokin, "Generation and dynamics of vortex lattices in coherent exciton-polariton fields," *Physical Review Letters*, vol. 101, p. 187401, Oct. 2008.

[21] R. Hivet, E. Cancellieri, T. Boulier, D. Ballarini, D. Sanvitto, F. M. Marchetti, M. H. Szymanska, C. Ciuti, E. Giacobino, and A. Bramati, "Interaction-shaped vortex-antivortex lattices in polariton fluids," *Phys. Rev. B*, vol. 89, p. 134501, Apr 2014.

[22] I. Carusotto and C. Ciuti, "Quantum fluids of light," *Reviews of Modern Physics*, vol. 85, pp. 299–366, Feb. 2013.

[23] M. Wouters, I. Carusotto, and C. Ciuti, "Spatial and spectral shape of inhomogeneous nonequilibrium exciton-polariton condensates," *Physical Review B*, vol. 77, p. 115340, Mar. 2008.

[24] C. Ciuti and I. Carusotto, "Quantum fluid effects and parametric instabilities in microcavities," *physica status solidi (b)*, vol. 242, no. 11, pp. 2224–2245, 2005.

[25] F. Liu and G. F. Mazenko, "Defect-defect correlation in the dynamics of first-order phase transitions," *Phys. Rev. B*, vol. 46, pp. 5963–5971, Sep 1992.

[26] R. Osborne, "On the dynamical theory of incompressible viscous fluids and the determination of the criterion," *Philosophical Transactions of the Royal Society of London. A*, vol. 186, pp. 123–164, 1895.

[27] L. D. Landau and E. M. Lifshitz, "chapter 6 : Superfluidity," in *Statistical Physics part 1 (2nd edition)*, Course of Theoretical Physics, Pergamon Press, Oxford, 1986.

Chapter 4.

Angular momentum conservation in polariton superfluids

Since the 4-pumps setup allows to independently control longitudinal and azimuthal angles of the pumps, it is possible for $\varphi \neq 0$ to inject a non-zero angular momentum in the system, unlike the mask setup in section 3.2. In this chapter we keep the same 4-pumps experimental setup as in the previous one and we focus on the $\varphi \neq 0$ case.

4.1. Motivations and Method

Building upon the previous observation of V-AV pair destruction, we now inject a controlled number of vortices of the same sign, without any antivortex. This is a first in polariton physics, where up to now only vortex-antivortex pairs [18, 15, 136, 122, 123], single vortex [135, 134] and $\ell = 2$ vortex [134] where studied. While angular momentum conservation seems natural in closed systems, it is not guaranteed for open systems. Driven-dissipative gases are a class of open systems since there is a strong coupling to the environment through which physical quantities can escape the system. Hence the relevance of the testing of angular momentum conservation in polariton fluids, in addition to its controlled injection and the study of its nucleation in elementary vortices.

We make this study in the steady state regime. Due to the similarities between the equilibrium and the driven-dissipative Gross-Pitaevskii equations under the steady-state condition, we may expect that angular momentum is in effect conserved. Indeed, in this regime the quantities continuously injected by the pumps are exactly compensated by the losses in the system, so that on average the fluid behaves like a closed system. This, however, is a speculation that deserves to be experimentally tested.

4.1.1. Injection method and vortex confinement

The polariton injection method is the same as in the previous chapter, but with $\varphi \neq 0$. See figure 4.1, copied below from 3.3.1.

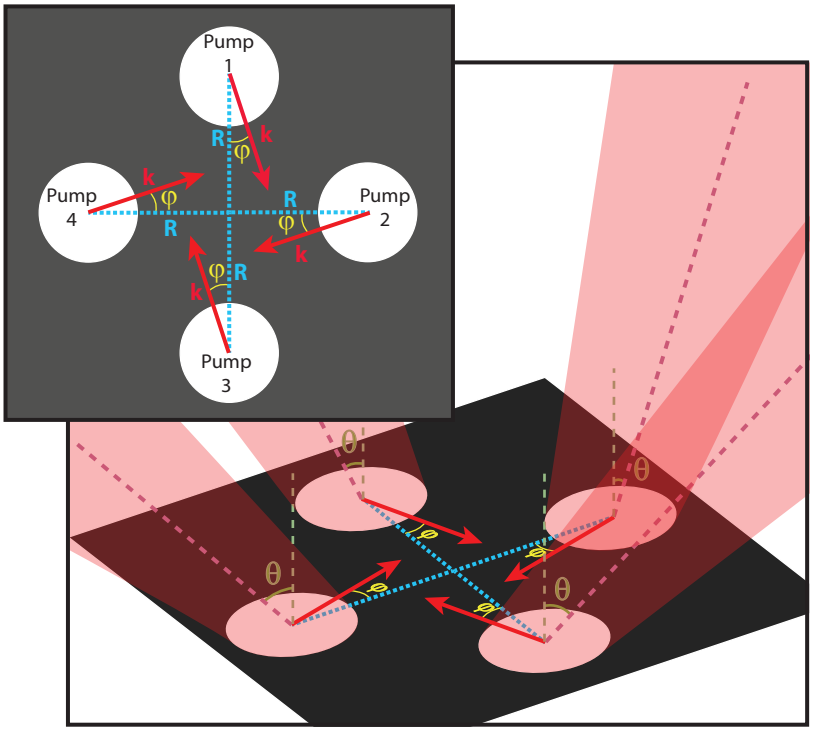

Figure 4.1.: Pumping scheme - Schematic representation of the four pumps arriving on the sample. θ is the incidence angle, on which depends the norm of the polariton wavevector. The in-plane polariton propagation direction is set through the azimuth angle φ. The blue dashed lines show the direction to the center ($\varphi = 0$) while the red arrows show the polariton direction of propagation for $\varphi \neq 0$.

Semiclassical approach

Using a semiclassical approach, we can estimate the angular momentum continuously injected by the pumps. Considering that the pumps form a perfect square and considering a circular trajectory going through their centers:

$$L_{sc} = \mathbf{R} \wedge \mathbf{p} = R\hbar k \sin\varphi = \frac{hR}{\lambda} \sin\theta \sin\varphi, \tag{4.1}$$

where λ is the laser wavelength, $\mathbf{p} = \hbar\mathbf{k}$ is the polariton momentum and R is the average pump distance to the square center ($\mathbf{R}$ is the corresponding position vector). φ and θ are respectively the (in-plane) azimuthal and the incidence pumping angles, as previously defined. Since in quantum mechanics the angular momentum is quantized by steps of $\hbar$

we can evaluate the number of vortices ℓ by:

$$\ell_{sc} = \frac{L_{sc}}{\hbar} = \frac{2\pi R}{\lambda} \sin\theta \sin\varphi = k_{las} R \sin\theta \sin\varphi = Rk \sin\varphi, \tag{4.2}$$

where $k_{las} = \frac{2\pi}{\lambda}$ is the laser wavevector norm and where $k = k_{las} \sin\theta$ is the polariton wavevector norm. Of course, ℓ_{sc} increases continuously with φ while the number of vortices is discrete. This means that ℓ_{sc} is simply a classical estimation of the actual number of vortex in the system.

Phase imprinting approach

There can be another source of angular momentum in this system. Since, like polaritons, the pumps have a phase then it is possible to imprint a winding phase to the polariton fluid by choosing a specific relation between the pumps relative phases. Indeed, if each right (left) neighbor pump has a $+\frac{\pi}{2}$ shift, the four pumps phases will be $\left[0,\ \frac{\pi}{2},\ \pi,\ \frac{3\pi}{2}\right]$ ($\left[2\pi,\ \frac{3\pi}{2},\ \pi,\ \frac{\pi}{2}\right]$) and the phase will wind from 0 to 2π (from 2π to 0) around the system center. We recognize here a characteristic of elementary vortices [1] and deduce that this method should imprint a vortex (antivortex) to the system. We can thus define ℓ_p, the number of 2π phase windings imposed to polaritons by this method. A numerical example of a vortex injected with this method only ($\varphi = \ell_{sc} = 0$, $\ell_p = 1$) is given in figure 4.2. Generally one could imagine using this method to inject more than one vortex. However with only four pumps this method breaks down if we attempt to inject $\ell_p \geq 2$ since, the phases being defined modulo 2π, the imprinted phase winding would amount to 0 (for ℓ_p even) or $\pm 2\pi$ (for ℓ_p odd). This phase degeneracy can be lifted if the number of pump increases, and ℓ_p can reach any value in theory for a continuous (ring-shaped) pump. We will see in the next chapter that this method can be implemented using Laguerre-Gauss modes in the pumping laser.
In the experiment, the length of each of the four arm in figure 3.11 is not controlled, their relative phases are random. This means that in the experiment the special $\pm\left[0,\ \frac{\pi}{2},\ \pi,\ \frac{3\pi}{2}\right]$ phase arrangement is not respected and $\ell_p = 0$. Therefore from now on in this chapter we write $\ell \equiv \ell_{sc}$.

Confinement

For vortices to be observed, polaritons must remain in the pumps square during their lifetime. This is implemented by placing the pumps close enough from each other to confine polaritons. For low and medium densities in the square center, the pumps act

1. see section 2.3

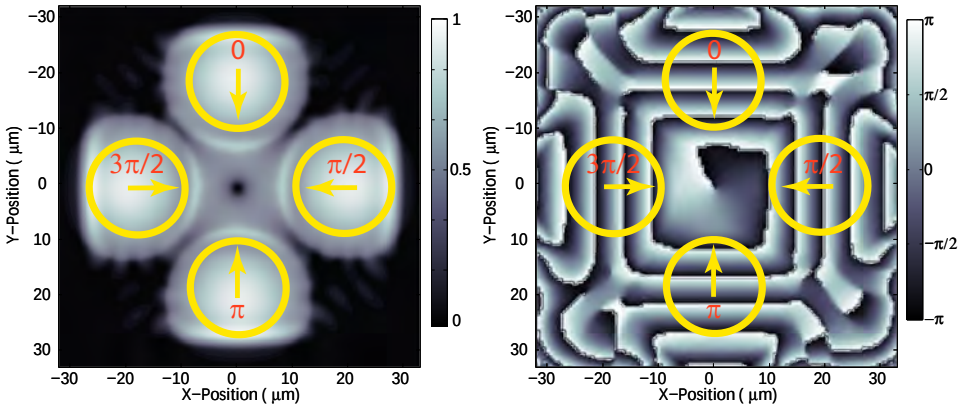

Figure 4.2.: Phase imprinting method - Simulation of a single elementary vortex injected while $\varphi = \ell_{sc} = 0$. The four pumps phases are chosen so that they increase from 0 to 2π, circling around the center, which implies $\ell_p = 1$.

like the square well in section 3.2: the polariton density difference is high between the pumped and the central, non-pumped region. Therefore polariton-polariton repulsion confines the polaritons and the V-AV pairs to the central non-pumped region. In the high density regime, however, it is possible to reach a constant density over the whole system (meaning the density at the center is the same as the density in the pumps). In that case interaction-based polariton confinement is not possible. However, as explained in the previous chapter, in this regime the four superfluids merge and from their phase (figure 3.16) we see the velocity field is radial and converging toward the center. Because of this converging flow polaritons are expected to not escape the system as delimited by the pumps, at least for small angles φ and for the polariton lifetime in our sample.

4.1.2. Limitations

The 4-pumps setup was designed to overcome the power loss present in the mask setup. There are however limitations to the angular momentum one can inject with this scheme. Indeed, for $|\varphi| > \frac{\pi}{4}$ each of the four polariton population propagates outside of the square formed by the pumps (see figure 4.1), meaning that they are not confined anymore and that the density at the center is very low. Similarly, as $|\varphi|$ approaches $\frac{\pi}{4}$ the four polariton populations are directed far from the center and thereby form a lowered density. This density was found not to be sufficient to erase the V-AV pairs in the system for angles $|\varphi| \gtrsim \frac{\pi}{8}$, and we will focus on $0 \leq |\varphi| \leq \frac{\pi}{8}$ in this chapter.

Additionally, a similar limitation arises for the angle of incidence θ. Indeed, as explained in the previous chapter the system needs to remain in the subsonic regime in order to be superfluid and to annihilate the V-AV pairs. For a given density, this means that the polariton wavevector norm, controlled by θ, should remain below a density-dependent

limit from which can be drawn a critical angle θ_C. We defined in (2.28) the local speed of sound $c_s^* = \sqrt{\frac{g\rho}{m_p}}$, where g is the polariton-polariton interaction strength and ρ the local polariton density. Since the polariton speed is $\frac{\hbar k}{m_p} = \frac{h}{\lambda m_p}\sin\theta$ we deduce that locally

$$\theta_C(\rho) = \arcsin\left(\frac{\lambda}{h}\sqrt{g\rho m_p}\right), \tag{4.3}$$

and for the whole system this critical angle can be estimated by taking the minimum density in the central region. In practice ρ depends on many parameters (pump power, δ, φ, system size, polariton lifetime, ...) and it is easier to estimate empirically θ_C. For our sample, with small φ and for pumps separated by about 50 µm, θ_C was found to be of the order of 5°.
If, in the high density regime, θ in increased to $\theta > \theta_C$ an interference pattern similar to the low density regime is recovered. This is illustrated in figure 4.3: for a constant $\varphi = 21°$, the angle of incidence is increased ($\theta = 3.5° < \theta_C$ (top), $\theta = 6.9° > \theta_C$ (middle), $\theta = 8.5° > \theta_C$ (bottom)). This increases ℓ as well as the wavevector of the injected polaritons and, as can be seen on the figure, the number of vortex increases. It is important to notice that the interferences are recovered at the center, and expand over a larger and larger region when $|\boldsymbol{k}|$ is increased. Indeed, because of the polariton decay the speed of sound at the center is reduced and this is where the fluid first becomes supersonic. Increasing the polariton speed then increases the supersonic region. This is why in the presented results we remain in the regime where $\theta < \theta_C$.

To send the four beams along similar trajectories they need to be reflected on different mirrors placed very close to each other. This made impossible to achieve low angles of incidence ($\theta < 2.5°$) without cutting at least one of the beams, strongly reducing its power and generating diffraction on the mirror border.

We saw that the pumps relative phases can influence the number of vortex in the system. Even when not adding or subtracting angular momentum the pumps relative phases were experimentally and numerically observed to directly influence the position of the phase singularities, and thus the vortices positions. Therefore it appears that any vortex lattice geometry is driven by the pumps in this system. While certainly an obstacle to the study of vortex-vortex interactions, let us note that this does not detract the experiment as its primary goal is to show the conservation of angular momentum in a polariton superfluid and the possibility of injecting a controlled number of vortices.

A different setup designed to overcome the present limitations will be introduced in the next chapter.

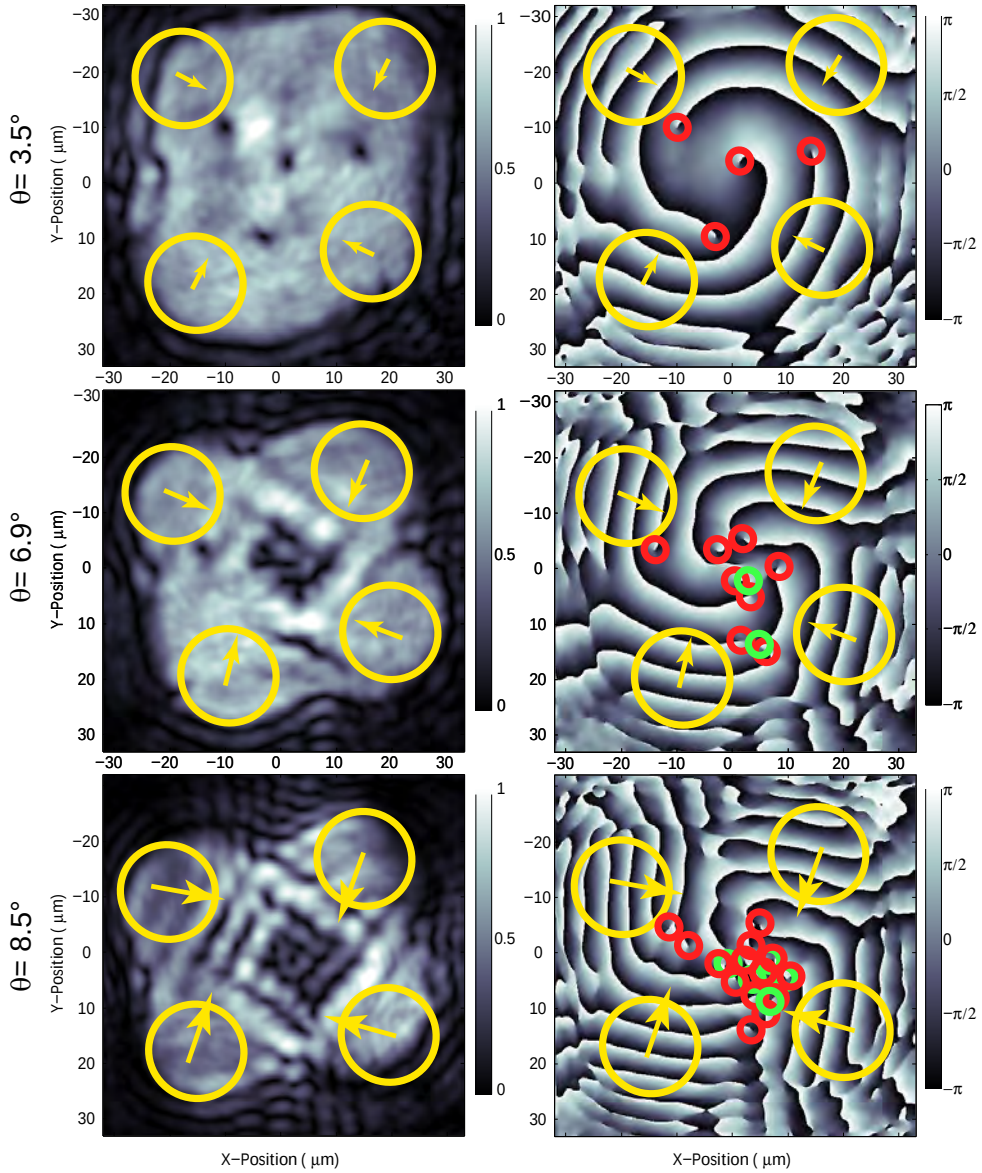

Figure 4.3.: Supersonic regime - Experimental comparison between $\theta = 3.5° < \theta_C$ (top), $\theta = 6.9° > \theta_C$ (middle), $\theta = 8.5° > \theta_C$ (bottom), obtained for $\varphi = 21°$. This corresponds to $|k| = 0.45\ \mu\text{m}^{-1}$ (top), $|k| = 0.9\ \mu\text{m}^{-1}$ (middle), $|k| = 1.1\ \mu\text{m}^{-1}$ (bottom). The intensity is presented on the left while the phase maps are on the right. The top panel has a small angle of incidence that allows the fluids to be subsonic (superfluid): the V-AV pairs as well as the interference vanish and the angular momentum remains, as four vortices. For the two bottom panels the angle of incidence is too high for the fluids to remain in the subsonic (superfluid) regime in the whole central region. An interference-like pattern is then recovered, like what would happen if instead the density were decreased. Here however, the injected angular momentum increases since ℓ increases with $|\boldsymbol{k}|$.

4.2. Results

Within the limitations on the angles θ and φ, we were able to inject angular momenta of quantum number (number of elementary vortex) $\ell = \pm\{0, 1, 2, 3, 4, 5\}$. All measurements were done on a slightly positively detuned area of the sample ($\delta = +0.5\,\text{meV}$) where the disorder is as small as possible. This detuning is a good balance between strong interactions and long propagation distance.

4.2.1. Direction of rotation

Note that we chose the term "vortex" to be relative to the four pumps direction of rotation (equivalently, to the sign of φ): a topological defect whose phase varies from 0 to 2π around a singularity *in the same direction as the pumps rotation* is called a vortex. "Antivortex" refers to a vortex whose phase rotates in a direction opposite to the four pumps. This mean that here the definition of what is a vortex and what is an antivortex is relative on the sign of φ.

This definition comes from the fact that the transformation $\varphi \to -\varphi$ only leads to reversed directions of rotation both for the pumps and the vortices/antivortices: $\varphi \to -\varphi$ acts like a $x \to -x$ mirror symmetry. An example is given in figure 4.4 with $\ell = \pm 1$ in the high density regime. The physics does not change, so that the system is invariant if we define the vortex direction of rotation relative to the sign of φ. This is why in the rest of the chapter the results are presented only for $\varphi > 0$.

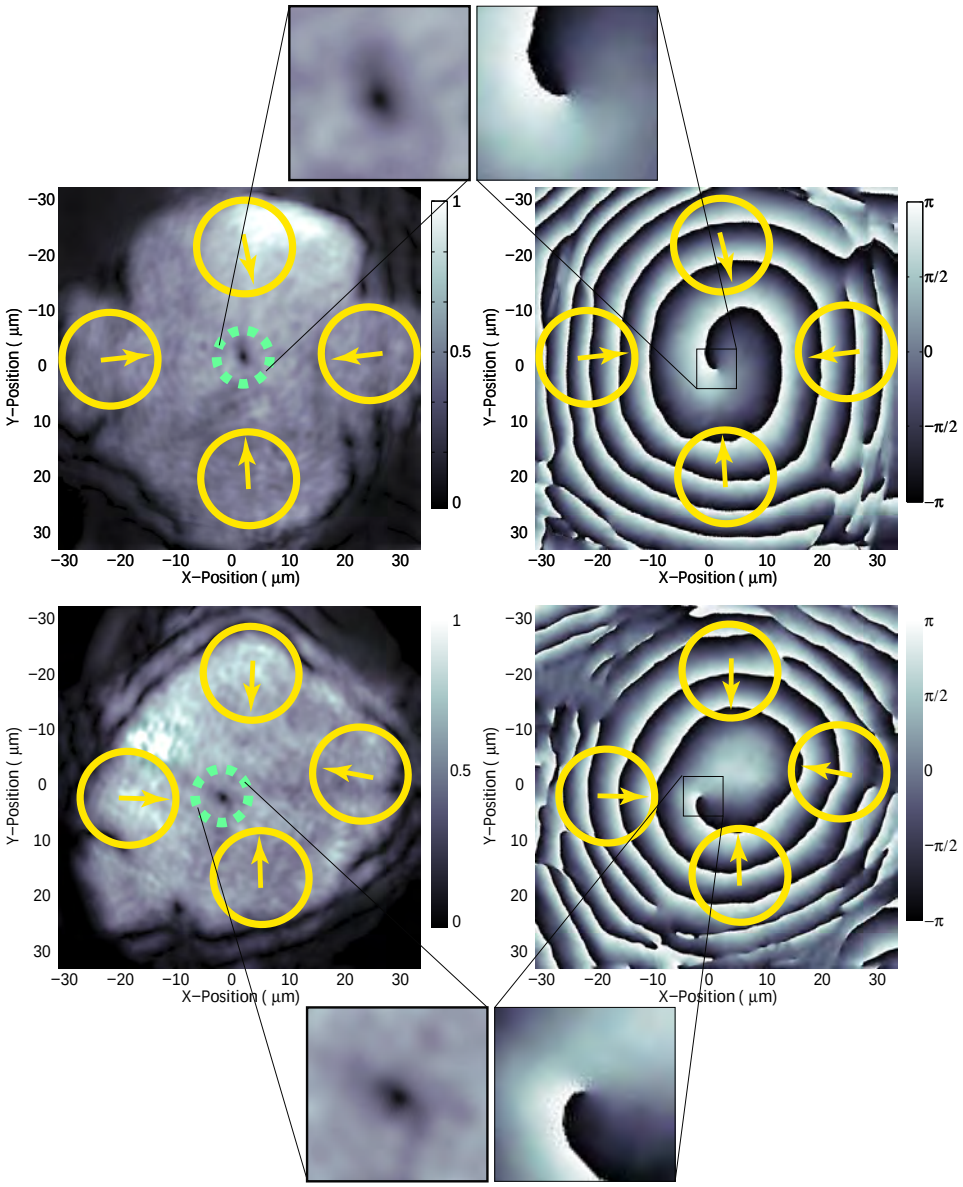

Figure 4.4.: Direction of rotation - Experimental comparison between $\ell = -1$ (up) and $\ell = +1$ (down), obtained for $\varphi = \pm 5.5°$ and $|k| = 0.45\ \mu\text{m}^{-1}$. The intensity is presented on the left while the phase maps are on the right. The pumps directions of rotation are inverted so that the injected angular momenta have different signs. The vortices, each visible as a black dot in the density plots (highlighted by a green dashed circle), turn in opposite directions (notice the opposite phase winding). The physics is unchanged, so that we can restrain the study to just one direction of rotation.

4.2.2. Low density regime

For low densities a square interference pattern is visible since polariton are not in the superfluid regime and interactions are too low to destroy V-AV pairs. The physics is very similar to the $\varphi = 0$ case, with the interference pattern now tilted accordingly to the pumps tilt φ. Moreover the numbers of vortices and antivortices are now unequal and the difference corresponds to the angular momentum expected from (4.2). This shows the conservation of angular momentum in the linear regime. Figure 4.5 gives an example of low density regime for $\varphi = 21°$ and $\varphi = 26°$ for a fixed $\theta \simeq 3.5° < \theta_C$ giving $|k| \simeq 0.45\ \mu\text{m}^{-1}$. This corresponds to $\ell = 4$ and $\ell = 5$.

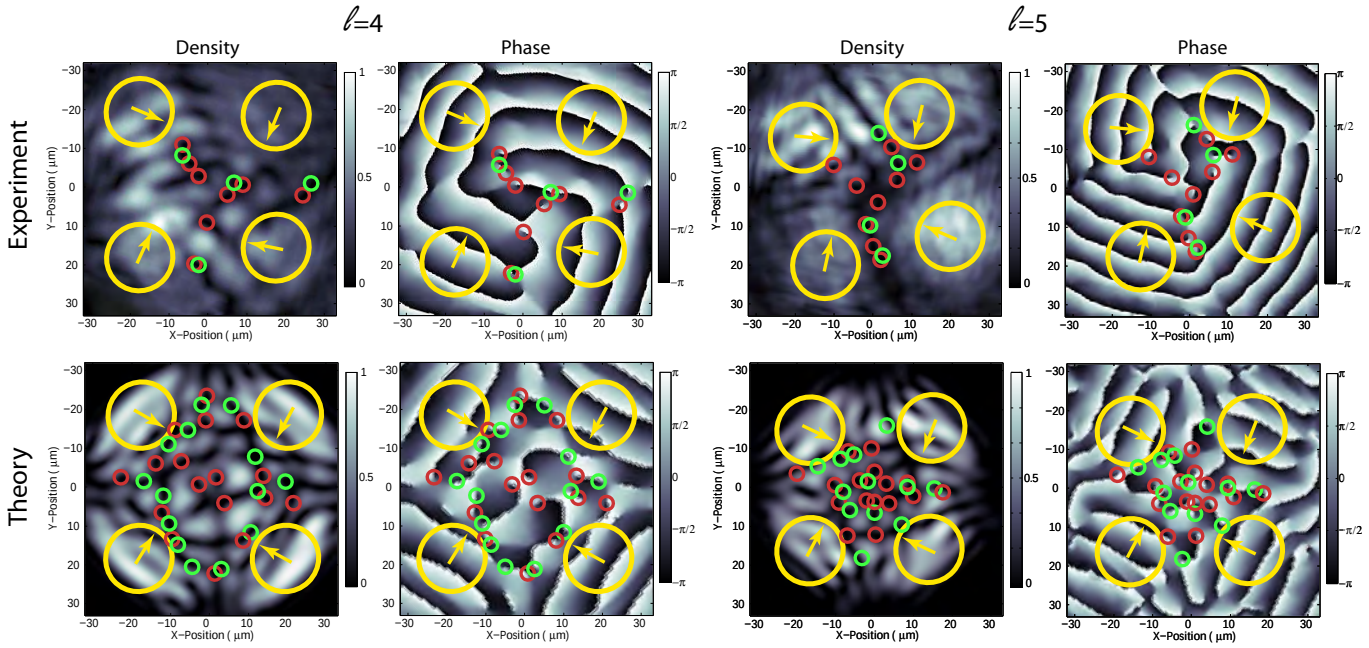

Figure 4.5.: Tilted interference pattern - Experimental and theoretical density map and phase map for $\varphi = 21°$ ($\ell = 4$, up) and for $\varphi = 26°$ ($\ell = 5$, down) in the low density regime. In the same way as in section 3.3, an interference pattern is visible and is accompanied by V-AV pairs. Since the injected angular momentum is not zero the number of vortex (highlighted by red circles) is now different from the number of antivortex (highlighted by green circles). The difference between the two gives the expected value for ℓ.

4.2.3. High density regime

When increasing the density to the point where the four polariton fluids are in the superfluid (and thus subsonic) regime, the interference pattern disappear, in the same way as in section 3.3. Here however a nonzero angular momentum exists which, in virtue of angular momentum conservation, cannot be destroyed. This results in the presence of

elementary vortices of the same sign remaining in the superfluid, where for $\varphi = 0$ there was none.

In such a superfluid regime, the vortex cores are round and well defined in the density. Therefore a healing length can be measured and those vortices are clearly defined in the hydrodynamical sense. This is to be contrasted with the low density regime vortices, where no clear healing length can be measured from the interference pattern. We can distinguish therefore the "optical vortices" present in the linear regime from the "hydrodynamical vortices" present in the nonlinear regime. From our experiment, the crossover can be estimated to happen at the onset of superfluidity in the surroundings of the phase singularity.

Within the tilt angle (φ) limits previously described, up to five vortices were observed without any antivortex. Figure 4.6 exhibits the experimental data for $\varphi \simeq 5.5°$ ($\ell \simeq 1.1$ [2].), $\varphi \simeq 10°$ ($\ell \simeq 2.0$), $\varphi \simeq 15°$ ($\ell \simeq 3.0$), $\varphi \simeq 21°$ ($\ell \simeq 4.0$), for a fixed $\theta \simeq 3.5° < \theta_C$ giving $|k| \simeq 0.45\ \mu\text{m}^{-1}$. As expected the number of vortex increases with φ. We observe that for a high enough density all V-AV pairs annihilate and only vortices are left. The vortices are generally placed at the system center (precisely at the system center if $\ell = 1$), but can drift close to the pumps edge if their number increase. Interestingly, this is even more visible in the simulations, where the vortices appear at the pumps edge whenever $\ell > 1$. No clear explanation for this behavior has been found so far.

A comparison between the observed number of vortex and the value of ℓ computed from the classical approach (4.2) is presented in figure 4.7. The agreement is good within the uncertainty on φ, showing the validity of this simple model.

For all the measurements each vortex has a similar healing length, of about 2 µm. Since the healing length depends on the polariton mean density and since all measurements were done at a constant mean density $\langle\rho\rangle \simeq 200\ \mu\text{m}^{-2}$, the vortex size was indeed bound to be constant.
Once in the high density regime, our setup didn't allow to increase the density much. Therefore the measure of the healing length evolution with the density was not conclusive (too few datapoints).

Since the vortex position is determined by the pumps, it follows that the apparition of a new vortex when increasing φ continuously is not sudden, as one might have expected from the observations made in other systems [79]. Rather, increasing φ continuously makes a new vortex enter the system from the side, between two adjacent pumps. An example is given in figure 4.8 for $\varphi \simeq 24°$ ($\ell \simeq 4.5$) where four vortices are well visible in the central area and a fifth vortex is located on the side (highlighted by a green circle in

2. The $\simeq$ signs denotes that, each pump possessing a finite size in k-space, an uncertainty of about $\pm 5\%$ exists on the measurement of both $|k|$ and φ

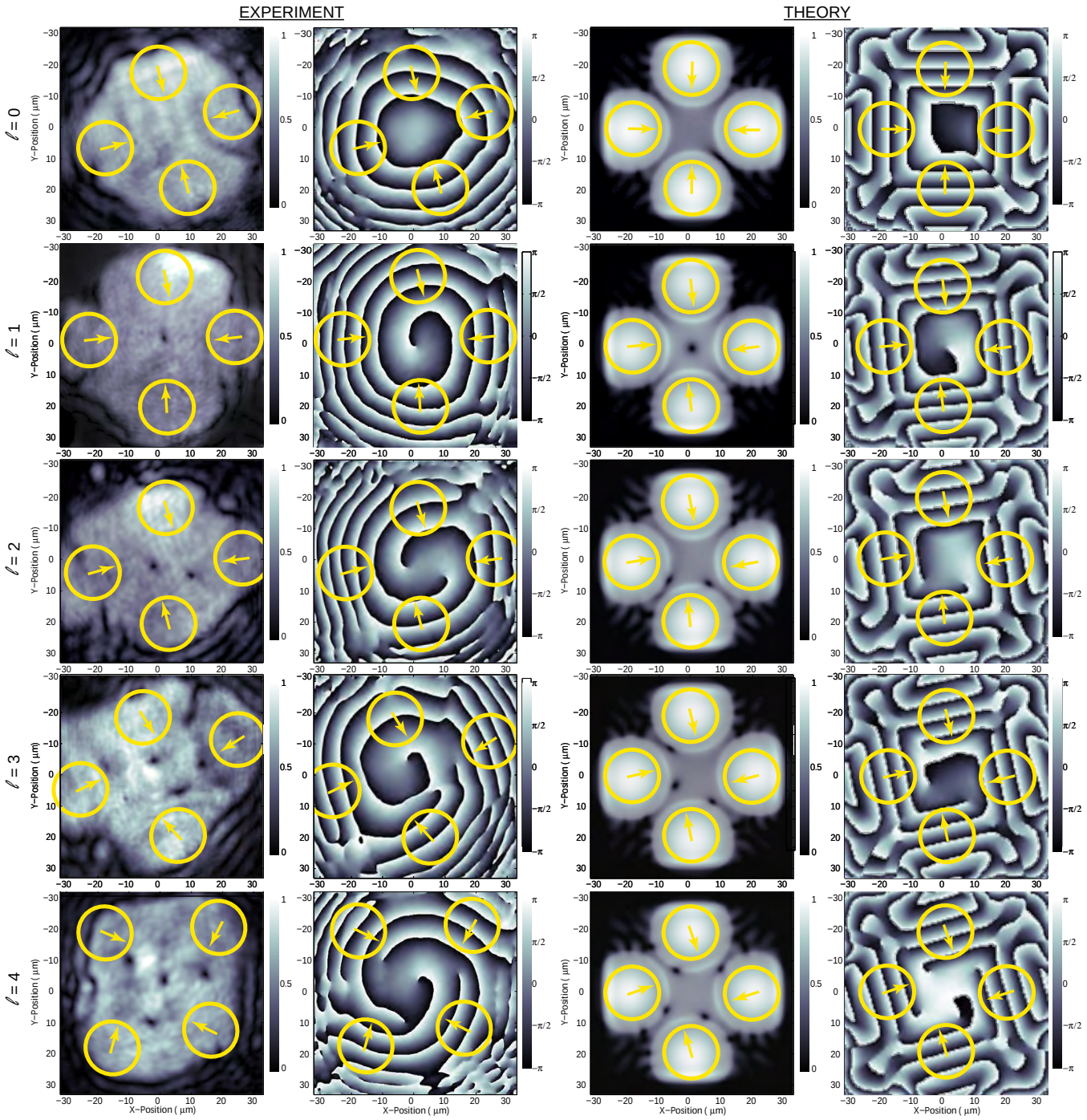

Figure 4.6.: Conserved angular momentum - Experimental and theoretical density and phase maps for $\ell \simeq 0, 1, 2, 3, 4$ (from top to bottom). A number $N = \ell$ of vortices are visible as black dots in the density, each associated with a singularity in the phase. On average $|k| = 0.45\ \mu\text{m}^{-1}$ and (from top to bottom) $\varphi \simeq 0°$, 5.5°, 10°, 15°, 21°.

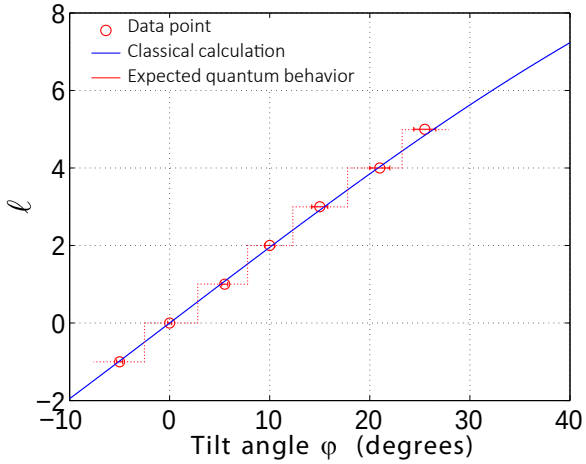

Figure 4.7.: Validity of equation (4.2) - Comparison between the observed number of vortex (red circles) and the value of ℓ computed from the classical approach (4.2) (blue line).

the figure). Increasing ℓ from 4 to 5 makes the fifth vortex approach the square center. This behavior is numerically observed and the vortex position depends on the pumps relative phases, which confirms the vortex position is pump-dependent.

This raises the question of how to count vortices. Indeed the vortex number is defined as counted in some arbitrarily defined area since the discrete nature of the four pumps and their finite size do not provides a natural limit. In the low density areas (figure 4.8) just at the edge of the merged superfluid, many V-AV pairs can be detected in the phase. Since the density is low these pairs are not well-defined in the density map and cannot be considered as physical vortices. Likewise, in the zero-density areas (visible in the corners of the experimental pictures) any vortex detected in the phase map is treated as measurement artifacts. We hence need to define a counting zone that is inside the fluid high density region. The chosen limit is the incircle of the square defined by the pumps centers as schematically delimited by the red circle on figure 4.8.

Similarly to section 3, it is informative to look at the Mach number in presence of vortices. Figure 4.9 is the Mach number map for $\ell = 4$ (same parameters as in the bottom panel of figure 4.6). As expected from the absence of interference pattern, the fluid is subsonic and, except inside the vortices, this plot is very similar to figure 3.16. This shows that the V-AV annihilating process described in section 3.3 is indeed at work here. Note however that polaritons within each vortex (within a healing length around each vortex core) are strongly supersonic. This is because the fluid rotates at high speed around the vortex core while the density is on the contrary decreased within a vortex. At the vortex core the Mach number should diverge and experimental values up to 100 are obtained.

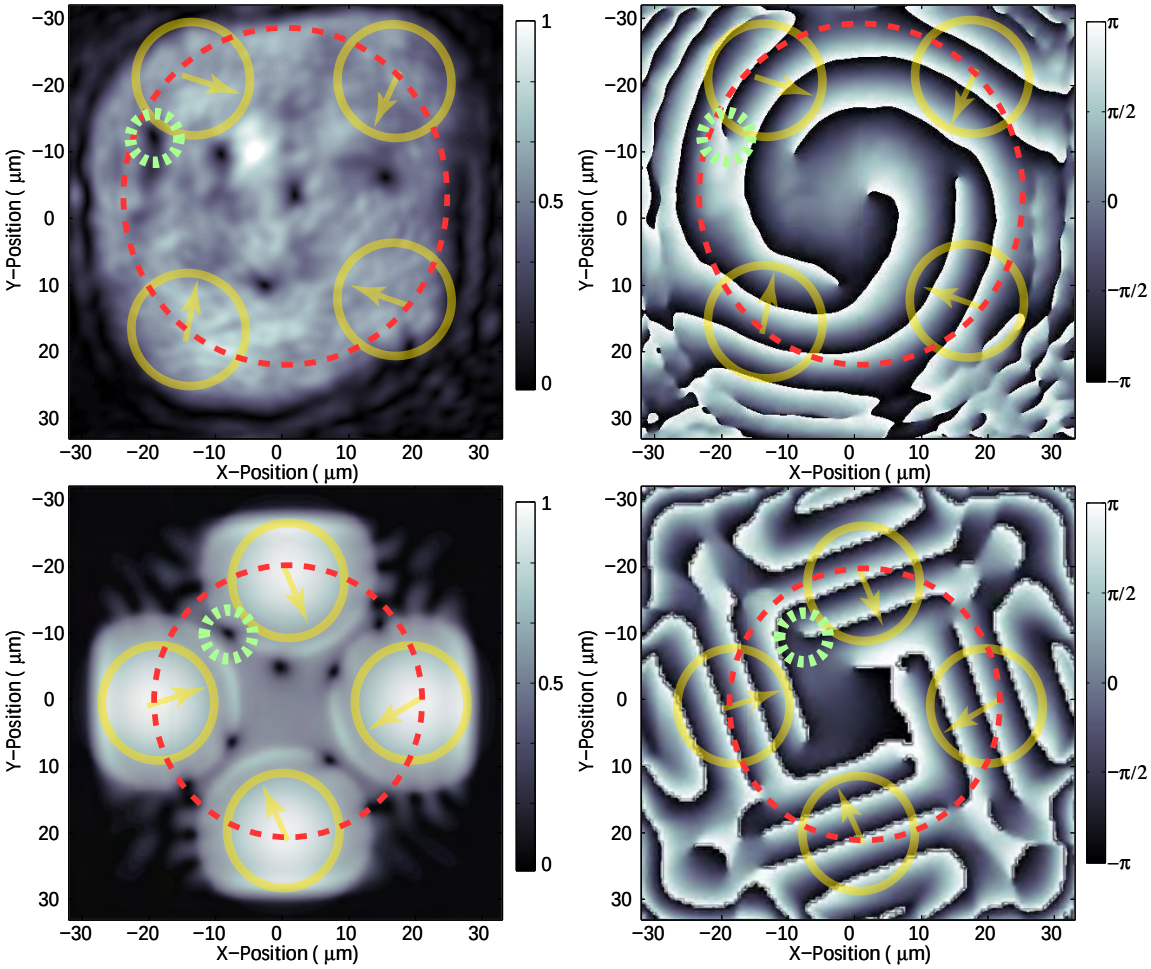

Figure 4.8.: Incoming vortex - Experimental (top) and theoretical (bottom) example of a new vortex entering the system, for $\ell = 4.5$. Four vortices are visible between the pumps (non-highlighted density dip correlated with phase singularities) while a fifth is entering the system (highlighted with a green circle). The red dashed line circle shows the vortex counting zone while each pump is marked by a yellow continuous circle.

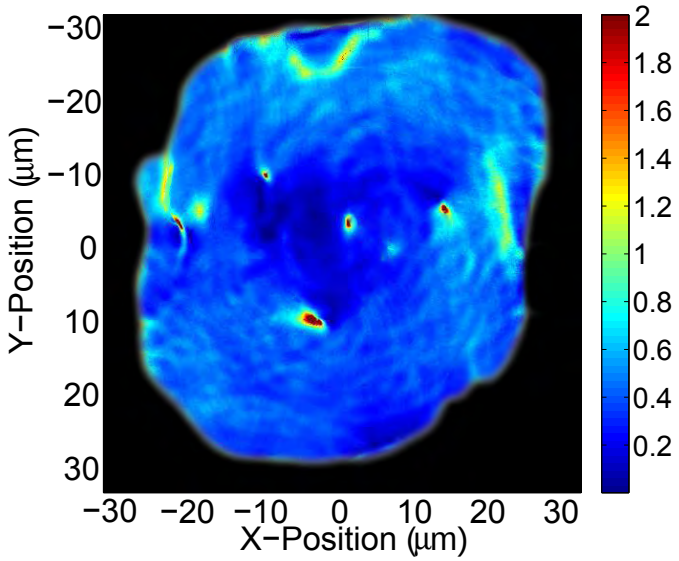

Figure 4.9.: Mach number map - Experimental map of the Mach number for the case of $\ell = 4$. The black zones signify areas outside of the superfluid, where the polariton density is too low for the Mach number to have a clear meaning. As expected from the absence of interference pattern, the fluid is subsonic. However, polaritons within each vortex are strongly supersonic, since they rotate at high speed around the vortex core and because the density is decreased. Note that the Mach number scale is voluntarily limited between 0 and 2 to make it readable; at the vortex core the Mach number should diverge and experimental values up to 100 are obtained.

4.3. Conclusion

As a conclusion we designed a scheme that allows us to inject a controlled angular momentum in a 2D dissipative polariton superfluid. The scheme makes use of four coherent polariton superfluids. While in the linear regime interferences appear and V-AV pairs are clearly visible, the same interference vanishing process as in chapter 3 happens at sufficiently high polariton density. This merged state of the four superfluids results in a single, rotating superfluid. Despite the open nature of the system, in the steady state the angular momentum is conserved. It is dispatched between elementary vortices, a behavior expected from such a quantum fluid. We therefore observed the injection, conservation and nucleation of angular momentum in a quantum superfluid of light.

This scheme is limited in that no more than five vortices of the same sign can be injected at the same time. The setup geometry is not rotational-invariant, and the vortex position depends on each superfluid phase, which suggests the vortex lattice shape is dominated by the geometry of the polariton superflow.

Chapter 5.

Injection of angular momentum: single rotating superfluid

In the previous chapter we saw that the four pumps setting was limited in angular momentum, both in the semiclassical (tilted pumps) approach and the phase imprinting approach. Up to 5 vortices were injected in the system. Moreover the vortex positions was found to strongly depend on the pumps relatives phases, in addition to the polariton-polariton interaction. In this chapter we take further the phase imprinting approach to inject angular momentum with a continuous, circularly symmetric pump possessing a $2\pi\ell$ phase winding.

5.1. Theoretical predictions

In the scientific literature, several theoretical works describe rotating polarion BEC [142, 143, 144]. While none precisely correspond to our quasi-resonant setup their predictions should be readily applicable. Keeling and Berloff in particular theoretically studied [142] a rotating polariton BEC (pumped out of resonance) trapped in a harmonic potential. The result of this numerical simulation is the spontaneous formation of a self-arranged lattice of vortices of the same sign. While the elementary lattice cell is not triangular as in an atomic BEC, the lattice shape is suggested to be driven by vortex-vortex interactions which would make the physics of this system to some degree similar to an Abrikosov type of lattice.

While our setup is different (quasi-resonant, absence of harmonic potential, presence of natural defects, ...), it is possible to design a pumping scheme that both injects a circular-symmetric rotating polariton fluid and traps it in a pump-free zone, where the fluid is able to freely evolve. We will see in the next section that the trap has the geometry of the pump, and is well approximated by a circular potential well. Here again the

quasi-resonant pumping minimizes the exciton reservoir that would interfere with the trapping scheme in an out-of-resonance setup.

An additional prediction to the presence of a vortex lattice is its solid body -like rotation [142, 143]. Its speed is of the order of the polariton propagation speed on the edge of the fluid, which makes a predicted rotation rate of the order of 10 GHz for typical polariton systems. This high rotation speed makes direct time-resolved detection very difficult, and time-averaged detection impossible since there is no steady-state. However indirect signatures of this rotation are predicted to be possible to observe with a time-averaged detection, such as energy sidebands [143, 144] and an apparent loss of coherence in the real space image (blurring due to time-averaging a non-static phase map, where the rotation occurs).
Let us note that this prediction does not take into account the natural cavity disorder. Our simulations shows that this rotation is very sensitive to disorder, and is easily stopped by vortex pinning on natural cavity defects. We will see in section 5.3 that we actually observe such a pinned lattice.

5.2. Experimental setup

The setup for this experiment is very similar to the one in chapter 3. The Ti:Sa laser, the cryogenic setup, the sample, the detection and the density control method are identical. However the pump laser is not divided into four arms anymore but is prepared into a Laguerre-Gaussian mode before pumping the cavity. An overview of this new setup is given in figure 5.1 and a more detailed description of the pump preparation is given thereafter.

5.2.1. Laguerre-Gauss beam preparation

At the heart of this experimental setup lays the Laguerre-Gaussian (LG) mode used to pump the sample. Here we describe what is such a mode, how we create it using a Spatial Light Modulator (SLM) and what is the resulting pump as received by the sample.

Mathematical description

Laguerre-Gauss beams are a class of cylindrical-invariant modes possessing a simple phase profile. The phase profile of a collimated LG beam possess a radial invariance: $\theta_{LG}(r,\phi) = \theta_{LG}(\phi)$ if $(r, \phi \in [0, 2\pi])$ are the polar coordinates in the plane orthogonal to

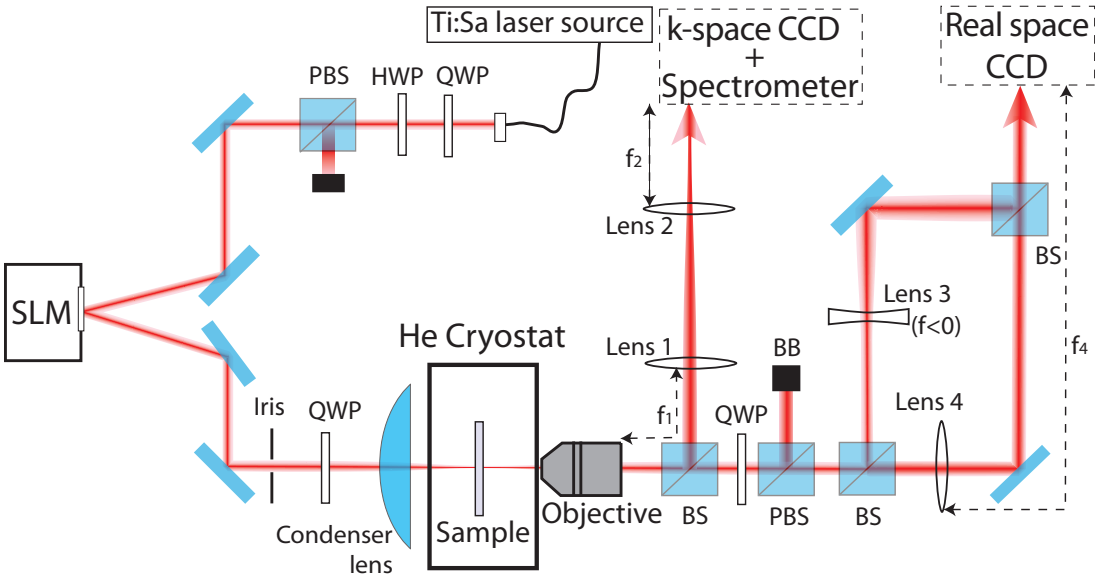

Figure 5.1.: Setup – Experimental setup scheme. The pumps are prepared with a pure-phase Spatial Light Modulator (SLM) and sent on the sample. The sample emission is collected and treated for detection in real space, momentum space and energy.

the propagation direction. The complex expression for the amplitude of a LG mode is:

$$LG_p^\ell(r,\phi,z) = \frac{C}{w_0}\left(\frac{r}{w_0}\right)^{|l|} e^{\frac{-r^2}{w_0^2}} e^{i\ell\phi} L_p^\ell\left(\frac{2r^2}{w_0^2}\right), \tag{5.1}$$

where ℓ and p respectively are the azimuthal and radial indexes, w_0 is the beam waist diameter parameter, C is a normalization constant and $L_p^\ell(x)$ is the generalized Laguerre polynomial. We see the phase is indeed radial-invariant and simply:

$$\theta_{LG_p^\ell}(\phi) = e^{i\ell\phi}, \tag{5.2}$$

so that ℓ corresponds to the angular momentum carried by the beam. The $r^{|\ell|}e^{\frac{-r^2}{w_0^2}}$ term ensures a ring shape to the intensity profile and the parameter p, only used in the Laguerre polynomial, is essentially the number of secondary rings. Examples of the first LG_p^ℓ beam intensity profiles are given in figure 5.2. It is worth noting that for $p = 0$ the Laguerre polynomial reduces to a constant so that a collimated LG_0^ℓ beam simplifies to :

$$LG_0^\ell(r,\phi,z) = A\left(\frac{r}{w_0}\right)^{|l|} e^{\frac{-r^2}{w_0^2}} e^{i\ell\phi}, \tag{5.3}$$

which is a single ring -shaped beam holding a $2\pi\ell$ phase winding around its core (A is a new normalization constant). This is equivalent to a continuous version of the four pumps setup. Therefore the total angular momentum such a pump can communicate to polaritons is simply the beam parameter ℓ.

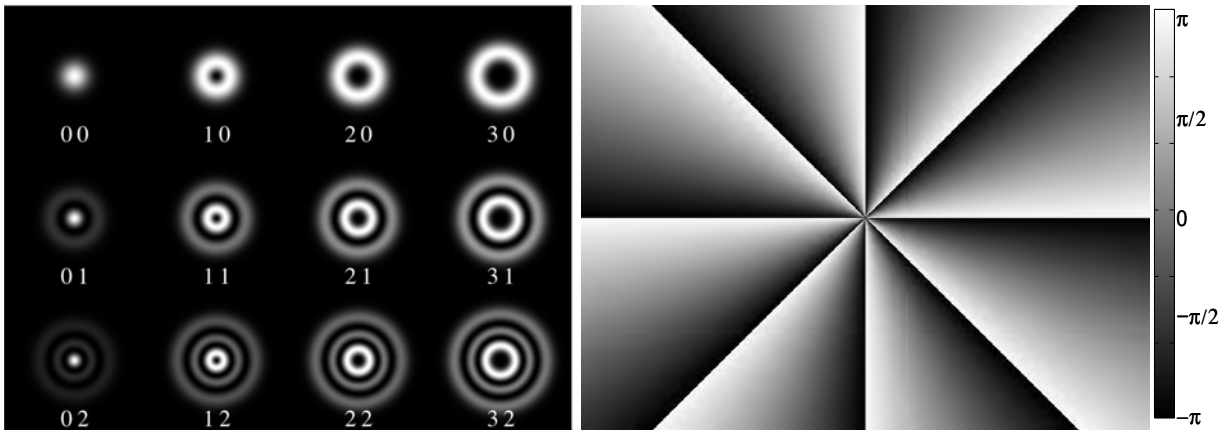

Figure 5.2.: Laguerre-Gaussian modes – (Left) - Intensity profiles of the first twelve Laguerre-Gaussian modes. ℓ controls the angular momentum held in the beam. If $\ell = p = 0$ the LG mode reduces to a Gaussian mode and for $\ell \neq 0$ the modes are always made of rings, with p determining the number of external secondary rings. The size of the main ring increases with ℓ. (Right) - Phase profile of a LG_p^8. This phase map can be used as a hologram to generate a superposition of the first LG_p^8 modes.

In order to make the polaritons propagate toward the center of the LG ring, the pump is slightly defocalized so that it hits the sample before the focal point. This way the LG beam is still convergent when it pumps the sample and polaritons are created with a converging radial component to their wavevector, similarly to the four pumps setup.

SLM and hologram choice

To shape the laser beam we use a pure-phase *Hamamatsu* LCOS-SLM. It is a 800x600 matrix of liquid-crystal pixels (each 40 μm in size) that can individually modify the phase of the light reflected on it. The control unit, plugged to a computer DVI output, receives a grayscale 800x600 pixel picture that determines the phase shift value of each SLM pixel. The actual phase shift on the reflected light is linear with the picture pixel value sent to the control unit. Therefore it is straightforward to numerically generate a phase map (or hologram) and send it to the SLM. To design the Laguerre-Gauss holograms we use Matlab, from which the hologram data is sent to the DVI output via the *psycho toolbox* plugin [1]. This way holograms can be designed, tested and modified on-the-fly.

A collimated LG beam has an invariant phase pattern trough propagation, meaning that its phase structure at infinity is the same as at z=0. This in turn means that one can simply use the theoretical LG phase map (presented in figure 5.2) as a hologram. The LKB group led by Nicolas Treps showed that a perfect, lossless spatial mode conversion

1. See http://psychtoolbox.org/

and entanglement is possible with an optimized hologram trough multiple reflection on the SLM [145, 146, 147, 148]. However such a scheme is difficult to implement on our setup and we found that a single reflection on the theoretical LG phase map leads to a mode of sufficient quality for our purpose. Indeed, the parameter ℓ being present in the hologram, the result after a single reflection is a mode of well-defined angular momentum. However the parameter p being absent (the LG phase map is the same for any p) such a mode is in fact a superposition of different p-valued modes. $p = 0$ is the dominant mode since the Gaussian beam sent on the SLM can be described as a LG_0^0 mode. An efficient workaround is to spatially filter the extra outer rings due to the higher p modes by mean of an iris. After this we obtain a good approximation of a LG_0^ℓ beam with a single SLM reflection.

Since with this scheme we create and trap polaritons within the LG ring, it is important that polaritons remain free to evolve within the ring. This means we need to make sure there is no laser light inside the ring. An additional advantage of this setup over the four pumps setup is the excellent rotational symmetry of the system. For both these reasons we need a well-defined LG beam hitting the sample. However higher ℓ-order LG modes are easily deformed by optical aberrations when strongly focused, as in this experiment. LG modes with satisfying quality up to $\ell = 10$ were obtained. However the beam size increases with ℓ, and for $\ell > 8$ the system is too large for polaritons to have the time to propagate to the center. This is why a good compromise between the system size, symmetry, and ℓ number was found for $\ell = 8$. All results presented in this chapter were obtained for this parameter, almost twice as high as in chapter 4.

Mode filtering

We just established that the higher p modes must be filtered out with an iris. In addition, to make sure there is no light at the center of the LG beam it is important to suppress the non-converted fraction of the light incident on the SLM. Indeed, according to the manufacturer, 5% of the reflected light is unmodified. Moreover the SLM only works with vertically polarized light, so this figure is achieved only with a perfect vertical polarization. The SLM acts like a mirror for both the non-converted 5% and the residual horizontal polarization. To separate this from the desired mode a grating hologram

$$\varphi_{grat}(x, y) = \frac{2\pi}{d} y, \tag{5.4}$$

where d controls the separation angle, is added to the LG hologram (mathematical sum modulo 2π). This vertically deviates the first order reflection holding the LG mode, allowing us to block the zero-order reflection with an iris. The total hologram (LG+grating)

used for this experiment and the resulting, experimental LG beam are presented in figure 5.3.

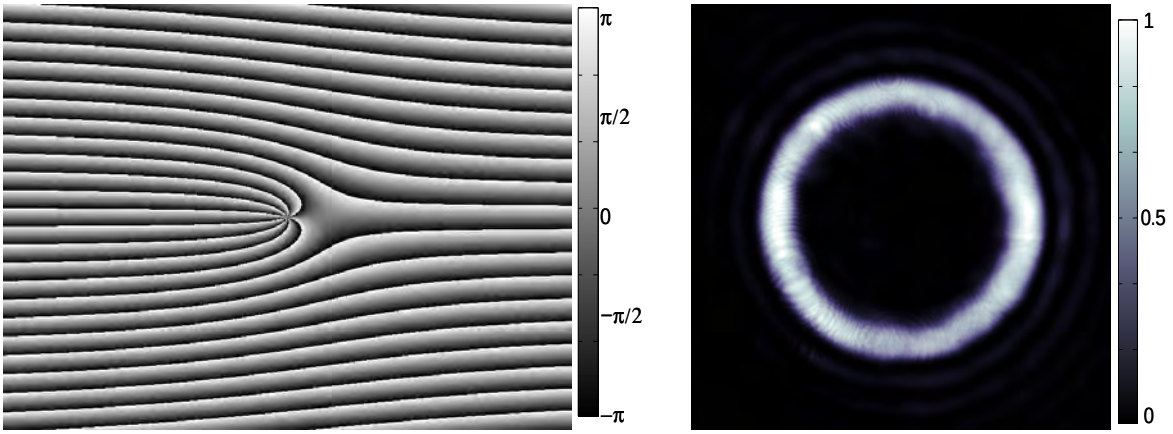

Figure 5.3.: Hologram and measured beam – Phase hologram (left) sent to the SLM to convert the laser Gaussian mode to a LG_0^8 beam. The resulting beam intensity map (right) shows a well defined ring with minor outer rings and an undetectable level of light at the center.

5.2.2. Effect of the bistability

Figure 5.3 (right) shows that the LG laser beam is already very dark at the center. In addition, following the reasoning of section 3.7, when pumping quasi-resonantly with a detuning $\Delta > \Delta_C$ only the highest part of the ring can be resonant. This implies two important things. First, if some parasite light (small to the point of not being visible on the scale of figure 5.3) was inside the ring then the polariton population it would create would be completely negligible. So that we can safely assume that no polariton can originate from the inside of the ring. Second, the bright ring region is resonant. As discussed in 3.7, this implies that the polariton density in this region is approximately constant. This is to our advantage since it smoothes any intensity irregularity along the ring and make it more symmetric. Therefore, from those two points we see that using the bistability, in addition to allowing us to access higher densities, erases the pump imperfections. A schematic view of the pump intensity profile and the corresponding polariton population density (neglecting any propagation) is presented in figure 5.4.

5.3. Results

In this section we present the results in the same fashion as in the previous chapters: The low density regime (where we can neglect polariton-polariton interaction) and the high

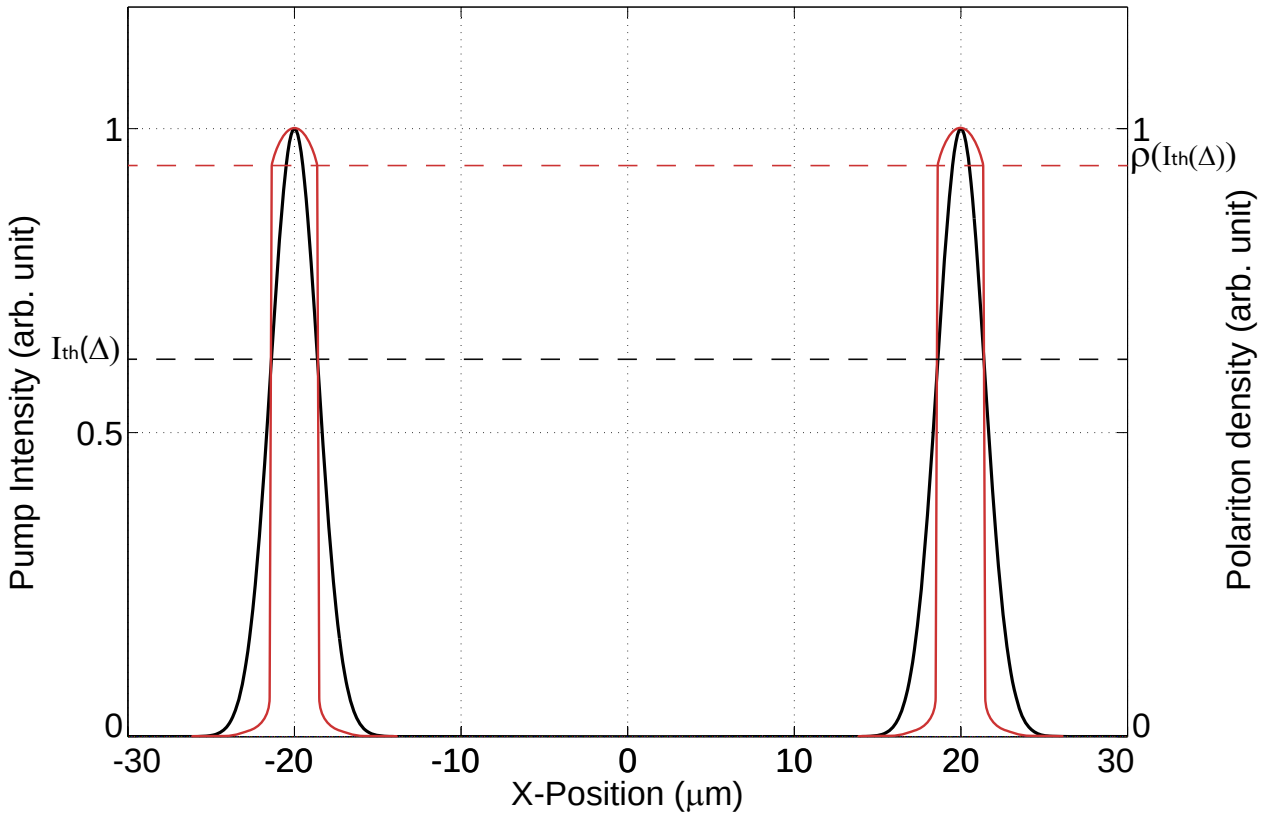

Figure 5.4.: Spatial bistability for the LG mode - Schematic view of a LG pump (black) intensity profile, and the pumped polariton (red) population density (both normalized to peak value). The function $\rho(I)$ being highly nonlinear in the bistable regime, only the regions where the local intensity is above the upper threshold (reached when decreasing the pump intensity) is resonant. The result is a polariton reservoir that has the form of a ring.

density regime (where interactions dominate and the system is superfluid) are discussed and compared to numerical simulations.

5.3.1. Low density regime

Figure 5.5 shows the density and the phase in the linear regime. Polariton propagate towards the center, where a zero density region is present. Immediately around it, an interference-like pattern of low density lines is distinguishable as a ragged edge to the dark region. V-AV pairs are visible in the phase map and the lines can *a priori* be interpreted as an actual interference pattern, very much like in the two previous chapters.

Simulations presented in figure 5.5 (middle with disorder, bottom without disorder) show that in absence of disorder the angular momentum does not nucleate and a single $\ell = 8$ vortex is present in polaritons. The dark core containing the singularity behaves like a forbidden zone for polaritons. The steady state is thus a single ring of rotating polariton,

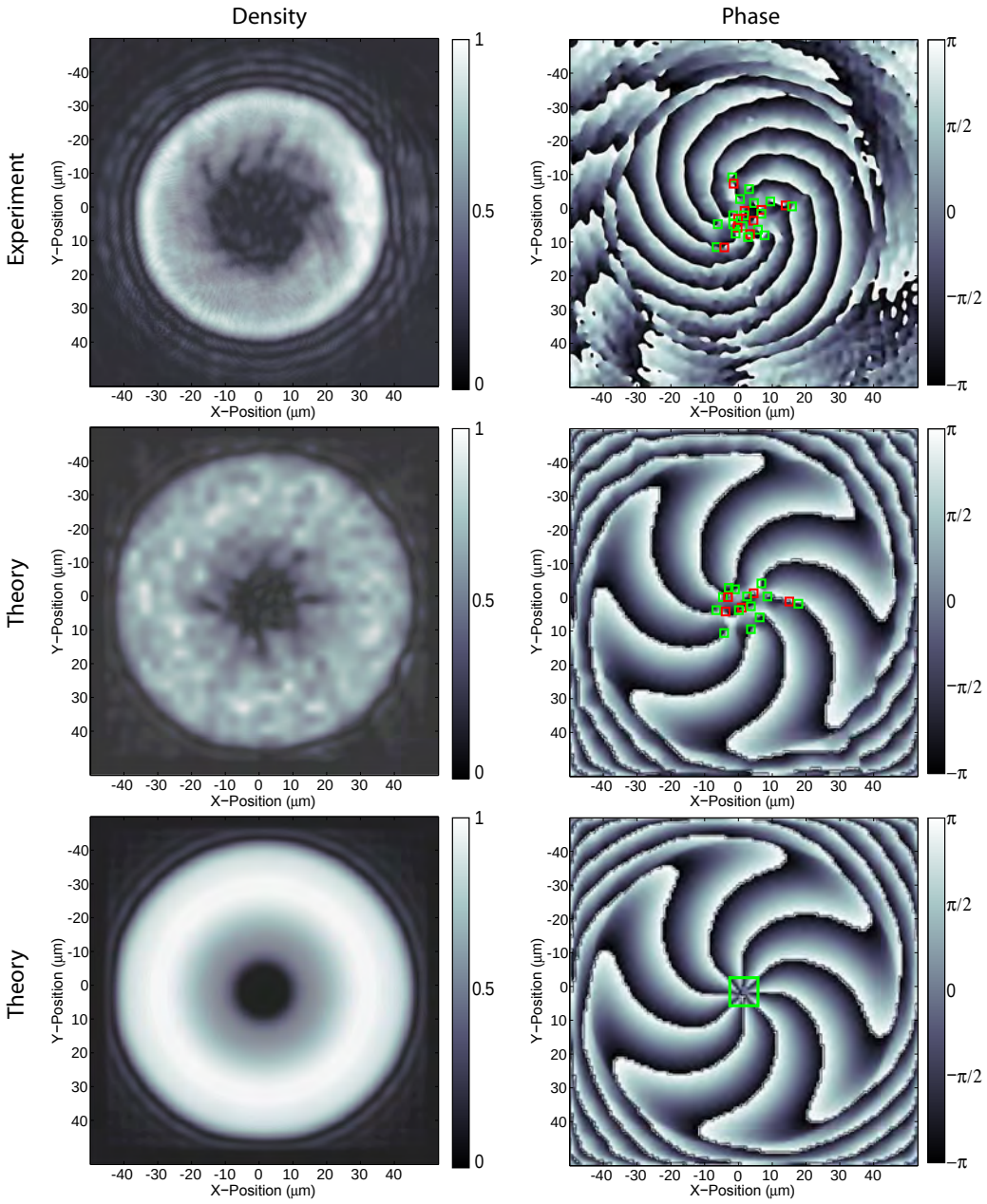

Figure 5.5.: Low density regime – Density (left, linear scale) and phase (right) map acquired experimentally (up) and through simulations including a random disorder potential (middle) and a simulation without disorder (down). The disorder is necessary to nucleate the $\ell = 8$ singularity and results in a vortex (green squares) - antivortex (red squares) lattice.

larger than the pump and with zero density at the core where the $\ell = 8$ singularity is present. Therefore without disorder the simulations fail to reproduce the weak signal present in the central part of the experiment.

Indeed, it is possible to numerically observe a structure very similar to the experiment when introducing disorder in the system. It appears from the simulations that removing

the rotational symmetry breaks up the $\ell = 8$ singularity into eight $\ell = 1$ vortices, plus V-AV pairs. Spots of non-zero density are present between the vortices. This is likely due to the break up of the main singularity and thus of the "forbidden zone" (the $\ell = 8$ healing length) by the presence of defects in the singularity. Polaritons scattered by the disorder populate the zone between the vortices, giving possibly rise to interference in the low density regime.

5.3.2. High density regime

Experimentally, when increasing the density and thus the strength of the interaction we observe a concentric ring-like structure at the center of which a dark zone similar to the low density case is visible. It is here smaller and better defined. Here too this dark zone contains vortices. Despite the density being low, vortices can be observed individually when analyzing the data in log scale, as in figure 5.6. We observe an absence of antivortex pairs in accordance with the chapter 3 results and the reduction of the area containing the vortices.

No rotation of vortices nor traces of rotation (energy sidebands, blurring of the density and the phase) can be detected. This is coherent with the interpretation that disorder both nucleates the main singularity and pins down the resulting vortices.

Simulations shown in figure 5.6 indicate that here, like in the linear regime, the observed vortices are a result of the disorder-induced symmetry breaking. Without disorder (bottom panel) a central $\ell = 8$ singularity is present as well as concentric rings around it. Adding disorder (middle panel) once again breaks this singularity into elementary vortices and results in density and phase maps in very good agreement with the experiment.

5.4. Interpretation

We can conclude that in this resonant, rotationnal-symmetric setup no spontaneous [2] nucleation of angular momentum is present. The disorder-free numerical experiment shows no vortex lattice and the system remains perfectly symmetric. Nucleation can be induced numerically by adding disorder, which reproduces well the experimental data. However the vortex position is determined by the disorder realization, and is thus random and non-rotating.
While the non-harmonic trap potential created by the pump should not be responsible for the lack of spontaneous angular momentum nucleation, the resonant pumping method

2. Meaning "triggered by vortex-vortex interaction".

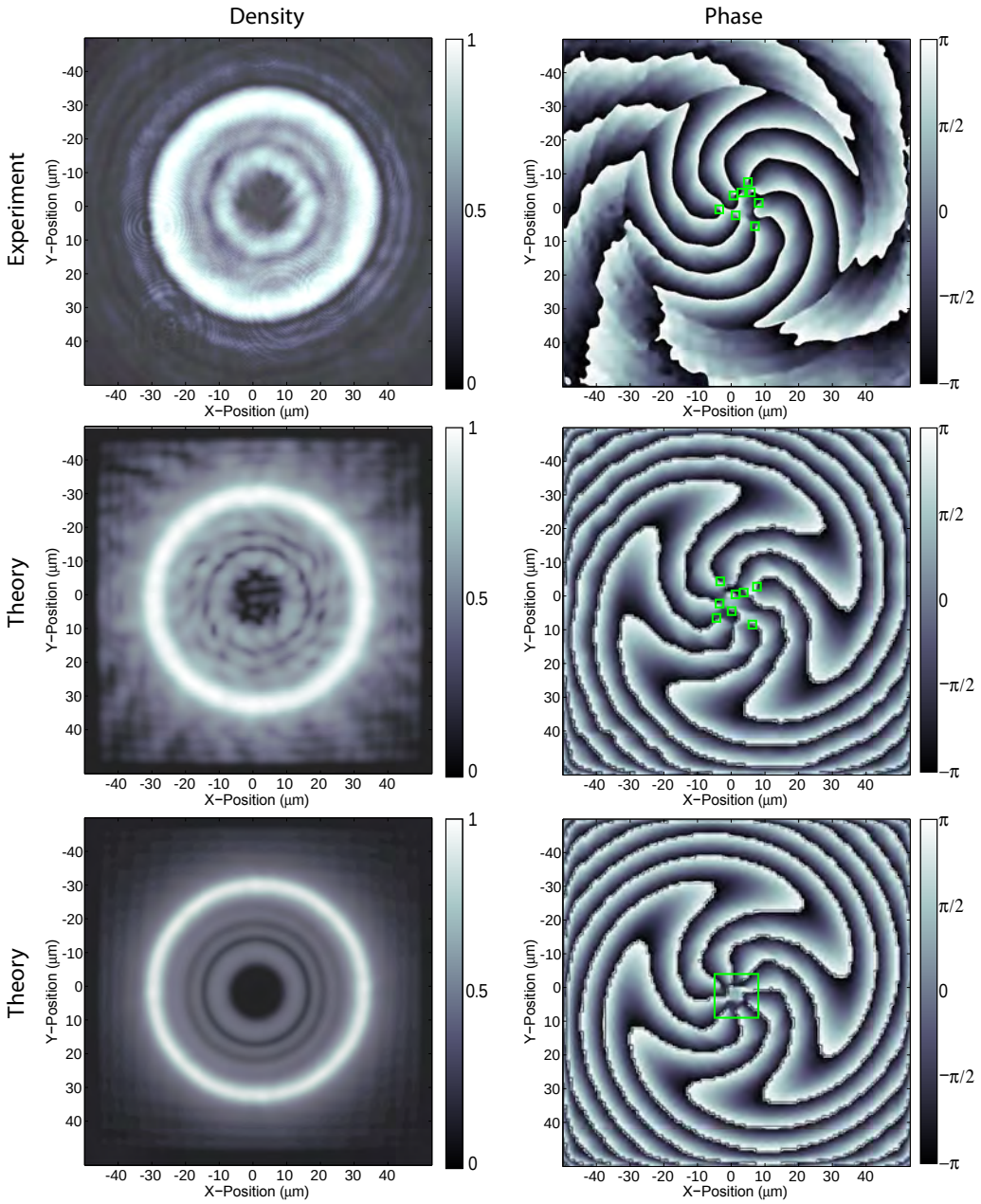

Figure 5.6.: High density regime – Density (left, log scale) and phase (right) map acquired experimentally (up) and through simulations including a random disorder potential (middle) and a simulation without disorder (down). Here too the disorder is necessary to nucleate the $\ell = 8$ singularity and results in a vortex-only (green squares) lattice.

imposes spatial border conditions that could prevent the system from evolving in a completely independent way. To explore the matter further, a non-resonant pumping scheme should be designed. This requires however to overcome some technical difficulties

concerning the spatial control of the exciton reservoir [3] and, more challenging, concerning how to stir the polariton condensate into rotation.

3. Since the exciton reservoir acts like a strong potential, controlling its shape is crucial to trap polaritons in an out-of-resonance setup.

Chapter 6.

Vortex chains in polariton superfluids

In the previous chapter we saw that angular momentum injected by a convergent Laguerre-Gauss beam only nucleates by scattering on natural cavity defects. The resulting vortex lattice is thus pinned by the disorder, and random in shape. The observation of a self-ordered Abrikosov lattice is thus not possible at the moment for this type of system. However we can, by constraining the system geometry, coerce the lattice into taking a deterministic, symmetric shape. This opens the way to the controlled injection of angular momentum in polariton fluid since the position as well as the number of vortex can now be engineered, a first in polariton physics. This in turns may allow the study of vortex position dependence on the fluid parameters such as the polariton-polariton interaction and the polariton flow. Eventually such an approach could lead to the exploration of vortex-vortex interactions in polaritonic systems.

6.1. Deterministic same-sign vortex chains

In a circular symmetry, the disorder-driven random vortex position does not offer the possibility of controlling the lattice shape and the inter-vortex distance. Furthermore, the vortices are pressed tightly at the center, making their study difficult. To circumvent this issue, the team of Guillaume Malpuech, at the Institut Pascal, Clermont-Ferrant, proposed a scheme to nucleate the fluid angular momentum in a controlled way, creating a regular, ring-shaped array of vortices of the same sign. The method consists in adding a small Gaussian pump at the center of a LG pump, at the same energy and with the same polarization. This way, the two coherent LG and Gaussian pumps merge in the high density regime with a non-zero angular momentum. As in chapter 4 the pumps relative phases influences the position of the vortices. This way the azimuthal vortex position is fixed by the pumps and any spontaneous rotation of the vortex lattice (here, a circular chain of vortices) is hindered. Therefore adding the small central Gaussian spot uses the

pumps influence on the vortex position in a controlled way to block the lattice rotation, to impose the lattice geometry and to break the central $\ell = 8$ singularity.
As we will see in section 6.3.3, in the high density regime the pumps are not the only relevant parameters for the vortex position. Indeed, when the interactions dominate the system, the merged superfluid exhibits a hydrodynamical behavior and the polariton superflow also has an impact on the vortex position. Simulations and experiments alike show that this is especially true in the radial direction. Therefore this open the way to the study of the interplay between polariton vortices and the flow of the surrounding superfluid.
This scheme also has the advantage of being straightforward to implement upon the previous LG pump setup, since the SLM hologram can easily be modified to create the superposition of a LG and a Gaussian mode. A similar approach to shape the polariton landscape and create a ring-shaped polariton condensate is used in [141], showing the versatility of the SLM method.
Interestingly, Dreismann *et al* [141] found that the simple constraining of a polariton condensate (pumped non-resonantly) into a ring shape triggers the condensate rotation. Since no angular momentum is injected in this scheme (something for now impossible with a non-resonant pump), it is the superposition of an angular momentum $+\ell$ and $-\ell$ that is observed, resulting in a "petal state" resembling a whispering gallery mode. Since in this setup no angular momentum in injected, no vortex is observed.

6.2. Experimental setup

Like in the previous chapter, the setup for this experiment is very similar to the one in chapter 3. The Ti:Sa laser, the cryogenic setup, the sample, the detection and the density control method are identical and the pump preparation by mean of the SLM is very similar to chapter 5. The only difference is the addition of the central Gaussian spot, obtained by designing a new hologram. The setup scheme (figure 6.1) is nonetheless reproduced here for convenience.

6.2.1. Pump preparation

We saw in section 5.2.1 how to prepare a hologram that generates a LG_0^ℓ. Adding the central Gaussian pump is straightforward since the mode impinging on the SLM is such a Gaussian mode: we simply need to impose a flat phase area in the LG_0^ℓ hologram. This

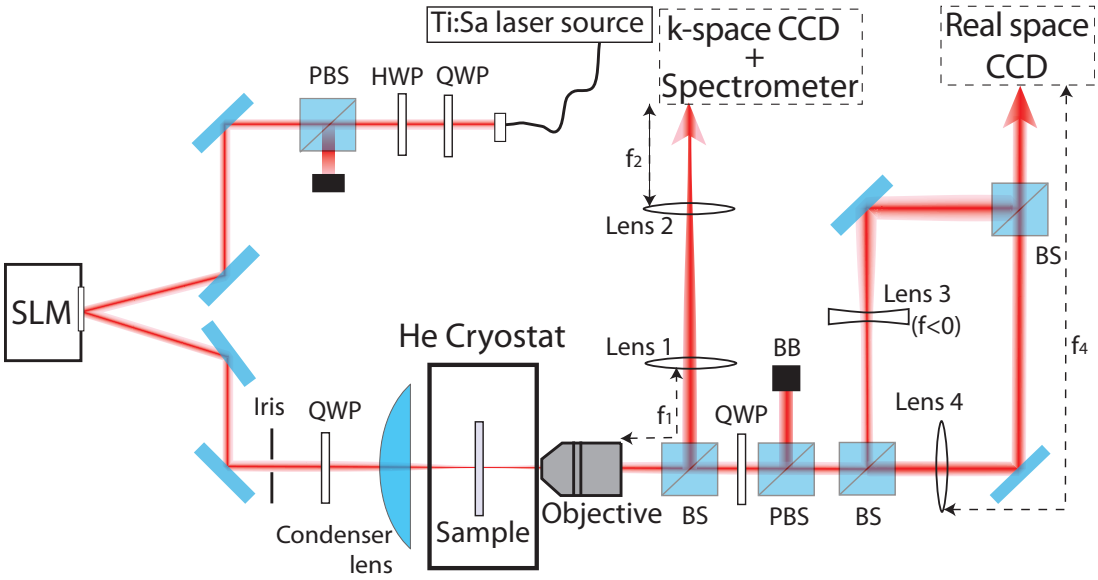

Figure 6.1.: Setup – Experimental setup scheme. The pumps are prepared with a pure-phase Spatial Light Modulator (SLM) and sent on the sample. The sample emission is collected and treated for detection in real space, momentum space and energy.

was done first by using the phase function

$$\varphi_{LG+G}(r,\phi) = \ell\phi H(r-r_0) + \pi(1-H(r-r_0))\ [2\pi], \tag{6.1}$$

where $H(r)$ is the Heavyside distribution and r_0 is a constant determining the LG/G intensity ratio. The resulting hologram is presented in figure 6.2 (up). For precisely the same reasons as in section 5.2.1 the same phase grating is added to the hologram (figure 6.2 (down)). Whether with or without this grating, we notice the presence of ℓ (here $\ell = 8$) phase singularities arranged in circle. This pattern looks like what we expect to spontaneously appear in polaritons, so some concerns existed over holograms already possessing this feature.

This is why another, more advanced, method was also used here to produce the same pumping beam. It consists of a "distributed flat phase" hologram where

$$\begin{cases} \varphi_{LG+G}(r,\phi) = \ell\phi\ [2\pi] \quad \text{if} \quad \ell\phi\ [2\pi] > a_0 \\ \varphi_{LG+G}(r,\phi) = 0 \quad \text{else} \end{cases} \tag{6.2}$$

where $a_0 \in [0, 2\pi]$ is another constant determining the LG/G intensity ratio. The resulting hologram is presented in Figure 6.3 (up without grating, bottom with the grating). This hologram presents the advantage of spreading the flat phase over the whole image, so that the $\ell = 8$ phase singularity is still present at the center rather than cut into a ring of 8 $\ell = 1$ phase singularities as in Figure 6.2. Both types of holograms form the same pump on

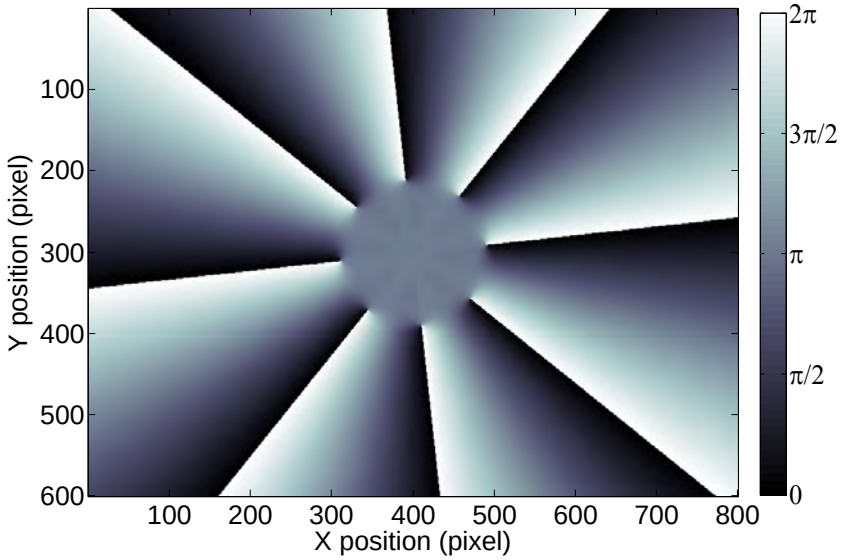

(a)

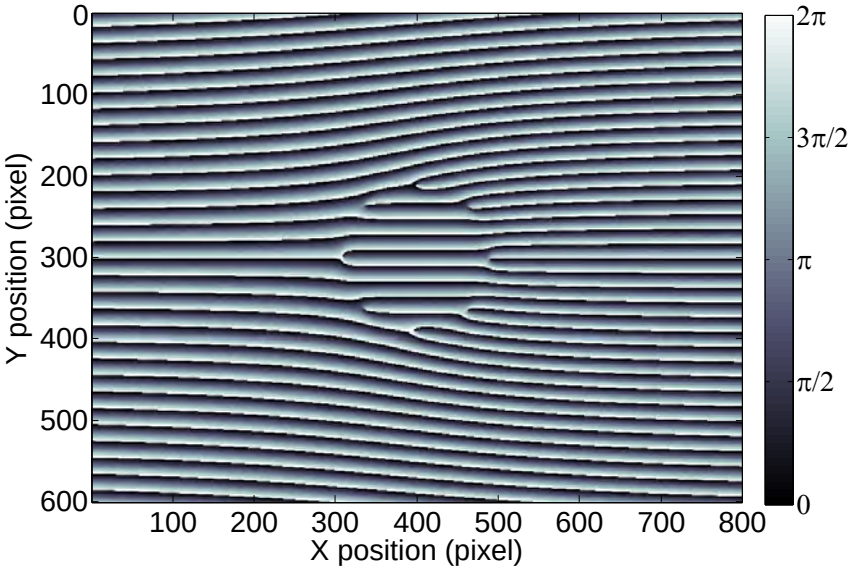

(b)

Figure 6.2.: Central flat phase hologram - Hologram corresponding to the first tested method, without (a) and with (b) the grating hologram. The Laguerre-Gaussian phase is cut at the center and replaced with a flat phase, which creates the Gaussian central beam.

the microcavity, but the "distributed flat phase" hologram provides the additional safety that it does not contain any information about a ring of elementary vortices. Therefore this proves the nucleation of the $\ell = 8$ singularity does not originates from the hologram choice.

Since the flat region is not condensed into a small zone anymore, this new hologram also has the advantage of reducing the diffraction on the Gaussian beam. This permits a

smaller Gaussian central pump, an essential characteristic for observing hydrodynamical effects in the system, as we will see in 6.3.3.

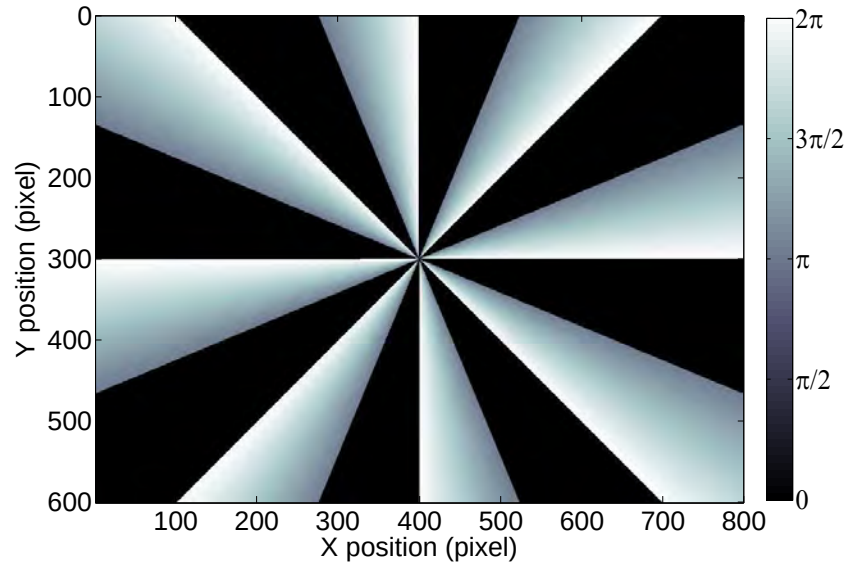

(a)

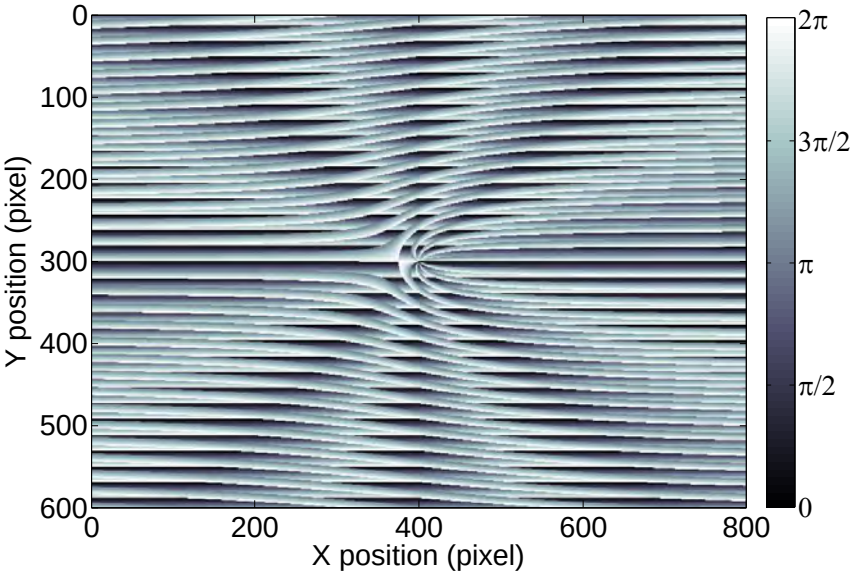

(b)

Figure 6.3.: Distributed flat phase hologram - Hologram corresponding to the second method, without (a) and with (b) the grating. A part of the Laguerre-Gaussian phase is replaced with a flat phase in a distributed way, depending on the local LG phase value. This also creates the Gaussian central beam but it ensures no elementary phase singularity is present in the hologram.

6.3. Results

6.3.1. Low density regime

In the linear regime, we observe - both experimentally and theoretically (figure 6.4) - a pattern looking very much like the pumps. A closer inspection in the dark region between the LG and the G shows a weak pattern in the density, resulting from the optical interference between the tails of the LG and G beams. In the phase this interference pattern consists in an eight-lobbed spiral with eight phase singularities. The annular phase singularity chain visible in figure 6.4 is thus imposed by the pump phase and the system can be explained in terms of linear optics.

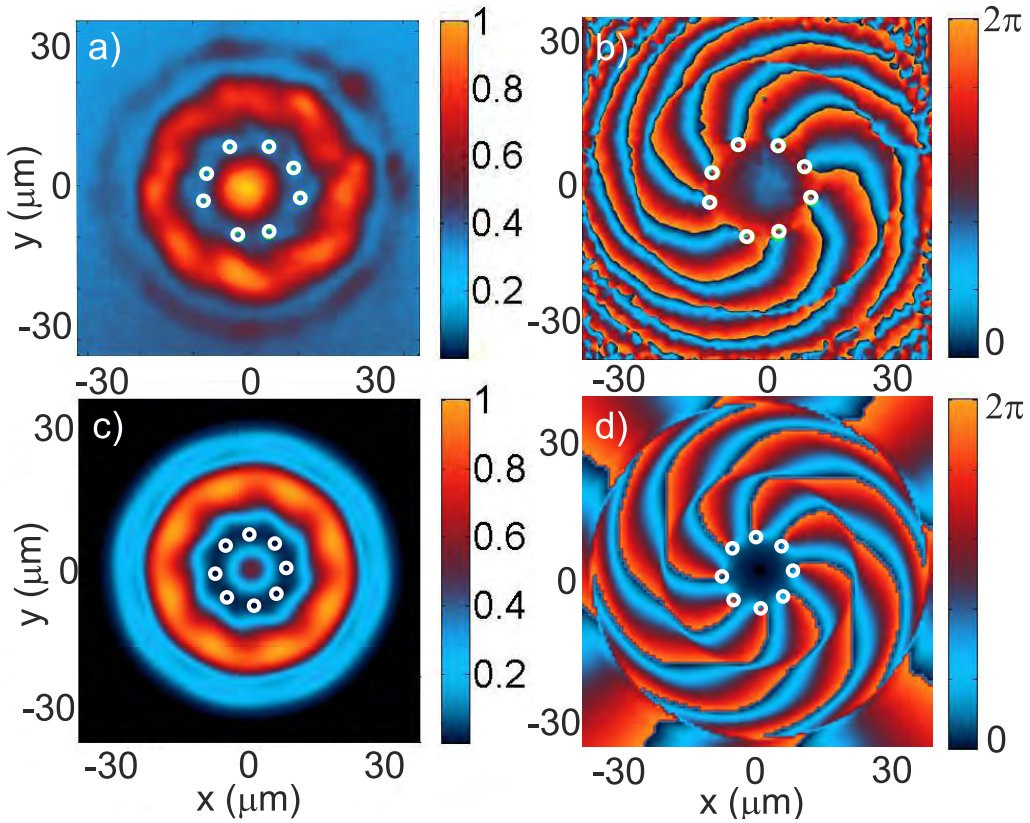

Figure 6.4.: Low density regime – Density (left) and phase (right) map acquired experimentally (up) and through simulations (down). The dark non-pumped zone between the LG and G beams presents traces of interference between the tails of the two beams. There, a ring of singularities is visible in the phase. However since the density is so low, according to our earlier definition these are not polariton vortices, but merely the result of the weak interference.

6.3.2. Medium to high density regimes

As the density increases, the nonlinear behavior of polaritons unveils, with a progressive deformation and disappearance of the interferences. Figure 6.5 shows the system for medium densities (obtained with $\Delta = 0.2 - 0.3$ meV). Polaritons propagate further due to repulsion and the interference pattern is deformed, but not completely erased. Each phase singularity is contained in a bean-shaped low density region, which are reminiscences of the interference fringes.

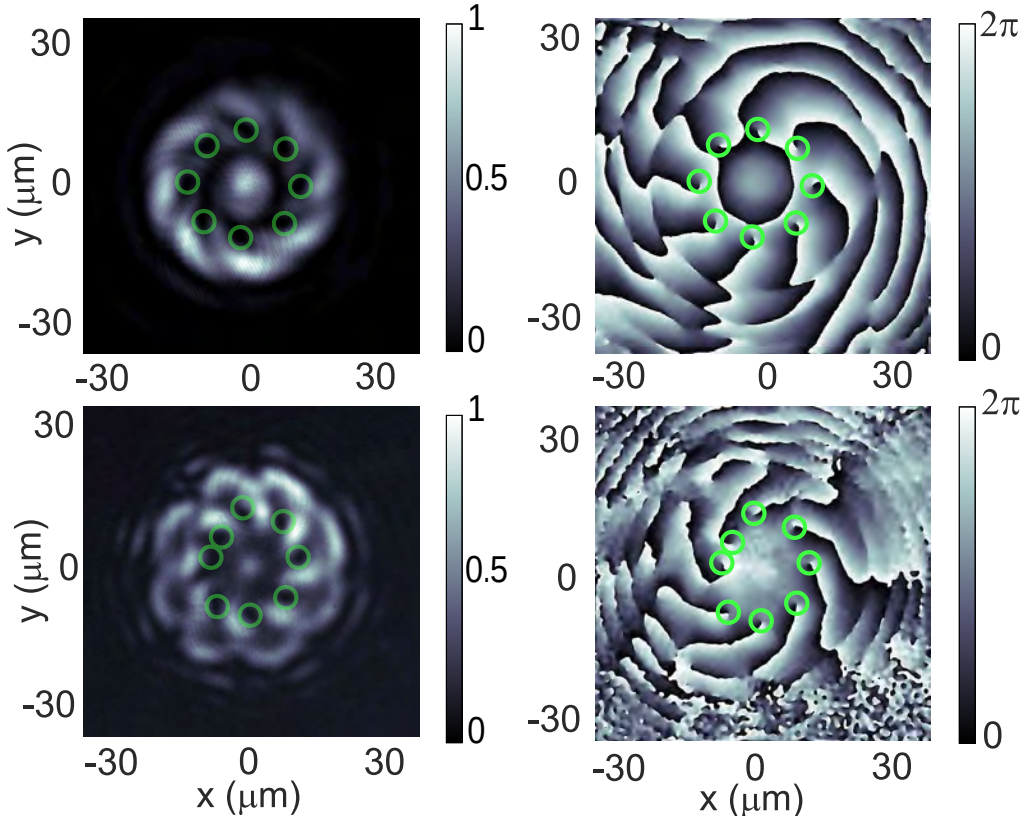

Figure 6.5.: Medium density regime – Density (left) and phase (right) map acquired experimentally for two values of the density, obtained with $\Delta = 0.2$ meV (up) and $\Delta = 0.3$ meV (down). We can observe the progressive deformation and disappearance of the interference pattern.

For $\Delta = 0.4$ meV the interference pattern shown in figure 6.6 is reduced to round-shaped dips with zero density at their center and containing a phase singularity. They are now fully formed elementary vortices, carrying the injected angular momentum. We observe a ring of same-sign vortices in a coherent superfluid of polariton, quite differently from the spiral interference pattern present in the low and medium density regimes. The absence of interference pattern indicates that the polariton phase is now different from the one of the pump and is modified through the nonlinear interactions, generating additional features compared to an optical interference pattern. Therefore this is in agreement with

the chapter 3 results showing the merging of several polariton fluids into one: here the merging fluids are the two populations generated by the G and the LG beam.

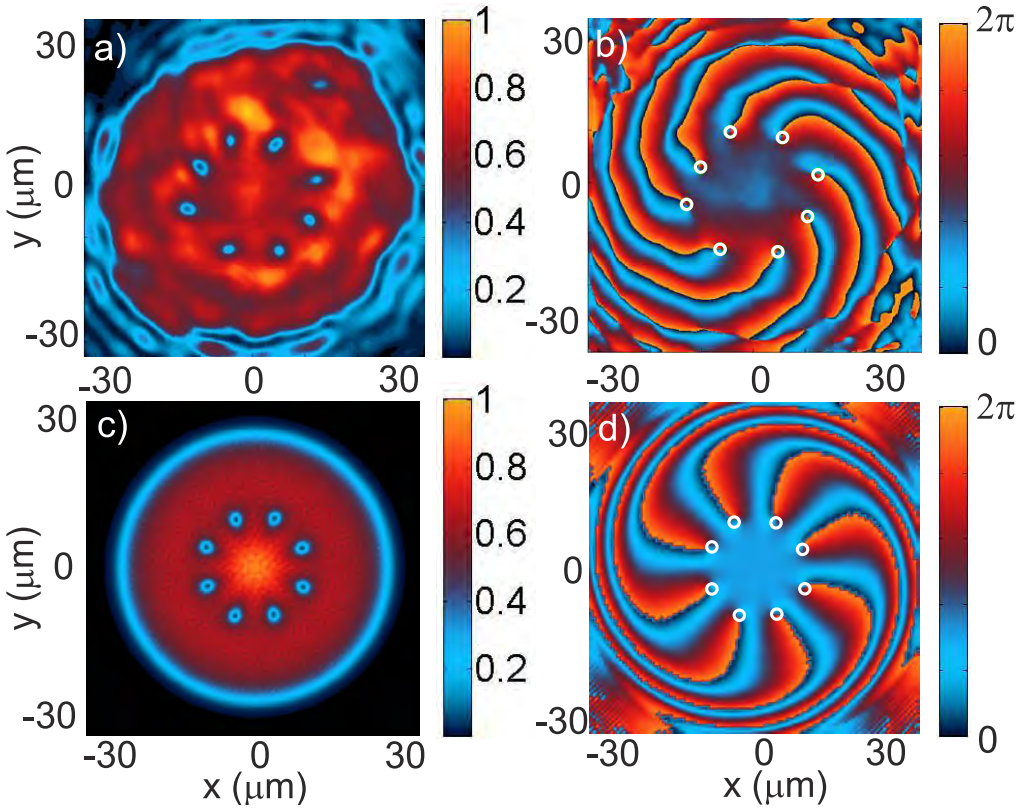

Figure 6.6.: High density regime – Density (left) and phase (right) map acquired experimentally (up) and through simulations (down). Here the interference fringes have disappeared and only polariton vortices remain.

6.3.3. Phase freedom in the nonlinear regime

Theoretical work done by the team of Guillaume Malpuech shows that in this system the vortex azimuthal position is fixed by the pumps (this is the mechanism expected to block the theoretically predicted vortex lattice rotation). This was confirmed experimentally by changing the relative phase between the LG and the G beams. The ring rotates with the phase difference, showing that the azimuthal position of the vortices is fixed by the pumps relative phase. Indeed, the interference pattern observed in the low density regime designates a "preferred birthplace" for the vortices through the phase singularities it holds. This acts in the high density regime as an underlying preferred region for the vortices, around which they are free to move depending on the surrounding polariton superflow. However their radial position, like the fluid phase, is free to evolve within the pump-free space between the LG and G beams. This leads to interesting phenomena (described below) that prove the hydrodynamic-like behavior of polariton fluids in the high density

regime, which in turn indicates that the annular vortex chain in this regime is not optically imposed by the pumping scheme.

Chain radius versus density

As direct consequence of their radial freedom, the vortex radial position is modified as the density $\rho = |\psi|^2$ increases, which is something easily observable. Thus a first test for the vortex position freedom is to measure the evolution of the ring radius R as a function of the mean polariton density $\rho \equiv n_0(\Delta, I_p)$. R is measured as the average distance of each vortex in the chain to their barycenter. The result, plotted in Figure 6.7 c), is an increase of the ring radius with the density. The density is increased by the same amount everywhere in the pumps when Δ increases (constant ratio $\frac{LG}{G}$), so that in a linear optics framework this behavior would be impossible since the interference pattern would not change.

In order to model the ring radius R, we use a variational method. The vortex chain solution is described with the ansatz:

$$\Psi[R] = \psi_{\mathrm{TF}}(r) \prod_{i=1}^{8} f_V(\mathbf{r} - \mathbf{r}_i), \quad f_V(r_i, \theta_i) = \sqrt{\frac{r_i^2}{r_i^2 + \xi^2}} e^{i\theta_i}, \tag{6.3}$$

where $\psi_{\mathrm{TF}}(r) = \rho^{1/2}[P_1(r)/A_1 + P_2(r)/A_2]$ is the Thomas-Fermi density profile induced by the pump, $\mathbf{r}_i = R(\cos\theta_i, \sin\theta_i)$ is the position of each vortex in the chain, and $\xi = \hbar/\sqrt{m\rho g}$ is the average healing length. In figure 6.7 a), we plot the variational profile given by Eq. (6.3). The value of R can then be extracted by minimizing the total energy $E[R] = E_{\mathrm{kin}} + E_{\mathrm{int}}$ and taking the physically relevant solution from the condition $\frac{\delta E}{\delta R} = 0$, where:

$$\begin{aligned} E_{\mathrm{kin}} &= \int d\mathbf{r} \left(\Psi^* \frac{\hbar^2 \nabla^2}{2m} \Psi \right), \\ E_{\mathrm{int}} &= \int d\mathbf{r} \left[\left(|\Psi| - \rho \right)^2 |\Psi|^2 \right]. \end{aligned} \tag{6.4}$$

In Figure 6.7 b) the energy E is plotted as a function of R for different values of $\xi \sim \rho^{-1/2}$. We observe that R decreases as the value of ξ (ρ) is increased. Since ρ increases with Δ, ξ decreases with Δ; it follows that R increases when we increase Δ. Figure 6.7 c) shows R as a function of ρ calculated by this method and the comparison with experimental data. As expected, the higher the density, the further from the center the vortices migrate. This behavior and the agreement between the variational method and experiment are a clear indication of the phase freedom obtained when interactions dominate, a feature that is independent from the optical interference.

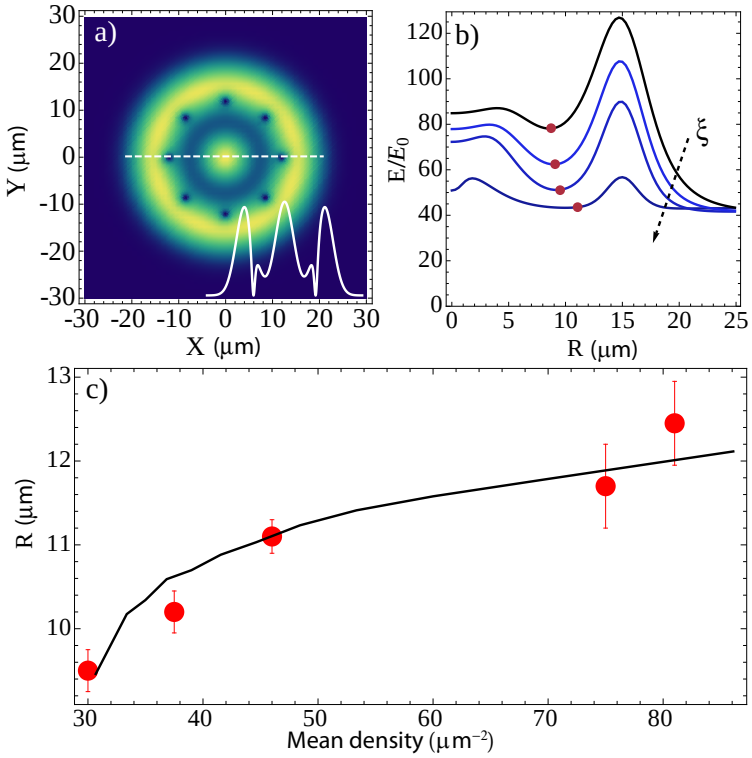

Figure 6.7.: Vortex positions (a) - Variational wave function in Eq. (6.3) used to determine the vortex chain radius R. The inset shows the radial profile for a cut at $Y = 0$. (b) - Variational energy E (in units of $E_0 = \hbar^2\rho/(4\pi m)$) showing a minimum (red dots) for different values of ξ. From top to bottom: $\xi = (3.0, 2.0, 1.0, 0.5)$ μm. (c) - Average chain radius R as a function of the pump detuning Δ obtained from the variational method (solid line) and the corresponding experimental data (dots). The experimental error bars are the statistical variance.

Hydrodynamic instabilities

As discussed in 3.7, in the upper bistability branch the polariton energy is renormalized through self-interaction to the pump energy, so that the pumping is resonant and yields high polariton densities. This is not the case in the lower bistability branch, where the pumping is non-resonant and inefficient. For large Δ, the low pump intensity regions in the lower bistability branch are far from resonance. In these regions, non-resonant pumping yields a negligible polariton population and can be considered as a pump-free region. This is illustrated in figure 6.8 for different values of Δ, neglecting any propagation: the higher is Δ, the higher is the pumped polariton density and the larger is the pump-free region. For example, near the threshold ($\Delta = 0.7$ meV when pumping with a power of 400 mW, in this setup) a large area between the LG and G is not pumped. This is represented in blue (Δ_2) in figure 6.8. Although no polariton is directly injected in this area, the density is not zero due to polaritons propagating from the pumped to the non-pumped area. The detuning Δ being high, the density in the upper bistability branch is high and the superfluid healing length is decreased. When the density in this pump-free area

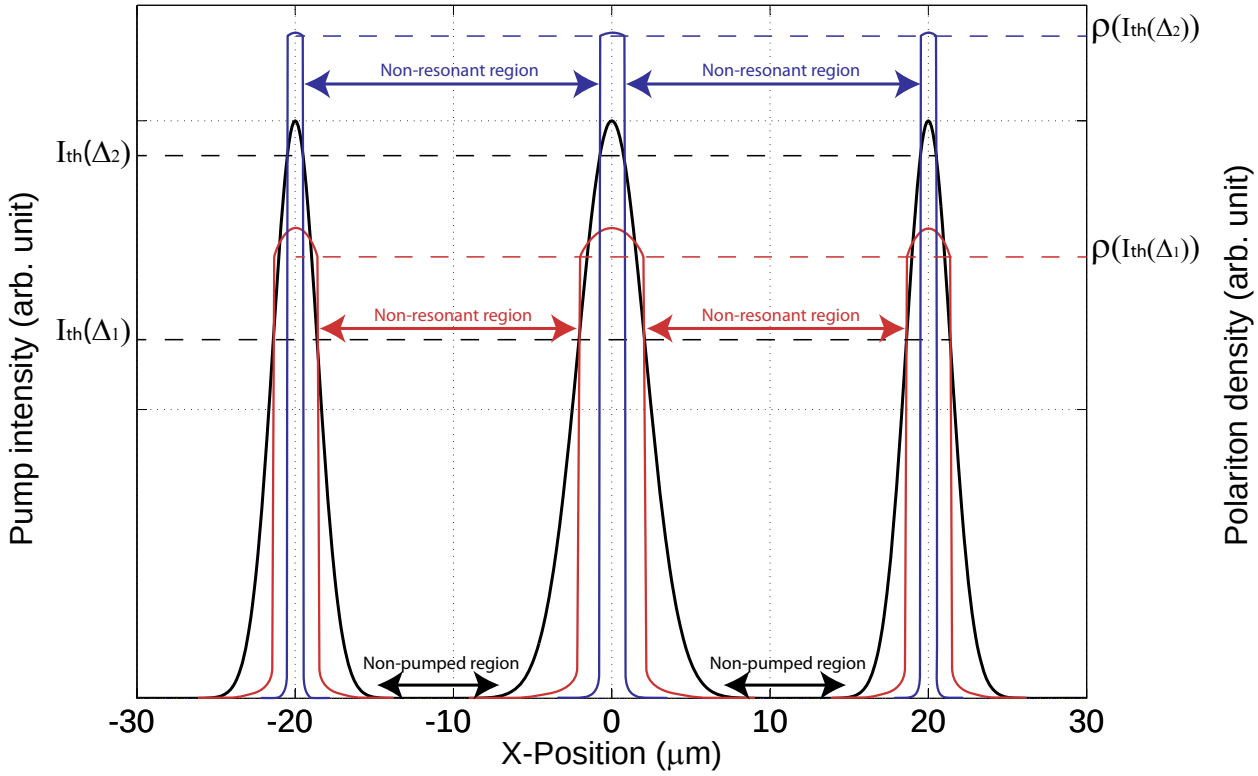

Figure 6.8.: Spatial bistability for the pump - Schematic view of a "LG+G" pump (black) intensity profile and the pumped polariton population density, for two values of Δ (red and blue). Any propagation is neglected. The blue curve corresponds to a detuning Δ_2 higher than the detuning Δ_1 ascociated with the red curve. A higher value of Δ leads both to higher densities in the resonant regions and to a smaller resonant region, due to a higher intensity threshold. Only the regions where the local intensity is above the upper threshold (reached when decreasing the pump intensity) is resonant. As a result the pump-free zone and the pumped polariton density increase in size as the Δ increases.

is large enough and when the size of this region is at least of the order of[1] $\sim 2\xi$, we observe the spontaneous nucleation of vortex-antivortex pairs. Four fully formed pairs are experimentally visible in figure 6.9 and eight in the theoretical figure. They form a low-density ring inside the vortex chain described in the section 6.3.2. This is due to a hydrodynamic instability of the same nature as the one observed in the $\ell = 0$ case [123], but here each pair formation is stimulated by the presence of a vortex which acts as a defect. The model confirms that the vortex-antivortex pairs are bound to the main vortex chain and that they appear in the absence of disorder. This feature also proves that the vortex distribution is not due to optical interference in the superfluid regime, but that it rather evolves with the density in a hydrodynamical manner.

The fact that we observe less pairs in the experiment than in the theory is due to the cavity wedge inducing an anisotropy in Δ. Indeed, the system size (about 50 μm)

1. This can be understood as the space necessary for two vortices of opposite signs to coexist.

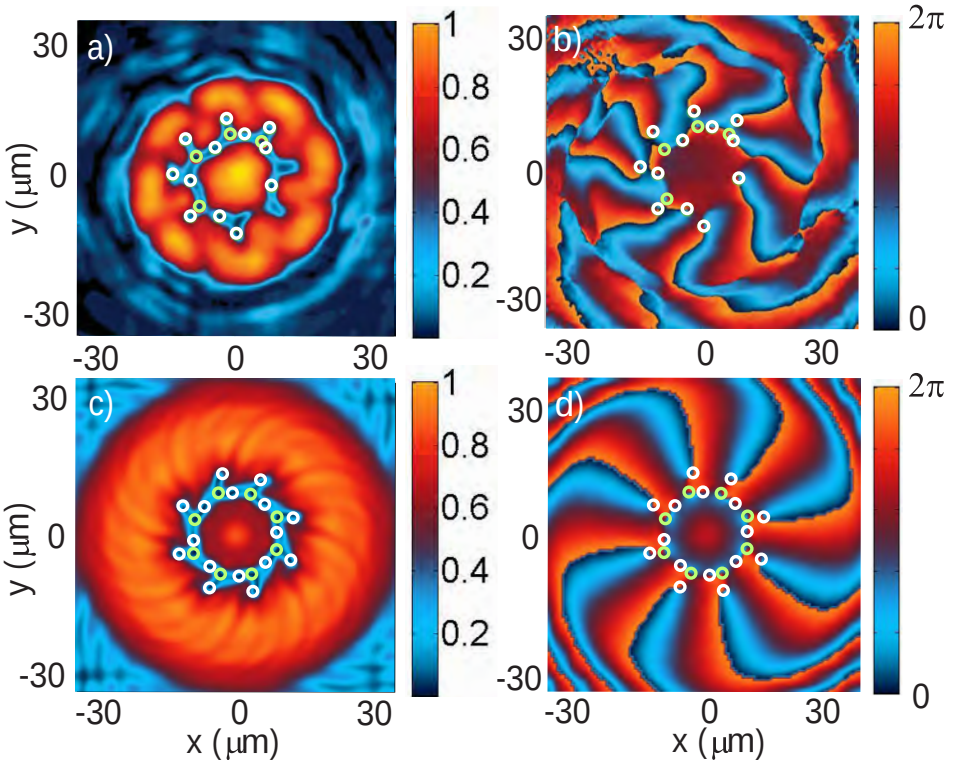

h[b]

Figure 6.9.: Phase instability - Experimental (above) and theoretical (below) images of the polariton field when the bistability threshold is close to the pump maxima (very high densities, $\Delta = 0.7\,\mathrm{meV}$). The intensity $|\psi|^2$ (normalized by the peak value) is shown on the left panels while the phase $\arg(\psi)$ is shown on the right panels. Vortices are indicated by white circles and antivortices by green circles both in the intensity and the phase. Here only the maxima of the pump are on the upper bistability branch (resonant pumping) and produce a significant polariton density. The nonresonant zone between the LG and G pumps is wide enough for the fluid to hydrodynamically nucleate into vortex-antivortex pairs, while preserving the annular vortex chain.

is sufficient to "feel" the wedge (about 710 μeVmm^{-1}), which changes the effective Δ. Moreover, since the pumps maxima must be at the bistability threshold, this system is very sensitive to variations in Δ. It is visible in the fact that the pairs that fail to form always do so in the same area, on the other side of the system relative to where the fully formed pairs are. Moreover those two areas are aligned in the direction of the thickness gradient.

6.4. Conclusion

In this chapter, we resonantly injected polaritons with a given total angular momentum and observe the formation of a ring of quantized single-charged vortices. For the first time, a regular ring pattern of elementary vortices of the same sign is reported in a polariton superfluid. In the superfluid regime, the radial position is not determined by the pump but rather depends on the polariton density. Experimental and theoretical indications of this property, due to very strong nonlinear interactions, are provided through the system hydrodynamical behavior. The mechanism leading to the creation of vortex chains results from the injection of angular momentum in a limited region of space. Note that this general behavior was experimentally and theoretically verified to be the same if the number of injected vortices is changed, whether odd or even. The present scheme could pave the way to study a series of new vortex collective phenomena that have not been possible so far [149, 150, 151].

6.5. General Conclusion

As a conclusion for Part I (chapters 3-6), we found that increasing the density can coerce any vortex-antivortex pairs to squeeze into a smaller and smaller zone. When the zone is small enough, the V-AV pairs annihilate, the interference pattern vanishes and the superfluids all merge into one. We then observe, both experimentally and in the simulations, a merging of the different superfluids. The single resulting superfluid presents a continuous phase across the whole system and is, as expected, in the subsonic regime.

In the steady-state regime, where the pumps inputs compensate the polariton decay "output", angular momentum is a conserved quantity. As a result in the merged system, if the pumps are modified to continuously inject angular momentum then this angular momentum is communicated to the polariton fluid and is conserved in the steady-state regime. This is especially interesting since through polariton pumping and decay the

system is open [2] and strongly out-of-equilibrium. Therefore no conservation law can be readily applied to explain this result, which opens the door to the study of quantum topological charges conservation in out-of-equilibrium open systems.
The four-beams pumping scheme allows the control of the injected angular momentum and, for the first time in a polariton superfluid, the observation of lattices of same-sign elementary vortices.

We learned that the nucleation of angular momentum for resonantly injected polaritons is only possible for non-rotational invariant pumping (chapter 4), in the presence of disorder (chapter 5) or if constrained by the pump geometry (chapter 6). In particular, pumping resonantly with a single Laguerre-Gaussian beam in a disorder-free cavity yields a single vortex of charge ℓ and thus no nucleation is observed. This is probably explained by the rotational-symmetric, continuous phase imposed by the pump at the system edge which is conveyed throughout the whole fluid and prevents the formation of multiple phase singularities. More experimental investigations will be required to completely explain this behavior. Adding disorder can disrupt this border condition and allow the formation of a random vortex lattice.
While spontaneous [3] nucleation of angular momentum is not observed, it is interesting to note that the vortex lattice does not have to be random. Indeed a modified pumping scheme can make the central singularity unstable and nucleate according to the pump geometry. In chapter 6 we use an additional Gaussian pump to do so and observe a regular annular vortex chain. In the highly interacting regime, it presents strong hydrodynamic characteristics showing a radial position freedom for each vortex.

Note that all phenomena seen here differ completely from vertical-cavity surface-emitting lasers (VCSELs) [114], in which in-plane transport is rapidly attenuated outside any pumped region. Polariton systems thus support an optical superfluid in which new nonlinear transitions can be induced and directly observed. Such understanding of superflows is crucial for harnessing superfluid polariton circuits and interferometric devices. Devices in prospect include gyroscopes based on polaritons flowing in a loop [152], analogous to helium superfluid gyroscopes which are capable of high-sensitivity measurement of the absolute rotation angle. Another class of devices are macroscopic quantum interference devices for quantum information processing, enabled by entangling different condensates in a polariton circuit or controlling polariton superfluid vortices. Since the strong coupling and the polariton condensation can be achieved at room temperature, this would thus enable practical polariton chips capable of high-sensitivity measurement. More specifically, the present series of experiments is a first step towards a new class of

2. In the sense that energy and momentum are exchanged with the environment.
3. Spontaneous is meant as triggered by vortex-vortex interactions and energy minimization as seen in section 2.3

rotating-frame experiments that could reveal self-arranged same-sign vortex lattices [142], unveiling the physics of vortex-vortex interactions in polariton superfluids.

Part II.

Squeezed states driven by polariton-polariton interactions in semiconductor micropillars

Chapter 7.

Polariton-based generation of squeezed states

The original idea that led the Quantum Optics group at LKB to study semiconductor microcavities in the strong coupling regime was the possibility to reduce the fluctuations in a light beam below the quantum limit by exploiting polariton-polariton interactions. This idea was investigated by H. Eleuch [153, 154], G. Messin [76], J. Ph. Karr [33] and A. Baas [132]. As we saw in section 2.2, the ($\boldsymbol{k} = 0\ \mu\text{m}^{-1}$) polariton medium is similar to a Kerr medium since the nonlinearity is of $\chi^{(3)}$ type. In agreement with this, a bistable behavior is present. The Kerr nonlinearity can also influence the fluctuations of the polariton field and thus, through the polariton photonic component, the fluctuations of the emitted beam. Therefore polaritons nonlinearities can be used for the generation of squeezed states in the microcavity emission.

In their thesis [33, 132] J. Ph. Karr and A. Baas investigated both theoretically and experimentally this mechanism for a planar microcavity similar to the one used throughout Part I. Detailed calculations, the results of which we present in section 7.2, led to the conclusion that a noise reduction below the SQL is possible. In the experimental part of J. Ph. Karr's thesis it was proven that polariton nonlinearities are able to strongly modify coherent states, resulting in a strong quadrature dependence on the fluctuations. The experimental detection of squeezing below the SQL came in 2004, and was reported in A. Baas' thesis [132] as well as in a publication [8]. While this is a convincing proof of concept, the measured squeezing was only 4% below the SQL.
In this chapter, we draw conclusions from this previous studies and achieve squeezing values up to an order of magnitude better, thanks to an optimized sample. As we will see in section 7.3 one of the main optimization is the 0-dimensional shape of the microcavity, from now on called a micropillar.

7.1. Noise properties of a scalar field

In order to describe the non-classical states of light that can be generated from polaritons, in this section we introduce the relevant notions of fluctuations, Standard Quantum Limit (SQL) and squeezed states. In the experiment we use only one spin population of polariton. Therefore, as in Part I, we can treat polaritons as a scalar field.

7.1.1. Notions of fluctuations and shot-noise

Let us consider a single mode of the electromagnetic field, characterized by an angular frequency ω, a wavevector $\boldsymbol{k}$ and a polarisation ϵ. In classical physics, the electric field associated is:

$$E(t) = E_P \sin(\omega t) + E_Q \cos(\omega t), \tag{7.1}$$

E_P and E_Q are the two field quadratures. In a quantum approach E_P and E_Q become two operators, called quadrature operators. They are given by $\hat{E}_P = \mathcal{E}_0 \left(\hat{a}_\omega + \hat{a}_\omega^\dagger\right)$ and $\hat{E}_Q = i\mathcal{E}_0 \left(\hat{a}_\omega - \hat{a}_\omega^\dagger\right)$, where $\hat{a}_\omega$ ($\hat{a}_\omega^\dagger$) is the photon annihilation (creation) operator. $\mathcal{E}_0 = \sqrt{\frac{\hbar\omega}{2\epsilon_0 c V}}$ is a normalization constant for a quantization volume V. Since $\hat{a}_\omega$ and $\hat{a}_\omega^\dagger$ obey the bosonic commutation relation, the two quadrature operators do not commute:

$$[\hat{E}_P, \hat{E}_Q] = 2i\mathcal{E}_0^2. \tag{7.2}$$

This commutation relation imposes a limit to the product of the two operator uncertainties. Therefore we have the Heisenberg inequality:

$$\Delta\hat{E}_P \Delta\hat{E}_Q \geq \mathcal{E}_0^2, \tag{7.3}$$

where the standard deviation on an operator $\hat{O}$ is:

$$\Delta\hat{O} = \sqrt{\left\langle \hat{O}^2 \right\rangle - \left\langle \hat{O} \right\rangle^2}. \tag{7.4}$$

The notation $\langle ... \rangle$ corresponds to the average over the considered quantum state.

The previous definition of $\hat{E}_P$ and $\hat{E}_Q$ corresponds to an arbitrary choice of the phase origin in the Fresnel space. A more general definition for any quadrature basis rotated by an angle θ in the Fresnel space is:

$$\hat{E}_{P\theta} = \mathcal{E}_0 \left(\hat{a}_\omega e^{i\theta} + \hat{a}_\omega^\dagger e^{-i\theta}\right), \tag{7.5}$$

$$\hat{E}_{Q\theta} = i\mathcal{E}_0 \left(\hat{a}_\omega e^{i\theta} - \hat{a}_\omega^\dagger e^{-i\theta} \right). \tag{7.6}$$

The Heisenberg inequality (7.3) is still valid with the generalized quadrature operators, for any θ.

If the considered mode is the vacuum, then there is no favored phase and all quadratures have the same fluctuations. These fluctuations are minimal and equal to $\mathcal{E}_0$ ($\Delta E_{P\theta} = \Delta E_{Q\theta} = \mathcal{E}_0$). $\mathcal{E}_0$ thus defines a reference for fluctuations called the Standard Quantum Limit (SQL). The Heisenberg inequality holds for the products of two conjugate quadratures. It does not forbid for one of them to go below the SQL, provided the conjugate operator has a standard deviation sufficiently high to respect the inequality. Such non-classical states are called *squeezed states*.
As represented on figure 7.1 a coherent state can be deformed into a squeezed state when propagating through a Kerr medium. Kerr media have an optical index that varies with the intensity. Therefore the phase acquired through propagation is different depending on the intensity fluctuations. If no noise is added during the process then the state becomes non-classical and one of the quadrature is squeezed below the SQL. Statistically, this means that the photon stream is antibunched: photons are arranged more orderly than in a state with fluctuations at the SQL, and their statistic follows a sub-Poisson law.

7.1.2. Quantum fluctuations for a laser

A CW laser in a regime far above the lasing threshold produces a state called a *coherent state*. A coherent state $|\alpha\rangle$ can be defined as the eigenmode of the annihilation operator $\hat{a}$, with the eigenvalue α. Therefore the vacuum is a peculiar case of a coherent state for which $\alpha = 0$. Hence, coherent states have the same uncertainties as the vacuum:

$$\Delta E_{P\theta} = \Delta E_{Q\theta} = \mathcal{E}_0, \tag{7.7}$$

for any θ. It follows that for a coherent state all quadratures are defined with the best possible precision allowed by quantum mechanics. These states are the closest to classical states. This is why coherent states are also sometime called *semi-classical states*. Coherent states are at the SQL, and their photon statistic follows a Poisson law.

7.1.3. Effect of losses on squeezing

Once a source generates squeezed states of light, the amount of squeezing is known through a measurement. Due to an imperfect transmission during the propagation to the detection setup or due to an imperfect quantum efficiency in the detectors, a fraction of the

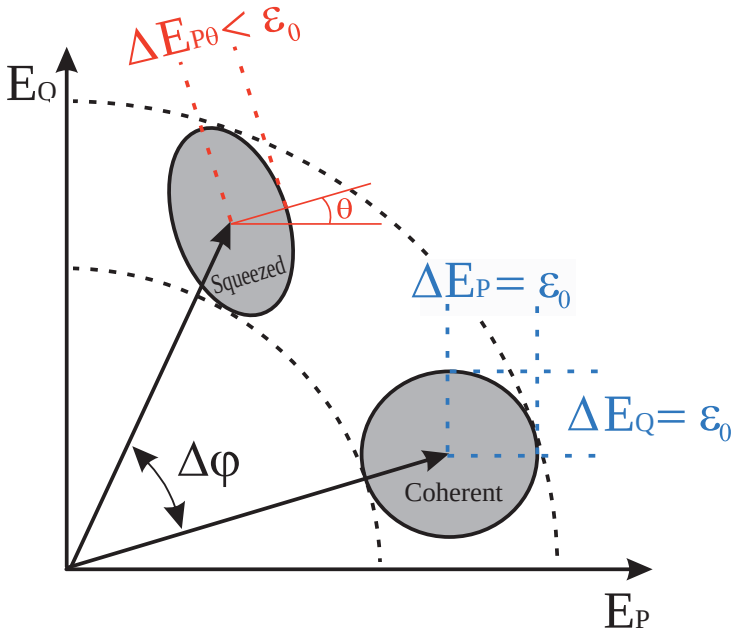

Figure 7.1.: Fresnel space representation of squeezing – Intensity-phase vector space (Fresnel space) in the arbitrary (P, Q) quadrature basis, on which are represented a coherent state and a squeezed state. The coherent state has isotropic, minimal (at the SQL) fluctuations $\Delta P = \Delta Q = \mathcal{E}_0$ under the laws of quantum mechanics. Fluctuations in the squeezed state are not isotropic, which allows a quadrature θ to possess a noise ΔP_θ below the SQL. A light field can be transformed from the former to the latter when propagating in a nonlinear medium possessing a Kerr-type nonlinearity. During this propagation a global phase $\Delta\varphi$ is gained, and the optical index being intensity-dependent, the state is deformed due to its fluctuations.

signal is lost. This corresponds to a fraction of the photons that are not detected. Which of the photons are lost is random and follows a Poisson statistic. Therefore the loss of photons, as a result of imperfect photon collection and detection, randomizes the statistical properties of squeezed states. As a result, the photon statistic tends toward a Poisson law and the squeezing is reduced when increasing the losses. The level of randomization is proportional to the fraction of losses. Therefore, effects such as attenuation or scattering reduce the degree of squeezing, and must be avoided as much as possible. However losses being present in any realistic system, it is important to measure them in order to infer the actual squeezing (as generated by the source) from the detected value.

7.2. Generation of squeezing in a polariton field

The polariton effective Kerr nonlinearity appears under the degenerate four wave mixing condition. We will therefore consider only the mode $\boldsymbol{k} = 0\ \mu\text{m}^{-1}$, with a quasi-resonant pumping.

Writing the Hamiltonian in the polariton basis offers a clear physical picture for the involved processes. However in order to write a precise evolution equation for the system, it is necessary to go back to the exciton-photon basis and take into account both the exciton and photon reservoirs. We will see that this approach leads to a non-averaged polariton evolution equation, unlike the Gross-Pitaevskii treatment derived in chapter 2. This allows the calculation of the polaritonic and photonic fields fluctuations and to predict the noise reduction in the cavity emission.

7.2.1. The Heisenberg-Langevin equation

From chapter 1 we can write the nonlinear Hamiltonian in the photon-exciton basis, for the mode $\boldsymbol{k} = 0\ \mu\text{m}^{-1}$:

$$\hat{H} = E^{exc}_{\boldsymbol{k}=0}\hat{b}_0^\dagger\hat{b}_0 + E^{ph}_{\boldsymbol{k}=0}\hat{a}_0^\dagger\hat{a}_0 + \frac{\hbar\Omega_R}{2}\left(\hat{a}_0^\dagger\hat{b}_0 + \hat{b}_0^\dagger\hat{a}_0\right) + \frac{V_0}{2}\hat{b}_0^\dagger\hat{b}_0^\dagger\hat{b}_0\hat{b}_0. \tag{7.8}$$

It is simply the linear Hamiltonian (1.34) completed with the "Kerr type" nonlinearity due to Coulombian interaction between excitons.

We consider the $\hat{a}_0$ and $\hat{b}_0$ operators to undergo a slow evolution. In the referential rotating at the laser frequency, we write:

$$\hat{a}(t) = \hat{a}_0(t)e^{i\omega_L t}, \qquad \hat{a}^\dagger(t) = \hat{a}_0^\dagger(t)e^{-i\omega_L t}, \tag{7.9}$$

$$\hat{b}(t) = \hat{b}_0(t)e^{i\omega_L t}, \qquad \hat{b}^\dagger(t) = \hat{b}_0^\dagger(t)e^{-i\omega_L t}. \tag{7.10}$$

We now write the equation evolution for $\hat{a}(t)$ and $\hat{b}(t)$. It is crucial to take into account their own decay rates γ_{ph} and γ_{exc} and the fact that each operator is coupled to a different reservoir. Indeed, $\hat{b}(t)$ is coupled to the exciton reservoir $B^{in}(t)$ and $\hat{a}(t)$ to the incoming laser photon reservoirs A_1^{in} and A_2^{in} . Note that there are two photon reservoirs: one for each side of the sample. Since the laser only pumps one side, A_2^{in} will represent the

vacuum. We obtain [33]:

$$i\hbar\frac{d\hat{a}}{dt} = (\Delta_a - i\hbar\gamma_{ph})\hat{a} + \frac{\hbar\Omega_R}{2}\hat{b} + i\hbar\left(\sqrt{2\gamma_1}A_1^{in} + \sqrt{2\gamma_2}A_2^{in}\right), \tag{7.11}$$

$$i\hbar\frac{d\hat{b}}{dt} = (\Delta_b - i\hbar\gamma_{exc})\hat{b} + \frac{\hbar\Omega_R}{2}\hat{a} + V_0\hat{b}^\dagger\hat{b}\hat{b} + i\hbar\sqrt{2\gamma_{exc}}B^{in}, \tag{7.12}$$

where γ_1 (γ_2) is the leaking rate of the front (back) mirror as defined in section 2.2.1. $\Delta_a = E^{las} - E^{ph}_{\boldsymbol{k}=0}$ and $\Delta_b = E^{las} - E^{exc}_{\boldsymbol{k}=0}$ are respectively the cavity-laser detuning and the exciton-laser detuning. The equations for the evolution of $\hat{a}^\dagger$ and $\hat{b}^\dagger$ are simply the hermitian conjugates of (7.11) and (7.12).

Now having the correct evolution equations for $\hat{a}$ and $\hat{b}$, we can go back to the polariton basis. We define the upper and lower polariton operators in the rotating basis, respectively:

$$\hat{q}(t) = X_0\hat{a}(t) + C_0\hat{b}(t), \tag{7.13}$$

$$\hat{p}(t) = X_0\hat{b}(t) - C_0\hat{a}(t), \tag{7.14}$$

with similar definitions for $\hat{p}^\dagger(t)$ and $\hat{q}^\dagger(t)$. The evolution equation for the lower polariton branch is:

$$i\hbar\frac{d\hat{p}}{dt} = (\Delta - i\hbar\gamma)\hat{p} + V_0X_0^4\hat{p}^\dagger\hat{p}\hat{p} + i\hbar\left(X_0\sqrt{2\gamma_{exc}}B^{in} + C_0\left(\sqrt{2\gamma_1}A_1^{in} + \sqrt{2\gamma_2}A_2^{in}\right)\right). \tag{7.15}$$

We recognize the evolution of the stationary polariton field plus a coupling to three reservoirs. It interesting to note that if we take the mean value of (7.15) then $\left\langle A_2^{in}\right\rangle = 0$ (vacuum state) and $\left\langle B^{in}\right\rangle = 0$ (incoherent population). Therefore the steady-state condition for the mean value of (7.15) gives precisely the bistability equation (2.32).

As expected, the excitonic $\chi^{(3)}$ nonlinearity gives rise to an effective Kerr effect for polaritons. We will study in the next section the fluctuations properties of the polariton field and look at how the different parameters impact the generation of squeezed states. It is crucial to remember that in (7.15) the particle is not a photon but a polariton. This means that the field properties now depend on δ the photon-exciton detuning. Indeed, the nonlinearities strength as well as the coupling with the extracavity field depend on C_0^2 and X_0^2 the photonic and excitonic fractions.

7.2.2. Extra-cavity fluctuations

From (7.15) it is possible to compute the polariton noise behavior by separating the fluctuations $\delta\hat{p}(t)$ from the mean field value $\langle\hat{p}(t)\rangle$ ($\hat{p}(t) = \langle\hat{p}(t)\rangle + \delta\hat{p}(t)$) and using the correlation matrix formalism. Calculations to the first order in $\delta\hat{p}(t)$ in the Fourier space lead to the noise power spectrum $S(\Omega)$. The experimental analysis frequency is limited to $\sim 20\,\mathrm{MHz}$ (less than $100\,\mathrm{neV}$), which is three orders of magnitude below the typical polariton linewidth. Therefore $S(\Omega)$ can be calculated with the approximation $\Omega \to 0\,\mathrm{Hz}$, which is where the noise reduction is expected to be the strongest according to [155]. From there we can derive the observable noise of the emitted light.

These calculations were previously done in our group [33, 132], and we will present here their results. The parameters explored in [33, 132] focus on the photon-exciton detuning δ, the laser-polariton detuning Δ, and an adjustable parameter called β, the polariton fraction scattered to $\boldsymbol{k} \neq 0\,\mu\mathrm{m}^{-1}$ (multimode coupling). However with this linear approximation one of the quadrature fluctuations diverges in the bistable regime at thresholds. Therefore higher order corrections are necessary. This is why in [33, 132] the calculations were done for Δ and I tuned to be below the onset of bistability (sub-bistable regime), where no threshold is present. However we expect these results can be extrapolated to when an actual bistable behavior exists (bistable regime).

Additionally it is also possible to use the coupled exciton-photon Heisenberg Langevin equations (7.11) and (7.12) to directly compute the fluctuations of the outgoing light field. This approach was used by M. Bamba, at the time postdoc in the group of C. Ciuti at the MPQ [1], with which we collaborated for this work to explore the noise behavior in the bistable regime.

Previous theoretical results

We briefly describe here the results obtained by J. Ph. Karr *et al.* in order to understand the impact of each parameter on the polariton field fluctuations. This is crucial to grasp under what circumstances one can hope to achieve the generation of squeezed states.

The main difference between our system and light in a Kerr cavity is the fact that the particles are polaritons rather than photons. We therefore have to take into account the photonic/excitonic fraction, controlled through the parameter δ. For $\delta < 0$, $C_0^2 > X_0^2$ and the system is mostly photonic. Thus the interaction effective strength is decreased but the coupling between the extra- and intra-cavity fields is enhanced, which results in

1. Laboratoire de Matériaux et Phénomènes Quantiques, Paris, France

diminished losses and a better noise reduction in the emitted light.
The strongest noise reduction happens around the bistability threshold [2]. This threshold depends on δ as well, as explicit in equation (2.38). Therefore, while decreasing δ towards negative values enhances the noise reduction, it also increases very rapidly the required intensity. This is easily understood as a compensation for the reduced nonlinearities (reduced excitonic fraction). On a planar microcavity, under the experimental conditions in [8], this means a compromise must be made between the exciton fraction losses and a reasonable intensity threshold. This is made visible on Figure 7.2 showing both the intensity threshold (right) and the maximum noise reduction (left). The choice made for the planar sample was $\delta \simeq 0$ meV [33, 8, 132].
The confinement provided by the micropillar design softens the need for a compromise since the polaritons remain on the same spot, while in the planar case the density is limited by polaritons propagating away from the pump spot [3]. Therefore the density for small pump spots is higher when confined, and we chose δ negative with the micropillars: a value of -5 meV was used in the present work. This corresponds to a photonic fraction of 89%.

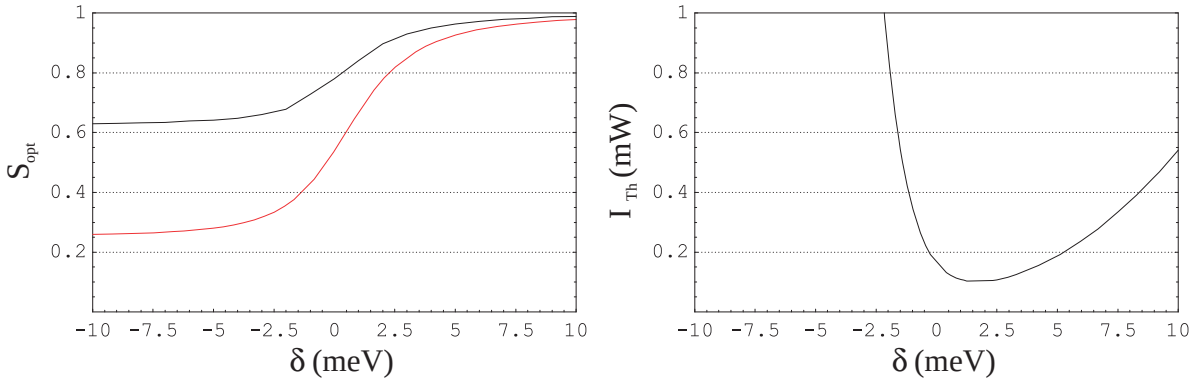

Figure 7.2.: δ-dependence – (Left) Evolution of the maximum achievable squeezing (minimum noise normalized to the SQL) with δ, the photon-exciton energy detuning. Maximum squeezing is meant in the sense that for each point Δ, I and the quadrature are set to optimize the noise reduction. Two values of β are used: 0 (red) and $5.\,10^{-5}$ (black). $\beta \neq 0$ acts like losses and reduce the maximum squeezing. (Right) Bistability intensity threshold as a function of δ. Both plots are from [33].

For a fixed δ, we can look at the impact of the laser- bare polariton energy detuning Δ on the noise. Figure 7.3 (left panels) is a plot of the maximum noise (in red), minimum noise (in green) and intensity noise (in blue) as a function of Δ for two fixed intensities

2. The expression "bistability threshold" is used both in the bistable and in the sub-bistable regimes. In the bistable regime this refers to the turning points, while in the sub-bistable regime this refers to the inflection point of the density $n_0(I)$ (equivalently, to the steepest point in the reflectance slope). The latter definition because this is where the two turning points appear at the onset of bistability.

3. This is because tightly focusing in one place implies a larger uncertainty on the wavevector, in addition to the polariton repelling each other away from the pump.

(one far in the sub-bistable regime and the other near the onset of bistability). The noise amplification (maximum noise) and de-amplification (minimum noise) are the strongest at the bistability threshold, as can be checked by looking at the reflectance curves (right panels). Near this point the intensity noise switches rapidly from minimum (just before the threshold) to maximum (just after the threshold). The minimum noise is constantly below the SQL, and so is the amplitude quadrature noise in a small zone before the threshold.
We see from the two examples in figure 7.3 that as we are near the bistable regime the behavior become sharper, with a stronger noise amplification and a slightly stronger de-amplification (from a minimal noise of 0.7 at $I = 0.5\,\mathrm{mW}$ to a minimal noise of 0.6 at $I = 1.4\,\mathrm{mW}$, at the threshold). Indeed, in the amplitude quadrature the zone where squeezing is achievable becomes smaller, but squeezing still happens before the threshold and noise amplification after the threshold. Extrapolating to the bistable regime, we expect this behavior to remain with the amplitude quadrature switch becoming steeper while the maximum (minimum) noise should continue to increase (decrease). Also since a bistable behavior is present in the density and the reflectance, it should also be visible in the noise for a fixed quadrature.

In order to predict by how much the polariton emission can be squeezed in the bistable regime, it is important to look at the maximum squeezing achievable by tuning the quadrature and Δ as a function of the pump intensity. This is presented in Figure 7.4 for several values of the multimode coupling constant β. Since Δ is tuned to give the maximum of noise reduction, each point is at the bistability threshold. Each plot converges toward a fixed squeezing value at high intensities. The $\beta = 0$ case tells us that for these parameters (in particular, $\delta = 0$) a squeezing of about 40% can be achieved at best.

In Figures 7.2 and 7.4, the parameter β acts like an additional noise. We will see in section 7.3 that with the micropillar design, the multimode coupling is strongly reduced and in our case we can consider $\beta \simeq 0$.

Calculations in the coupled exciton-photon basis

Due to divergences in the linearized treatment in the bistable regime, the calculations in [33, 132] are done in the sub-bistable regime. A numerical approach from the coupled exciton-photon Heisenberg-Langevin model allows to predict the noise properties in the bistable regime. Moreover, this model uses cavity parameters corresponding exactly to our micropillar sample, described in section 7.4. While the model is presented here, the calculations were done by M. Bamba, in collaboration with the group led by C. Ciuti.

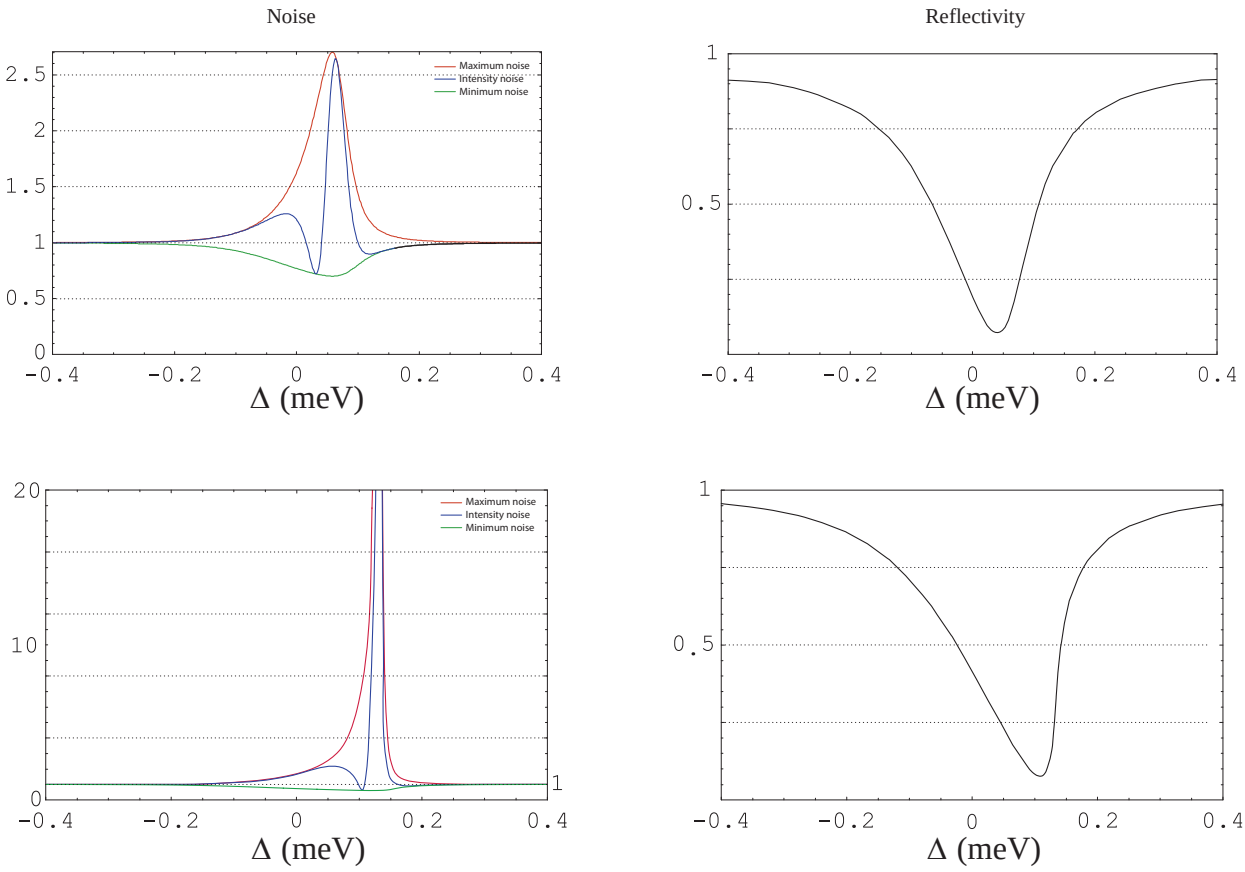

Figure 7.3.: Δ-dependence – Evolution of the maximum noise (red), the minimum noise (green) and the noise in the amplitude quadrature (blue) as a function of Δ for two values of the pump intensity: $I = 0.5\,\mathrm{mW}$ (top) and $I = 1.4\,\mathrm{mW}$ (bottom). The noise is normalized to the SQL. δ is fixed to 0 meV and $\beta = 0$ for all plots. The minimum noise for the upper panel is 0.7 at the threshold while it is 0.6 for the bottom panel. The reflectivity is plotted on the right panels for the corresponding pump intensities. The nonlinear process is maximum near the bistability threshold. From [33].

Due to the lateral confinement of the micropillar, the polariton modes are well identified and we can pump a single polariton mode. Therefore for the theoretical analysis, we simply consider a single cavity mode with frequency ω_c and an exciton state with frequency ω_x. The Hamiltonian of the coupled system (polariton) in the microcavity is:

$$\hat{H}_0 = \hbar\omega_\mathrm{c}\hat{a}^\dagger\hat{a} + \hbar\omega_\mathrm{x}\hat{b}^\dagger\hat{b} + \frac{\hbar\Omega_\mathrm{R}}{2}\left(\hat{a}^\dagger\hat{b} + \hat{b}^\dagger\hat{a}\right) + \frac{\hbar g}{2}\hat{b}^\dagger\hat{b}^\dagger\hat{b}\hat{b}, \tag{7.16}$$

Where $\hat{a}$ and $\hat{b}$ are the annihilation operators of a photon and an exciton, respectively, and Ω_R is the coupling strength (vacuum Rabi splitting) between the cavity photon and the exciton. The last term represents a third-order nonlinearity for the excitons with strength g. The polaritons are subject to an effective Kerr effect through it. Additionally,

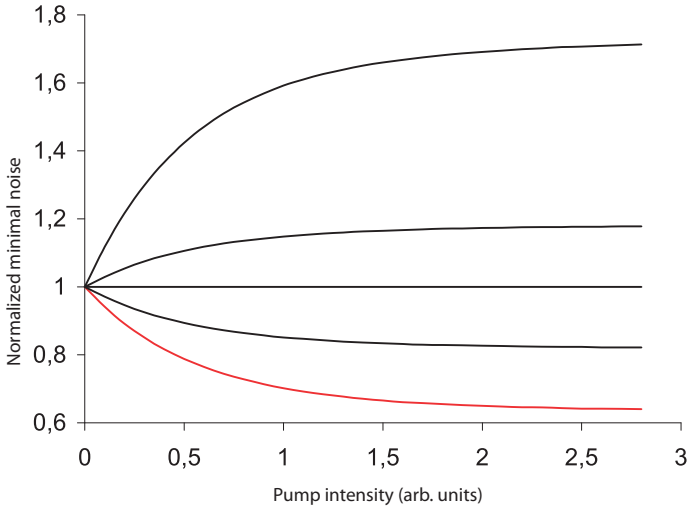

Figure 7.4.: Intensity dependence – Evolution of the minimum noise, normalized to the SQL, as a function of the pump intensity for different values of β (0, $5.\,10^{-5}$, 10^{-4}, $1.5\,10^{-4}$, $2.\,10^{-4}$, from bottom to top). The red curve corresponds to $\beta = 0$. The Δ are optimized so that each point is at the bistability threshold. The quadrature is optimized for the maximum noise reduction. δ is fixed to 0 meV for all plots. From [33].

considering the photonic and excitonic reservoirs, the quantum Langevin equations for the cavity photons and the excitons are, respectively, derived as:

$$i\frac{\partial \hat{a}}{\partial t} = \left(\omega_{\mathrm{c}} - \frac{i\gamma_{ph}}{2}\right)\hat{a} + \left(\frac{\Omega_{\mathrm{R}}}{2}\right)\hat{b} - i\sqrt{\gamma_{ph}}\left(\hat{a}_{\mathrm{in}} + F_{\mathrm{p}}e^{-i\omega_{\mathrm{p}}t}\right), \tag{7.17}$$

$$i\frac{\partial \hat{b}}{\partial t} = \left(\omega_{\mathrm{x}} - \frac{i\gamma_{exc}}{2}\right)\hat{b} + \left(\frac{\Omega_{\mathrm{R}}}{2}\right)\hat{a} + g\hat{b}^{\dagger}\hat{b}\hat{b} - i\sqrt{\gamma_{exc}}\hat{b}_{\mathrm{in}}. \tag{7.18}$$

Here, γ_{ph} and γ_{exc} are the dissipation rates of the cavity photon and exciton, respectively. $\hat{a}_{\mathrm{in}}$ and $\hat{b}_{\mathrm{in}}$ are the input operators from photonic and excitonic reservoirs, respectively, and we assume they have a zero average $\langle\hat{a}_{\mathrm{in}}\rangle = \langle\hat{b}_{\mathrm{in}}\rangle = 0$ (incoherent input). Instead, we explicitly consider an applied coherent pumping with amplitude F_{p} and frequency ω_{p}. Then, the input-output relation for the photon operators is expressed as:

$$\hat{a}_{\mathrm{out}} = \hat{a}_{\mathrm{in}} + F_{\mathrm{p}}e^{-i\omega_{\mathrm{p}}t} + \sqrt{\gamma_{ph}}\hat{a}. \tag{7.19}$$

From the above Langevin equations, we first calculate the mean fields of the cavity photon and exciton induced by the coherent pump. Supposing $\langle \hat{a} \rangle = \alpha e^{-i\omega_{\mathrm{p}} t}$ and $\langle \hat{b} \rangle = \zeta e^{-i\omega_{\mathrm{p}} t}$, the steady-state mean fields are:

$$i\frac{\partial}{\partial t}\alpha = \left(\omega_{\mathrm{c}} - \omega_{\mathrm{p}} - \frac{i\gamma_{ph}}{2}\right)\alpha + \left(\frac{\Omega_{\mathrm{R}}}{2}\right)\zeta - i\sqrt{\gamma_{ph}}F_{\mathrm{p}} = 0, \tag{7.20}$$

$$i\frac{\partial}{\partial t}\zeta = \left(\omega_{\mathrm{x}} - \omega_{\mathrm{p}} - \frac{i\gamma_{exc}}{2}\right)\zeta + \left(\frac{\Omega_{\mathrm{R}}}{2}\right)\alpha + g\left|\zeta\right|^2\zeta = 0. \tag{7.21}$$

Once the mean fields are determined, the reflectance is calculated via the input-output relation as:

$$\langle \hat{a}_{\mathrm{out}} \rangle = \alpha_{\mathrm{out}} e^{-i\omega_{\mathrm{p}} t} = \left(F_{\mathrm{p}} + \sqrt{\gamma_{ph}}\alpha\right) e^{-i\omega_{\mathrm{p}} t}, \tag{7.22}$$

$$R = \frac{\left|\langle \hat{a}_{\mathrm{out}} \rangle\right|^2}{\left|\left\langle \hat{a}_{\mathrm{in}} + F_{\mathrm{p}} e^{-i\omega_{\mathrm{p}} t} \right\rangle\right|^2} = \frac{\left|F_{\mathrm{p}} + \sqrt{\gamma_{ph}}\alpha\right|^2}{\left|F_{\mathrm{p}}\right|^2}. \tag{7.23}$$

The intensity noise is calculated by the fluctuation around the mean field value. Defining the fluctuation operators as $\delta\hat{a} = \hat{a}e^{i\omega_{\mathrm{p}} t} - \alpha$ and $\delta\hat{b} = \hat{b}e^{i\omega_{\mathrm{p}} t} - \zeta$, and linearizing the corresponding equations, the quantum Langevin equations are rewritten as:

$$i\frac{\partial}{\partial t}\delta\hat{a} = \left(\omega_{\mathrm{c}} - \omega_{\mathrm{p}} - \frac{i\gamma_{ph}}{2}\right)\delta\hat{a} + \left(\frac{\Omega_{\mathrm{R}}}{2}\right)\delta\hat{b} - i\sqrt{\gamma_{ph}}\hat{a}_{\mathrm{in}}, \tag{7.24}$$

$$i\frac{\partial}{\partial t}\delta\hat{b} = \left(\omega_{\mathrm{x}} + 2g\left|\zeta\right|^2 - \omega_{\mathrm{p}} - \frac{i\gamma_{exc}}{2}\right)\delta\hat{b} + \left(\frac{\Omega_{\mathrm{R}}}{2}\right)\delta\hat{a} + g\zeta^2\delta\hat{b}^\dagger - i\sqrt{\gamma_{exc}}\hat{b}_{\mathrm{in}}. \tag{7.25}$$

From these equations and the input-output relation, we can infer the fluctuation $\delta\hat{a}_{\mathrm{out}} = \hat{a}_{\mathrm{out}} e^{i\omega_{\mathrm{p}} t} - \alpha_{\mathrm{out}}$ of the output photons. The variance of the output field is expressed as:

$$(\Delta N)^2 = \left\langle \hat{a}^\dagger_{\rm out}\hat{a}^\dagger_{\rm out}\hat{a}_{\rm out}\hat{a}_{\rm out}\right\rangle - \left\langle \hat{a}^\dagger_{\rm out}\hat{a}_{\rm out}\right\rangle^2 = 2\left|\alpha_{\rm out}\right|^2\left\langle \delta\hat{a}^\dagger_{\rm out}\delta\hat{a}_{\rm out}\right\rangle + 2\,{\rm Re}\left[(\alpha^*_{\rm out})^2\left\langle \delta\hat{a}_{\rm out}\delta\hat{a}_{\rm out}\right\rangle\right]. \tag{7.26}$$

Then, the normalized intensity noise is expressed as:

$$\frac{(\Delta N)^2}{\left\langle \hat{a}^\dagger_{\rm out}\hat{a}_{\rm out}\right\rangle} = 2\left\langle \delta\hat{a}^\dagger_{\rm out}\delta\hat{a}_{\rm out}\right\rangle + 2\,{\rm Re}\left[\left(\frac{\alpha^*_{\rm out}}{|\alpha_{\rm out}|}\right)^2\left\langle \delta\hat{a}_{\rm out}\delta\hat{a}_{\rm out}\right\rangle\right]. \tag{7.27}$$

The correlations of the output are calculated from the ones of input operators. Here, we assume that the correlation of the photonic input as $\left\langle \hat{a}^\dagger_{\rm in}(t)\hat{a}_{\rm in}(t')\right\rangle = \left\langle \hat{a}_{\rm in}(t)\hat{a}_{\rm in}(t')\right\rangle = 0$ (extracavity photon vacuum) while the excitonic reservoir has an incoherent population, namely $\left\langle \hat{b}^\dagger_{\rm in}(t)\hat{b}_{\rm in}(t')\right\rangle = N_{th}\delta(t-t')$ and $\left\langle \hat{b}_{\rm in}(t)\hat{b}_{\rm in}(t')\right\rangle = 0$. We also assume that there is no correlation between the photonic and excitonic inputs.

The resulting minimum noise is predicted to be below the SQL on a wide region of the parameter space around the bistable thresholds. The noise behavior for the coupled exciton-photon model is in good agreement with the calculations done in the polariton basis. The best achievable squeezing is about 75%, close to the extrapolated value from [33, 132], for a very negative δ detuning and with no multimode coupling ($\beta = 0$), in the bistable regime. As expected this maximum squeezing happens at the bistablity threshold. The new calculations complete the ones previously done in [33, 132] in the polariton basis and together they can predict the noise behavior for polaritons across a wide region of the parameter space. This is unlike what can be found in the literature, as each article probed a limited set of parameters [155, 156, 8].

7.3. Squeezing in polaritons: context

7.3.1. Advantages of polaritons

While very efficient sources of non-classical light, essentially based on bulk non-linear crystals, have been developed in the last twenty years, the quest for integrated quantum sources is a major challenge for the cutting edge research activity in the field of quantum information technologies. In this context polaritons offer the appealing possibility to generate non-classical states of light from an all-semiconductor, microscopic structure.

Even more interesting is the fact that such a polariton device would work in the continuous variable regime. Indeed, despite several theoretical proposals [157, 158] the continuous variables regime has seen so far only very few experimental achievements [159, 8, 43] of squeezed states of light in semiconductor materials. Additionally, as we will see in the following, the working intensity zone is substantially lower than in other semiconductor systems. In small-size devices such as the micropillars we use here, this means the power needed for such devices (5-20mW) is lower than in previous experiments [159].

7.3.2. Previous experimental results on a planar microcavity

The challenge that originally attracted the attention of our group - namely the polariton-based generation of light squeezed below the SQL - was met by J. Ph. Karr *et al* on a planar microcavity [8]. A planar microcavity usable both in transmission and reflection modes is pumped with a coherent state at normal incidence. The microcavity emission shows in the sub-bistable regime a noise reduction below the SQL just before the bistability threshold. To achieve this, a spatial filtering was necessary in order to select the light coming from only a small sample area possessing a homogeneous set of parameters.

Figure 7.5 is the main result from [8] and shows the noise amplitude dependence on the quadrature. This type of detection is called a *homodyne detection* and will be described later as one of the two detection methods used for noise measurements. The noise is below the SQL by about 4% after the loss corrections (cf. discussion 7.1.3). These corrections are simply the loss coefficient in the detection setup: the non-perfect transmission and the photodiodes detection efficiency.

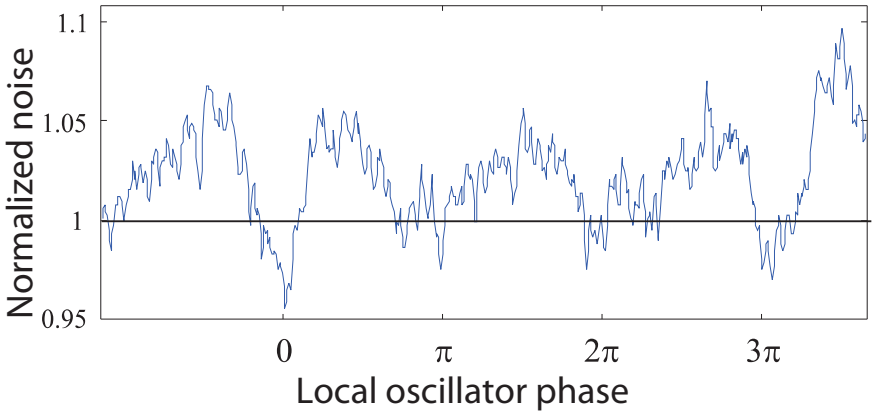

Figure 7.5.: Homodyne detection – Extracavity light field fluctuations amplitude as a function of the quadrature. The dependence on the quadrature is an unambiguous signature that polariton nonlinearities can deform a coherent state. Intensity noise reduction of about 4% below the SQL is visible. From [132].

7.3.3. Micropillar design

Significant improvements of this first result were prevented by the excess noise coming from the intrinsic multimode nature of the emission in a planar microcavity, which is characterized by a continuum of polariton modes. In addition to allowing the population of $\boldsymbol{k} \neq 0\ \mu\text{m}^{-1}$ modes through polariton repulsion and polariton-phonon scattering (non-zero values of β), it is favorable to the coupling with lattice phonons, a non-radiative loss channel. Very recently, it has been predicted [156] that a large amount of squeezing could be achieved by quantizing the in-plane polariton field modes via a geometric confinement ("strong localization limit"). This tight confinement separates the modes energetically, severely reducing any multimode coupling responsible for increased excess noise and reduced quantum effects. In the present thesis we apply this method in a controlled way making use of semiconductor micropillars [3, 37]. This way only one mode can be considered and we can set $\beta \simeq 0$. Similarly any coupling to the phonon reservoir is drastically decreased, due to the lowered mode density, by virtue of Fermi's golden rule.

The micropillars are etched into a planar microcavity sample possessing a thickness gradient for the optical cavity. This way each pillar has a slightly different exciton-photon detuning δ and this parameter can be chosen by selecting a pillar out of the many present on the sample. The precision on δ is high since the typical pillar diameter is of the order of a few microns. This small size also has the advantage of a small working region (small surface), meaning that the spatial filtering present in [8] is automatically implemented without losses. Additionnally, this small surface and the confinement ensure high polariton densities for a small pump power. Additionally, it has been shown that the confinement increases the polariton-polariton interactions [160], enhancing the nonlinear effects. Therefore with the micropillar design it is possible to work with a strongly negative value of δ which, as we saw in 7.2.2, increases the photonic fraction. This results in a better squeezing value in the emitted light since the excitonic fraction X_0^2, acting like a loss term, is reduced.

Finally the Bragg mirrors themselves are optimized for a better noise reduction. First, the cavity finesse (about 700) is lower than for other cavities. This increases the value of γ and γ_{ph}, respectively the polariton and photon decay rates, which in turn maximizes the radiative to nonradiative decay ratio. This is important as it minimizes the impact of the nonradiative loss channels that add noise. In addition, the two Bragg mirrors do not have the same thickness: the bottom mirror is twice as thick as the top mirror. We thus have $\gamma_1 \gg \gamma_2$ and the cavity is optimized for reflection-configuration experiments.

All these optimizations result in an improved noise reduction in the pillar emission through the top mirror. In the next section we present the experimental results of

bistability and noise properties in a micropillar, and show a squeezing value of 37% below the SQL in the intensity noise.

7.4. Experimental setup: Sample, cooling and pumping

Here we present the experiment on the noise characterization for a micropillar-confined polariton emission. Section 7.4 and 7.5 describe the sample and the setup while the results are presented in section 7.6.

7.4.1. Sample

In our setup the sample is an array of microscopic-sized pillars. The pillars are fabricated by etching a λ GaAs microcavity containing two GaAs-InGaAs quantum wells, resulting in a polariton Rabi splitting of about 5 meV. The cavity finesse is on the order of 700, which gives a 0.1 meV polariton linewidth. Figure 7.6 shows the energy separation of the polariton modes due to the finite size of the pillar.

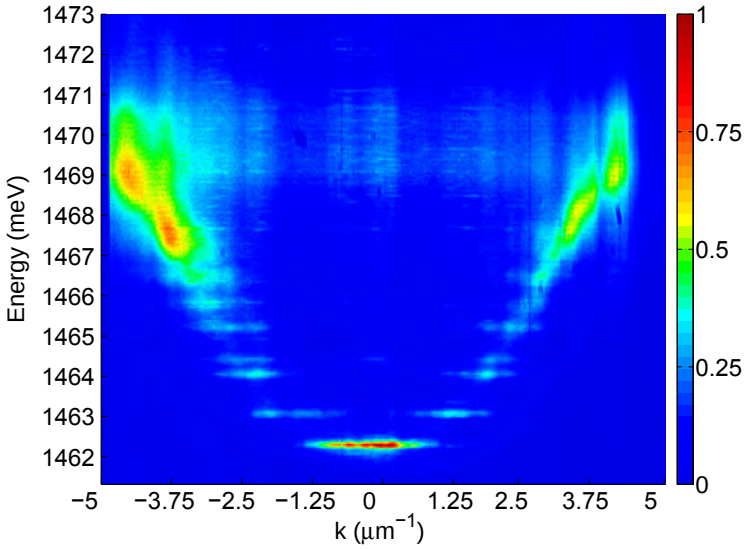

Figure 7.6.: Quantized dispersion curve – Dispersion curve for the 6 µm circular pillar used in the experiment (−5 meV exciton-photon detuning), obtained with a non-resonant pumping at 1550 meV. The lower polariton branch with several spatial modes and the weakly excited upper branch are visible. The modes are energetically separated and squeezing is protected against multimode coupling.

As represented on figure 7.7 (left) the cavity mirrors are asymmetric with the bottom Bragg mirror twice thicker than the top one: 30 pairs of $Al_{0.1}Ga_{0.9}As - Al_{0.95}Ga_{0.05}As$ versus 15 pairs for the top mirror. As previously discussed this optimizes the cavity for

noise reduction in the emitted field, in reflection configuration. The cavity is wedged in one direction, providing a large choice of photon-exciton detuning δ by selecting pillars placed at different positions on the chip. We can select the shape and size of the micropillars in order to choose the spatial distribution of the confined modes and their energy separation. Figure 7.7 (right) shows the large square-shaped pillars (width of 20 µm) and small square or round-shaped pillars (width from 6 µm to 2 µm) available on the studied sample. For the pump-pillar mode matching to be optimum, round pillars of 6 µm were preferred. The pillar height is about 10 µm, making the smallest ones very fragile.

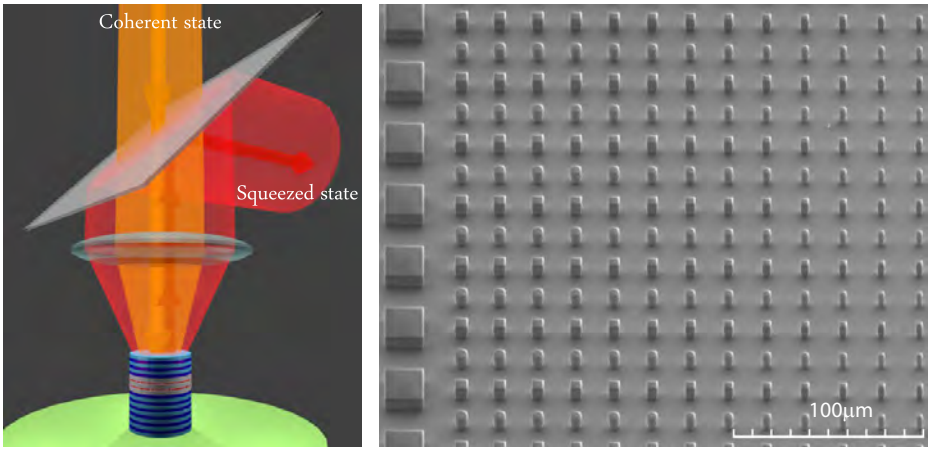

Figure 7.7.: Pillar and Sample – Left: principle of squeezed light production with a pillar-shaped microcavity. The microcavity is made of a pair of quantum wells (grey-red-grey layers) sandwiched by two Bragg mirrors (alternation of light blue and dark blue layers); the green layer is the substrate. The orange beam represents the pump laser arriving on the sample at normal incidence, slightly blueshifted with respect to the energy of the lower polariton branch. The red beam represents the squeezed light emitted by the squeezed polariton field present in the microcavity. **Right:** image of the sample obtained with scanning electron microscopy. The different shapes and sizes of the pillars are visible. The scale bar corresponds to 100 µm.

7.4.2. Laser source

The laser source is the same homemade Ti:Sa presented in section 3.1, with the addition of an intensity lock. Indeed, it is crucial to have laser fluctuation as low as possible (especially at low-frequencies and around the analysis frequency), whether classical and quantum.

If the laser is not in a coherent state at the analyzed frequency (7 MHz) then its quantum fluctuations are not minimal (they are wider than the SQL). This adds unnecessary noise to the polariton field and hinders the nonlinear noise reduction. Therefore we checked that our Ti:Sa is sufficiently far above the lasing threshold for the output state to be coherent.

The measured fluctuations were indeed at the SQL for frequencies above 1 MHz.
Secondly, as we saw in section 7.2.2, the noise behavior (and especially the intensity noise) is very sensitive on the distance to the bistability threshold. This means that the classical low frequency intensity fluctuations (due to polarization, mechanical or thermal fluctuations in the fiber or laser) will have a great impact on the system noise by randomly moving the system on the bistability curve.

In order to minimize the low frequency ($0 - 1$ MHz) fluctuations we implemented an intensity lock. It is made of a feedback loop acting on a Electro-Optical Modulator (EOM) coupled with a PBS. The error signal is collected after the fiber to take into account the thermal and mechanical fluctuations acting on the guided light. This is presented in figure 7.8. The result is a reduction by an order of magnitude of the fluctuations, from $\frac{\Delta I}{I} = 2\%$ to $\frac{\Delta I}{I} = 0.2\%$.
The output spatial mode is filtered by a 5 m long single-mode optical fiber shielded against

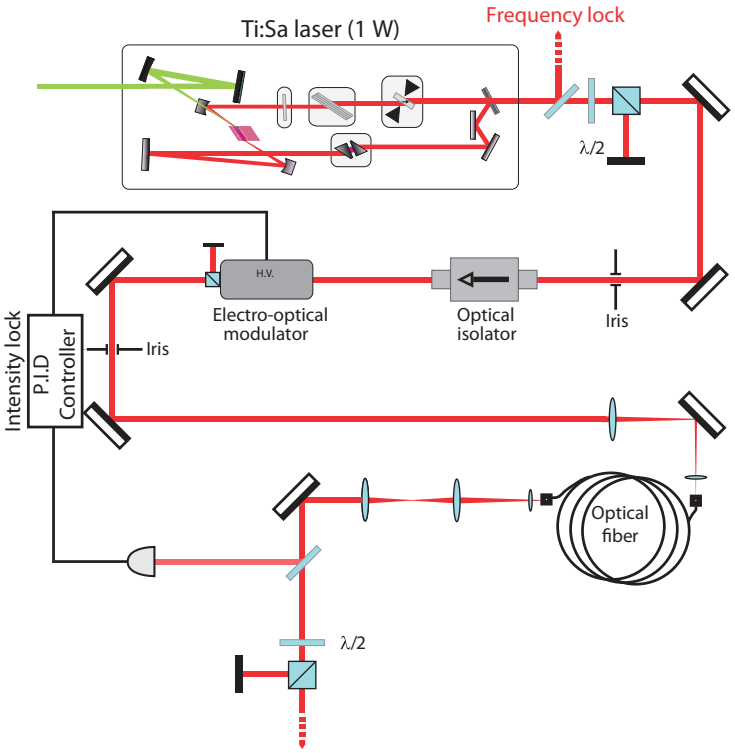

Figure 7.8.: Intensity lock – Schematic view of the EOM intensity lock. It is able to reduce the low-frequency fluctuations by an order of magnitude. From [132].

thermal fluctuations. The beam used to excite the sample is thus a TEM_{00}.

7.4.3. Cryogenic setup

The cryogenic setup used in the noise measurement experiments is almost the same as in 3.1. The only difference is that the vacuum pump is turned off to avoid its mechanical vibrations. When turned off, the pump acts like a simple pipe. The helium flow is assured by having a higher pressure in the helium storage dewar than the room pressure: the liquid is pushed by the pressure difference. The pressure can easily be built up from the helium natural evaporation in the dewar.

7.5. Experimental setup: detection

A *homodyne detection* gives access to the fluctuations in any quadrature of a given electromagnetic field. To that end this field must interfere with another field acting like a reference, called the local oscillator (LO). A piezoelectric transducer controls the phase difference θ between the LO and the measured field. The two fields have orthogonal linear polarizations. They are then recombined on a PBS. To make them interfere, we make use of a second PBS ahead of which is a half wave plate set to make the polarizations turn so that each field has the same projection on the second PBS basis. Two photodiodes collect the cube reflection (Ph1) and transmission (Ph2) (see figure 7.9).

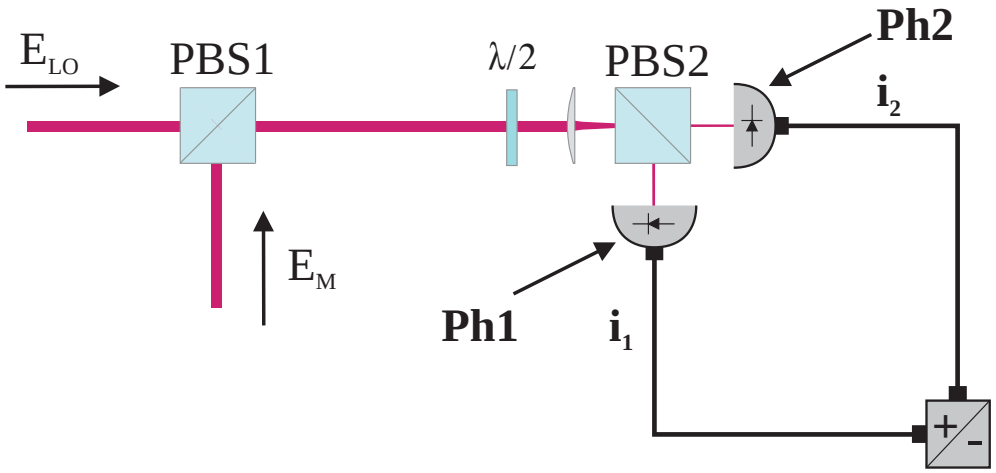

Figure 7.9.: Principle of homodyne detection – Schematic view of a homodyne detection. The field to be measured is mixed with a local oscillator (LO). From [33].

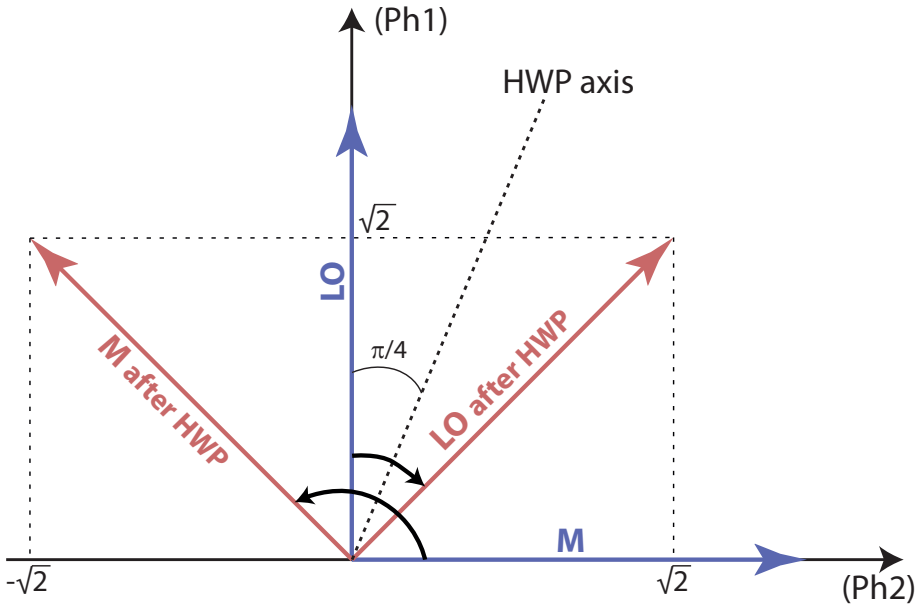

Figure 7.10.: Projection on the photodiodes – Scheme explaining the relative sign difference for each photodiode. Each photodiode (Ph1 and Ph2) corresponds to a PBS axis, on which the signal (M) and the local oscillator (LO) are projected. For the projection amplitudes to be equal, the half wave plate (HWP) must be placed at a $\frac{\pi}{4}$ angle relatively to one of the PBS axis. The arrows represent the orientation of the signal and the LO polarization in the PBS basis before (blue) and after (red) the HWP.

We call respectively E_{LO} and E_M the local oscillator field and the field to be measured as they hit the first PBS. The field detected by the Ph1 photodiode is thus equal to $\frac{(E_{LO}+E_M)}{\sqrt{2}}$ while Ph2 will detect a field equal to $\frac{(E_{LO}-E_M)}{\sqrt{2}}$. Indeed, due to the half-wave plate the two projections of E_M on the PBS2 basis acquire opposite signs relative to one another, while the projections of E_{LO} do not. See figure 7.10.

If we decompose E_{LO} and E_M into a negative (containing annihilation operators) and a positive frequency part (containing creation operators), and consider that the LO is much more intense than the signal, then $E_{LO} = A_{LO}(t)e^{-i\omega_L t} - A^*_{LO}(t)e^{i\omega_L t}$ and $\hat{E}_M = \hat{A}_M(t)e^{-i\omega_L t} - \hat{A}^\dagger_M(t)e^{i\omega_L t}$ (E_{LO} is treated as a classical field).

The photocurrent operator $\hat{i}$ from a photodiode with 100% of detection efficiency detecting a field $\hat{E} = \hat{E}^+ + \hat{E}^-$ is [161]:

$$\hat{i} = \hat{E}^+\hat{E}^-. \tag{7.28}$$

Ph1 and Ph2 then each deliver a photocurrent:

$$\hat{i}_1 = \frac{(A_{LO}(t)e^{-i\omega_L t} + \hat{A}_M(t)e^{-i\omega_L t})(A^*_{LO}(t)e^{i\omega_L t} + \hat{A}^\dagger_M(t)e^{i\omega_L t})}{2}, \tag{7.29}$$

$$\hat{i}_2 = \frac{(A_{LO}(t)e^{-i\omega_L t} - \hat{A}_M(t)e^{-i\omega_L t})(A^*_{LO}(t)e^{i\omega_L t} - \hat{A}^\dagger_M(t)e^{i\omega_L t})}{2}. \tag{7.30}$$

Each photocurrent is amplified by the same amount g. The detection signal I_- is then the difference between the two photodiodes signals and only contains the interference terms:

$$\hat{I}_- = g(\hat{i}_1 - \hat{i}_2) = g\left(A_{LO}(t)\hat{A}^\dagger_M(t) + \hat{A}_M(t)A^*_{LO}(t)\right). \tag{7.31}$$

We now decompose the fields into the mean part and the quantum fluctuations. The measured field is $\hat{A}_M(t) = \langle\hat{A}_M(t)\rangle + \delta\hat{A}_M(t)$. For the local oscillator, one must take into account the phase θ:

$$A_{LO}(t) = \left\langle A_{LO}(t)\right\rangle e^{i\theta}, \tag{7.32}$$

where $\langle\hat{A}_M\rangle$ and $\langle A_{LO}\rangle$ are real numbers. We find that the fluctuations in the difference signal are:

$$\delta I_-(t) = g\left\langle A_{LO}(t)\right\rangle\left(\delta\hat{A}_M(t)e^{i\theta} + \delta\hat{A}^\dagger_M(t)e^{-i\theta}\right), \tag{7.33}$$

7.5.1. Homodyne detection

The homodyne setup is realized with the LO beam much more powerful than the signal from the pillar. This justifies the classical treatment of the LO field in equation (7.33), where we see that the noise $S_{I_-}(\Omega)$ for I_- is proportional to $S_{E^\theta_M}(\Omega)$ for E^θ_M.

The LO fluctuation $S_{I^{LO}_-}(\Omega)$ is measured by blocking the measured beam. It is proportional to the vacuum noise power spectrum, since the LO is in coherent state. It thus defines the noise level associated with the SQL. The difference signal for the LO is:

$$\delta I^{LO}_-(t) = g\left\langle\hat{A}_L O(t)\right\rangle\left(\delta A_{vac}(t) + \delta A^\dagger_{vac}(t)\right). \tag{7.34}$$

Therefore under this strong LO approximation, the normalized noise in the quadrature θ is:

$$S^\theta(\Omega) = \frac{S^\theta_{I_-}(\Omega)}{S_{I^{LO}_-}(\Omega)}, \tag{7.35}$$

and after removing the electronic noise (also called the *dark noise*):

$$S^\theta(\Omega) = \frac{S^\theta_{I_-}(\Omega) - S_{dark}(\Omega)}{S_{I^{LO}_-}(\Omega) - S_{dark}(\Omega)}. \tag{7.36}$$

7.5.2. Balanced detection

Here we describe a method used to measure the amplitude quadrature. For this, the LO is blocked and we only consider the signal beam. Therefore θ is here fixed to 0.

Even in absence of LO, vacuum fluctuations exist and must be taken into account. It is then the measured beam that acts like a local oscillator for vacuum fluctuations entering through the PBS. Replacing $\hat{A}_M$ by A_{vac} and A_{LO} by $\hat{A}_M$ in (7.33) we get:

$$\delta I_-(t) = g \left\langle \hat{A}_M(t) \right\rangle \left(\delta A_{vac}(t) + \delta A_{vac}^\dagger(t) \right). \tag{7.37}$$

The fluctuations $S_{I_-}(\Omega)$ for I_- are thus proportional to the vacuum noise, which is a coherent state.

To gain access to the amplitude fluctuations of the measured beam we use the addition of the two photocurrents $\hat{I}_+ = g(\hat{i}_1 + \hat{i}_2)$, equal to:

$$\delta I_+(t) = g \left\langle \hat{A}_M(t) \right\rangle \left(\delta \hat{A}_M(t) + \delta \hat{A}_M^\dagger(t) \right). \tag{7.38}$$

We see that the fluctuations $S_{I_+}(\Omega)$ for I_+ are indeed proportional to the intensity noise of the measured beam. It is, in fact, what a single photodiode would detect from the undivided beam. The great advantage of the two-photodiodes system is the straightforward detection of the amplitude noise normalized by the SQL $S_{\theta=0}(\Omega)$:

$$S_{\theta=0}(\Omega) = \frac{S_{I_+}(\Omega)}{S_{I_-}(\Omega)}, \tag{7.39}$$

which is independent from both g and the mean value of the field. It is thus possible to measure the amplitude fluctuations only, without any LO. Like for the homodyne detection, the presented intensity noise measurements are obtained after subtraction of the dark noise from both the noise and the shot noise:

$$S_{\theta=0}(\Omega) = \frac{S_{I_+}(\Omega) - S_{dark}(\Omega)}{S_{I_-}(\Omega) - S_{dark}(\Omega)}. \tag{7.40}$$

7.5.3. Practical description

The pillars are cooled down to 4 K in the cryostat mounted in reflection configuration and excited with the Gaussian CW single-mode Ti:Sa laser. It is tuned to be quasi-resonant with the ground state level of the lower polariton branch. The laser beam is focused by a microscope objective treated with a near-infrared optimized coating and excites the

sample at normal incidence.
Upstream of the microscope objective, a motorized $\frac{\lambda}{2}$ plate coupled with a PBS allows us to finely control the pump power on the sample. A $\frac{\lambda}{4}$ plate placed between the beam splitter and the objective ensures that the light coming on the sample is circularly polarized. With the PBS, the $\frac{\lambda}{4}$ plate forms an optical circulator since the light re-emitted from the sample was estimated to be 95% circularly polarized, as expected from angular momentum conservation in a resonant setup. The light reflected from the cavity is thus collected and sent to the detectors.

The shape of the laser spot on the sample is Gaussian with a waist diameter of 5.5 µm, well matched to the round pillars with a diameter of 6 µm. We hence use a round micropillar of 6 µm, which ensures an optimal mode matching between its fundamental mode and the focalized excitation laser. The emitted light is collected by the same microscope objective (3 mm of working distance, 0.6 of numerical aperture and with an infrared coating) and sent through a telescope and a spatial filter, allowing us to select only the light coming out of the pillar or some specific region if needed.

The collected light is then split into two equal parts by a $\frac{\lambda}{2}$ plate associated to a polarizing beam splitter (PBS 2) and each beam is collected by a photodiode. The high frequency (AC) outputs of the two identical photodiodes (81% quantum efficiency, with home-made low-noise electronics) are added or subtracted with a passive circuit, amplified by a low-noise, high frequency amplifier and sent to a spectrum analyzer giving us the spectral noise power. The choice of addition or subtraction on the passive circuit allows to quickly switch between the measurement of the intensity noise or the SQL. The common mode rejection ratio of the balanced diodes (quality of classically correlated noise cancellation in the subtraction mode) was 45dB (tested at 7 MHz).

The spectrum analyzer scanning range can be set to zero (fixed frequency) in order to observe the time evolution, or non-zero in order to inspect the frequency dependence of the noise reduction. For a fixed analysis frequency a slow scan (on the order of 10 s) can be used to check the stability of the system (steady-state measurement). It is also convenient to check the noise evolution with a chosen parameter by making it change continuously with time. This is how we measured the noise versus intensity plots presented in the next section. For such scans, the spectrum analyzer was set to zero frequency span and centered at 7 MHz where the signal-to-noise ratio of the detection is maximum, with a sweep time ranging from 1 s to 20 s depending on the type of measurement. 7 MHz is a balance between the laser coherent state (above 1 MHz) and the photodiodes response time. The resolution bandwidth (spectral bandwidth of the measurement) was 300 kHz with a 30 Hz video bandwidth (temporal integration over a 30 Hz bandwidth). For the noise dependence on the pump power the motorized plate controlling the excitation power

on the pillar is scanned at the same time as the spectrum analyzer. We then compare the measured noise to the shot noise. The protocol involves recording the shot noise in difference mode, immediately switching to addition mode to record the intensity noise and then switching back to shot noise measurement (difference mode again) in order to check its stability. The dark noise was recorded after each measurement by measuring the electronic noise when the laser beam is blocked.

Homodyne setup

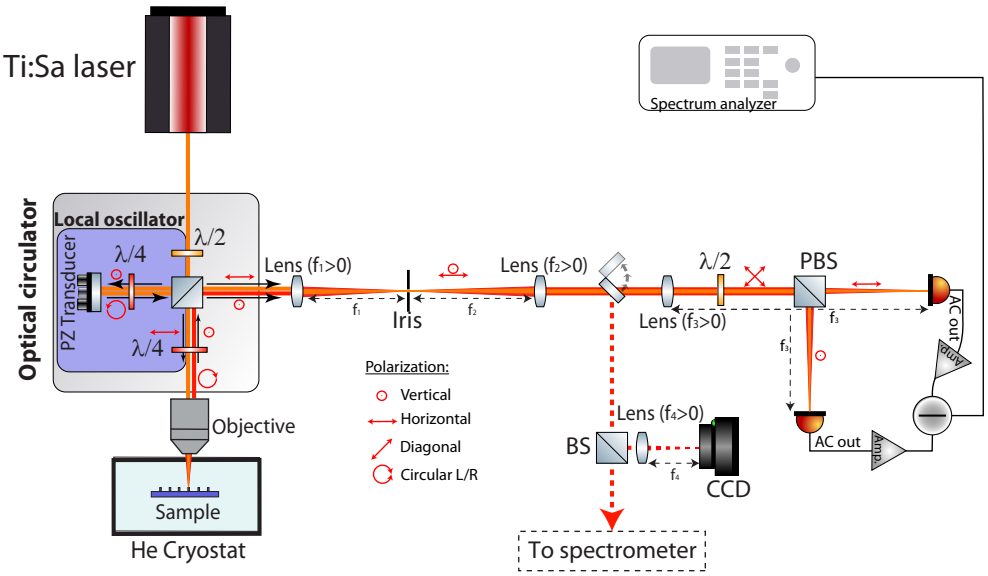

Figure 7.11.: Homodyne detection – Schematic view of the homodyne detection.

For the homodyne detection a portion of the pump laser is mixed on PBS 1 with the light emitted by the micropillar with an orthogonal polarization: it is the local oscillator. The relative phase between the local oscillator and the reflected field is controlled with the piezoelectric transducer-mounted mirror, allowing to measure all the quadratures. As we previously saw the AC output of the photodiodes are subtracted and the signal gives the noise in the quadrature of the reflected field that is in phase with the local oscillator.

Here it is important to note that the spatial mode of the sample emission can be strongly distorted by the non-linear interactions and it is no longer Gaussian-shaped at high polariton densities. An example is given in figure 7.12. For this reason it was found very difficult to achieve the mode matching with the local oscillator, necessary to have efficient homodyne detection. Indeed, an imperfect mode matching will act like a loss term for the detection and bring the signal down to SQL level. The special case of a low detuning Δ, such that we are in the sub-bistable regime, offers a low density of polariton even above threshold. There, the decreased nonlinearities have a much lower impact

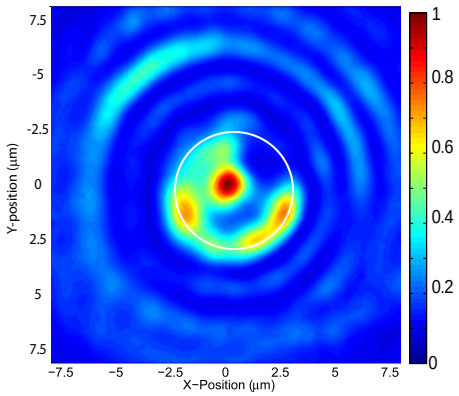

Figure 7.12.: Polariton density map of a round 6 µm pillar above the bistability threshold. The scale is linear and normalized to the peak intensity. The white marker delimits the pillar edge. The pump mode is Gaussian. We observe a strong nonlinear deformation. The absence of central symmetry aspect is likely due to an imperfect alignment ($k \neq 0$ µm).

on the spatial mode, which mostly retains its Gaussian nature. Under this condition proper homodyne detection was achieved (mode matching of 90%). However as we saw in section 7.2, such a low detuning is not optimal and thus the squeezing measured with the homodyne detection is lower than at the optimum detuning.

Balanced setup

Measuring the noise in the amplitude quadrature is easier and much less sensitive to ambient mechanical vibration than in another quadrature, since it does not require an interferometric setup. Moreover, since the amplitude quadrature squeezing is expected to happen just before the bistability threshold then its value should be very close the maximum squeezing. This is why the main measurement tool is the balanced detection setup, from which we can obtain the intensity fluctuations normalized to the SQL. The setup layout is presented in figure 7.13.

7.6. Results

Here we present the experimental results obtained for the confined polariton emission.

7.6.1. Bistable behavior

The bistability is visible in the density, the noise, the reflectance and the transmittance. The experiment being done in reflection configuration, the most convenient way of studying

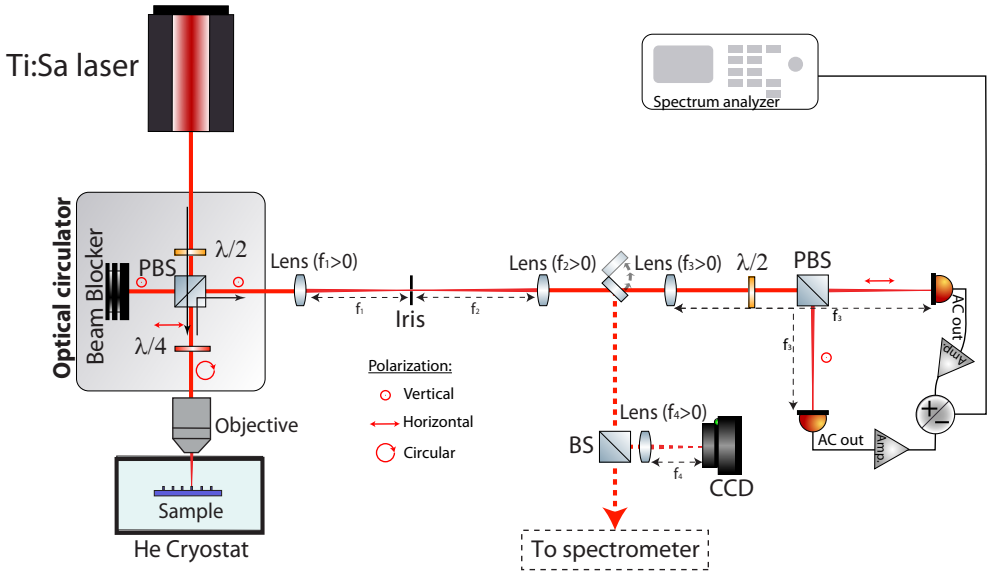

Figure 7.13.: Balanced detection – Schematic view of the balanced detection.

the bistablity is via the reflectance. This is easily done by observing the DC output of the photodiodes.

We observe a behavior in good agreement with the theory: the bistability is obtained for a critical value of $\Delta_c = \sqrt{3}\hbar\gamma$ and become wider and wider with increasing Δ. The experimental value of the sub-bistable - bistable transition is about $\Delta_c \simeq 0.19\,\text{meV}$, which respects the relation (2.35) since $\sqrt{3}\gamma \simeq 0.19\,\text{meV}$ for our sample. Figures 7.14 and 7.15 are example of sub-bistable behaviors and figures 7.16 and 7.17 show the bistability observed in the reflectance for, respectively, $\Delta = 0.10\,\text{meV}$, $0.19\,\text{meV}$, $0.21\,\text{meV}$ and $0.3\,\text{meV}$.

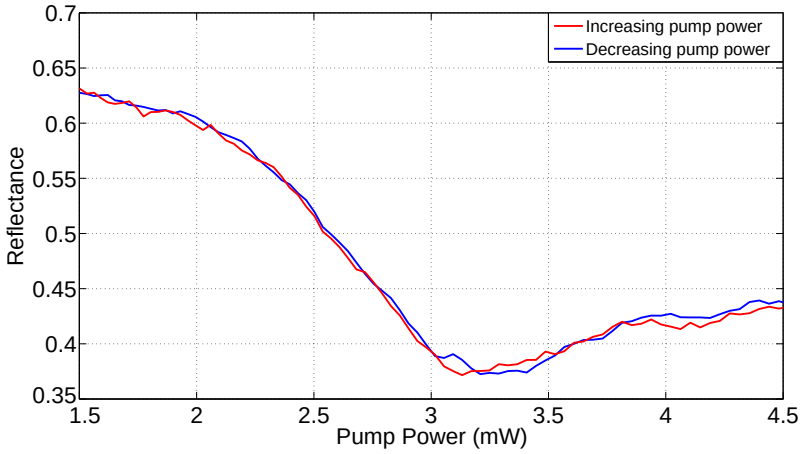

Figure 7.14.: Plot of the reflectance as a function of the pump power for a pump-polariton detuning of 0.10 meV. The pillar is 6 µm of diameter and the cavity detuning is $\delta = -5$ meV. The red line is obtained by increasing pump power and the blue line by decreasing it. The pump-polariton detuning is too low to observe any bistable behavior.

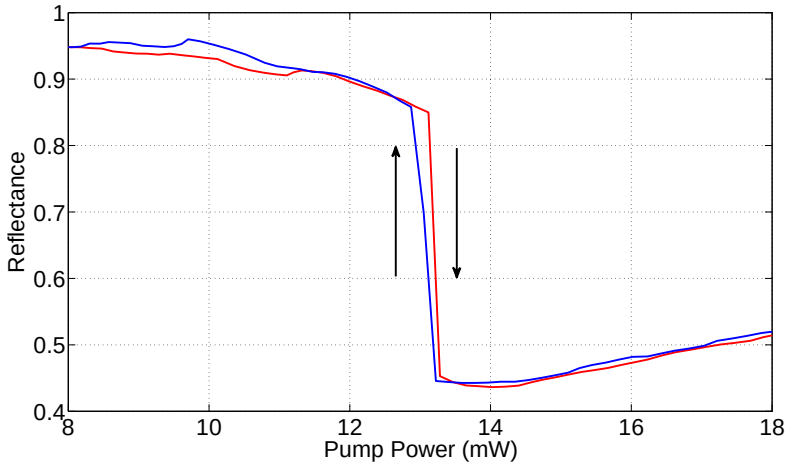

Figure 7.15.: Plot of the reflectance as a function of the pump power for a pump-polariton detuning of 0.19 meV. This corresponds to the onset of bistability. The pillar is 6 µm of diameter and the cavity detuning is $\delta = -5$ meV. The red line is obtained by increasing pump power and the blue line by decreasing it. The detuning is just high enough to show a small bistable behavior: this is the critical detuning Δ_C.

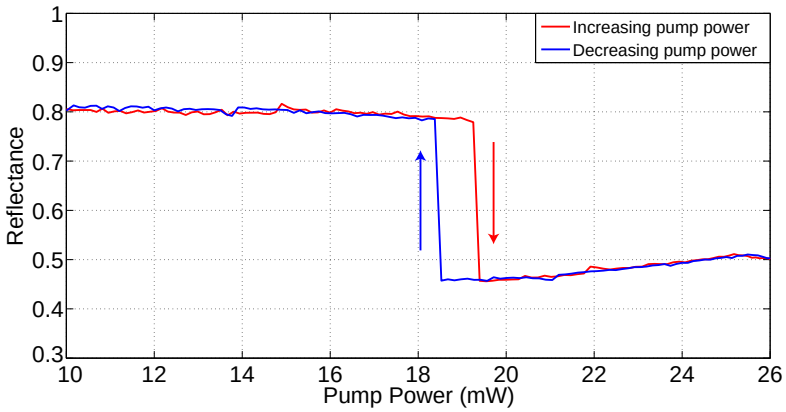

Figure 7.16.: Plot of the reflectance as a function of the pump power for a pump-polariton detuning of 0.21 meV. The pillar is 6 µm of diameter and the cavity detuning is $\delta = -5$ meV. The red line is obtained by increasing pump power and the blue line by decreasing it. The detuning is high enough to show a bistable behavior.

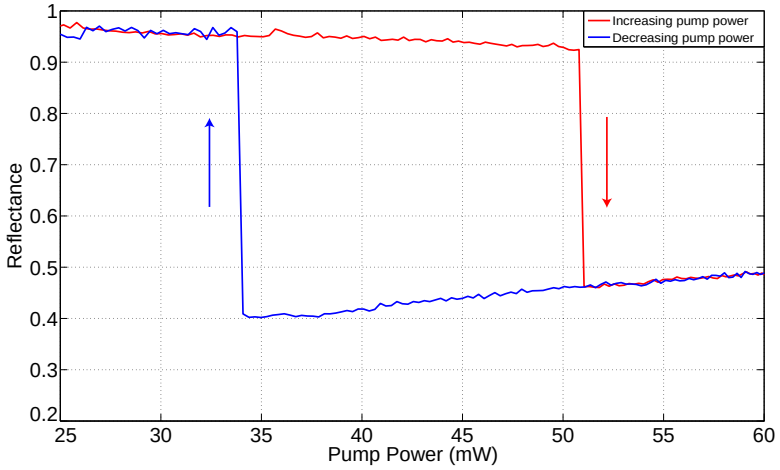

Figure 7.17.: Plot of the reflectance as a function of the pump power for a pump-polariton detuning of 0.30 meV. The pillar is 6 µm of diameter and the cavity detuning is $\delta = -5$ meV. The red line is obtained by increasing pump power and the blue line by decreasing it. Δ is now large compared to γ the polariton linewidth, and the hysteresis cycle is large.

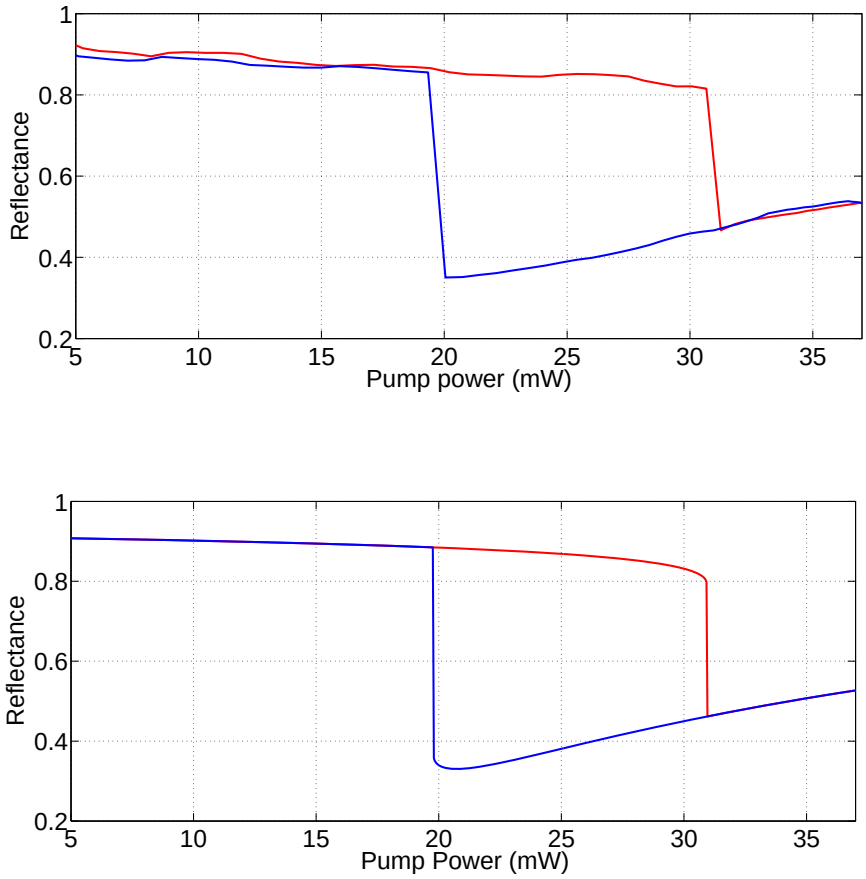

Figure 7.18.: Theory vs experiment - Experimental (up) and theoretical (bottom) plots of the reflectance as a function of the pump power for a pump-polariton detuning of 0.26 meV. The pillar is 6 μm of diameter and the cavity detuning is $\delta = -5$ meV. The red line is obtained by increasing pump power and the blue line by decreasing it.

7.6.2. Intensity noise as a function of the pump power

We now look at the intensity noise (fluctuations in the amplitude quadrature) as a function of the pump power at different fixed values of Δ. This is done with the previously described balanced detection.

As expected theoretically, a bistable behavior is also present in the noise for $\Delta > \Delta_C$. In the bistable regime, the two thresholds are separated and the noise is different for each threshold. The best noise reduction, where squeezing is observed, is present at the turning point reached when decreasing the pump intensity. This behavior is not surprising when considering that the lower bistability branch, being non-resonant with the laser, only yields increased fluctuations. Being the only turning point laying on the upper branch, it is the only one able to produce a noise reduction below the SQL. This behavior is well visible in figures 7.21 and 7.22, showing the bistability observed in the intensity noise for the same parameters as in the previous reflectance plots (0.21 meV and 0.3 meV, respectively).

In the sub-bistable regime the nonlinearities are not as important as in the bistable regime, and squeezing should thus be lower. While this is indeed observed, in the bistable regime the zone where intensity squeezing is present is much smaller and its detection rapidly become very hard due to residual low-frequency fluctuations. A good trade-off is to use $\Delta \simeq \Delta_c$, the onset of bistability. This is what is realized in figure 7.15 and 7.20 and this is where the best squeezing was observed, about -2 dB below the SQL after the corrections for the setup losses.

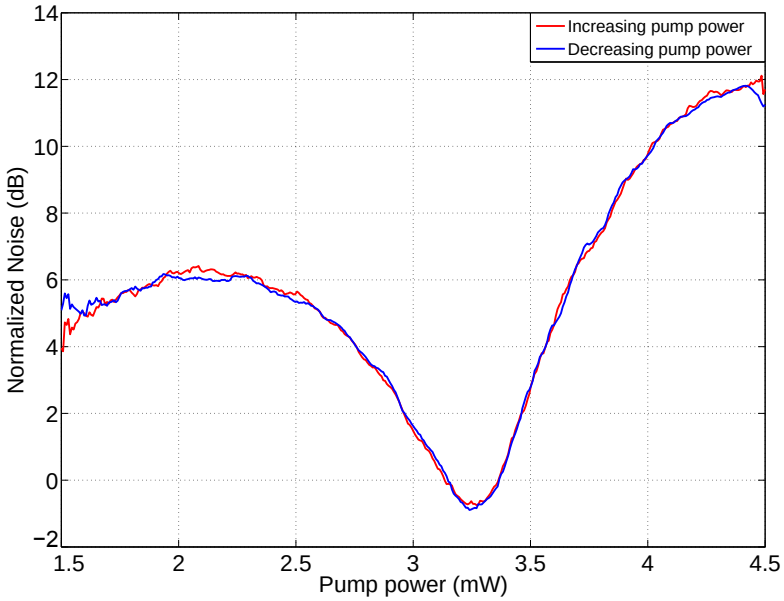

Figure 7.19.: Plot of the intensity noise as a function of the pump power for a pump-polariton detuning of 0.10 meV. The pillar is 6 µm of diameter and the cavity detuning is $\delta = -5$ meV. The red line is obtained by increasing pump power and the blue line by decreasing it. The squeezing here is about 0.8 dB (17% below the shot noise).

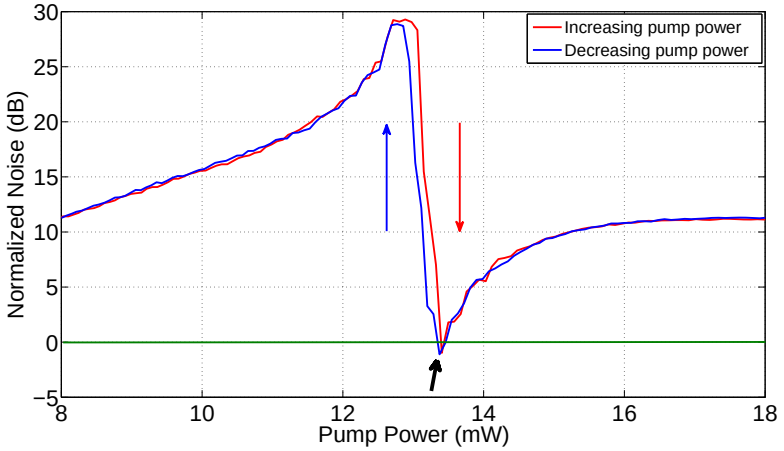

Figure 7.20.: Intensity noise (spectral noise power, semi-logarithmic scale) as a function of the pump power for a pump-polariton detuning of 0.19 meV. This corresponds to the onset of bistability. The pillar is 6 µm of diameter and the cavity detuning is $\delta = -5$ meV. In red is the curve obtained by increasing the pump power, in blue is the curve obtained by decreasing the pump power and the green line represents the shot noise (normalized to one). The black arrow shows the working point for the squeezing, at which figure 7.24 was recorded.

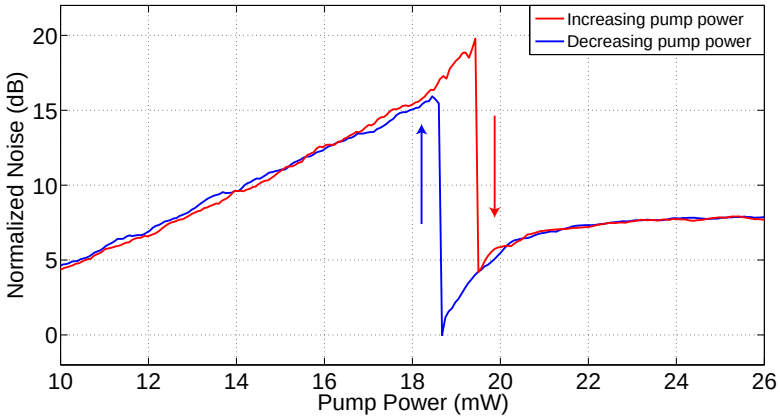

Figure 7.21.: Plot of the intensity noise as a function of the pump power for a pump-polariton detuning of 0.21 meV. The pillar is 6 µm of diameter and the cavity detuning is $\delta = -5$ meV. The red line is obtained by increasing pump power and the blue line by decreasing it. The hysteresis cycle is also present.

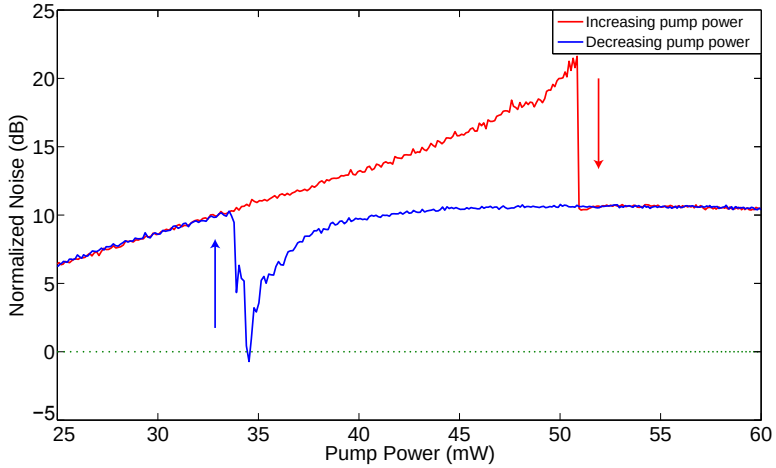

Figure 7.22.: Plot of the intensity noise as a function of the pump power for a pump-polariton detuning of 0.30 meV. The pillar is 6 µm of diameter and the cavity detuning is $\delta = -5$ meV. The red line is obtained by increasing pump power and the blue line by decreasing it.

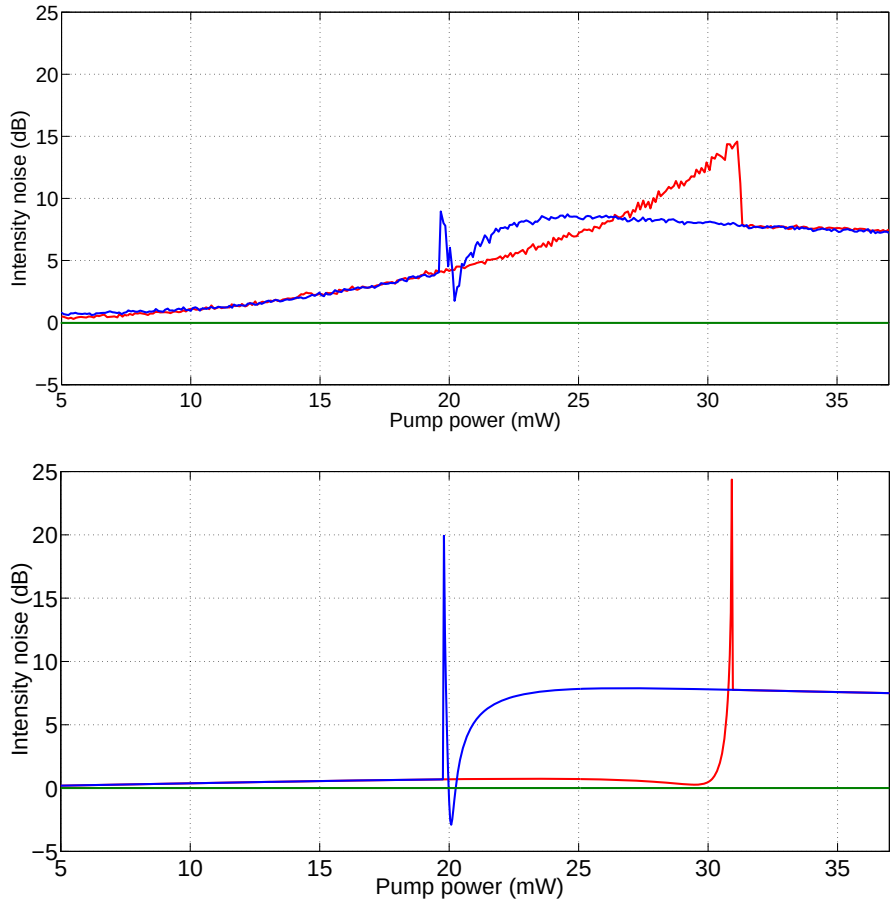

Figure 7.23.: Theory vs experiment - Experimental (up) and theoretical (bottom) plots of the intensity noise as a function of the pump power for a pump-polariton detuning of 0.26 meV. The pillar is 6 µm of diameter and the cavity detuning is $\delta = -5$ meV. The red line is obtained by increasing pump power and the blue line by decreasing it. The predicted behavior is in good agreement with the experiments for intensities above the thresholds. The discrepancy below the threshold is conjectured to be due to the cavity disorder, which is expected to play no role above threshold where the high polariton density smoothes out the irregularities.

7.6.3. Amplitude quadrature detection at fixed pump intensity

It is also important to check the stability of the setup producing the squeezed light. In addition this allows to record many data points and have a more accurate estimation of the squeezing value than the previous pump power scans. Figure 7.24 presents a record of the intensity noise versus time for all parameters fixed. They correspond to the optimum parameter values, for which $\Delta \simeq \Delta_c$ and the intensity is set to be just after the threshold (black arrow in figure 7.20).

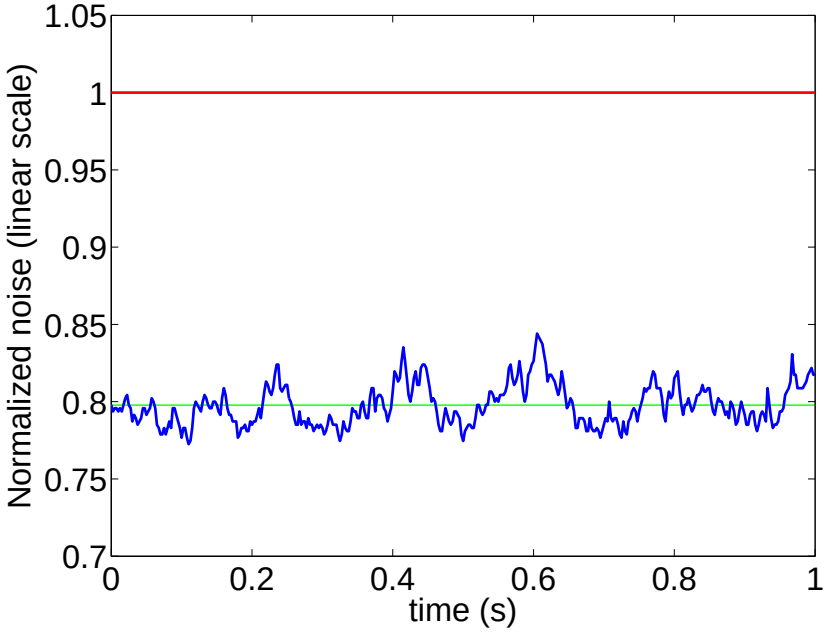

Figure 7.24.: Plot of the intensity noise (blue line) as a function of time for a pump-polariton detuning of 0.19 meV. The pillar is 6 µm of diameter and the cavity detuning is $\delta = -5$ meV. The red line is the SQL and the green line is the average noise, from which a squeezing value of 21% is derived.

The result is a stable noise reduction below the SQL by an amount of $20.3 \pm 1.5\%$ in the raw data. As with the previous results one needs to correct this measured value with the detection system losses (transmission rate and quantum efficiency of the detectors) in order to infer the actual, usable squeezing in the light. The correction is done by summing the loss terms and rescaling the raw data with the total transmission. In our case the losses are 43.3% (70% of total transmission and 81% of detection rate for each photodiode). The inferred squeezing at the output of the pillar is then $S_{ext} = 35.8 \pm 2.6\%$. This is about an order of magnitude better than the 2004 result [8], and demonstrates the efficiency of the confinement method for generating non-classical states with polaritons.

7.6.4. Amplitude quadrature spectrum

Additional information can be drawn from the previous measurement if one sets the spectrum analyzer to scan a non-zero range of frequencies. This is what was done in figure 7.25, in a range relevant with the detection bandwidth.
For $\Omega < 1\,\mathrm{MHz}$, a low frequency peak dominates the record. This originates from relaxation oscillations in the laser, which presents the same behavior. Between 2 MHz and 9 MHz the noise is reduced and constant below the SQL. Since the polariton linewidth is of the order of $\gamma = 330\,\mathrm{GHz}$, the dependence on Ω for such a short range is negligible. The fact that the squeezing in constant is thus coherent and shows the validity of the $\frac{\Omega}{\gamma} \simeq 0$ approximation. Above 9 MHz the measured squeezing continuously decreases, in accordance to the photodiodes response time. Indeed, above 20 MHz the photodiodes are unable to detect the signal and the record is dominated by the electronic noise.

7.6.5. Homodyne detection

Finally the noise at a single, fixed frequency is measured along all quadratures with the homodyne detection. The analysis frequency is set to 7 MHz like for the balanced detection, in the middle of the flat squeezed region visible in figure 7.25.
As explained in 7.5.3, the nonlinearities responsible for the nonclassical states are also responsible for a nonlinear spatial mode deformation. This means that the local oscillator and the signal are in a different spatial mode at the optimal working point. Therefore the mode matching is low and homodyne detection is very difficult. According to the theory as well as the balanced detection scans the maximum squeezing is not dramatically lowered when crossing to the sub-bistable regime. The mode deformation, however, is. Therefore we chose a lower value of Δ for the homodyne experiment. This allowed us to achieve a mode matching of about 90% with, in theory, an acceptable loss in squeezing (the maximum theoretical squeezing is 50%, versus 75% in the bistable regime).
The resulting quadrature scan is presented in figure 7.26 for a value of $\Delta = 0.10\,\mathrm{meV}$.

The dependence on the quadrature is clearly visible, showing strong nonlinearities in the noise behavior. As expected from the balanced detection and the previous studies, the noise drops below the SQL at the amplitude quadrature (0, π, 2π, ...). The measured squeezing value is here 16% before correction and 25% after. This lower value is due both to the choice of a sub-bistable regime and the fact that the homodyne detection is much more sensitive to mechanical instabilities.

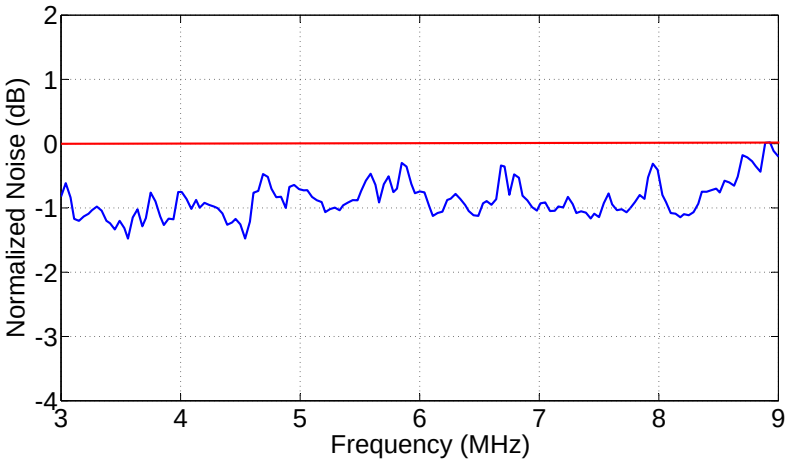

Figure 7.25.: Plot of the intensity noise (blue line) as a function of the analysis frequency for a pump-polariton detuning of 0.19 meV, after corrections. The pillar is 6 µm of diameter and the cavity detuning is $\delta = -5$ meV. The red line is the SQL.

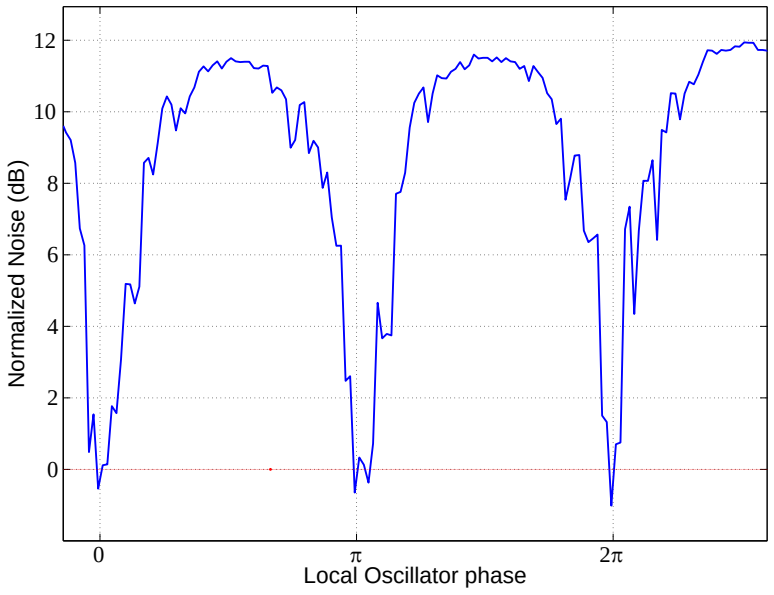

Figure 7.26.: Experimental measurement of squeezing with homodyne detection for a pump-polariton detuning of 0.10 meV. The minima were verified to be in the amplitude quadrature. The squeezing obtained from the average between the values at 0, π and 2π is 16% (−0.75dB) before corrections and 25% after corrections. The reduced value of the squeezing here is mainly due to the non-optimal laser-polariton detuning.

7.7. Conclusion

In conclusion we have experimentally demonstrated the strong enhancement of squeezed light generation with confined polaritons in semiconductor micropillars. The best intensity squeezing was inferred to be $35.8\% \pm 2.6\%$ below the shot noise limit and was confirmed by measurements with a homodyne detection setup. Several original optimizations allowed to reach these results. In particular, the design of the pillars ensures a near-perfect mode matching between the pump and the polariton field; the discretization of the polariton energy modes allows for a strong reduction of the excess noise coming from phonon coupling. The reduced reflectivity of the upper Bragg mirror relative to that of the bottom mirror enhances the emission of light toward the top of the pillar, optimizing the light collection. Finally the reduced quality factor of the cavity increases the radiative to non-radiative losses ratio which, together with the choice of a working point with a high photonic fraction, results in a larger squeezing in the emitted light. The squeezing values are now on the same order of magnitude as in other semiconductor systems [159], with the device size being smaller and the required power lower. These results demonstrate the improvement of intensity-squeezed light and light-matter fields brought by reduced dimensionality in semiconductor microstructures and open the way to the realization of low threshold integrated sources for the quantum information-processing technology.

Additionally it may be possible to design a sample with an even lower coupling mirror reflectivity (thinner top Bragg mirror) to further improve the noise reduction outside the cavity. Finally, designing a pillar optimized for transmission experiment might automatically ensure that no parasitic reflection of the pump laser reach the detection setup. This ensures that only light modified by the polariton field is observed and therefore increases the non-classicity of the observed light.

Appendix A.

Phase reconstruction method

To extract the polariton phase (and a reconstructed version of the amplitude) from the recorded interferogram, we use a technique known as digital off-axis holography [162]. It consists of performing a two-dimensional Fast Fourier Transform (FFT) of the interferogram. The fringes of the interferogram provide off-axis contributions in the Fourier plane, which can be differentiated from the zero-frequency contributions. Removing the zero-frequency and the eventual parasitic interference contributions in the Fourrier plane, offseting the result to zero frequency and performing an inverse FFT (IFFT) allows one to isolate the fringes information. The amplitude and phase are then straightforwardly extracted as the amplitude and the phase of the resulting complex image. This provides the full information (intensity and phase of the emission) on the coherent polariton field. The reconstructed intensity is checked against the direct imaging to detect any flaw in this numerical process.

The algorithm steps are:

(a) Load interference, signal, reference and dark files.

(b) Image preparation: signal, reference and dark removal. This gives the interference pattern modulated by the local contrast.

(c) Image preparation: center and crop on the region of interest.

(d) FFT of the prepared image.

(e) Recognition of the frequency contribution of interest (relevant fringe pattern).

(f) Determination of the relevant fringe wavevector $\boldsymbol{k}$.

(g) All non-relevant contributions are set to zero (only the positive frequency component of the relevant signal is kept).

(h) The relevant contribution is centered to zero frequency ($-\boldsymbol{k}$ shift).

(i) IFFT is performed

(j) The complex array amplitude is used to reconstruct the intensity, while the complex array argument is used as the phase map.

A 2D fit of the unwinded phase map can then be used to compute the polariton field velocity. Considering an error in the local sound velocity which takes into account the 2D fit standard deviation, as well as a systematic error on the scaling method and an estimation of the non-flatness of the reference beam, the precision on the local velocity is estimated to 25

Appendix B.

Publications

Vortex Chain in a Resonantly Pumped Polariton Superfluid

T. Boulier,[1] H. Terças,[2] D. D. Solnyshkov,[2] Q. Glorieux,[1] E. Giacobino,[1] G. Malpuech,[2,*] and A. Bramati[1,†]

[1] *Laboratoire Kastler Brossel, Université Pierre et Marie Curie, Ecole Normale Supérieure et CNRS, UPMC Case 74, 4 place Jussieu, 75252 Paris Cedex 05, France*

[2] *Institut Pascal, PHOTON-N2, Clermont Université, Blaise Pascal University, CNRS,24 Avenue des Landais, 63177 Aubière Cedex, France*

(Dated: October 12, 2014)

Exciton-Polaritons are photonic states interacting via their exciton fraction. They can be excited, manipulated, and detected using all the versatile techniques of modern optics. An exciton-polariton gas is therefore a unique platform to study out-of-equilibrium interacting quantum fluids. In this work, we report the formation of a ring-shaped array of same sign vortices after injection of angular momentum in a polariton superfluid. The angular momentum is injected by a $\ell = 8$ Laguerre-Gauss beam, whereas the global rotation of the fluid is hindered by a narrow Gaussian beam placed at its center. In the linear regime, a spiral interference pattern containing phase defects is visible. In the nonlinear (superfluid) regime, the interference disappears and the vortices nucleate as a consequence of the angular momentum quantization. The radial position of the vortices evolves freely in the region between the two pumps as a function of the density. Hydrodynamic instabilities resulting in the spontaneous nucleation of vortex-antivortex pairs when the system size is sufficiently large confirm that the vortices are not constrained by interference when nonlinearities dominate the system.

Quantized vortices have been extensively investigated in different fields of physics, such as superconductivity [1], matter-wave superfluids [2] and nonlinear optics [3]. In this context, half-light, half-matter polariton fluids offer an unprecedented opportunity to study the quantum-fluid aspects of interacting photons, a rich field at the interface of condensed matter and quantum optics. The recent discovery of polariton Bose-Einstein condensation in semiconductor microcavities [4–6] has renewed the possibilities of observing superfluidity in quantum fluids of light [7]. As a consequence, the understanding of the mechanism of vortex nucleation and vortex dynamics in such systems becomes particularly important. Vortices are natural topological solutions in interacting photonic systems [8]. Indeed, the nucleation of vortices [9–13] and half-vortices [14, 15] in polariton fluids have been reported in several experiments.

Several schemes to produce vortices and vortex lattices have been proposed and implemented. Liew *et al* [16] predicted the formation of regular triangular lattices and of Penrose triangular lattices with coherently pumped polariton condensates, while Gorbarch and coworkers [17] proposed to create robust half-vortex lattices in the optical parametric oscillator (OPO) scheme. Spontaneous self-ordered vortex-antivortex pairs have been recently reported in [18, 19] and Hivet *et al* [20] experimentally demonstrated the formation of regular vortex-antivortex lattices in square and triangle trapping potentials. Nevertheless, none of these schemes allow the effective transfer of a global angular momentum, therefore preventing the spontaneous nucleation of same-sign Abrikosov-like vortex lattices. A scheme for the production of such self-ordered, single-sign vortex lattices has been put forward in Ref. [21]. However, in this ideal, disorder-free scheme, an important experimental limitation arises, as the lattice rotates at very high angular velocities, therefore making time-resolved interferometry measurements a very difficult task.

In this work, as a first step towards the physics of rotating polariton quantum fluids, we theoretically propose and experimentally implement a scheme that generates stable chains of same-sign vortices in a coherently driven polariton superfluid. The scheme consists of a Laguerre-Gauss (LG) laser beam with orbital angular momentum ℓ and an additional Gaussian beam (G) with zero angular momentum located at the center. The central Gaussian beam allows to lock the azimuthal position of the vortices and thus to circumvent the issue of fast rotation. We use a Spatial Light Modulator (SLM) to produce the spatial profile of the resonant pumps. This hologram-based optical technique is very versatile and can be used to generate a wide variety of pumping schemes for polaritons. Based on a variational analysis of the modified Gross-Pitaevskii equation, we then show that the vortex chain is a consequence of the quantization of the total angular momentum transferred to the superfluid, thus different from a trivial interference pattern imposed by the pumps. The quantum nature of the fluid is also confirmed by the appearance of hydrodynamical instabilities, resulting in the nucleation of vortex−antivortex pairs.

Significance. Vortex lattices and chains of same-sign vortices are a distinctive feature of superfluids. In solid-state polariton superfluids - which are available at much higher temperatures and in much simpler experimental setups than atomic ones - vortex nucleation is also possible. Nevertheless, most of the experiments performed so far only reveal stable vortex-antivortex patterns, which are not such a good proof of angular momentum quantization as the Abrikosov lattice would be. We report here the formation of a stable, steady-state chain of same-sign vortices in polariton superfluids as a result of the angular momentum injected by a Laguerre-Gauss laser beam.

Experimental setup. We make use of a CW single mode, frequency-locked Ti:Sa laser to resonantly excite the cavity. Resonant pumping creates a low-density exciton gas, which allows us to neglect interactions between polaritons and the exciton reservoir (in contrast with experiments performed under non-resonant pumping [19]). The laser is then tuned to be quasi-resonant with the ground state of the lower polariton

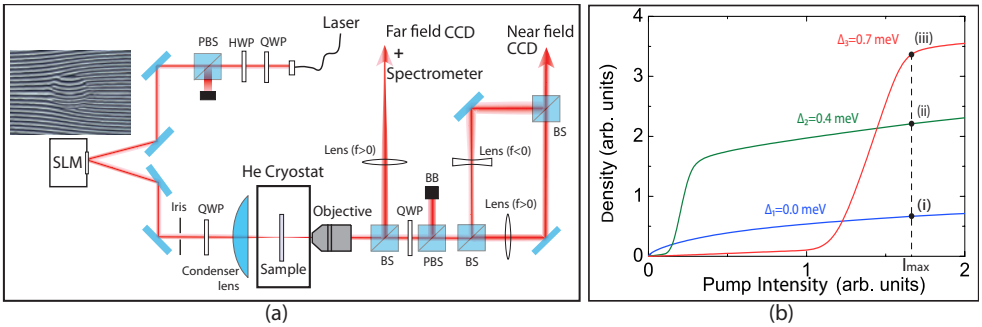

Figure 1: (color online) **Setup and bistability** (a) - Experimental setup scheme. The pumps are prepared with a pure-phase SLM and sent on the sample. The sample emission is collected and treated for detection in real space, momentum space and energy. The inset shows the hologram used on the SLM. (b) - Scheme of the different regimes of bistability used (only the curve obtained when decreasing the density is shown). A stronger bistability (higher Δ) provides higher densities for high pump intensities. $I_{\max}$ indicates the pump peak intensity.

(LP) branch (~ 837 nm), such that the detuning with respect to the bottom of the LP branch is given by $\Delta = \omega_{\text{laser}} - \omega_{\text{pol}}$, where ω_{laser} and ω_{pol} are respectively the pump and bare polariton energies at normal incidence $k = 0\,\mu\text{m}^{-1}$. A single-mode, polarization-preserving fiber selects the TEM_{00} mode. The polarization is linear (vertical) after the fiber and the remaining polarization fluctuations are cut by a polarizing beam splitter (PBS). The collimated laser beam is then sent to a SLM, which allows us to arbitrarily modify the spatial phase profile of the beam.

By programming a specifically designed phase hologram on the SLM, we can create beams with well-defined intensity and phase profiles. We create a coherent superposition of a Laguerre-Gauss (LG) beam of orbital momentum $\ell = 8$ and a Gaussian (G) beam of zero orbital momentum at the center. Both the spot size and the intensity of the laser beams are fully determined by the hologram. The LG-beam width σ_1 is chosen to be larger than the width σ_2 the G-beam. As a result, their spatial overlap is small, allowing for the interference to be very weak. To avoid spin-dependent phenomena, the $(LG_0^8 + LG_0^0)$ polarization is set to circular with a quarter-wave plate, before being focused on the sample by an aspherical condenser. In [22], a SLM was used to create a similar, ring shaped condensate, but using non-resonant optical excitation. As a result, the condensate created was in a superposition of two states with opposite angular momentum without the formation of a vortex lattice.

Sample. The sample is a 2λ-GaAs planar microcavity containing three GaAs-InGaAs quantum wells, with a polariton Rabi splitting of 5.1 meV. The cavity finesse is $F = 3000$, which results in a polariton linewidth of about 0.1 meV. The cavity is wedged in one direction, providing a large choice of cavity-exciton detunings by pumping at different positions in the sample. In order to enhance the polariton-polariton interactions, we use a cavity-exciton detuning of $\Delta = \omega_C - \omega_X = 1$ meV ($\omega_{X(C)}$ is the excitonic (cavity) energy at normal incidence, $k = 0\,\mu\text{m}^{-1}$), thus increasing the exciton fraction of polaritons and, consequently, the nonlinear effects. The microcavity is cooled down to 5 K in a cryostat and the measurements are taken in transmission. Above a critical value of Δ, a bistable behavior appears [23]. By increasing Δ and working within the upper bistability branch, we increase the polariton density. This is necessary to reach the regime where nonlinearities dominate. We therefore use the polariton bistability to control the density as follows: in the upper bistability branch, at constant pump power $I_p = 300$ mW, we modify Δ. We consider three different cases: low density ($\Delta_1 \approx 0$ meV, point (i) in Fig.1 (b)), high density far from the bistability threshold ($\Delta_2 = 0.4$ meV, point (ii) in Fig.1 (b)) and near the bistability threshold ($\Delta_3 = 0.7$ meV, point (iii) in Fig.1 (b)).

Detection. The detection is simultaneously made in energy and in real- and momentum space. An objective collects the sample emission. CCD cameras are used for direct imaging of the real- and the momentum space, while the energy (wavelength) is measured with a spectrometer. We only collect circularly-polarized light, therefore filtering out any residual spin-flip effect. The polariton phase is measured with an off-axis interferometry setup: a beam splitter divides the real-space image into two parts, one of which is expanded to generate a phase reference beam. The selection of the Gaussian part at the center of the image ensures a flat phase reference, which is used to make an off-axis interference pattern. With this method, the vortex position in the image is independent of the phase of the reference beam [24]. The actual phase map is then numerically reconstructed with a standard off-axis phase detection method.

Theory. In order to describe the configuration under study, we numerically solve the driven-dissipative Gross-Pitaevskii equation, which in the parabolic approximation reads

$$i\hbar\frac{\partial\psi}{\partial t} = -\frac{\hbar^2\nabla^2}{2m}\psi - \frac{i\hbar}{2\tau}\psi + \alpha_1|\psi|^2\psi + P(\mathbf{r})e^{i\Delta t}. \quad (1)$$

Here, $P(\mathbf{r}) = P_{LG}(\mathbf{r}) + P_G(\mathbf{r})$ with $P_{LG}(\mathbf{r}) = A_1(r/\sigma_1)^{|\ell|}e^{-r^2/\sigma_1^2}e^{i\ell\varphi}$ and $P_G(\mathbf{r}) = A_2 e^{-r^2/\sigma_2^2}$; A_1 and A_2 are the amplitudes of the pumping lasers. To match

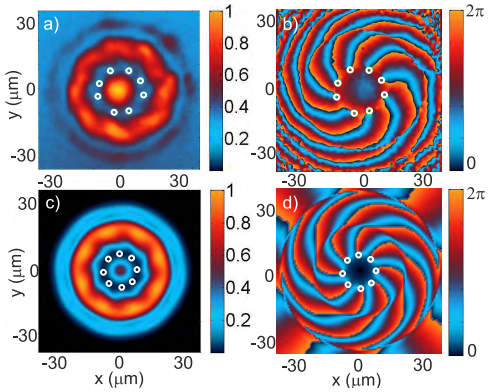

Figure 2: (color online) **Linear regime** - Experimental (above) and theoretical (below) images of the polariton field in the linear regime (low densities, $\Delta \approx 0$ meV). The intensity $|\psi|^2$ (normalized to the peak value) is shown on the left panels while the phase $\arg(\psi)$ is shown on the right panels. Vortices are indicated by white circles both in the intensity and the phase. At low densities the nonlinear interactions are negligible: the pattern is the result of optical interference, fixing the vortex positions.

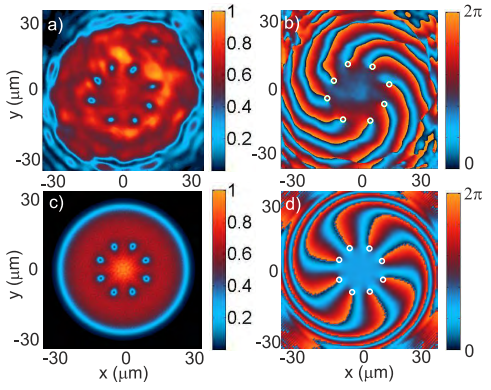

Figure 3: (color online) **Nucleation of vortices** - Experimental (above) and theoretical (below) images of the polariton field in the nonlinear regime (high densities, $\Delta = 0.4$ meV). The intensity $|\psi|^2$ (normalized by the peak value) is shown on the left panels while the phase $\arg(\psi)$ is shown on the right panels. Vortices are clearly visible as eight zero-density dips in a) and c) and are indicated by white circles in the phase (diagrams b) and d)). The polariton density is high enough to enter the superfluid regime and to suppress the pump interference through nonlinear interactions.

the experimental configuration, we set $\sigma_1 = 5.0$ μm and $\sigma_2 = 3.0$ μm. Direct comparison with the experiments is then performed by extracting the steady-state density $|\psi|^2$ and phase $\arg(\psi)$.

Results. In the linear regime ($\Delta = \Delta_1 \approx 0$ meV), we observe - both experimentally (Fig.2 a),b)) and theoretically (Fig. 2 c),d)) - a pattern resulting from the optical interference between the LG and G beams. This interference pattern consists in an eight-lobbed spiral (Fig.2 a),c)) with eight phase singularities (Fig.2 b),d)). The annular phase singularity chain visible in Fig.2 is thus imposed by the pump phase. As the density increases, the nonlinear behavior of polaritons is unveiled, with a progressive deformation and disappearance of the interferences. For $\Delta = \Delta_2 = 0.4$ meV (point (ii) in Fig. 1 (b)), the interference pattern shown in Fig.3 is reduced to round-shaped dips of quasi-zero density containing the phase singularities: the elementary vortices carrying quanta of the injected angular momentum. We observe a ring of same-sign vortices in a coherent superfluid of polaritons, quite differently from the spiral interference pattern present in the linear regime. The absence of interference pattern means that the polariton phase is now different from the one of the pump and is modified through the nonlinear interactions, generating additional features compared to an optical interference pattern. Our observations are consistent with other resonant and non-resonant pumping experiments done in absence of angular momentum [19, 20]. The formation of a ring of l single-charged vortices from a pump with angular momentum ℓ is a manifestation of the quantum nature of the polariton fluid, similar to the formation of the Abrikosov lattice from a single highly-charged vortex.

It is important to remark that the spatial freedom of the vortices provides a quantitative test of our model. As mentioned above, nonlinear vortices exhibit a radial phase freedom: despite the fact that the azimuthal position of the vortices is locked by the pump phase, their radial position is modified as the density $\rho = |\psi|^2$ increases. In order to quantify the dependence of the ring radius R on the relevant experimental parameters, we employ a variational method. We describe the vortex chain solution with the variational ansatz

$$\Psi[R] = \psi_{\rm TF}(r) \prod_{i=1}^{8} f_V(\mathbf{r}-\mathbf{r}_i), \quad f_V(r_i,\theta_i) = \sqrt{\frac{r_i^2}{r_i^2+\xi^2}} e^{i\theta_i}, \tag{2}$$

where $\psi_{\rm TF}(r) = \rho^{1/2}[P_1(r)/A_1 + P_2(r)/A_2]$ is the Thomas-Fermi density profile induced by the pump, $\mathbf{r}_i = R(\cos\theta_i, \sin\theta_i)$ is the position of each vortex in the chain, and $\xi = \hbar/\sqrt{m\rho\alpha_1}$ is the average healing length. In Fig. 4 a), we plot the variational profile given by Eq. (2). The value of R can then be extracted by minimizing the total energy $E[R] = E_{\rm kin} + E_{\rm int}$ and taking the physically relevant solution of the condition $\delta E/\delta R = 0$, where

$$\begin{aligned} E_{\rm kin} &= \int d\mathbf{r} \left(\Psi^* \frac{\hbar^2 \nabla^2}{2m} \Psi \right), \\ E_{\rm int} &= \int d\mathbf{r} \left[\left(|\Psi| - \rho \right)^2 |\Psi|^2 \right]. \end{aligned} \tag{3}$$

In Fig. 4 b), we plot the energy E as a function of R for different values of $\xi \sim \rho^{-1/2}$. We observe that R decreases as the value of ξ (ρ) is increased. Since ρ increases with Δ, ξ decreases with Δ; it follows that R increases with Δ. Fig.4 c) shows R as a function of ρ calculated by this method and the comparison with experimental data. As expected, the higher the density, the further from the center the vortices migrate. This behavior and the agreement between the varia-

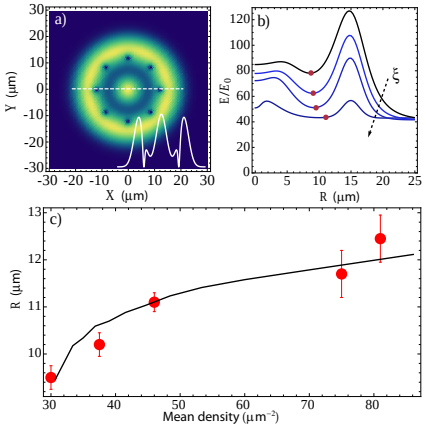

Figure 4: (color online) **Vortex positions** (a) - Variational wave function in Eq. (2) used to determine the vortex chain radius R. The inset shows the radial profile for a cut at $Y = 0$. (b) - Variational energy E (in units of $E_0 = \hbar^2\rho/(4\pi m)$) showing a minimum (red dots) for different values of ξ. From top to bottom: $\xi = (3.0, 2.0, 1.0, 0.5)$ μm. (c) - Average chain radius R as a function of the pump detuning Δ obtained from the variational method (solid line) and the corresponding experimental data (dots).

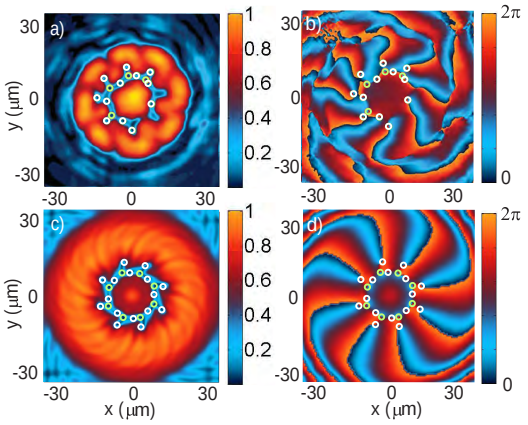

Figure 5: (color online) **Phase instability** - Experimental (above) and theoretical (below) images of the polariton field when the bistability threshold is close to the pump maxima (very high densities, $\Delta = 0.7$ meV). The intensity $|\psi|^2$ (normalized by the peak value) is shown on the left panels while the phase $\arg(\psi)$ is shown on the right panels. Vortices are indicated by white circles and antivortices by green circles both in the intensity and the phase. Here only the maxima of the pump are on the upper bistability branch (resonant pumping) and produce a significant polariton density. The nonresonant zone between the LG and G pumps is wide enough for the fluid to hydrodynamically nucleate into vortex-antivortex pairs, while preserving the annular vortex chain.

tional method and experiment are a clear indication of the phase freedom obtained when interactions dominate, a feature that is independent from the optical interference.

In the upper bistability branch, the polariton energy is renormalized through self-interaction to the pump energy, so that the pumping is resonant and yields high polariton densities. This is not the case in the lower bistability branch, where the pumping is not resonant and thus inefficient. For large Δ, the low pump intensity regions in the lower bistability branch are off-resonant, as can be seen in Fig.1 (b). In these regions, non-resonant pumping yields a negligible polariton population and can be considered as a pump-free region. For example, near the threshold, for $\Delta = \Delta_3 = 0.7$ meV (point (iii) in Fig.1 (b)), a large area between the LG and G pumps is not pumped. Although no polariton is directly injected in this area, the density is not zero due to polaritons propagating from the pumped to the non-pumped area. In this region, the phase is free to evolve, which explains the radial chain expansion. Moreover, when the density in this pump-free area is large enough and when the size of this region is at least of the order of the vortex core $\sim \xi$, we observe the spontaneous nucleation of vortex-antivortex pairs. Four pairs are experimentally visible in Fig.5 and eight in the theoretical figure. This small discrepancy between theory and experiment for the number of pairs is due to the cavity wedge making the experimental cavity anisotropic, a property that is absent in the simulations. They form a low-density ring inside the vortex chain described above. This is due to a hydrodynamic instability of the same nature as the one observed in the $\ell = 0$ case [13], but here each pair formation is stimulated by the presence of a vortex which acts as a defect. The disorder-free model confirms that the vortex-antivortex pairs are generated by the vortices of the main chain and not by the disorder. This feature also proves that the vortex distribution is not due to optical interference in the superfluid regime, but that it rather evolves with the density.

We now note that in rotating cold-atom condensates [29–31], the angular momentum is externally transferred either by stirring or via rotation of the trapping potential. In this case, the vortices nucleate and self-organize into an Abrikosov lattice. In our case, the ring geometry is imposed by the pumps, resulting in an additional constraint. Furthermore, the angular momentum is injected when the polariton fluid is generated and not imposed by an external additional field. These differences, together with the out-of-equilibrium nature of our system, may provide new physical phenomena that remain to be explored in the future. One particular aspect relates the quantum correlations of the created state, which may qualitatively differ from the equilibrium case. For example, the phase transition between a triangular vortex lattice phase and strongly correlated vortex liquid phases occurring in cold atoms may be different in this case [32], as well as the collective dynamics of the vortex chain (Tkachenko modes) [26], for which the polariton life-time is expected to play a central role in the mode damping.

Conclusion. In the present work, we resonantly inject polaritons with a given total angular momentum and observe the formation of a ring of quantized single-charged vortices. For the first time, a regular ring pattern of elementary vortices of the same sign is reported

in a polariton superfluid. In the superfluid regime, the radial position of each vortex is not determined by the pump but rather depends on the polariton density. Experimental and theoretical indications of this behavior, due to very strong nonlinear interactions, are provided through the system hydrodynamical comportment. The mechanism leading to the creation of vortex chains results from the combination of the saturation of the radial counterflow instability with the injection of angular momentum in a limited region of space. Let us note that this general behavior was experimentally and theoretically verified to be the same if the number of injected vortices is changed, whether odd or even. We expect that the present scheme will pave the stage to study a series of new vortex collective phenomena that has not been possible so far [2, 25, 26]. It is also a first step towards a new class of rotating-frame experiments that could reveal self-arranged same-sign vortex lattices [21], unveiling the physics of vortex-vortex interactions in polariton superfluids.

Methods: Hologram and pump preparation. Collimated Laguerre-Gauss beams are a class of modes possessing a simple phase profile with radial invariance. The phase profile of a LG_0^ℓ mode is given by the function $\varphi_{\mathrm{LG}}(r,\phi) = \ell\phi\,[2\pi]$, where $(r, \phi \in [0, 2\pi])$ are the polar coordinates in the SLM plane. However, imposing this phase on the SLM produces a superposition of LG_0^ℓ and weak higher modes in the condenser lens focal plane. Since the higher modes are spatially more extended, they can be cut with an iris placed before the condenser lens, which solves the problem. The result is a good quality LG_0^ℓ beam. Adding the central Gaussian pump is straightforward as the mode imprinted on the SLM is Gaussian: we simply need to impose a flat phase in the LG_0^ℓ hologram. This has been done by using the phase function $\varphi_{\mathrm{LG+G}}(r,\phi) = \ell\phi H(r-r_0)+\pi(1-H(r-r_0))$, where $H(r)$ is the Heaviside distribution and r_0 is a constant determining the LG/G intensity ratio. The resulting hologram is presented in Fig. 6 (a). Another, more advanced, tested possibility is a "distributed flat phase" hologram, where $\varphi_{LG+G}(r,\phi) = \ell\phi\,[2\pi]$ if $\ell\phi\,[2\pi] > a_0$ and $\varphi_{\mathrm{LG+G}}(r,\phi) = 0$ else ($a_0 \in [0, 2\pi]$ is another constant determining the LG/G intensity ratio). The resulting hologram is presented in Fig. 7 (a). Both holograms resulted in very similar results, so we chose the first one to perform the experiment described in the manuscript.

A small fraction of the light is not modified by the SLM, for which it acts like a mirror. To separate this from the desired mode a grating hologram ($\varphi_{\mathrm{grat}}(x,y) = \frac{2\pi}{d}y$, where d controls the separation angle) is added to the LG+G hologram (mathematical sum modulo 2π). This vertically deviates the first order reflection forming the pump, allowing us to block the zero-order reflection. The final holograms are presented for both methods in Fig. 6 (b) (central flat phase method) and Fig. 7 (b) distributed method).

Acknowledgments. We acknowledge the financial support of the ANR Quandyde (ANR-11-BS10-001), ANR Labex GANEX (ANR-11-LABX-0014) and IRSES POLAPHEN (246912).

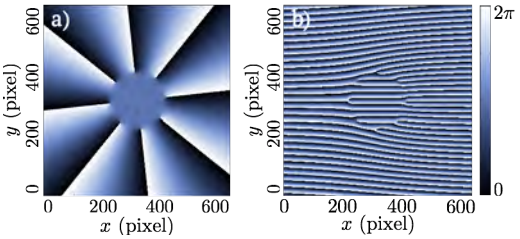

Figure 6: **Central flat phase hologram** - Hologram corresponding to the first method described in the text, without (a) and with (b) the grating. The Laguerre-Gaussian phase is cut at the center and replaced with a flat phase, which creates the Gaussian central beam.

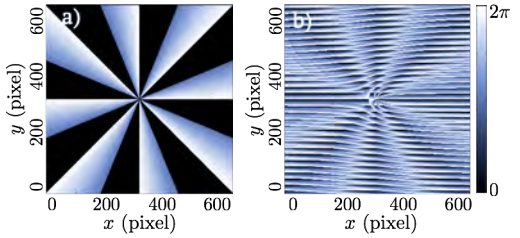

Figure 7: **Distributed flat phase hologram** - Hologram corresponding to the second method described in the text, without (a) and with (b) the grating. A part of the Laguerre-Gaussian phase is replaced with a flat phase in a distributed way, depending on the local LG phase value. This also creates the Gaussian central beam but it ensures no elementary phase singularity is present in the hologram.

* Electronic address: malpuech@univ-bpclermont.fr
† Electronic address: bramati@spectro.jussieu.fr

[1] L. Pismen, *Vortices in Nonlinear Fields*, Clarendon Press, Oxford (1999).
[2] A. L. Fetter, Rev. Mod. Phys. **81**, 647 (2009).
[3] A. S. Desyatnikov, Y. S. Kivshar, and L. Torner, Prog. Opt. **47**, 291 (2005).
[4] J. Kasprzak et al., Nature **443**, 409 (2006).
[5] R. Balili, V. Hartwell, D. Snoke, L. Pfeiffer, and K. West, Science **316**, 1007 (2007).
[6] C. W. Lai et al., Nature **450**, 529 (2007).
[7] I. Carusotto and C. Ciuti, Rev. Mod. Phys. **85**, 299 (2013).
[8] C. O. Weiss, Phys. Rep. **219**, 311 (1992); C. O. Weiss, H. R. Telle, K. Staliunas, and M. Brambilla, Phys. Rev. A **47**, 1616 (1993).
[9] G. Roumpos, M. D. Fraser, A. Löffler, S. Höfling, A. Forchel, and Y. Yamamoto, Nature Physics **7**, 129 (2011).
[10] G. Nardin, G. Grosso, Y. Léger, B. Pi?tka, F. Morier-Genoud, and B. Deveaud-Plédran, Nature Physics **7**, 610 (2011).
[11] D. Sanvitto, S. Pigeon, A. Amo, D. Ballarini, M. De Giorgi, I. Carusotto, R. Hivet, F. Pisanello, V. G. Sala, P. S. S. Guimaraes, R. Houdré, E. Giacobino, C. Ciuti, A. Bramati, and G. Gigli, Nature Photonics **5**, 610–614 (2011).
[12] K. G. Lagoudakis, M. Wouters, M. Richard, A. Baas, I. Carusotto, R. André, Le Si Dang, and B. Deveaud-

Plédran, Nat. Phys. **4**, 706 (2008).
[13] F. Manni, Y. Léger, Y.G. Rubo, R. André, and B. Deveaud, Nat. Comm. **4**, 2590 (2013).
[14] F. Manni, K. G. Lagoudakis, T. C. H. Liew, R. André, V. Savona, and B. Deveaud, Nat. Comm. **4**, 1309 (2012).
[15] K. G. Lagoudakis, Ostatnický T, Kavokin A.V., Rubo Y.G., and B. Deveaud-Plédran, Science **32**, 974 (2009).
[16] T. C. H. Liew, Y. G. Rubo. and A. V. Kavokin, Phys. Rev. Lett. **101**, 187401 (2008).
[17] A. V. Gorbach, R. Hartley, and D. V. Skryabin, Phys. Rev. Lett. **104**, 213903 (2010).
[18] F. Manni, T. C. H. Liew, K. G. Lagoudakis, C. Ouellet-Plamondon, R. André, V. Savona, and B. Deveaud, Phys. Rev. B **88**, 201303(R) (2013).
[19] P. Cristofolini, A. Dreismann, G. Christmann, G. Franchetti, N.G. Berloff, P. Tsotsis, Z. Hatzopoulos, P. G. Savvidis, and J. J. Baumberg, Phys. Rev. Lett. **110**, 186403 (2013).
[20] R. Hivet, E. Cancelieri, T. Boulier, D. Ballarini, D. Sanvitto, F. M. Marchetti, M. H. Szymanska, C. Ciuti, E. Giacobino, and A. Bramati, Phys. Rev. B, **89**, 134501 (2014).
[21] J. Keeling and N. Berloff, Phys. Rev. Lett. **100**, 250401 (2008).
[22] A. Dreismanna, P. Cristofolini, R. Balili, G. Christmann, F Pinsker, N. G. Berloffb, Z Hatzopoulos, P.G. Savvidis, and J. J.Baumberg, Coupled counterrotating polariton condensates in optically defined annular potentials, PNAS,111,8770,(2014).
[23] Baas, A., Karr, J.Ph., Eleuch, H. and Giacobino, E., Optical bistability in semiconductor microcavities. Phys. Rev. A **69,** 023809–023817, (2004).
[24] Bolda, E. L., Walls., Dan F., Detection of Vorticity in Bose-Einstein Condensed Gases by Matter-Wave Interference Phys. Rev. Lett. **81**, 5477 (1998).
[25] E. B. Sonin, Phys. Rev. A **71**, 011603(R) (2005); E. B. Sonin, Phys. Rev. A **72**, 021606 (2005).
[26] I. Coddington, P. Engels, V. Schweikhard, and E. A. Cornell, Phys. Rev. Lett. **91**, 100402 (2003).
[27] H. J. Schulz, Phys. Rev. Lett. **71**, 1864 (1993).
[28] H. Terças, D. D. Solnyshkov, and G. Malpuech, Phys. Rev. Lett. **110**, 035303 (2013).
[29] F. Chevy, K. W. Madison, and J. Dalibard, Phys. Rev. Lett. **85**, 2223 (2000).
[30] K. W. Madison, F. Chevy, W. Wohlleben, J. Dalibard, J . Mod. Opt. **47** , 2715 (2000).
[31] M. R. Matthews, B. P. Anderson, P. C. Haljan, D. S. Hall, C. E. Wieman, and E. A. Cornell, Phys. Rev. Lett. **83**, 2498 (1999).
[32] N. R. Cooper, N. K. Wilkin, and J. M. F. Gunn, Phys. Rev. Lett. **87**, 120405 (2001).

nature COMMUNICATIONS

ARTICLE

Received 7 Jun 2013 | Accepted 15 Jan 2014 | Published 12 Feb 2014

DOI: 10.1038/ncomms4260

Polariton-generated intensity squeezing in semiconductor micropillars

T. Boulier[1], M. Bamba[2], A. Amo[1,3], C. Adrados[1], A. Lemaitre[3], E. Galopin[3], I. Sagnes[3], J. Bloch[3], C. Ciuti[4], E. Giacobino[1] & A. Bramati[1]

The generation of squeezed and entangled light fields is a crucial ingredient for the implementation of quantum information protocols. In this context, semiconductor materials offer a strong potential for the implementation of on-chip devices operating at the quantum level. Here we demonstrate a novel source of continuous variable squeezed light in pillar-shaped semiconductor microcavities in the strong coupling regime. Degenerate polariton four-wave mixing is obtained by exciting the pillar at normal incidence. We observe a bistable behaviour and we demonstrate the generation of squeezing near the turning point of the bistability curve. The confined pillar geometry allows for a larger amount of squeezing than planar microcavities due to the discrete energy levels protected from excess noise. By analysing the noise of the emitted light, we obtain a measured intensity squeezing of 20.3%, inferred to be 35.8% after corrections.

[1] Laboratoire Kastler Brossel, Université Pierre et Marie Curie, Ecole Normale Supérieure and CNRS, UPMC Case 74, 4 place Jussieu, 75252 Paris Cedex 05, France. [2] Department of Physics, Osaka University, 1-1 Machikaneyama, Toyonaka, Osaka 560-0043, Japan. [3] Laboratoire Photonique et Nanostructures, CNRS, Route de Nozay, 91460 Marcoussis, France. [4] Laboratoire Matériaux et Phénomènes Quantique, Université Paris Diderot et CNRS, Bâtiment Condorcet, 10 rue Alice Domon et Léonie Duquet, 75205 Paris Cedex 13, France. Correspondence and requests for materials should be addressed to A.B. (email: bramati@spectro.jussieu.fr).

While very efficient sources of non-classical light, essentially based on bulk nonlinear crystals, have been developed in the last 20 years, the quest for integrated quantum sources is a major challenge for the cutting edge research activity in the field of quantum information technologies.

Successful examples in the discrete variable regime are represented by efficient single and entangled photons sources in semiconductor quantum dots[1–3]. Photon antibunching and squeezing were theoretically predicted and experimentally demonstrated in pioneering resonance fluorescence experiments[4–7]. In strong contrast, despite several theoretical proposals[8,9], the continuous variables regime has seen so far only very few experimental achievements[10–12] of squeezed states of light in semiconductor materials.

Here, for the first time in this type of systems, we achieve a high degree of intensity squeezing exploiting an effective Kerr effect for microcavity polaritons. Let us note that, due to the giant polariton nonlinearities[13], the power range used here (5–20 mW) is two orders of magnitudes lower than in previous experiments[10]. These results open the way to the implementation of ultra-low threshold quantum devices integrated in a semiconductor platform.

Exciton-polaritons are half-light half-matter bosonic particles arising from the strong coupling between excitons and photons in semiconductor microcavities[14]. They exhibit strong nonlinearities due to the Coulomb interactions of their excitonic part, responsible for the rich variety of quantum effects recently unveiled[15], ranging from Bose–Einstein condensation[16] and superfluidity[17,18] to more complex phenomena such as dark and bright solitons[19,20], magnetic monopole-like half-solitons[21], half-vortices[22] and vortex lattices[23].

The great potential of polaritons for non-classical fields generation was recognized very soon after the experimental demonstration of the coherent nonlinear optical response of microcavity polaritons allowing for the observation of parametric amplification and oscillation in such systems[24–26]. Especially interesting is the case of degenerate polariton four-wave mixing in which the strong nonlinearities originating in the polariton–polariton interactions allow describing the polariton system as an effective Kerr medium whose refractive index depends on the light intensity[12,27,28]. Kerr media are well known to be very efficient sources of quadrature-squeezed light. Indeed, quadrature squeezing of about 4% was observed in a planar semiconductor microcavity, by using degenerate polariton four-wave mixing in 2004 (ref. 11). Despite several attempts with specifically designed planar microcavity samples, significant improvements of this first result were prevented by the excess noise coming from the intrinsic multimode nature of the emission in a planar microcavity, which is characterized by a continuum of polariton modes and is favourable to the coupling with lattice phonons. Very recently, it has been predicted[29] that a large amount of squeezing could be achieved by quantizing the in-plane polariton field modes via a geometric confinement (strong localization limit[29]). This tight confinement separates the modes energetically, severely reducing any nonlinear multimode coupling responsible for increased excess noise and reduced quantum effects. In this paper, we apply this method in a controlled way making use of semiconductor micropillars[30,31] and we demonstrate up to 20.3% of directly measured squeezing in the amplitude quadrature of the emitted light.

Results

Experimental configuration. In our set-up, the pillars are fabricated by etching a λ GaAs microcavity containing two GaAs–InGaAs quantum wells, resulting in a polariton Rabi splitting of about 4 meV. The cavity finesse is of the order of 700, which gives a 0.1 meV polariton linewidth. Figure 1 shows the energy separation of the polariton modes due to the finite size of the pillar. As shown in Fig. 2a, the cavity mirrors are asymmetric with the bottom Bragg mirror twice thicker than the top one (30 pairs of $Al_{0.1}Ga_{0.9}As - Al_{0.95}Ga_{0.05}As$ versus 15 pairs for the top mirror), optimizing the cavity for experiments in reflection configuration. The cavity is wedged in one direction, providing a large choice of cavity–exciton detuning by selecting pillars placed in different positions on the chip. We can choose the shape and size of the micropillars in order to engineer the spatial distribution of the confined modes and their energy separation. Figure 2b shows the large square-shaped pillars (width of 20 µm) and small square or round-shaped pillars (width from 6 µm to 2 µm) available on the studied sample.

The pillars are cooled down to 5 K in a cryostat mounted in reflection configuration and excited with a CW single-mode Ti:Sa laser tuned to be quasi-resonant with the ground-state level of the lower polariton branch. The laser is frequency locked to a Fabry–Perot cavity and its intensity is stabilized by means of an electro-optical modulator. The laser was verified to be at the shot noise for frequencies above 1 MHz. The spatial mode is filtered by a five meters long single-mode optical fibre shielded against thermal fluctuations. The laser beam is focused by a microscope objective treated with a near-infrared optimized coating and excites the sample at normal incidence. Upstream of the microscope objective, a motorized $\frac{\lambda}{2}$ plate coupled with a polarizing beam splitter (PBS) allows us to finely control the pump power on the sample and a $\frac{\lambda}{4}$ plate placed between the beam splitter and the objective ensures that the light coming on the sample is circularly polarized. With the polarized beam splitter, the $\frac{\lambda}{4}$ plate forms an optical circulator since the light re-emitted from the sample was measured to be 95% circularly polarized, as expected from spin conservation. The light reflected from the cavity is thus collected and sent to the detectors.

The shape of the laser spot on the sample is Gaussian with a waist of 5.5 µm, well matched to the round pillars with a diameter of 6 µm. In the studies presented here, we hence use a round micropillar of 6 µm, which ensures an optimal mode matching between its polaritonic ground state and the focalized excitation

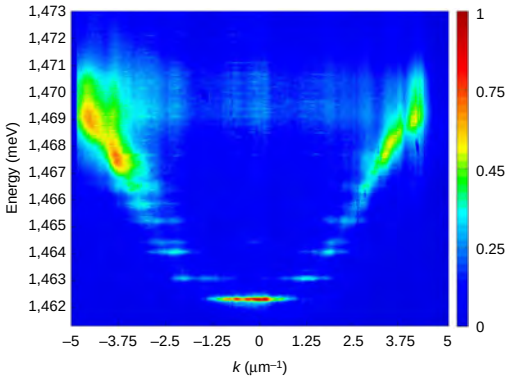

Figure 1 | Energy modes separation. Dispersion curve for the 6 µm circular pillar used in the experiment (− 5 meV cavity detuning), obtained with a non-resonant pumping at 1, 550 meV. The lower polariton branch with several spatial modes and the weakly excited upper branch are visible. The modes are energetically separated and squeezing is protected against multimode nonlinear coupling.

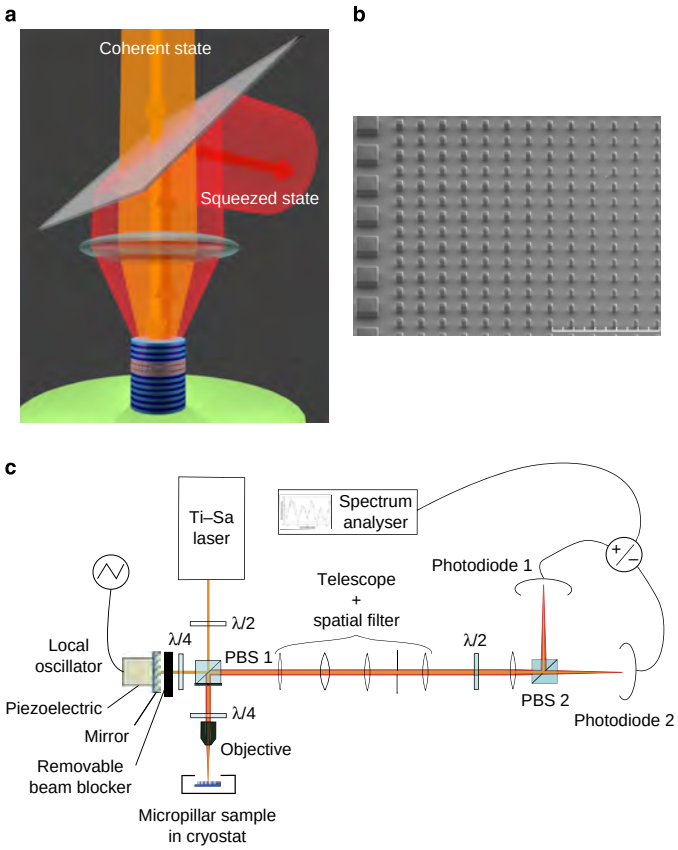

Figure 2 | Sample and set-up. (**a**) Principle of squeezed light production with a pillar-shaped microcavity. The microcavity is made of a pair of quantum wells (white-red-white layers) sandwiched by two Bragg mirrors (alternation of light blue and dark blue layers); the green layer is the substrate. The orange beam represents the pump laser arriving on the sample at normal incidence, slightly blueshifted with respect to the energy of the lower polariton branch. The red beam represents the squeezed light emitted by the squeezed polariton field present in the microcavity. (**b**) Image of the sample obtained with scanning electron microscopy. The different shapes and sizes of the pillars are visible. The scale bar corresponds to 100 μm. (**c**) Scheme of the experimental set-up for the noise detection. The higher squeezing values were measured with the balanced detection set-up, realized by blocking the local oscillator with the beam blocker. The choice of adding (+) or subtracting (−) the photodiodes signals determines the measurement: intensity noise (+) or shot noise (−). To measure the noise quadratures of the field one unblocks the local oscillator and set the mixer to (−); in this case, the shot noise is measured by blocking the light reflected from the microcavity. PBS: polarizing beam splitter; $\frac{\lambda}{2}$, $\frac{\lambda}{4}$: half-wave, quarter-wave plate.

laser. The re-emitted light is collected by the same microscope objective and sent through a telescope and a spatial filter, allowing us to select only the light coming out of the pillar or some specific region if needed. As shown in Fig. 2c, the sample emission is collected in a set-up allowing performing both balanced and homodyne detections.

For the balanced detection, the collected light is equally split into two parts by a $\frac{\lambda}{2}$ plate associated to a a polarizing beam splitter (PBS 2) and each beam is collected by a photodiode. The high frequency (HF) outputs of the two identical photodiodes (81% quantum efficiency, with home-made low-noise electronics) are added or subtracted with a passive circuit, amplified by a low-noise, HF amplifier and sent to a spectrum analyser giving us the spectral noise power (thereafter simply called 'noise'). The choice of addition or subtraction allows us to quickly switch between the measurement of the intensity noise (addition mode) or the shot noise (difference mode). The common mode rejection of the balanced diodes was 45 dB at 7 MHz.

For the homodyne detection, a portion of the pump laser is mixed on PBS 1 with the light emitted by the micropillar with an orthogonal polarization, and acts as local oscillator. In this case, the HF output of the photodiodes are subtracted and the measured quantity gives the noise in the quadrature of the reflected field that is in phase with the local oscillator. The relative phase between the local oscillator and the reflected field is controlled with a piezoelectric-mounted mirror, allowing measuring all quadratures. The shot noise is measured by blocking the light reflected from the microcavity.

For the homodyne set-up, it is important to note that the spatial mode of the sample emission can be strongly distorted by the nonlinear interactions and it is no longer Gaussian-shaped at high polariton densities. For this reason, it was found very

difficult to achieve the mode matching with the local oscillator necessary to have efficient homodyne detection, except in the special case of very low detuning of the pump laser with respect to the ground-state level of the lower polariton branch (since in this case we have a low density of polariton even above threshold). There, proper homodyne detection was achieved (mode matching of 90%). However, such a low detuning is not optimal and thus the squeezing measured with the homodyne detection is lower than at the optimum detuning.

Intensity squeezing measurements at the optimum pump–polariton detuning were performed with the balanced set-up. Figure 3a,b shows the intensity noise measured with a balanced detection: a scan at fixed pump power in Fig. 3a and a scan of the noise versus pump power in Fig. 3b for a polariton–laser detuning $\Delta = 0.19$ meV that we have identified as optimal for squeezing. In Figs 3 and 4, the spectrum analyser was set to zero frequency span and centred at 7 MHz where the signal-to-noise ratio of the detection is maximum, with a sweep time ranging from 1 s to 20 s depending on the type of measurement. The resolution bandwidth (spectral bandwidth of the measurement) was 300 kHz with a 30 Hz video bandwidth (temporal integration over a 30 Hz bandwidth). For the noise dependence on the pump power (Fig. 3b), the motorized plate controlling the excitation power on the pillar is scanned at the same time as the spectrum analyser. We then compare the measured noise to the shot noise. The protocol involves recording the shot noise in difference mode, immediately switching to addition mode to record the intensity noise and then switching back to shot noise measurement (difference mode again) in order to check its stability. The dark noise was recorded after each measurement by recording the electronic noise when the laser beam is blocked. All the presented noise measurements are obtained by normalizing the noise traces by the shot noise after subtraction of the dark noise from both the noise and the shot noise.

A slight energy detuning between the pump laser and the ground state of the lower polariton branch gives rise to optical bistability[12] (see Fig. 3c), characteristic in Kerr nonlinear media. According to theoretical predictions, the best squeezing rate is expected in the vicinity of the turning points of the bistability, as in other nonlinear systems[32]. We therefore chose to sweep the pump power in the vicinity of the bistable region (noise profile measurement, Fig. 3b) to identify the best working points and we performed noise measurements with a fixed pump power corresponding to the maximum of intensity squeezing (steady-state measurement, Fig. 3a).

Squeezing was achieved in a reproducible way in repeated experiments on several different neighbouring pillars. According to previous calculations[33], the best squeezing is expected for a slightly negative cavity–exciton detuning ($0 > \delta > -1$ meV) in planar microcavities. Here the spatial confinement of pillars tends to enhance the polariton–polariton nonlinear interactions with respect to planar microcavities due to the increase in polariton density. We hence chose to work at larger negative cavity–exciton detuning ($\delta \approx -5$ meV) to have a larger photonic fraction, while preserving strong enough nonlinearities from the excitonic component.

Experimental and theoretical results. The strongest noise reduction at fixed pump power was obtained with the laser energy blue-detuned by about $\Delta = 0.19$ meV from the polariton lower energy level on a 6 μm pillar with a cavity–exciton detuning at $\delta \approx -5$ meV. The measured intensity squeezing is 20.3 ± 1.5%, as shown in Fig. 3a. After correction for detection efficiency (81%) and transmission losses ($T = 70\%$), we infer a squeezing in the outgoing field of 35.8 ± 2.6%.

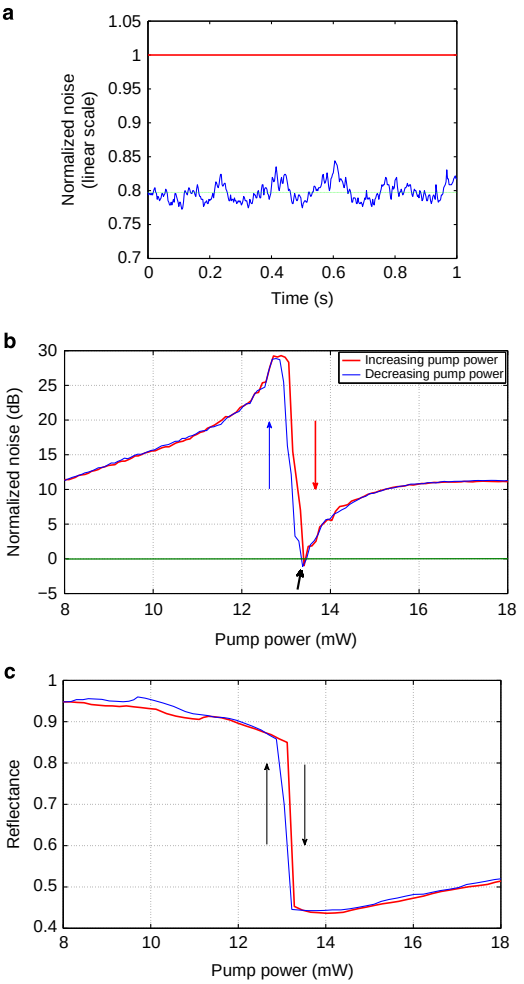

Figure 3 | Intensity squeezing and bistability. (**a**) Squeezed intensity noise at fixed pump power near the lower turning point (linear scale), on a 6 μm pillar at cavity–exciton detuning of −5 meV and a polariton–laser detuning of 0.19 meV. The noise data were normalized with a measurement of the shot noise and a measurement of the dark noise, with $S(t) = (\text{noise}(t) - \langle \text{dark}(t) \rangle)/(\langle \text{shotnoise}(t) \rangle - \langle \text{dark}(t) \rangle)$, $\langle ... \rangle$ being the time average. The measured noise reduction is 20.3 ± 1.5% (−1 dB) below the shot noise limit before corrections, 35.8 ± 2.6% after. The dashed green line is the average noise and the red line is the shot noise. (**b**) Intensity noise (spectral noise power, semi-logarithmic scale) as a function of the pump power for the same pillar under the same conditions as in **a**. The noise increases smoothly towards a peak just before the bistability threshold, then suddenly drops to form a gap where intensity squeezing is observed, with about the same value as in **a**. Here also the normalized spectral noise is obtained with three measurements (noise, shot noise and dark noise). In red is the curve obtained by increasing the pump power, in blue is the curve obtained by decreasing the pump power and the green line represents the shot noise (normalized to one). The thick black arrow points to where **a** was recorded. (**c**) Bistability curve obtained by plotting the reflectance versus the pump power, for the same pillar under the same conditions as in **a**,**b**. The colour code is the same as in **b**. Above the thresholds the transmission is increased, hence a sharp reduction on the reflectance.

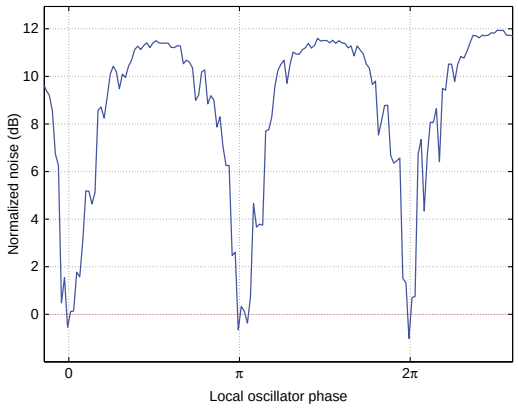

Figure 4 | Homodyne detection. Experimental measurement of squeezing with homodyne detection for a pump–polariton detuning of 0.10 meV on the same pillar as in Fig. 3. The minima were verified to be in the amplitude quadrature. The squeezing obtained from the average between the values at 0, π and 2π is 16% (-0.75 dB) before corrections and 25% after corrections. The reduced value of the squeezing here is mainly due to the non-optimal laser–polariton detuning.

This result was established with a laser intensity lock reducing the low frequency (0–100 kHz) intensity variations to 0.2%. The use of the spatial filter was found not to be crucial, as the laser spot was well matched to the size of the six pillars. On the other hand, excessive spatial filtering led to a reduction of the squeezing, as expected from increasing losses. A coupled exciton–photon model with pump, losses and Kerr nonlinearity (described in Methods) predicts a squeezing value under these conditions of about 40%, in agreement with the experimental value.

Effect of the pump–polariton detuning. The values of pump power at which the optimal working points occur as well as the specific shape of the bistability curve depend on Δ. This parameter is also expected to influence the intensity noise profile and the squeezing value. The noise dependence on the pump power for the same pillar and parameter values as mentioned above is shown in Fig. 3b. Outside of the bistable region there is an excess noise due to thermal exciton reservoir populated by the pump laser. In the vicinity of the bistability thresholds, this noise undergoes amplification or deamplification due to the nonlinear effects. The intensity noise strongly increases below the bistability thresholds then decreases, as observed in other nonlinear systems[15,32,33].

At higher values of Δ, the pump power required to reach the bistability threshold increases and the noise profiles are drastically altered. Indeed a bistable behaviour appears above some critical value of Δ. For rather large Δ only the lower turning point (reached by decreasing the pump power) is able to produce intensity squeezing. If Δ is lower than the critical value, strong nonlinear modifications of the noise and reflectance can be observed despite the lack of bistable behaviour and the noise curves are the same when increasing or decreasing the pump power. These effects were studied in our experiment by repeating the noise measurements at different polariton–laser detunings and are discussed in the Supplementary Note 1. Supplementary Figs 1 and 2 show, respectively, the reflectance and the noise plots obtained for $\Delta = 0.10$ meV while Supplementary Figs 3 and 4 show, respectively, the reflectance and the noise plots obtained for $\Delta = 0.21$ meV and Supplementary Figs 5 and 6 show the reflectance and the noise plots obtained for $\Delta = 0.30$ meV. The optimal detuning for squeezing that we present here corresponds to the onset of the bistability behaviour where the hysteresis cycle is very narrow (Fig. 3b).

Homodyne detection. To confirm these findings, we have measured the noise along all the field quadratures with the homodyne detection and checked that squeezing occurs only in the amplitude quadrature at the bistability turning points. As previously mentioned, for low Δ the output of the pillar is nearly Gaussian. In such conditions, we were able to achieve good mode matching between the local oscillator and the spatial mode emitted by the micropillar (about 90%) and implement an efficient homodyne detection. The path difference between the two beams, set to change linearly with time, determines the measured quadrature. The result is presented in Fig. 4 for a laser–polariton detuning of $\Delta = 0.10$ meV. Squeezing is observed at the minima of the curve showing the characteristic arches. Let us note that the anti-squeezed quadrature (phase quadrature) exhibits a large excess noise of the order of 12 dB due to thermal noise input. The fluctuations and irregularities of the noise arches are due to the fact that the interferometric homodyne set-up is more sensitive to mechanical instabilities. A comparison with the intensity measurements set-up allows checking that the squeezed quadrature indeed corresponds to the amplitude quadrature. The observed squeezing with this set-up was of about 16% (25% inferred after corrections).

Discussion

In conclusion, we have reported an experimental demonstration of strong enhancement of squeezed light generation with confined polaritons in semiconductor micropillars. The best intensity squeezing was inferred to be $35.8 \pm 2.6\%$ below the shot noise limit and was confirmed by measurements with a homodyne detection set-up. Several original optimizations allowed to reach these results. In particular, the special design of the pillars ensures a near-perfect mode matching between the pump and the polariton field; the discretization of the polariton energy modes allows for a strong reduction of the excess noise coming from phonon coupling. The reduced reflectivity of the upper Bragg mirror relative to that of the bottom mirror enhances the emission of light towards the top of the pillar, optimizing the light collection. Finally the relatively low-quality factor of the cavity increases the radiative to non-radiative losses ratio which, together with the choice of a working point with a high photonic fraction, results in a larger squeezing in the emitted light. These results demonstrate the improvement of intensity-squeezed light and light–matter fields brought by reduced dimensionality in semiconductor microstructures and open the way to the realization of ultra-low threshold integrated sources for the quantum information-processing technology.

Methods

Theoretical model. Owing to the lateral confinement of the micropillar, the polariton modes are well identified and we can selectively pump a polariton mode by tuning the spatial and spectral profile of the pumping light. For the theoretical analysis, we simply consider a single-cavity mode with frequency ω_c and an exciton state with frequency ω_x. The Hamiltonian of the coupled system (polariton) in the microcavity is:

$$\hat{H}_0 = \hbar\omega_c \hat{a}^\dagger \hat{a} + \hbar\omega_x \hat{b}^\dagger \hat{b} + \frac{\hbar\Omega_R}{2}\left(\hat{a}^\dagger \hat{b} + \hat{b}^\dagger \hat{a}\right) + \frac{\hbar g}{2}\hat{b}^\dagger \hat{b}^\dagger \hat{b}\hat{b} \qquad (1)$$

Here, $\hat{a}$ and $\hat{b}$ are the annihilation operators of a photon and an exciton, respectively, and Ω_R is the coupling strength (vacuum Rabi splitting) between the cavity photon and the exciton. The last term represents a third-order nonlinearity

for the excitons with strength g. The polaritons are subject to an effective Kerr effect through it. In addition, considering the photonic and excitonic reservoirs, the quantum Langevin equations for the cavity photons and the excitons are, respectively, derived as follows:

$$i\frac{\partial \hat{a}}{\partial t}=\left(\omega_c-\frac{i\kappa}{2}\right)\hat{a}+\left(\frac{\Omega_R}{2}\right)\hat{b}-i\sqrt{\kappa}\left(\hat{a}_{in}+F_p e^{-i\omega_p t}\right) \quad (2)$$

$$i\frac{\partial \hat{b}}{\partial t}=\left(\omega_x-\frac{i\gamma}{2}\right)\hat{b}+\left(\frac{\Omega_R}{2}\right)\hat{a}+g\hat{b}^{\dagger}\hat{b}\hat{b}-i\sqrt{\gamma}\hat{b}_{in} \quad (3)$$

Here, κ and γ are the dissipation rates of the cavity photon and exciton, respectively. $\hat{a}_{in}$ and $\hat{b}_{in}$ are the input operators from photonic and excitonic reservoirs, respectively, and we assume they have a zero average $\langle\hat{a}_{in}\rangle=\langle\hat{b}_{in}\rangle=0$ (incoherent input). Instead, we explicitly consider an applied coherent pumping with amplitude F_p and frequency ω_p. Then, the input–output relation for the photon operators is expressed as:

$$\hat{a}_{out}=\hat{a}_{in}+F_p e^{-i\omega_p t}+\sqrt{\kappa}\hat{a} \quad (4)$$

From the above Langevin equations, we first calculate the mean fields of the cavity photon and exciton induced by the coherent pump. Assuming $\langle\hat{a}\rangle=\alpha e^{-i\omega_p t}$ and $\langle\hat{b}\rangle=\beta e^{-i\omega_p t}$, the steady-state mean fields are as follows:

$$i\frac{\partial}{\partial t}\alpha=\left(\omega_c-\omega_p-\frac{i\kappa}{2}\right)\alpha+\left(\frac{\Omega_R}{2}\right)\beta-i\sqrt{\kappa}F_p=0 \quad (5)$$

$$i\frac{\partial}{\partial t}\beta=\left(\omega_x-\omega_p-\frac{i\gamma}{2}\right)\beta+\left(\frac{\Omega_R}{2}\right)\alpha+g|\beta|^2\beta=0 \quad (6)$$

Once the mean fields are determined, the reflectance is calculated via the input–output relation as follows:

$$\langle\hat{a}_{out}\rangle=\alpha_{out}e^{-i\omega_p t}=\left(F_p+\sqrt{\kappa}\alpha\right)e^{-i\omega_p t} \quad (7)$$

$$R=\frac{|\langle\hat{a}_{out}\rangle|^2}{\left|\langle\hat{a}_{in}+F_p e^{-i\omega_p t}\rangle\right|^2}=\frac{\left|F_p+\sqrt{\kappa}\alpha\right|^2}{|F_p|^2} \quad (8)$$

The intensity noise is calculated by the fluctuations around the mean field value. Defining the fluctuation operators as $\delta\hat{a}=\hat{a}e^{i\omega_p t}-\alpha$ and $\delta\hat{b}=\hat{b}e^{i\omega_p t}-\beta$, and linearizing the corresponding equations, the quantum Langevin equations are rewritten as follows:

$$i\frac{\partial}{\partial t}\delta\hat{a}=\left(\omega_c-\omega_p-\frac{i\kappa}{2}\right)\delta\hat{a}+\left(\frac{\Omega_R}{2}\right)\delta\hat{b}-i\sqrt{\kappa}\hat{a}_{in} \quad (9)$$

$$i\frac{\partial}{\partial t}\delta\hat{b}=\left(\omega_x+2g|\beta|^2-\omega_p-\frac{i\gamma}{2}\right)\delta\hat{b}+\left(\frac{\Omega_R}{2}\right)\delta\hat{a}+g\beta^2\delta\hat{b}^{\dagger}-i\sqrt{\gamma}\hat{b}_{in} \quad (10)$$

From these equations and the input–output relation, we can infer the fluctuations $\delta\hat{a}_{out}=\hat{a}_{out}e^{i\omega_p t}-\alpha_{out}$ of the output photons. The variance of the output is expressed as follows:

$$\begin{aligned}(\Delta N)^2&=\left\langle\hat{a}_{out}^{\dagger}\hat{a}_{out}^{\dagger}\hat{a}_{out}\hat{a}_{out}\right\rangle-\left\langle\hat{a}_{out}^{\dagger}\hat{a}_{out}\right\rangle^2\\&=2|\alpha_{out}|^2\left\langle\delta\hat{a}_{out}^{\dagger}\delta\hat{a}_{out}\right\rangle+2Re\left[\left(\alpha_{out}^{*}\right)^2\langle\delta\hat{a}_{out}\delta\hat{a}_{out}\rangle\right]\end{aligned} \quad (11)$$

Then, the normalized intensity noise is expressed as follows:

$$\frac{(\Delta N)^2}{\left\langle\hat{a}_{out}^{\dagger}\hat{a}_{out}\right\rangle}=2\left\langle\delta\hat{a}_{out}^{\dagger}\delta\hat{a}_{out}\right\rangle+2Re\left[\left(\frac{\alpha_{out}^{*}}{|\alpha_{out}|}\right)^2\langle\delta\hat{a}_{out}\delta\hat{a}_{out}\rangle\right] \quad (12)$$

The correlations of the output are calculated from the ones of input operators. Here, we assume that the correlation of the photonic input as $\langle\hat{a}_{in}^{\dagger}(t)\hat{a}_{in}(t')\rangle=\langle\hat{a}_{in}(t)\hat{a}_{in}(t')\rangle=0$ (extracavity photon vacuum) while the excitonic reservoir has an incoherent population, namely $\langle\hat{b}_{in}^{\dagger}(t)\hat{b}_{in}(t')\rangle=N_{th}\delta(t-t')$ and $\langle\hat{b}_{in}(t)\hat{b}_{in}(t')\rangle=0$. We also assume that there is no correlation between the photonic and excitonic inputs. N_{th} represents the thermal noise and is chosen to be linear with the pump power ($N_{th}=\sigma\cdot W_p$(mW), with σ the proportionality constant and W_p the pump power).

Parameters. In the calculations, we have used the following values: $\delta=\omega_c-\omega_x=-5$ meV, $\Omega_R=4$ meV and $\kappa=0.11$ meV. The other parameters have been estimated by fitting experimental data for several values of Δ, the pump–polariton detuning and are shown in Table 1. From the theoretical results of this simple model, we observe that the excitonic dissipation rate γ tends to increase with Δ. This can be explained by an increased population in the excitonic reservoir.

This model is able to reproduce correctly the reflectance traces obtained in the experiment, and the intensity noise for pump intensities above the bistability threshold. Note that the prediction of the intensity noise for low pump intensities does not reproduce well the experimental data. This is probably due to the fact that our model does not take disorder effects into account. For very low densities, the disorder becomes the dominant effect, so we cannot capture the corresponding noise behaviour adequately.

Table 1 | Parameters.

$\Delta=\omega_p-\omega_{polariton}$ (meV)	γ (meV)	σ (mW^{-1})
0.14	0.43	0.2
0.15	0.40	0.3
0.19	0.89	0.12
0.26	0.63	0.06

Table of parameters used in the theory, deduced by fitting the experimental data of the reflectance.

Supplementary Fig. 7 shows the comparison between the model and the experiment for the intensity noise at $\Delta=0.15$ meV. The bistability curve of the reflectance and the corresponding intensity noise dependence on the pump power for a pump–polariton detuning of 0.26 meV are shown in Supplementary Fig. 8 and in Supplementary Fig. 9, respectively.

References

1. Loo, V. *et al.* Optical nonlinearity for few-photon pulses on a quantum dot-pillar cavity device. *Phys. Rev. Lett.* **109,** 166806 (2012).
2. Claudon, J. *et al.* A highly efficient single-photon source based on a quantum dot in a photonic nanowire. *Nat. Photon.* **4,** 174–177 (2010).
3. Dousse, A. *et al.* Ultrabright source of entangled photon pairs. *Nature* **466,** 217–220 (2010).
4. Kira, M., Jahnke, F. & Koch, S. W. Quantum theory of secondary emission in optically excited semiconductor quantum wells. *Phys. Rev. Lett.* **82,** 3544–3547 (1999).
5. Carmichael, H. J. & Walls, D. F. Proposal for the measurement of the resonant Stark effect by photon correlation techniques. *J. Phys. B* **9,** 43–48 (1976).
6. Kimble, H. J., Dagenais, M. & Mandel, L. Photon antibunching in resonance fluorescence. *Phys. Rev. Lett.* **39,** 691–695 (1977).
7. Slusher, R. E., Hollberg, L. W., Yurke, B., Mertz, J. C. & Valley, J. F. Observation of squeezed states generated by four-wave mixing in an optical cavity. *Phys. Rev. Lett.* **55,** 2409–2412 (1985).
8. Liew, T. & Savona, V. Multipartite polariton entanglement in semiconductor microcavities. *Phys. Rev. A* **84,** 032301 (2011).
9. Liew, T. & Savona, V. Quantum entanglement in nanocavity arrays. *Phys. Rev. A* **85,** 050301(R) (2012).
10. Fox, A. M., Baumberg, J. J., Dabbicco, M., Huttner, B. & Ryan, J. F. Squeezed light generation in semiconductors. *Phys. Rev. Lett.* **74,** 1728–1731 (1995).
11. Karr, J. Ph., Baas, A., Houdre, R. & Giacobino, E. Squeezing in semiconductor microcavities in the strong coupling regime. *Phys. Rev. A* **69,** 031802(R) (2004).
12. Baas, A., Karr, J. Ph., Eleuch, H. & Giacobino, E. Optical bistability in semiconductor microcavities. *Phys. Rev. A* **69,** 023809 (2004).
13. Saba, M. *et al.* High-temperature ultrafast polariton parametric amplification in semiconductor microcavities. *Nature* **414,** 731–735 (2001).
14. Weisbuch, C., Nishioka, M., Ishikawa, A. & Arakawa, Y. Observation of the coupled exciton-photon mode splitting in a semiconductor quantum microcavity. *Phys. Rev. Lett.* **69,** 3314–3317 (1992).
15. Carusotto, I. & Ciuti, C. Quantum fluids of light. *Rev. Mod. Phys.* **85,** 299–366 (2013).
16. Kasprzak, J. *et al.* Bose–Einstein condensation of exciton polaritons. *Nature* **443,** 409–414 (2006).
17. Amo, A. *et al.* Collective fluid dynamics of a polariton condensate in a semiconductor microcavity. *Nature* **457,** 291–295 (2009).
18. Amo, A. *et al.* Superfluidity of polaritons in semiconductor microcavities. *Nat. Phys.* **5,** 805–810 (2009).
19. Amo, A. *et al.* Polariton superfluids reveal quantum hydrodynamic solitons. *Science* **332,** 1167–1170 (2011).
20. Sich, M. *et al.* Observation of bright polariton solitons in a semiconductor microcavity. *Nat. Photon.* **6,** 50–55 (2011).
21. Hivet, R. *et al.* Half-solitons in a polariton quantum fluid behave like magnetic monopoles. *Nat. Phys.* **8,** 724–728 (2012).
22. Lagoudakis, K. G. *et al.* Observation of half-quantum vortices in an exciton-polariton condensate. *Science* **326,** 974–976 (2009).
23. Tosi, G. *et al.* Geometrically locked vortex lattices in semiconductor quantum fluids. *Nat. Commun.* **3,** 1243 (2012).
24. Savvidis, P. G. *et al.* Angle-resonant stimulated polariton amplifier. *Phys. Rev. Lett.* **84,** 1547–1550 (2000).
25. Stevenson, R. M. *et al.* Continuous wave observation of massive polariton redistribution by stimulated scattering in semiconductor microcavities. *Phys. Rev. Lett.* **85,** 3680–3683 (2000).
26. Messin, G. *et al.* Parametric polariton amplification in semiconductor microcavities. *Phys. Rev. Lett.* **87,** 127403 (2001).
27. Tassone, F. & Yamamoto, Y. Lasing and squeezing of composite bosons in a semiconductor microcavity. *Phys. Rev. A* **62,** 063809 (2000).

28. Schwendimann, P., Ciuti, C. & Quattropani, A. Statistics of polaritons in the nonlinear regime. *Phys. Rev. B* **68,** 165324 (2003).
29. Bamba, M., Pigeon, S. & Cuiti, C. Quantum squeezing generation versus photon localization in a disordered planar microcavity. *Phys. Rev. Lett.* **104,** 213604 (2010).
30. Bloch, J. *et al.* Strong-coupling regime in pillar semiconductor microcavities. *Superlattices Microstructures* **22,** 371–374 (1997).
31. Bajoni, D. *et al.* Polariton laser using single micropillar GaAs-GaAlAs semiconductor cavities. *Phys. Rev. Lett.* **100,** 047401 (2008).
32. Hilico, L., Fabre, C., Reynaud, S. & Giacobino, E. Linear input-output method for quantum fluctuations in optical bistability with two-level atoms. *Phys. Rev. A* **46,** 4397–4406 (1992).
33. Romanelli, M., Karr, J. Ph., Leyder, C., Giacobino, E. & Bramati, A. Two-mode squeezing in polariton four-wave mixing. *Phys. Rev. B* **82,** 155313 (2010).

Acknowledgements

This work was partly supported by the FP7 ITN 'Clermont4' (235114), by the ANR projects PNANO-07-005 'GEMINI' and Quandyde (ANR-11-BS10-001), by the French RENATECH network and the KAKENHI 24-632 grant. The authors are grateful to J. Ph. Karr and Q. Glorieux for useful discussions.

Author contributions

All authors contributed to all aspects of this work.

Additional information

Supplementary Information accompanies this paper at http://www.nature.com/naturecommunications

Competing financial interests: The authors declare no competing financial interests.

Reprints and permission information is available online at http://npg.nature.com/reprintsandpermissions/

How to cite this article: Boulier, T. *et al.* Polariton-generated intensity squeezing in semiconductor micropillars. *Nat. Commun.* 5:3260 doi: 10.1038/ncomms4260 (2014).

LETTERS
PUBLISHED ONLINE: 26 AUGUST 2012 | DOI: 10.1038/NPHYS2406
nature physics

Half-solitons in a polariton quantum fluid behave like magnetic monopoles

R. Hivet[1], H. Flayac[2], D. D. Solnyshkov[2], D. Tanese[3], T. Boulier[1], D. Andreoli[1], E. Giacobino[1], J. Bloch[3], A. Bramati[1]*, G. Malpuech[2] and A. Amo[3]*

Magnetic monopoles[1] are point-like sources of magnetic field, never observed as fundamental particles. This has triggered the search for monopole analogues in the form of emergent particles in the solid state, with recent observations in spin-ice crystals[2–4] and one-dimensional ferromagnetic nanowires[5]. Alternatively, topological excitations of spinor Bose–Einstein condensates have been predicted to demonstrate monopole textures[6–8]. Here we show the formation of monopole analogues in an exciton–polariton spinor condensate hitting a defect potential in a semiconductor microcavity. Oblique dark solitons are nucleated in the wake of the defect[9,10] in the presence of an effective magnetic field acting on the polariton pseudo-spin[11]. The field splits the integer soliton into a pair of oblique half-solitons[12] of opposite magnetic charge, subject to opposite effective magnetic forces. These mixed spin-phase excitations thus behave like one-dimensional monopoles[13]. Our results open the way to the generation of stable magnetic currents in photonic quantum fluids.

Magnetic monopoles are the magnetic counterparts of electric charges, characterized by a divergent field. The seminal work of Dirac[1] showed that monopoles are not forbidden by the laws of quantum mechanics. In particular, he considered particles characterized by a wavefunction with a nodal line and a non-integrable phase around it. One route to create an object behaving like a monopole is thus to engineer a wavefunction with such characteristics. A model system to do this is a spinor Bose–Einstein condensate[14–16], demonstrating properties such as superfluidity or persistent currents. In reduced dimensions, not only do these quantum fluids support topological defects[17], such as vortices (two dimensional; 2D) or solitons (1D) characterized by a node, but an adequate spin distribution can also provide a vector field with a non-zero divergence, satisfying Maxwell's equations for a point magnetic charge[6–8]. Monopoles can then be arranged in spinor condensates in the form of mixed spin-phase topological excitations, with a magnetic analogue of the Coulomb force acting on them[13].

Exciton–polariton (polariton) condensates seem a well-suited system to evidence and study such original effects in quantum fluids. Polaritons are the quasi-particles arising from the strong coupling between excitons and photons confined in planar semiconductor microcavities (InGaAs/GaAs/AlGaAs in our case)[18]. Polariton fluids are easy to manipulate with standard optical techniques[19–22] and they have recently become a model system for the study of quantum fluid effects such as superfluidity[23], vortex formation[24,25] or oblique solitons[9,10]. Their spin structure is especially interesting: polaritons are bosons with only two allowed spin projections ± 1 on the growth axis of the sample, which couple to circularly polarized ($\sigma_{\pm}$) photons in and out of the cavity. A coherent superposition of different spin populations

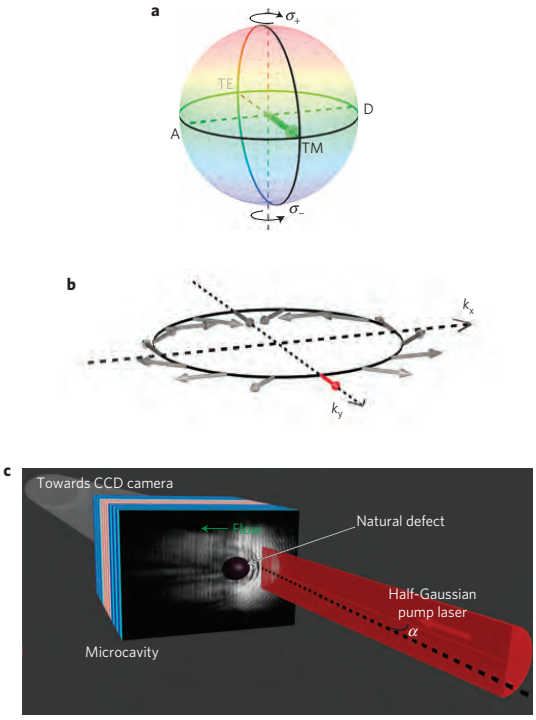

Figure 1 | Polariton pseudospin, effective magnetic field and experimental set-up. a, Bloch sphere representing all of the possible spin configurations of the polariton gas and the associated polarizations: the poles represent circular polarization, the equator represents linearly polarized states and the intermediate latitudes represent elliptically polarized states. **b**, Direction of the effective magnetic field created by the TE–TM splitting for polaritons propagating in different directions. **c**, Scheme of the resonant injection of the polariton fluid above a round potential barrier present in the sample. Half-solitons nucleate in its wake. α is the angle of incidence of the excitation beam with respect to the normal to the microcavity plane.

[1]Laboratoire Kastler Brossel, Université Pierre et Marie Curie, Ecole Normale Supérieure et CNRS, UPMC case 74, 4 place Jussieu, 75005 Paris, France, [2]Institut Pascal, PHOTON-N2, Clermont Université, University Blaise Pascal, CNRS, 24 avenue des Landais, 63177 Aubière cedex, France, [3]Laboratoire de Photonique et Nanostructures, CNRS, Route de Nozay, 91460 Marcoussis, France. *e-mail: bramati@spectro.jussieu.fr; alberto.amo@lpn.cnrs.fr.

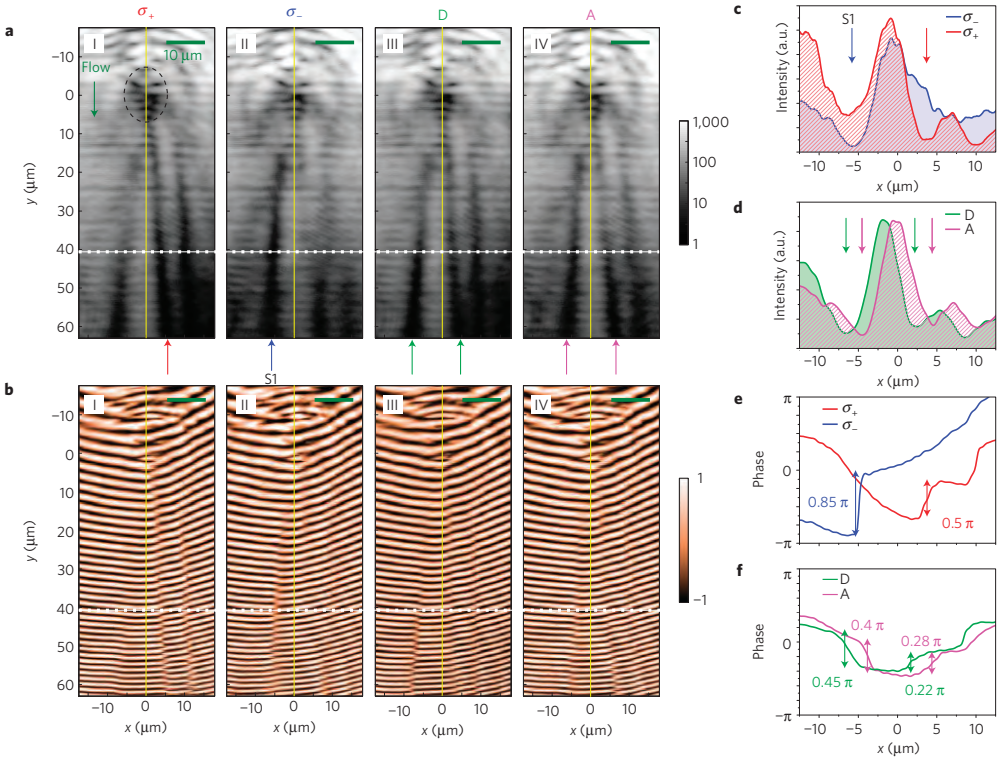

Figure 2 | Density and phase tomography of the half-solitons. a, Emitted intensity of the polariton gas in σ_+ (I) and σ_- (II) circularly polarized components and in the diagonal (III) and antidiagonal (IV) linearly polarized components with respect to the TM polarization of injection. Half-solitons spontaneously nucleate in the wake of the potential barrier (dashed circle in **a**-I) and are evidenced as dark traces present only in one circular polarization component (arrows). The yellow line is a guide to the eye. S1 indicates the half-soliton discussed in the text. **b**, Corresponding interferometric images obtained from the interference of the real-space emission with a beam of homogeneous phase. **c**,**d**, Density profiles of the σ_+ and σ_- (**c**), and diagonal and antidiagonal (**d**) polarized emission along the dotted line in **a**-I–IV. The arrows indicate the position of the inner half-solitons, present only in a given circular polarization and in both diagonal polarizations. **e**,**f**, Associated phase jump (obtained from **b**-I–IV). The phase jumps observed in diagonal/antidiagonal polarizations have half the value of that measured in circular polarization, hence the term half-solitons. D represents diagonal and A antidiagonal polarized emmisions in **d** and **f**. The error bars in the estimation of the phase jumps shown in **e** and **f** represent $\pm 0.08\pi$.

gives rise to polarization states that can be described by a pseudospin vector **S** mapped onto a Bloch sphere (Fig. 1a). Another remarkable feature of microcavities is the presence of an effective in-plane magnetic field (Fig. 1b) induced by the polarization splitting between the transverse electric (TE)–transverse magnetic (TM) polarization modes[11]. The effective field interacts with the polariton pseudospin, adding a magnetic energy term $H_{\mathrm{TE-TM}} = -\mathbf{S}\cdot\mathbf{\Omega}_{\mathrm{TE-TM}}$ to the Hamiltonian (see Supplementary Information) and it provides the analogue of a Coulomb force acting on topological monopoles[13]. Finally, polariton–polariton interactions are strongly spin-anisotropic of the antiferromagnetic type[26]. This is an absolute requirement for the observation of any stable monopole structure[7,8]. Indeed, a topological monopole in a two-component spinor condensate is stable against its destruction by an in-plane effective magnetic field if the difference in the interaction energy between the same and opposite spins exceeds the magnetic energy[13].

One kind of spin-phase topological defect already reported in polariton quantum fluids are the so-called half-vortices[27,28]. However, no probing of the monopole behaviour has been possible yet, because of the disorder-induced pinning[28]. The 1D counterpart of a half-vortex is a dark half-soliton, characterized by a notch in the polariton density of the fluid, and a simultaneous phase and polarization rotation of up to $\pi/2$ in the condensate wavefunction across the soliton[12].

Here, we report on the experimental observation of oblique half-solitons and on their separation and acceleration caused by the effective magnetic field present in semiconductor microcavities. Oblique solitons (or half-solitons in the spinor case) are formed in the wake of a localized potential barrier present in the path of a flowing condensate[9]. They can be seen as the trajectories of 1D solitons in the direction perpendicular to the flow (x), travelling across a 2D flow. The second spatial coordinate (y, parallel to the flow) represents the time coordinate of the 1D system ($t = y/v_{\mathrm{f}}$, where v_{f} is the flow velocity). This means that the soliton trajectory becomes traceable in a steady state regime[29]. Studying such trajectories, we demonstrate that an integer oblique soliton separates into a pair of half-solitons of opposite magnetic charge accelerated in opposite directions.

In our experiments we create a polariton fluid in a semiconductor microcavity (see Methods) at a temperature of 10 K by quasi-resonant excitation of the lower polariton branch with a continuous

wave Ti:sapphire monomode laser. Polarization-resolved real-space images of the polariton fluid in the transmission geometry are then recorded on a CCD (charge-coupled device) camera owing to the photons escaping out of the cavity (Fig. 1c). The fluid is injected at supersonic speed (in-plane momentum of $k_P = 1.3\,\mu m^{-1}$, see Methods), upstream from the potential barrier formed by a structural photonic defect present in our sample. Under these conditions, a circularly polarized excitation beam leads to the formation of pairs of oblique dark solitons in the wake of the barrier[9], characterized by a phase jump close to π across each notch (see Supplementary Information). In the present experiments, we create a polariton gas with linear polarization parallel to the flow (TM polarization, along the y direction). This is a key feature needed to explore the nucleation of spin-phase topological excitations, which can be evidenced by analysing the circularly polarized components of the emission.

First, we demonstrate the formation of half-integer solitons. Figure 2a-I shows the nucleation of two oblique dark solitons to the right of the barrier wake in the σ_+ component of the emission. They can be identified as dark straight notches in the polariton density. These solitons are almost absent in the σ_- component (Fig. 2a-II). In turn, in the σ_- emission, a deep soliton (S1) clearly appears to the left of the barrier wake (blue arrow), where only a very shallow one is present in σ_+ (see the profiles in Fig. 2c). The absence of mirror symmetry between Fig. 2a-I and a-II arises from the specific and uncontrolled form of the natural potential barrier. The individual dark solitons in each of the $S_z = \pm 1$ states of the fluid appear as long spatial traces with a high degree of circular polarization ($\rho_c = (I^+ - I^-)/(I^+ + I^-)$, where $I^\pm$ is the emitted intensity in $\sigma_\pm$ polarization), as shown in Fig. 3a. Interferometric images obtained by combining the real-space emission with a reference beam of homogeneous phase (Fig. 2b-I and b-II) give access to the phase jump across each soliton. For instance, for the soliton S1 observed in σ_-, 42 µm after the obstacle we measure a phase jump of $\Delta\theta_- = 0.85\pi$ (Fig. 2e; note that it would be π for a strict dark soliton with zero density at its centre[9]), whereas in the same region the phase in the σ_+ component does not change ($\Delta\theta_+ \approx 0$).

A dark soliton present in just one spin component of the fluid is the fingerprint of a half-soliton[12]. The mixed spin-phase character of these topological excitations is further evidenced when analysing them in the linear polarization basis. In the regions where the two circular polarizations are of equal intensity (that is, the fluid surrounding the half-solitons) we can define a linear polarization angle $\eta = (\theta_+ - \theta_-)/2$ and a global phase $\phi = (\theta_+ + \theta_-)/2$, where θ_+ and θ_- are the local phases of each circularly polarized component[12,27]. In our experiments we directly access the phase jump $\Delta\phi$ and the change of η across the solitons by studying the linearly polarized emission in the diagonal and anti-diagonal directions (polarization plane rotated by $+45°$ and $-45°$ with respect to the TM direction). Figure 2d,f shows that the half-soliton S1 is also present in these polarizations with a phase jump of $\Delta\phi \approx 0.4\pi$. This confirms that across the half-solitons, ϕ undergoes a jump $\Delta\phi \approx 0.85\pi/2 \approx (\Delta\theta_+ + \Delta\theta_-)/2$, that is, one-half the phase jump observed in the circularly polarized component in which the soliton is present. We also expect a similar jump $\Delta\eta$ of the direction of polarization. This is demonstrated in Fig. 3b, where all the half-solitons present in our fluid (dashed lines extracted from Fig. 2a-I and a-II) appear as walls between domains of diagonal (magenta) and anti-diagonal (green) polarization. Mapping the linear polarization vector in the vicinity of soliton S1 (Fig. 4a), we deduce a jump of the polarization direction of $\Delta\eta \approx 0.32\pi$ (Fig. 4c), close to $\Delta\phi$, the ideal expected value.

Analysing the half-soliton trajectory from polarization-resolved real-space measurements, we study their acceleration in the field $\mathbf{\Omega}_{TE-TM}$ originating from the TE–TM splitting present in the structure[11], pointing in the direction of the flow (y, red arrow in Fig. 1b). The acceleration arises from the interaction between this

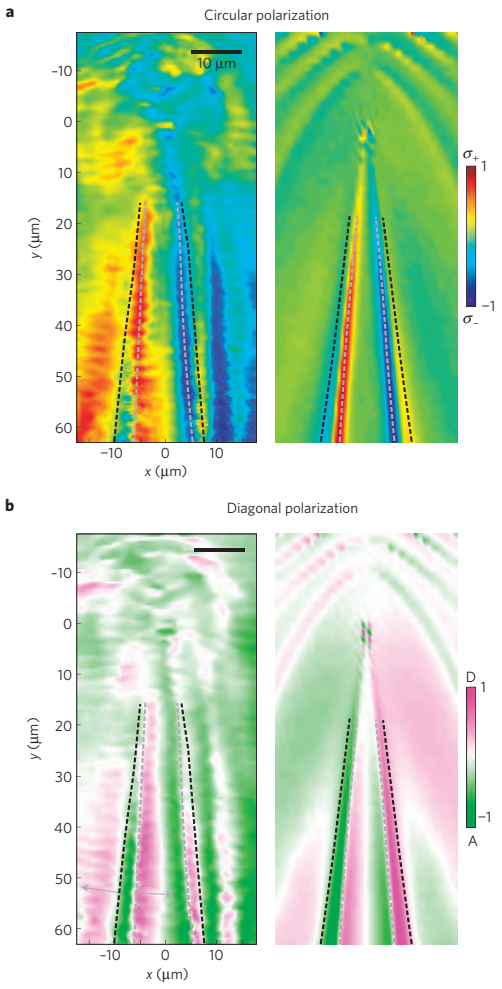

Figure 3 | Polarization texture of half-solitons. a,b, Left panels, the measured degree of circular and diagonal polarizations, respectively; right panels, the calculated patterns from the solution of the nonlinear spin-dependent Schrödinger equation describing the system in the conditions of the experiment (see Supplementary Information). The dashed lines show the trajectory of the inner (grey) and outer (black) half-solitons extracted from Fig. 2a-I and a-II. The trajectories of the half-solitons appear as extremes of circular polarization, and as domain walls in diagonal polarization. The grey arrows in **b** indicate the direction of acceleration of the half-solitons induced by the effective magnetic field.

magnetic field and the pseudospin texture of the half-soliton, shown in Fig. 4b for S1. In the direction perpendicular to the soliton (dotted line), the in-plane pseudospin $\mathbf{S}$ is divergent, because it points away from S1 on both sides, as expected for a magnetic charge.

We are able to evaluate the force acting on the half-soliton as the gradient of the magnetic energy with respect to the half-soliton position x_0. The magnetic energy per unit length is $\int -\mathbf{S}(x' - x_0) \cdot \mathbf{\Omega}_{TE-TM}\, dx'$, where the integral is performed along the x' transverse direction, perpendicular to the half-soliton located at x_0. The energy has a positive contribution from the left of the

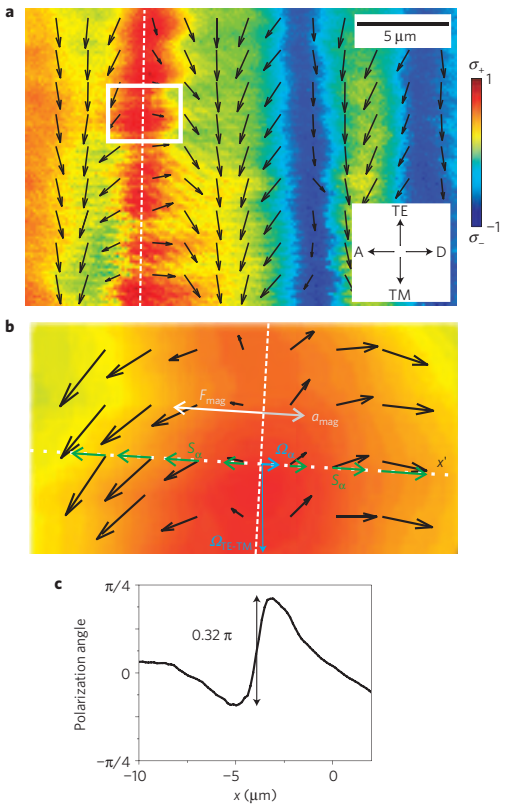

Figure 4 | Magnetic force acting on the half-solitons. a, Complete spin texture of the polariton fluid in the region between 30 and 50 µm below the barrier. The colour scale indicates the degree of circular polarization (latitude in the Bloch sphere), and the arrows the direction of the linear polarization as defined in the equator of the Bloch sphere. **b**, Higher magnification of the area outlined by a white rectangle in **a**. The half-soliton, marked by a white dashed line in **a** and **b**, provides a pseudospin field analogous to that of a point charge in the direction perpendicular to its trajectory (white dotted line). The TE–TM effective magnetic field (Ω_{TE-TM}) has a component Ω_α perpendicular to the half-soliton, which exerts a force F_{mag} causing it to accelerate at a_{mag}. **c**, Angle of the linear polarization plane measured along the direction perpendicular to the half-soliton (shown in **b** as green arrows along the dotted white line). The angle jumps from the antidiagonal to the diagonal direction when crossing the half-soliton.

half-soliton ($\mathbf{S}$ and $\mathbf{\Omega}_{TE-TM}$ pointing in opposite directions), and a negative one from the right ($\mathbf{S}$ and $\mathbf{\Omega}_{TE-TM}$ having the same direction). For the magnetic energy to be minimized, a magnetic force appears, pushing the half-soliton towards the left, increasing the negative contribution. As solitons are density notches, their effective mass is negative[17] and, therefore, the acceleration is in the direction opposite to the force. Thus, the half-soliton S1 that appears in the σ_- component of the fluid accelerates towards the right, as sketched in Fig. 4b. The direction of the acceleration is opposite for the soliton present in the σ_+ component (see arrows in Fig. 3b).

The monopole dynamics allows an understanding of the mechanisms of formation of the half-solitons in our experiments. An integer soliton nucleated right behind the obstacle can be seen as a superposition of two half-solitons of opposite magnetic charges. The presence of the TE–TM effective magnetic field makes them experience opposite magnetic forces, leading to their separation and to the curved trajectories depicted as dashed lines in Fig. 3, a behaviour similar to the monopole separation in spin ice under a magnetic field[3]. The half-solitons pushed towards the centre are slowed down, gaining stability and becoming darker as the trajectory becomes parallel to the field. Those pushed outwards gain velocity and become shallower until they eventually disappear (see Supplementary Information and the black dashed lines in Fig. 3). The trajectories of these expelled secondary half-solitons are perturbed far from the obstacle axis by the presence of further solitons nucleated by the large barrier, particularly on the right side of the images. The monopole behaviour and soliton separation are well reproduced by a nonlinear Schrödinger equation including spin and the effective magnetic field present in our microcavities (see Fig. 3 and Supplementary Information). The analogy of half-solitons with magnetic monopoles goes well beyond the behaviour reported here under an applied magnetic field. Our theoretical model predicts repulsive and attractive interactions between half-solitons depending on their respective charges (see Supplementary Information).

A remarkable feature of half-soliton monopoles is that they can be thought of as charged partly photonic quasiparticles, propagating with a high velocity in a fluid that supports superflow[23]. Their generation can be well controlled by the phase and density engineering of the polariton wavefunction, their trajectories can be easily followed using standard optical techniques and their dynamics can be controlled by applying strain or external electric fields, which modify the effective magnetic field[30]. Furthermore, owing to the developed engineering of the polariton landscape[19,20], we open the way to the realization of magnetronic circuits in a polariton chip.

Methods

Sample description. The experimental observations have been performed at 10 K in a 2λ GaAs microcavity containing three $In_{0.05}Ga_{0.95}As$ quantum wells. The top and bottom Bragg mirrors embedding the cavity have, respectively, 21 and 24 pairs of GaAs/AlGaAs alternating layers with an optical thickness of $\lambda/4$, with λ being the wavelength of the confined cavity mode. The resulting Rabi splitting is 5.1 meV, and the polariton lifetime is about 10 ps. During the molecular beam epitaxy growth of the distributed Bragg reflectors, the slight mismatch between the lattice constants of each layer results in an accumulated stress that relaxes in the form of structural defects. These photonic defects create high potential barriers in the polariton energy landscape.

Excitation scheme. To create a polariton fluid we excite the microcavity with a continuous-wave single-mode Ti:sapphire laser resonant with the lower polariton branch. We use a confocal excitation scheme in which the laser is focused in an intermediate plane where a mask is placed to hide the upper part of the Gaussian spot. Then, an image of this intermediate plane is created on the sample, producing a spot with the shape of a half-Gaussian. Polaritons are resonantly injected into the microcavity with a well-defined wave vector, in the region above the defect. In these conditions, polaritons move out of the excitation spot with a free phase, no longer imposed by the pump beam. This is essential for the observation of quantum hydrodynamic effects involving topological excitations with phase discontinuities[9].

The momentum of the injected polaritons is set by the angle of incidence α of the excitation laser on the microcavity. This allows us to control the in-plane wave vector of the polariton fluid through the relation $k = k_0 \sin(\alpha)$, where k_0 is the wave vector of the laser field. At the injected polariton momentum $k = 1.3\,\mu m^{-1}$, the polariton velocity is $v_t = \hbar k/m_{pol} = 1.5\,\mu m\,ps^{-1}$ ($m_{pol} = 10^{-4} m_{electron}$). This velocity is higher than the speed of sound of the fluid for the polariton densities of our experiments, as evidenced by the presence of ship waves upstream of the obstacle in Fig. 2a (see ref. 23). For this value of the momentum, we measure a TE–TM splitting of 20 µeV, resulting in the effective magnetic field sketched in Fig. 1b.

Polaritons are photocreated in our microcavity with TM linear polarization. This corresponds to a pseudospin pointing in the direction of the flow as marked by the arrow in Fig. 1a.

Detection scheme. The observations reported in this work require the complete knowledge of the polariton spin. To gain this, a complete polarization tomography

of the emission is performed through the measurement of the three Stokes parameters $S_1 = (I_{TE} - I_{TM})/I_{tot}$, $S_2 = (I_D - I_A)/I_{tot}$ and $S_3 = (I_{\sigma+} - I_{\sigma-})/I_{tot}$, where I_j is the light intensity emitted with polarization j, and I_{tot} is the total emitted intensity. This requires measuring six different polarizations: I_H, I_V, I_{+45}, I_{-45}, $I_{\sigma+}$ and $I_{\sigma-}$, which, respectively, represent linear horizontal, linear vertical, linear diagonal, linear anti-diagonal, left circularly and right circularly polarized emitted intensity. A combination of wave plates and polarizing beam splitters is used to image each of the polarization components of the emitted light on a CCD camera.

Received 13 March 2012; accepted 19 July 2012; published online 26 August 2012

References

1. Dirac, P. A. M. Quantised singularities in the electromagnetic field. *Proc. R. Soc. Lond. A* **133,** 60–72 (1931).
2. Morris, D. J. P. *et al.* Strings and magnetic monopoles in the spin ice $Dy_2Ti_2O_7$. *Science* **326,** 411–414 (2009).
3. Bramwell, S. T. *et al.* Measurement of the charge and current of magnetic monopoles in spin ice. *Nature* **461,** 956–959 (2009).
4. Fennell, T. *et al.* Magnetic Coulomb phase in the spin ice $Ho_2Ti_2O_7$. *Science* **326,** 415–417 (2009).
5. Ono, T. *et al.* Propagation of a magnetic domain wall in a submicrometer magnetic wire. *Science* **284,** 468–470 (1999).
6. Busch, T. & Anglin, J. R. Wave-function monopoles in Bose–Einstein condensates. *Phys. Rev. A* **60,** R2669–R2672 (1999).
7. Stoof, H. T. C., Vliegen, E. & Al Khawaja, U. Monopoles in an antiferromagnetic Bose–Einstein condensate. *Phys. Rev. Lett.* **87,** 120407 (2001).
8. Pietilä, V. & Möttönen, M. Creation of Dirac monopoles in spinor Bose–Einstein condensates. *Phys. Rev. Lett.* **103,** 030401 (2009).
9. Amo, A. *et al.* Polariton superfluids reveal quantum hydrodynamic solitons. *Science* **332,** 1167–1170 (2011).
10. Grosso, G., Nardin, G., Morier-Genoud, F., Léger, Y. & Deveaud-Plédran, B. Soliton instabilities and vortex street formation in a polariton quantum fluid. *Phys. Rev. Lett.* **107,** 245301 (2011).
11. Kavokin, A., Malpuech, G. & Glazov, M. Optical spin Hall effect. *Phys. Rev. Lett.* **95,** 136601 (2005).
12. Flayac, H., Solnyshkov, D. D. & Malpuech, G. Oblique half-solitons and their generation in exciton–polariton condensates. *Phys. Rev. B* **83,** 193305 (2011).
13. Solnyshkov, D. D., Flayac, H. & Malpuech, G. Stable magnetic monopoles in spinor polariton condensates. *Phys. Rev. B* **85,** 073105 (2012).
14. Stenger, J. *et al.* Spin domains in ground-state Bose–Einstein condensates. *Nature* **396,** 345–348 (1998).
15. Leanhardt, A. E., Shin, Y., Kielpinski, D., Pritchard, D. E. & Ketterle, W. Coreless vortex formation in a spinor Bose–Einstein condensate. *Phys. Rev. Lett.* **90,** 140403 (2003).
16. Sadler, L. E., Higbie, J. M., Leslie, S. R., Vengalattore, M. & Stamper-Kurn, D. M. Spontaneous symmetry breaking in a quenched ferromagnetic spinor Bose–Einstein condensate. *Nature* **443,** 312–315 (2006).
17. Pitaevskii, L. & Stringari, S. *Bose–Einstein Condensation* (Clarendon, 2003).
18. Kavokin, A., Baumberg, J. J., Malpuech, G. & Laussy, F. P. *Microcavities* (Oxford Univ. Press, 2007).
19. Amo, A. *et al.* Light engineering of the polariton landscape in semiconductor microcavities. *Phys. Rev. B* **82,** 081301 (2010).
20. Wertz, E. *et al.* Spontaneous formation and optical manipulation of extended polariton condensates. *Nature Phys.* **6,** 860–864 (2010).
21. Sanvitto, D. *et al.* All-optical control of the quantum flow of a polariton superfluid. *Nature Photon.* **5,** 610–614 (2011).
22. Tosi, G. *et al.* Sculpting oscillators with light within a nonlinear quantum fluid. *Nature Phys.* **8,** 190–194 (2012).
23. Amo, A. *et al.* Superfluidity of polaritons in semiconductor microcavities. *Nature Phys.* **5,** 805–810 (2009).
24. Lagoudakis, K. G. *et al.* Quantized vortices in an exciton–polariton condensate. *Nature Phys.* **4,** 706–710 (2008).
25. Nardin, G. *et al.* Hydrodynamic nucleation of quantized vortex pairs in a polariton quantum fluid. *Nature Phys.* **7,** 635–641 (2011).
26. Renucci, P. *et al.* Microcavity polariton spin quantum beats without a magnetic field: A manifestation of Coulomb exchange in dense and polarized polariton systems. *Phys. Rev. B* **72,** 075317 (2005).
27. Rubo, Y. G. Half vortices in exciton polariton condensates. *Phys. Rev. Lett.* **99,** 106401–106404 (2007).
28. Lagoudakis, K. G. *et al.* Observation of half-quantum vortices in an exciton–polariton condensate. *Science* **326,** 974–976 (2009).
29. El, G. A., Gammal, A. & Kamchatnov, A. M. Oblique dark solitons in supersonic flow of a Bose–Einstein condensate. *Phys. Rev. Lett.* **97,** 180405 (2006).
30. Malpuech, G., Glazov, M. M., Shelykh, I. A., Bigenwald, P. & Kavokin, K. V. Electronic control of the polarization of light emitted by polariton lasers. *Appl. Phys. Lett.* **88,** 111118 (2006).

Acknowledgements

We thank R. Houdré for the microcavity sample and P. Voisin for fruitful discussions. This work was supported by the Agence Nationale de la Recherche (contract ANR-11-BS10-001), the RTRA (contract Boseflow1D), IFRAF, the FP7 ITNs Clermont4 (235114) and Spin-Optronics (237252), and the FP7 IRSES 'Polaphen' (246912). A.B. is a member of the Institut Universitaire de France.

Author contributions

All authors contributed to all aspects of this work.

Additional information

Supplementary information is available in the online version of the paper. Reprints and permissions information is available online at www.nature.com/reprints. Correspondence and requests for materials should be addressed to A.B. or A.A.

Competing financial interests

The authors declare no competing financial interests.

Appendix C.

List of publications and oral presentations

Communications

— Speaker at NIST/UMD seminar, Maryland, USA, September 2014
— Speaker at EPFL seminar, Lausanne, Switzerland, July 2014
— Speaker at CPDOS, Trieste, Italy, May 2014
— Speaker at LKB Quantum Optics group seminar, Paris, France, January 2014
— Poster presentation at EOCS13, Rome, Italy, September 2013
— Speaker at Quandid meeting, Marcoussi, France, September 2013
— Speaker at PLMCN14, Heraklion, Greece, April 2013
— Attended ISNP summer school, Phuket, Thailand, April 2012

Publications

— **T. Boulier**, H. Terças, D. D. Solnyshkov, Q. Glorieux, E. Giacobino, G. Malpuech and A. Bramati, Annular Vortex Chain in a Resonantly Pumped Polariton Superfluid., submitted on 22/10/2014
— E. Cancellieri, **T. Boulier**, R. Hivet, D. Ballarini, D. Sanvitto, M. H. Szymanska, C. Ciuti, E. Giacobino, A. Bramati, Merging of vortices and antivortices in polariton superfluids, submitted on 08/10/2014
— R. Hivet, E. Cancellieri, **T. Boulier**, D. Ballarini, D. Sanvitto, F. M. Marchetti, M. H. Szymanska, C. Ciuti, E. Giacobino, A. Bramati, Interaction-shaped vortex-antivortex lattices in polariton fluids, *Phys. Rev. B* **89,** 134501 (2014)
— **T. Boulier**, M. Bamba, A. Amo, C. Adrados, A. Lemaitre, E. Galopin, I. Sagnes, J.Bloch, C. Ciuti, E. Giacobino and A. Bramati, Polariton-Generated Intensity Squeezing in Semiconductor Micropillars, *Nature Communications* **5,** 3260 (2014)

— R. Hivet, H. Flayac, D. D. Solnyshkov, D. Tanese, **T. Boulier**, D. Andreoli, E. Giacobino, J. Bloch, A. Bramati, G. Malpuech and A. Amo, Half-solitons in a polariton quantum fluid behave like magnetic monopoles, *Nature Physics* **8,** 724–728 (2012)

Bibliography

[1] I. Carusotto and C. Ciuti. Quantum fluids of light. *Review of Modern Physic*, 85:299–366, February 2013.

[2] C. Weisbuch, M Nishioka, A Ishikawa, and Y Arakawa. Observation of the coupled exciton-photon mode splitting in a semiconductor quantum microcavity. *Physical Review Letters*, 69(23):3314, 1992.

[3] J. Bloch and J. Y. Marzin. Photoluminescence dynamics of cavity polaritons under resonant excitation in the picosecond range. *Physical Review B*, 56:2103, 1997.

[4] R. Houdré, C. Weisbuch, R. P. Stanley, U. Oesterle, P. Pellandini, and M. Ilegems. Measurement of cavity-polariton dispersion curve from angle-resolved photoluminescence experiments. *Physical Review Letter*, 73:2043, 1994.

[5] R. P. Stanley, C. Weisbuch, R. Houdré, U. Oesterle, and M. Ilegems. Cavity-polariton photoluminescence in semiconductor microcavities: Experimental evidence. *Physical Review B*, 53:10995, 1996.

[6] S. Christopoulos, G. Baldassarri Höger von Högersthal, A. J. D. Grundy, P. G. Lagoudakis, A. V. Kavokin, J. J. Baumberg, G. Christmann, R. Butté, E. Feltin, J.-F. Carlin, and N. Grandjean. Room-temperature polariton lasing in semiconductor microcavities. *Physical Review Letter*, 98:126405, March 2007.

[7] M. Romanelli. *Mélange à quatre ondes de polaritons dans des microcavités semiconductrices*. PhD thesis, Université Pierre et Marie Curie, 2005.

[8] J.Ph. Karr, A.Baas, R. Houdre, and E. Giacobino. Squeezing in semiconductor microcavities in the strong coupling regime. *Physical Review A*, 69:031802, 2004.

[9] T. Ostatnicky, D. Read, and A. V. Kavokin. Polarization and depolarization in scattering of cavity polaritons. *Physical Review B*, 80:115328, September 2009.

[10] A Amo, TCH Liew, C Adrados, R Houdré, E Giacobino, AV Kavokin, and A Bramati. Exciton–polariton spin switches. *Nature Photonics*, 4(6):361–366, 2010.

[11] A. Amo, S. Pigeon, C. Adrados, R. Houdré, E. Giacobino, C. Ciuti, and A. Bramati. Light engineering of the polariton landscape in semiconductor microcavities. *Physical Review B*, 82:081301, August 2010.

[12] D. Ballarini, M. De Giorgi, E. Cancellieri, R. Houdré, E. Giacobino, R. Cingolani, A. Bramati, G. Gigli, and D. Sanvitto. All-optical polariton transistor. *Nature Communications*, 4:1778, April 2013.

[13] A. Amo, J. Lefrère, S. Pigeon, C. Adrados, C. Ciuti, I. Carusotto, R. Houdré, E. Giacobino, and A. Bramati. Superfluidity of polaritons in semiconductor microcavities. *Nature Physics*, 5(11):805–810, 2009.

[14] A Amo, D Sanvitto, FP Laussy, D Ballarini, E Del Valle, MD Martin, A Lemaitre, J Bloch, DN Krizhanovskii, and MS Skolnick. Collective fluid dynamics of a polariton condensate in a semiconductor microcavity. *Nature*, 457(7227):291–295, 2009.

[15] K. G. Lagoudakis, M. Wouters, M. Richard, A. Baas, I. Carusotto, R. André, L. S. Dang, and B. Deveaud-Plédran. Quantized vortices in an exciton–polariton condensate. *Nature Physics*, 4(9):706–710, 2008.

[16] A Amo, S Pigeon, D Sanvitto, VG Sala, R Hivet, I Carusotto, F Pisanello, G Leménager, R Houdré, E Giacobino, C. Ciuti, and A. Bramati. Polariton superfluids reveal quantum hydrodynamic solitons. *Science*, 332(6034):1167–1170, 2011.

[17] M Sich, DN Krizhanovskii, MS Skolnick, Andriy V Gorbach, Robin Hartley, Dmitry V Skryabin, EA Cerda-Méndez, K Biermann, R Hey, and PV Santos. Observation of bright polariton solitons in a semiconductor microcavity. *Nature Photonics*, 6(1):50–55, 2012.

[18] G. Nardin, G. Grosso, Y. Léger, B. Pietka, F. Morier-Genoud, and B. Deveaud-Plédran. Hydrodynamic nucleation of quantized vortex pairs in a polariton quantum fluid. *Nature Physics*, 7(8):635–641, 2011.

[19] G Grosso, G Nardin, F Morier-Genoud, Y Léger, and B Deveaud-Plédran. Soliton instabilities and vortex street formation in a polariton quantum fluid. *Physical review letters*, 107(24):245301, 2011.

[20] R. Hivet, H. Flayac, D. D. Solnyshkov, D. Tanese, T. Boulier, D. Andreoli, E. Giacobino, J. Bloch, A. Bramati, G. Malpuech, and A. Amo. Half-solitons in a polariton quantum fluid behave like magnetic monopoles. *Nature Physics*, 8:724–728, 2012.

[21] J. Frenkel. On the transformation of light into heat in solids. i. *Physical Review*, 37:17–44, January 1931.

[22] W. Y. Liang. Excitons. *Physics Education*, 5:226–228, July 1970.

[23] R. Hivet. *Solitons, demi-solitons et réseaux de vortex dans un fluide quantique de polaritons*. PhD thesis, Université Pierre et Marie Curie, 2013.

[24] V. G. Sala. *Coherence, dynamics and polarization properties of polariton condensates in single and coupled micropillars*. PhD thesis, Université Pierre et Marie Curie, 2013.

[25] B. Deveaud, F. Clérot, N. Roy, K. Satzke, B. Sermage, and D. S. Katzer. Enhanced radiative recombination of free excitons in gaas quantum wells. *Physical Review Letter*, 67:2355–2358, October 1991.

[26] J.J. Hopfield. Theory of the contribution of excitons to the complex dielectric constant of crystals. *Physical Review*, 112:1555, 1958.

[27] D. Bajoni, M. Perrin, P. Senellart, A. Lemaître, B. Sermage, and J. Bloch. Dynamics of microcavity polaritons in the presence of an electron gas. *Physical Review B*, 73:205344, May 2006.

[28] H. A. Macleod. *Thin-film optical filters*. CRC Press, 2001.

[29] C. J. R. Sheppard. Approximate calculation of the reflection coefficient from a stratified medium. *Pure and Applied Optics : Journal of the European Optical Society Part A*, 4:665–669, 1995.

[30] H. Benisty, J.M. Gérard, R. Houdré, J. Rarity, and C. Weisbuch. Linear optical properties of semiconductor microcavities with embedded quantum wells, 1998. Confined Photon Systems, Fundamentals and Applications, Summerschool of Carghese, Corse.

[31] C. Leyder. *Optique Quantique et Dynamique de Spin dans les Microcavités Semiconductrices*. PhD thesis, Université Pierre et Marie Curie, 2007.

[32] A. Kavokin, J.J. Baumberg, G. Malpuech, and F.P. Laussy. *Microcavities*. Oxford University Press, 2007.

[33] J.P. Karr. *Effets non linéaires et quantiques dans les microcavités semi–conductrices*. PhD thesis, Université Pierre et Marie Curie, 2001.

[34] C. Ciuti, V. Savona, C. Piermarocchi, A. Quattropani, and P. Schwendimann. Threshold behavior in the collision broadening of microcavity polaritons. *Physical Review B*, 58:R10123–R10126, 1998.

[35] V. Savona, C. Piermarocchi, A. Quattropani, F. Tassone, and P. Schwendimann. Microscopic theory of motional narrowing of microcavity polaritons in a disordered potential. *Physical Review Letter*, 78:4470–4473, 1997.

[36] F. Tassone, C. Piermarocchi, V. Savona, A. Quattropani, and P. Schwendimann. Bottleneck effects in the relaxation and photoluminescence of microcavity polaritons. *Physical Review B*, 56:7554–7563, September 1997.

[37] D. Bajoni, P. Senellart, E. Wertz, I. Sagnes, A. Miard, A. Lemaître, and J. Bloch. Polariton laser using single micropillar gaas-gaalas semiconductor cavities. *Physical Review Letter*, 100:047401, January 2008.

[38] E. Wertz. *Formation spontanée de condensats de polaritons dans des microcavitées à base de GaAs*. PhD thesis, Université Paris–Sud 11, 2010.

[39] L. Ferrier, E. Wertz, R. Johne, D. D. Solnyshkov, P. Senellart, I. Sagnes, A. Lemaître, G. Malpuech, and J. Bloch. Interactions in confined polariton condensates. *Physical Review Letter*, 106:126401, March 2011.

[40] C. Ciuti, V. Savona, C. Piermarocchi, A. Quattropani, and P. Schwendimann. Role of the exchange of carriers in elastic exciton-exciton scattering in quantum wells. *Physical Review B*, 58:7928–7033, 1998.

[41] G. Rochat, C. Ciuti, V. Savona, C. Piermarocchi, A. Quattropani, and P. Schwendimann. Excitonic bloch equations for a two-dimensional system of interacting excitons. *Physical Review B*, 61:13856–13862, May 2000.

[42] C Ciuti, P Schwendimann, and A Quattropani. Theory of polariton parametric interactions in semiconductor microcavities. *Semiconductor science and technology*, 18(10):S279, 2003.

[43] A. Baas, J. Ph. Karr, H. Eleuch, , and E. Giacobino. Optical bistability in semiconductor microcavities. *Physical Review A*, 69:023809, 2004.

[44] T. Usui. Excitations in a high density electron gas. *Progress of Theoretical Physics*, 23:787, May 1960.

[45] C. Adrados. *Polaritons en microcavité semi-conductrice : dynamique de guide quantique, effets de spin et mesures de bruit en régime d'oscillation paramétrique*. PhD thesis, Université Pierre et Marie Curie, 2011.

[46] J. Kasprzak, M. Richard, S. Kundermann, A. Baas, P. Jeambrun, J. M. J. Keeling, F. M. Marchetti, M. H. Szymanska, R. André, J. L. Staehli, V. Savona, P. B. Littlewood, B. Deveaud, and Le Si Dang. Bose–einstein condensation of exciton polaritons. *Nature*, 443:409–414, September 2006.

[47] KG Lagoudakis, T Ostatnickỳ, AV Kavokin, YG Rubo, R André, and B Deveaud-Plédran. Observation of half-quantum vortices in an exciton-polariton condensate. *Science*, 326(5955):974–976, 2009.

[48] Y. G. Rubo. Half vortices in exciton polariton condensates. *Physical review letters*, 99(10):106401, 2007.

[49] Eugene P Gross. Structure of a quantized vortex in boson systems. *Il Nuovo Cimento Series 10*, 20(3):454–477, 1961.

[50] LP Pitaevskii. Vortex lines in an imperfect bose gas. *Sov. Phys. JETP*, 13(2):451–454, 1961.

[51] L Pitaevskii and Sandro Stringari. Bose-einstein condensation, 2003.

[52] SN Bose. Planck law and the light quantum hypothesis. *Z. Phys*, 26:178–181, 1924.

[53] A Einstein. Quantum theory of the monoatomic ideal gas. *Sitzungsberichte der Preussischen Akademie der Wissenschaften, Physikalischmathematische Klasse*, pages 261–267, 1924.

[54] M. H. Anderson, J. R. Ensher, M. R. Matthews, C. E. Wieman, and E. A. Cornell. Observation of bose-einstein condensation in a dilute atomic vapor. *science*, 269(5221):198–201, 1995.

[55] DN Krizhanovskii, KG Lagoudakis, M Wouters, B Pietka, RA Bradley, K Guda, DM Whittaker, MS Skolnick, B Deveaud-Plédran, Maxime Richard, et al. Coexisting nonequilibrium condensates with long-range spatial coherence in semiconductor microcavities. *Physical Review B*, 80(4):045317, 2009.

[56] JF Allen and AD Misener. Flow of liquid helium ii. *Nature*, 141(3558):75, 1938.

[57] P Kapitza. Viscosity of liquid helium below the l-point. *Nature*, 141(3558):74, 1938.

[58] F. London. On the bose-einstein condensation. *Physical Review*, 54(11):947, 1938.

[59] LD Landau. The theory of superfluidity of helium ii. *J. Phys*, 5(1):71–90, 1941.

[60] S Utsunomiya, L Tian, G Roumpos, CW Lai, N Kumada, T Fujisawa, M Kuwata-Gonokami, A Löffler, S Höfling, and A Forchel. Observation of bogoliubov excitations in exciton-polariton condensates. *Nature Physics*, 4(9):700–705, 2008.

[61] A Amo, TCH Liew, C Adrados, E Giacobino, AV Kavokin, and A Bramati. Anisotropic optical spin hall effect in semiconductor microcavities. *Physical Review B*, 80(16):165325, 2009.

[62] C. Ciuti and I. Carusotto. Quantum fluid effects and parametric instabilities in microcavities. *physica status solidi*, 242, issue 11:2224–2245, 2005.

[63] I. Carusotto and C. Ciuti. Probing microcavity polariton superfluidity through resonant rayleigh scattering. *Physical review letters*, 93(16):166401, 2004.

[64] R. W. Boyd. *Nonlinear optics*. Academic press, 2003.

[65] R. Boyd. *Contemporary nonlinear optics*. Academic Press, 1992.

[66] V. V. Dodonov and V. I. Man'ko. *Theory of nonclassical states of light*. CRC Press, 2003.

[67] A. Baas, J-Ph Karr, M. Romanelli, A. Bramati, and E. Giacobino. Optical bistability in semiconductor microcavities in the nondegenerate parametric oscillation regime: Analogy with the optical parametric oscillator. *Physical Review B*, 70(16):161307, 2004.

[68] EB Magnusson, IG Savenko, and IA Shelykh. Bistability phenomena in one-dimensional polariton wires. *Physical Review B*, 84(19):195308, 2011.

[69] NA Gippius, IA Shelykh, DD Solnyshkov, SS Gavrilov, Yuri G Rubo, AV Kavokin, SG Tikhodeev, and G Malpuech. Polarization multistability of cavity polaritons. *Physical review letters*, 98(23):236401, 2007.

[70] TK Paraïso, M Wouters, Y Léger, F Morier-Genoud, and B Deveaud-Plédran. Multistability of a coherent spin ensemble in a semiconductor microcavity. *Nature materials*, 9(8):655–660, 2010.

[71] D Sarkar, SS Gavrilov, M Sich, JH Quilter, RA Bradley, NA Gippius, K Guda, VD Kulakovskii, MS Skolnick, and DN Krizhanovskii. Polarization bistability and resultant spin rings in semiconductor microcavities. *Physical review letters*, 105(21):216402, 2010.

[72] C Adrados, A Amo, TCH Liew, R Hivet, R Houdré, E Giacobino, AV Kavokin, and A Bramati. Spin rings in bistable planar semiconductor microcavities. *Physical review letters*, 105(21):216403, 2010.

[73] G. Grynberg, A. Aspect, and C. Fabre. *Introduction aux lasers et à l'optique quantique*. Ecole polytechnique, Département de physique, 1997.

[74] Le Si Dang, D Heger, R André, F Boeuf, and R Romestain. Stimulation of polariton photoluminescence in semiconductor microcavity. *Physical Review Letters*, 81(18):3920, 1998.

[75] PG Savvidis, JJ Baumberg, RM Stevenson, MS Skolnick, DM Whittaker, and JS Roberts. Angle-resonant stimulated polariton amplifier. *Physical Review Letters*, 84(7):1547, 2000.

[76] G. Messin. *Luminescence, bruit et effets non linéaires dans les microcavitées semiconductrices*. PhD thesis, Université Pierre et Marie Curie, 2000.

[77] A. L. Fetter. Vortices in an imperfect bose gas. i. the condensate. *Physical Review*, 138(2A):A429, 1965.

[78] MP Kawatra and RK Pathria. Quantized vortices in an imperfect bose gas and the breakdown of superfluidity in liquid helium ii. *Physical Review*, 151(1):132, 1966.

[79] F. Chevy, K. W. Madison, and J. Dalibard. Measurement of the angular momentum of a rotating bose-einstein condensate. *Physical Review Letter*, 85:2223–2227, September 2000.

[80] A. A. Abrikosov. *Sov. Phys. JETP*, 5:1174, 1957.

[81] KW Madison, F Chevy, W Wohlleben, and J Dalibard. Vortex formation in a stirred bose-einstein condensate. *Physical Review Letters*, 84(5):806, 2000.

[82] A. Imamoglu, R. J. Ram, S. Pau, and Y. Yamamoto. Nonequilibrium condensates and lasers without inversion: Exciton-polariton lasers. *Physical Review A*, 53:4250–4253, June 1996.

[83] A. J. Leggett. Nobel lecture: Superfluid 3 he: the early days as seen by. *Reviews of modern physics*, 76, 2004.

[84] P. Nozières and D. Pines. *The theory of quantum liquids*. Perseus, 1999.

[85] G. D. Mahan. *Many-particle physics*. Springer, 2000.

[86] J. R. Schrieffer. *Theory of superconductivity, Advanced book classics*. Perseus Books, Reading, 1999.

[87] M. Tinkham. *Introduction to superconductivity*. Courier Dover Publications, 2012.

[88] I. Bloch, J. Dalibard, and W. Zwerger. Many-body physics with ultracold gases. *Reviews of Modern Physics*, 80(3):885, 2008.

[89] F. Dalfovo, S. Giorgini, L. P. Pitaevskii, and S. Stringari. Theory of bose-einstein condensation in trapped gases. *Reviews of Modern Physics*, 71(3):463, 1999.

[90] S. Giorgini, L. P. Pitaevskii, and S. Stringari. Theory of ultracold atomic fermi gases. *Reviews of Modern Physics*, 80(4):1215, 2008.

[91] S. Sarkar, H. Satz, and B.C. Sinha. *The physics of the quark-gluon plasma*. Springer, 2010.

[92] K. Yagi, T. Hatsuda, and Y. Miake. *Quark-gluon plasma: From big bang to little bang*, volume 23. Cambridge University Press, 2005.

[93] P. Ring and P. Schuck. *The nuclear many-body problem*. Springer, 2004.

[94] W. Heisenberg and H. Euler. Folgerungen aus der diracschen theorie des positrons. *Zeitschrift für Physik*, 98(11-12):714–732, 1936.

[95] P. N. Butcher and D. Cotter. *The elements of nonlinear optics*, volume 9. Cambridge University Press, 1991.

[96] M. Brambilla, L. A. Lugiato, V. Penna, F. Prati, C. Tamm, and C. O. Weiss. Transverse laser patterns. ii. variational principle for pattern selection, spatial multistability, and laser hydrodynamics. *Physical Review A*, 43:5114–5120, May 1991.

[97] K Staliunas. Laser ginzburg-landau equation and laser hydrodynamics. *Physical Review A*, 48(2):1573, 1993.

[98] G. A. Swartzlander and C. T. Law. Optical vortex solitons observed in kerr nonlinear media. *Physical Review Letter*, 69:2503–2506, October 1992.

[99] M. Vaupel, K. Staliunas, and C. O. Weiss. Hydrodynamic phenomena in laser physics: Modes with flow and vortices behind an obstacle in an optical channel. *Physical Review A*, 54:880–892, July 1996.

[100] A. Griffin, D. W. Snoke, and S. Stringari. *Bose-Einstein Condensation*. Cambridge University Press, 1996.

[101] JP Eisenstein and AH MacDonald. Bose–einstein condensation of excitons in bilayer electron systems. *Nature*, 432(7018):691–694, 2004.

[102] LV Butov. Cold exciton gases in coupled quantum well structures. *Journal of Physics: Condensed Matter*, 19(29):295202, 2007.

[103] AA High, JR Leonard, M Remeika, LV Butov, M Hanson, and AC Gossard. Condensation of excitons in a trap. *Nano letters*, 12(5):2605–2609, 2012.

[104] J. J. Baumberg, P. G. Savvidis, R. M. Stevenson, A. I. Tartakovskii, M. S. Skolnick, D. M. Whittaker, and J. S. Roberts. Parametric oscillation in a vertical microcavity: A polariton condensate or micro-optical parametric oscillation. *Physical Review B*, 62:R16247–R16250, December 2000.

[105] R. M. Stevenson, V. N. Astratov, M. S. Skolnick, D. M. Whittaker, M. Emam-Ismail, A. I. Tartakovskii, P. G. Savvidis, J. J. Baumberg, and J. S. Roberts. Continuous wave observation of massive polariton redistribution by stimulated scattering in semiconductor microcavities. *Physical Review Letter*, 85:3680–3683, October 2000.

[106] C. Ciuti, P. Schwendimann, B. Deveaud, and A. Quattropani. Theory of the angle-resonant polariton amplifier. *Physical Review B*, 62:R4825–R4828, August 2000.

[107] C. Ciuti, P. Schwendimann, and A. Quattropani. Parametric luminescence of microcavity polaritons. *Physical Review B*, 63:041303, January 2001.

[108] D. M. Whittaker. Classical treatment of parametric processes in a strong-coupling planar microcavity. *Physical Review B*, 63:193305, April 2001.

[109] A. Baas, J.-Ph. Karr, M. Romanelli, A. Bramati, and E. Giacobino. Quantum degeneracy of microcavity polaritons. *Physical Review Letter*, 96:176401, May 2006.

[110] I. Carusotto and C. Ciuti. Spontaneous microcavity-polariton coherence across the parametric threshold: Quantum monte carlo studies. *Physical Review B*, 72:125335, September 2005.

[111] H. Deng, G. Weihs, C. Santori, J. Bloch, and Y. Yamamoto. Condensation of semiconductor microcavity exciton polaritons. *Science*, 298(5591):199–202, 2002.

[112] M Richard, J Kasprzak, R André, R Romestain, Le Si Dang, G Malpuech, and A Kavokin. Experimental evidence for nonequilibrium bose condensation of exciton polaritons. *Physical Review B*, 72(20):201301, 2005.

[113] M. Richard, J. Kasprzak, R. Romestain, R. André, and L. S. Dang. Spontaneous coherent phase transition of polaritons in cdte microcavities. *Physical review letters*, 94(18):187401, 2005.

[114] J Scheuer and M Orenstein. Optical vortices crystals: Spontaneous generation in nonlinear semiconductor microcavities. *Science*, 285(5425):230–233, 1999.

[115] R. Y. Chiao and J. Boyce. Bogoliubov dispersion relation and the possibility of superfluidity for weakly interacting photons in a two-dimensional photon fluid. *Physical Review A*, 60:4114–4121, November 1999.

[116] A. Tanzini and S. P. Sorella. Bose–einstein condensation and superfluidity of a weakly-interacting photon gas in a nonlinear fabry–perot cavity. *Physics Letters A*, 263(1):43–47, 1999.

[117] E. L. Bolda, R. Y. Chiao, and W. H. Zurek. Dissipative optical flow in a nonlinear fabry-pérot cavity. *Physical Review Letter*, 86:416–419, January 2001.

[118] D Sanvitto, S Pigeon, A Amo, D Ballarini, M De Giorgi, I Carusotto, R Hivet, F Pisanello, VG Sala, and PSS Guimaraes. All-optical control of the quantum flow of a polariton condensate. *Nature photonics*, 5(10):610–614, 2011.

[119] CO Weiss. Spatio-temporal structures. part ii. vortices and defects in lasers. *Physics reports*, 219(3):311–338, 1992.

[120] CO Weiss, HR Telle, K Staliunas, and M Brambilla. Restless optical vortex. *Physical Review A*, 47(3):R1616, 1993.

[121] S. Pigeon, I. Carusotto, and C. Ciuti. Hydrodynamic nucleation of vortices and solitons in a resonantly excited polariton superfluid. *Physical Review B*, 83:144513, April 2011.

[122] G. Roumpos, M. D Fraser, A. Löffler, S. Höfling, A. Forchel, and Y. Yamamoto. Single vortex-antivortex pair in an exciton-polariton condensate. *Nature Physics*, 7(2):129–133, 2011.

[123] F Manni, TCH Liew, KG Lagoudakis, C Ouellet-Plamondon, R André, V Savona, and B Deveaud. Spontaneous self-ordered states of vortex-antivortex pairs in a polariton condensate. *Physical Review B*, 88(20):201303, 2013.

[124] Zhenghan W. *Topological quantum computation*. Number 112. American Mathematical Soc., 2010.

[125] M. Freedman, A. Kitaev, M. Larsen, and Z. Wang. Topological quantum computation. *Bulletin of the American Mathematical Society*, 40(1):31–38, 2003.

[126] C. Nayak, Steven H Simon, Ady Stern, Michael Freedman, and Sankar Das Sarma. Non-abelian anyons and topological quantum computation. *Reviews of Modern Physics*, 80(3):1083, 2008.

[127] R Houdré, C Weisbuch, RP Stanley, U Oesterle, and M Ilegems. Coherence effects in light scattering of two-dimensional photonic disordered systems: Elastic scattering of cavity polaritons. *Physical Review B*, 61(20):R13333, 2000.

[128] R Houdré, C Weisbuch, RP Stanley, U Oesterle, and M Ilegems. Nonlinear emission of semiconductor microcavities in the strong coupling regime. *Physical review letters*, 85(13):2793, 2000.

[129] Vincenzo Savona. Effect of interface disorder on quantum well excitons and microcavity polaritons. *Journal of Physics: Condensed Matter*, 19(29):295208, 2007.

[130] K. G. Lagoudakis, F. Manni, B. Pietka, M. Wouters, T. C. H. Liew, V. Savona, A. V. Kavokin, R. André, and B. Deveaud-Plédran. Probing the dynamics of spontaneous quantum vortices in polariton superfluids. *Physical Review Letter*, 106:115301, March 2011.

[131] M. D. Fraser, G. Roumpos, and Y. Yamamoto. Vortex–antivortex pair dynamics in an exciton–polariton condensate. *New Journal of Physics*, 11(11):113048, 2009.

[132] A. Baas. *Amplification paramétrique et réduction du bruit quantique dans des microcavités semiconductrices*. PhD thesis, Université Pierre et Marie Curie-Paris VI, 2003.

[133] Eric L. Bolda and Dan F. Walls. Detection of vorticity in bose-einstein condensed gases by matter-wave interference. *Physical Review Letter*, 81:5477–5480, December 1998.

[134] D Sanvitto, FM Marchetti, MH Szymańska, G Tosi, M Baudisch, FP Laussy, DN Krizhanovskii, MS Skolnick, L Marrucci, A Lemaitre, J Bloch, C Tejedor, and L Vina. Persistent currents and quantized vortices in a polariton superfluid. *Nature Physics*, 6(7):527–533, 2010.

[135] L. Dominici, J. M Fellows, S. Donati, D. Ballarini, M. De Giorgi, F. M. Marchetti, B. Piccirillo, L. Marrucci, A. Bramati, and G. Gigli. Vortex and half-vortex stability in coherently driven spinor polariton fluid. *arXiv preprint arXiv:1403.0487*, 2014.

[136] G Tosi, G Christmann, NG Berloff, P Tsotsis, T Gao, Z Hatzopoulos, PG Savvidis, and JJ Baumberg. Geometrically locked vortex lattices in semiconductor quantum fluids. *Nature communications*, 3:1243, 2012.

[137] M. Vladimirova, S. Cronenberger, D. Scalbert, KV Kavokin, A. Miard, A. Lemaître, J. Bloch, D Solnyshkov, G. Malpuech, and AV Kavokin. Polariton-polariton interaction constants in microcavities. *Physical Review B*, 82(7):075301, 2010.

[138] R. Hivet, E. Cancelieri, T. Boulier, D. Ballarini, D. Sanvitto, F. M. Marchetti, M. H. Szymanska, C. Ciuti, E. Giacobino, and A. Bramati. interaction-shaping vortex-antivortex lattices in polariton fluid. *Physical Review B*, 89:134501, 2014.

[139] C. Leyder, M. Romanelli, J. Ph. Karr, E. Giacobino, T. C. H. Liew, M. M. Glazov, A. V. Kavokin, G. Malpuech, and A Bramati. Observation of the optical spin hall effect. *Nature Physics*, 3:628–631, 2007.

[140] P Cristofolini, A Dreismann, G Christmann, G Franchetti, NG Berloff, P Tsotsis, Z Hatzopoulos, PG Savvidis, and JJ Baumberg. Optical superfluid phase transitions and trapping of polariton condensates. *Physical review letters*, 110(18):186403, 2013.

[141] A. Dreismann, P. Cristofolini, R. Balili, G. Christmann, F. Pinsker, N. G. Berloff, Z. Hatzopoulos, P. G. Savvidis, and J. J. Baumberg. Coupled counterrotating polariton condensates in optically defined annular potentials. *Proceedings of the National Academy of Sciences*, page 201401988, 2014.

[142] J. Keeling and N. G. Berloff. Spontaneous rotating vortex lattices in a pumped decaying condensate. *Physical review letters*, 100(25):250401, 2008.

[143] M. O Borgh, G. Franchetti, J. Keeling, and N. G. Berloff. Robustness and observability of rotating vortex lattices in an exciton-polariton condensate. *Physical Review B*, 86(3):035307, 2012.

[144] JO Hamp, AK Balin, FM Marchetti, D Sanvitto, and MH Szymanska. Spontaneous vortex arrays in a parametrically driven polariton condensate. *arXiv preprint arXiv:1403.3234*, 2014.

[145] J. Morizur, L. Nicholls, P. Jian, S. Armstrong, N. Treps, B. Hage, M. Hsu, W. Bowen, J. Janousek, and H.-A. Bachor. Programmable unitary spatial mode manipulation. *JOSA A*, 27(11):2524–2531, 2010.

[146] J-F Morizur, S Armstrong, N Treps, J Janousek, and H-A Bachor. Spatial reshaping of a squeezed state of light. *The European Physical Journal D-Atomic, Molecular, Optical and Plasma Physics*, 61(1):237–239, 2011.

[147] G. Labroille, B. Denolle, P. Jian, P. Genevaux, N. Treps, and J. Morizur. Efficient and mode selective spatial mode multiplexer based on multi-plane light conversion. *arXiv preprint arXiv:1404.6455*, 2014.

[148] S. Armstrong, J.-F. Morizur, J. Janousek, B. Hage, N. Treps, P. K. Lam, and H.-A. Bachor. Programmable multimode quantum networks. *Nature communications*, 3:1026, 2012.

[149] A. L. Fetter. Rotating trapped bose-einstein condensates. *Reviews of Modern Physics*, 81(2):647, 2009.

[150] EB Sonin. Continuum theory of tkachenko modes in rotating bose-einstein condensate. *Physical Review A*, 71(1):011603, 2005.

[151] I Coddington, P Engels, V Schweikhard, and EA Cornell. Observation of tkachenko oscillations in rapidly rotating bose-einstein condensates. *Physical review letters*, 91(10):100402, 2003.

[152] G. Franchetti, Natalia G. Berloff, and J. J. Baumberg. Exploiting quantum coherence of polaritons for ultra sensitive detectors. *arXiv preprint arXiv:1210.1187*, 2012.

[153] H. Eleuch. *Etude théorique des fluctuations quantiques dans la lumière sortant d'une microcavité semiconductrice*. PhD thesis, Université Pierre et Marie Curie-Paris VI, 1998.

[154] H Eleuch, JM Courty, G Messin, C Fabre, and E Giacobino. Cavity qed effects in semiconductor microcavities. *Journal of Optics B: Quantum and Semiclassical Optics*, 1(1):1, 1999.

[155] P. Schwendimann, C. Ciuti, and A. Quattropani. Statistics of polaritons in the nonlinear regime. *Physical Review B*, 68(16):165324, 2003.

[156] Motoaki Bamba, Simon Pigeon, and Cristiano Cuiti. Quantum squeezing generation versus photon localization in a disordered planar microcavity. *Physical Review Lett*, 104:213604, 2010.

[157] TCH Liew and V Savona. Multipartite polariton entanglement in semiconductor microcavities. *Physical Review A*, 84(3):032301, 2011.

[158] TCH Liew and V Savona. Quantum entanglement in nanocavity arrays. *Physical Review A*, 85(5):050301, 2012.

[159] AM Fox, JJ Baumberg, M Dabbicco, B Huttner, and JF Ryan. Squeezed light generation in semiconductors. *Physical review letters*, 74(10):1728, 1995.

[160] Arnaud Verger, Cristiano Ciuti, and Iacopo Carusotto. Polariton quantum blockade in a photonic dot. *Physical Review B*, 73(19):193306, 2006.

[161] RJ Glauber, C DeWitt, A Blandin, and Co Cohen-Tannoudji. Quantum optics and electronics, 1965.

[162] T. Kreis. Holographic interferometry: principles and methods. In *Simulation and Experiment in Laser Metrology: Proceedings of the International Symposium on Laser Applications in Precision Measurements Held in Balatonfüred/Hungary, June 3-6, 1996*, volume 2, page 323. John Wiley & Sons, 1996.